

QUANTUM METROLOGY USING LARGE ENSEMBLES OF  
ENTANGLED ATOMS

A DISSERTATION  
SUBMITTED TO THE DEPARTMENT OF PHYSICS  
AND THE COMMITTEE ON GRADUATE STUDIES  
OF STANFORD UNIVERSITY  
IN PARTIAL FULFILLMENT OF THE REQUIREMENTS  
FOR THE DEGREE OF  
DOCTOR OF PHILOSOPHY

Nils Johan Engelsen

December 2016

© 2016 by Nils Johan Engelsen. All Rights Reserved.  
Re-distributed by Stanford University under license with the author.



This work is licensed under a Creative Commons Attribution-  
Noncommercial 3.0 United States License.  
<http://creativecommons.org/licenses/by-nc/3.0/us/>

This dissertation is online at: <http://purl.stanford.edu/th219jv5647>

I certify that I have read this dissertation and that, in my opinion, it is fully adequate in scope and quality as a dissertation for the degree of Doctor of Philosophy.

**Mark Kasevich, Primary Adviser**

I certify that I have read this dissertation and that, in my opinion, it is fully adequate in scope and quality as a dissertation for the degree of Doctor of Philosophy.

**Leo Hollberg**

I certify that I have read this dissertation and that, in my opinion, it is fully adequate in scope and quality as a dissertation for the degree of Doctor of Philosophy.

**Monika Schleier-Smith**

Approved for the Stanford University Committee on Graduate Studies.

**Patricia J. Gumpert, Vice Provost for Graduate Education**

*This signature page was generated electronically upon submission of this dissertation in electronic format. An original signed hard copy of the signature page is on file in University Archives.*

# Abstract

Atomic sensors are pushing the boundaries in precision for timekeeping, magnetometry, and gravity gradiometry. Conventional atomic sensors achieve impressive performance, but are ultimately limited by the quantum projection noise. The quantum projection noise arises due to the counting statistics of uncorrelated particles. In quantum metrology, this limit on sensing precision is circumvented by exploiting entanglement—quantum correlations between the atoms. A promising path to quantum metrology with atoms is the generation of spin-squeezed states.

A precise, collective quantum non-demolition measurement on an ensemble of atoms can be used to create spin-squeezed states. This work was therefore predominantly focused on constructing a cavity-based detection system capable of non-destructive measurement of the  $^{87}\text{Rb}$  hyperfine clock states. Using this detection system, spin-squeezed states of  $5 \times 10^5$   $^{87}\text{Rb}$  atoms with sensing capability 20.0(3) dB below the quantum projection noise were demonstrated. Proof of principle metrology was then performed showing 18.5(3) dB quantum enhancement with  $6.5 \times 10^5$  atoms. The single-shot phase resolution of this system surpasses the best unentangled cold atom sensors. Finally, an atomic clock with 10.5(3) dB-squeezed states was demonstrated, showing 11 times faster averaging than an unentangled atomic clock with the same atom number.

The entanglement of the spin-squeezed states was characterized by showing that the states contain ensembles of at least 1590(130) entangled particles. Additionally, it was demonstrated that the states contain Bell correlations—correlations stronger than those allowed by classical physics—to 124 standard deviations of statistical significance.

All previous methods for entanglement-enhanced measurement have been limited by the performance of the detection system. In this thesis, a method called quantum phase magnification was developed that circumvents this requirement. The quantum phase magnification scheme demonstrated 8 dB metrological enhancement using a fluorescence detection system operating at 10 dB above the quantum projection noise. Quantum phase magnification can be used to perform quantum metrology in many systems where detection beyond the quantum projection noise limit is impractical.

# Acknowledgments

First of all, I want to thank my advisor Mark Kasevich. Mark’s unbridled enthusiasm for physics and doing important work is inspiring. Mark has the ability to not only pull factors of 10 out of thin air, but to also make you believe it is achievable. His help in finding the component adding noise to your measurement is invaluable. When working on a precision measurement experiment, it is tempting to always strive for perfection. It is therefore good to have Mark’s voice of sanity asking if you really need to understand this thing, or if you’re at a stage where it’s ‘good enough for government work’ and you should ‘get the data while it’s running’.

I would also like to thank my examination committee, Mark Kasevich, Monika Schleier-Smith, Leo Hollberg, Amir Safavi-Naeini, and Mary Wootters, for their time. I am also grateful to my reading committee, consisting of Mark, Leo and Monika, for their comments on the thesis, which greatly improved it.

I will be grateful if I ever get to work with another scientist as talented as my postdoc Onur Hosten. Onur epitomizes the absent-minded scientist—his most uttered phrase in the lab is ‘What was I doing?’’. Onur is uniquely gifted in both theory and experiment—he is someone who can both bring you the post-it note with the correct equation describing the experiment and build auto-locking, high bandwidth feedback circuits. Rajiv Krishnakumar has been my fellow graduate student for most of graduate school, his early schedule complements mine and ensures that there is someone around for surprise morning visits. Raj’s good sense of humor keeps us all from frustration in the face of experimental physics. Yunfan Wu joined the group towards the end of my PhD. Her eagerness to learn and good attitude brightens up the lab and I am sure she will do a good job taking over the experiment.

The true enabler of great experimental work is to have an apparatus that makes the study of rich physics possible. For this, I am indebted to Geert Vrijsen, Jongmin Lee, and Igor Teper, who built the initial version of the apparatus. I also want to especially thank Geert Vrijsen. Geert taught me a lot in the time we overlapped and instilled in me the Kasevich group spirit. I hope he is proud his monkey is now fully trained.

I would like to thank the rest of the Kasevich group members, both past and present: Catherine Kealhofer, Brannon Klopfer, Alex Sugarbaker, Christoph Kohstall, Joshua Francis, Gunnar Skulason, Seth Foreman, Peter Asenbaum, Jason Hogan, Susannah Dickerson, David Berryrieser, Chris Overstreet, Christine Donnelly, Kaspar Sakmann, Raphaël Bouganne, Fan Xiao, Tim Kovachy, Sheng-wey Chow, Hui-Chun Chien, Jan Rudolph, Patrick Medley, Michael Minar, Stewart Koppell, and Thomas Juffmann. Sean Roy deserves special thanks for teaching the cavity QED group to multiply by 1.024. Special thanks to Jan Rudolph, while his AOM coupling techniques will not be forgotten, his main contribution for me was to pass on his love and appreciation of coffee, and teaching me how to use the Varian espresso machine.

My office mates through the years deserve an extra mention—Joshua Francis, Seth Foreman, Geert Vrijsen, Jongmin Lee, Rajiv Krishnakumar, Gunnar Skulason, Brannon Klopfer, Yunfan Wu, and Fan Xiao. They have had to endure more than their fair share of identified and unidentified flying objects. While Brannon’s open source enthusiasm can get the best of us all at times, his programming and Blender expertise will be sorely missed. Hopefully, the barcode scanner will remain a hobby. Without Gunnar, it has been substantially more difficult to figure out if something can be put under vacuum and to get food on campus after 6 pm.

The Schleier-Smith group has also been a great addition to the Varian building hallway. Their enthusiasm for building cavities as well as baking is appreciated amongst all Kasevich group members.

The Kasevich group administrators, Ping and Sha, deserve a lot of credit for helping with all the paperwork involved in doing research and completing a PhD. Similarly, I also want to thank the Physics Student Services Officer, Maria Frank, for her help in navigating Stanford’s paperwork requirements.

I really enjoyed making things in the machine shop—there is nothing quite like a fly-cut piece of aluminum. I want to thank Mehmet for teaching me things that I could never learn from a book, as well as Karlheinz and the rest of the machine shop staff for keeping things in order.

Alex Sugarbaker introduced me to great beer and helped Deborah and I find lodging. Together with Matt Sieth, he also introduced me to board games. I think I have played every board game in existence with Matt, but only once. We have been very happy to stay at 94 Palmer this past year—the housemates have been good company.

I also want to thank my batchmates, Dickson, Jimmy, Max, and Yonas. I hope they will remember that mathematical rigor is not allowed after 10.30 pm. Furthermore, I would like to thank my friends inside and outside the Stanford physics department. Their support and friendship has been much appreciated.

My parents have been very supportive of me throughout my (long) education and I am grateful to them both for coming to visit me during my studies here. My father, Steinar, taught me physics and mathematics at a young age. I look forward to going reindeer hunting again when I am closer. My mother, Ingvild, ensured I was more well-rounded and not spend my entire youth playing computer games—I am grateful for those tennis lessons now. My brother Peder will be a doctor only shortly after me. I am glad that we also have a medical doctor in the family—after all not every problem can be solved with physics.

Additionally, I want to thank my grandparents, Nils Johan, Ingrid (Fanni), Gudmund, and Marit. My grandfather, Nils Johan, is the only other family member with a PhD. He completed his PhD in Theology at Yale. I am grateful for the times I had with him as a child, throwing rocks in the water to make big splashes. His wife, Ingrid, taught me to read while looking after me in the day. I hope they would both be proud. I hope to visit Marit and Gudmund more often in the coming years. The lessons in project management (building a treehouse) from Gudmund came in handy during my PhD. Deborah and I are always happy to be invited to their home when we are in Norway.

While I have been far away from my family for the last six years, I am always

happy to come home for Christmas or otherwise, and I hope that now I will be able to visit more often and go on trips to Beitostølen.

I am proud to be married to my wife, Deborah. She has supported me every step of the way through graduate school and I am fortunate that she joined me at Stanford for the last year.

# Contents

<b>Abstract</b>	<b>iv</b>
<b>Acknowledgments</b>	<b>vi</b>
<b>1 Introduction</b>	<b>1</b>
<b>2 Atoms, cavities, and spin-squeezing</b>	<b>5</b>
2.1 Introduction to squeezing . . . . .	6
2.1.1 The Bloch sphere model . . . . .	6
2.2 The optical cavity . . . . .	9
2.2.1 The dispersive signal . . . . .	9
2.2.2 Cavity QED for spin-squeezing . . . . .	11
2.3 Spin-squeezing methods and limits . . . . .	16
2.3.1 Cavity-aided quantum non-demolition measurement . . . . .	16
2.3.2 Atomic scattering into free space . . . . .	17
2.3.3 Limits on measurement-induced squeezing . . . . .	18
2.3.4 Atom-cavity coupling inhomogeneity . . . . .	22
2.3.5 Squeezing through collective interactions . . . . .	24
2.3.6 Introduction to quantum phase magnification . . . . .	25
2.3.7 Magnification limits . . . . .	33
2.3.8 Antisqueezing from QND measurement . . . . .	35
2.4 Entanglement measures . . . . .	37
2.4.1 Entanglement depth in symmetric states . . . . .	37
2.4.2 Entanglement depth in nonsymmetric states . . . . .	39

2.4.3	Coherence for entanglement bounds . . . . .	41
2.4.4	Symmetric and nonsymmetric coherence . . . . .	43
<b>3</b>	<b>Experimental apparatus</b>	<b>45</b>
3.1	Cold atom source . . . . .	46
3.1.1	Vacuum chamber . . . . .	46
3.1.2	Laser setup . . . . .	46
3.1.3	Microwave source . . . . .	51
3.1.4	State preparation . . . . .	53
3.1.5	Fluorescence imaging . . . . .	53
3.1.6	Atom cooling . . . . .	59
3.1.7	Timing sequence . . . . .	66
3.2	Dual-wavelength optical cavity . . . . .	69
3.2.1	Cavity parameters . . . . .	71
3.2.2	Cavity laser stabilization . . . . .	71
3.2.3	Cavity-atom detuning stabilization . . . . .	74
3.2.4	Lattice intensity stabilization . . . . .	76
3.2.5	Homodyne detection module . . . . .	78
3.2.6	Probe detuning stabilization . . . . .	81
3.2.7	Cavity frequency measurement . . . . .	84
3.3	Characterization of atom-cavity interactions . . . . .	89
3.3.1	ac-Stark shift measurements . . . . .	89
3.3.2	Atom-cavity coupling measurement . . . . .	89
3.3.3	Lattice characterization . . . . .	90
3.3.4	Measurement of atom-broadened linewidth . . . . .	97
3.3.5	Effect of thermal atoms . . . . .	100
3.3.6	Cavity-atom coupling as a function of atom number . . . . .	102
<b>4</b>	<b>Spin-squeezing through measurement</b>	<b>104</b>
4.1	Squeezed state characterization . . . . .	104
4.1.1	Coherent state noise . . . . .	104
4.1.2	Pre-squeezing . . . . .	105

4.1.3	Squeezing as a function of measurement strength . . . . .	109
4.1.4	Characterization of anti-squeezing . . . . .	111
4.1.5	Coherence measurements . . . . .	113
4.1.6	Saturation of squeezing with atom number . . . . .	114
4.2	Quantum metrology demonstrations . . . . .	118
4.2.1	Measurement of a small rotation . . . . .	118
4.2.2	Squeezed atomic clock demonstration . . . . .	119
4.3	Free-space release and entanglement . . . . .	122
4.3.1	Inhomogeneity analysis for free-space release . . . . .	122
4.3.2	Calculation of entanglement depth . . . . .	127
<b>5</b>	<b>Bell Correlations in squeezed states</b>	<b>130</b>
5.1	Witnesses of Bell correlations . . . . .	131
5.2	Experimental demonstration of Bell correlations . . . . .	134
5.2.1	Conditionally squeezed states in Bell inequalities . . . . .	141
5.3	Error calculations and statistical significance . . . . .	141
5.4	Conclusion . . . . .	142
<b>6</b>	<b>Quantum phase magnification</b>	<b>144</b>
6.1	Squeezed state generation through collective interactions . . . . .	146
6.2	Basic magnification scheme . . . . .	147
6.3	Noise re-focusing scheme . . . . .	152
6.3.1	Noise-refocusing measurement-squeezed states . . . . .	153
<b>7</b>	<b>Conclusions and further work</b>	<b>158</b>
<b>A</b>	<b>The dispersive signal</b>	<b>160</b>
	<b>Bibliography</b>	<b>166</b>

# List of Tables

3.1	List of cooling stage parameters . . . . .	62
3.2	Timing sequence . . . . .	68
3.3	List of important cavity parameters . . . . .	70
5.1	Table of Bell violation $p$ -values . . . . .	143

# List of Figures

2.1	Coherent and squeezed state displayed on Bloch spheres . . . . .	7
2.2	Illustration of Wineland criterion . . . . .	8
2.3	Cavity-atom probe detuning . . . . .	16
2.4	Shearing interaction . . . . .	26
2.5	Quantum phase magnification illustration . . . . .	27
3.1	Top-down view of vacuum chamber . . . . .	47
3.2	Picture of vacuum chamber . . . . .	48
3.3	Rubidium laser setup . . . . .	49
3.4	Overview of push beam and beatnote setup . . . . .	50
3.5	Microwave generation . . . . .	51
3.6	Composite $\pi/2$ -pulse Bloch sphere trajectory . . . . .	52
3.7	Amplitude sensitivity of composite $\pi/2$ -pulse . . . . .	54
3.8	State preparation sequence . . . . .	55
3.9	Sample state tomography images . . . . .	57
3.10	State tomography calibration curve . . . . .	58
3.11	Sample time-of-flight temperature measurement . . . . .	60
3.12	Sample image fits . . . . .	61
3.13	Lasing peaks during cooling . . . . .	64
3.14	Raman lasing threshold behavior . . . . .	65
3.15	Temperatures before and after tuning of cooling parameters . . . . .	67
3.16	Cavity 3D render . . . . .	69
3.17	Cavity registration . . . . .	70
3.18	Cavity laser setup . . . . .	72

3.19	Frequency doubling overview . . . . .	73
3.20	Cavity-atom detuning stabilization setup . . . . .	75
3.21	1560 nm intensity stabilization . . . . .	76
3.22	Lattice intensity during cycle . . . . .	77
3.23	Homodyne detection system . . . . .	79
3.24	Picture of homodyne module . . . . .	80
3.25	Noise performance of homodyne detection system . . . . .	82
3.26	Differential shift in cavity lengths at 780 nm and 1560 nm . . . . .	83
3.27	Pulsed cavity resonance measurement templates . . . . .	85
3.28	Cavity detuning calibration . . . . .	87
3.29	In-cycle back to back measurements . . . . .	88
3.30	ac-Stark shift measurement sequence . . . . .	89
3.31	Sample trap frequency measurement . . . . .	93
3.32	Transverse lattice trap frequency as a function of transmitted power .	94
3.33	Clock state differential ac-Stark Shift as a function of transmitted power	96
3.34	Excited state shift due to 1560 nm optical lattice . . . . .	98
3.35	Atom-broadened cavity linewidth calibration . . . . .	99
3.36	Absorption from thermal atoms . . . . .	101
3.37	Atom-cavity coupling as a function of atom number . . . . .	103
4.1	Coherent state noise measurement sequence . . . . .	105
4.2	Coherent state noise histogram for $2 \times 10^5$ atoms . . . . .	106
4.3	Coherent state noise as a function of atom number . . . . .	107
4.4	$J_z$ histograms from pre-squeezing . . . . .	108
4.5	Sequence for squeezed state characterization . . . . .	109
4.6	Squeezing dependence on measurement strength . . . . .	110
4.7	Sequence for measuring antisqueezing . . . . .	111
4.8	Antisqueezing as a function of measurement strength . . . . .	112
4.9	Coherence measurement sequence . . . . .	113
4.10	Squeezed state on the Bloch sphere . . . . .	114
4.11	Coherence as a function of measurement strength . . . . .	115

4.12	Histograms of squeezed and unsqueezed states . . . . .	116
4.13	Atom number dependence of squeezing . . . . .	117
4.14	Sequence for measurement of a small rotation . . . . .	118
4.15	Small rotation on the Bloch sphere . . . . .	119
4.16	Small rotation measurement . . . . .	120
4.17	Full-fringe Rabi oscillation of a squeezed state . . . . .	121
4.18	Clock measurement sequence . . . . .	122
4.19	Coherent and squeezed state clock sequences . . . . .	123
4.20	Atomic clock measurement . . . . .	124
4.21	Clock enhancement as a function of interrogation time . . . . .	125
4.22	Sequence for cavity inhomogeneity measurement . . . . .	126
4.23	Cavity inhomogeneity measurement . . . . .	128
4.24	Entanglement depth . . . . .	129
5.1	Illustration of squeezed state with Bell violation measurement axes .	135
5.2	Full-fringe Rabi oscillations . . . . .	136
5.3	Plot of Bell correlation witness function . . . . .	138
5.4	Plot of Bell correlation boundary . . . . .	140
6.1	Quantum phase magnification illustration . . . . .	145
6.2	Coherent state magnification sequences . . . . .	148
6.3	Histograms of magnified coherent state . . . . .	149
6.4	Parametric dependencies of magnification . . . . .	150
6.5	Normalized SNR as a function of magnification . . . . .	151
6.6	Noise refocusing magnification sequences . . . . .	152
6.7	Postmagnification $J_z$ noise as a function of magnification . . . . .	154
6.8	Histograms of squeezed states before and after magnification . . . . .	155
6.9	Sequence for magnifying QND squeezed states . . . . .	156
6.10	Magnified conditionally squeezed states . . . . .	157
A.1	Cavity reflection diagram . . . . .	161

# Chapter 1

## Introduction

In 1879, when Lord Kelvin proposed to use atomic transitions as reference for measurements of fundamental quantities [1, 2], he could not have predicted the advances made during the 20th century. However, his insight on why atoms would be suitable for such pursuits still holds today:

“The recent discoveries due to the Kinetic theory of gases and to Spectrum analysis (especially when it is applied to the light of the heavenly bodies) indicate to us *natural standard* pieces of matter such as atoms of hydrogen or sodium, ready made in infinite numbers, all absolutely alike in every physical property. The time of vibration of a sodium particle corresponding to any one of its modes of vibration is known to be absolutely independent of its position in the universe, and it will probably remain the same so long as the particle itself exists. The wave-length for that particular ray, *i.e.* the space through which light is propagated *in vacuo* during the time of one complete vibration of this period, gives a perfectly invariable unit of length, and it is possible that at some not very distant day the mass of such a sodium particle may be employed as a natural standard for the remaining fundamental unit.”

It would be another 70 years before the techniques necessary for atomic clocks were developed by Rabi [3] and advanced by Ramsey [4]. Today, atoms are the best

known frequency reference and have been used for timekeeping since the late 1940s [5]. Sensing with atoms has been most successful in the area of timekeeping, where atomic clocks have advanced stability by at least six orders of magnitude [6, 7]. While Lord Kelvin correctly predicted that atoms would be used to create standards for time, it was discovered that atoms were not, after all, completely unaffected by their environment. This turned out to be a blessing in disguise, as it enabled the use of atoms in precision measurements of quantities other than time. Atomic sensors have been used for magnetometry [8, 9], gravity gradient measurements [10, 11], inertial navigation [12], and fundamental physics experiments [13].

Atoms are used for a wide array of measurements which are all fundamentally limited by the same noise source—the quantum projection noise. After the atoms ‘sample’ the environment in a quantum superposition, the quantum state of the atoms must be measured projectively. This is where the quantum projection noise enters. Spin-squeezing provides a path to surpass this limit by redistributing the noise from one quadrature to another [14–17]. While this thesis will focus on spin-squeezing in atomic systems, squeezing has also been shown in other systems, including optical [18–21] and microwave [22] photons, and ions [23, 24].

There have been many proposed methods of performing squeezing in atomic systems [25, 26]. The first atomic spin-squeezing experiments used interactions in Bose-Einstein condensates to generate squeezing [27–35]. Another pioneering experiment mapped squeezing from light into squeezing on atoms [36]. While these experimental setups had the potential to produce large amounts of squeezing, it was challenging to make the necessary measurements in order to verify and utilize the squeezing.

The use of quantum non-demolition (QND) measurements allow generation and characterization of squeezed states through measurements [25, 37–39]. An attractive feature of measurement-based systems is that it reduces the two challenges of squeezing into one: the same system does the squeezing and the characterization. Additionally, the system can do the final readout of precision measurements utilizing squeezed states. Measurement-based squeezing is also an illustration of one of the basic tenets of quantum mechanics—that the act of measurement influences the state. In this case, the uncertainty of the collective state is reduced to the uncertainty of the measurement.

It is therefore necessary to make a measurement of lower uncertainty than the quantum projection noise. The measurement must only measure the collective state of the atoms. Entanglement between individual atoms is enabled by the lack of ‘welcher-weg’ information. As is typical in atomic physics, the workhorse of this type of collective measurement is light. In order to facilitate such a collective measurement, it is vital that each atom has a low probability of scattering a photon. Photons scattered into free space give information to the environment about the state of individual atoms and thus destroy the entanglement necessary for spin-squeezing. To approach the quantum limits of this technique, the measurement must be purely photon shot noise limited and photon loss must be minimized. Due to the limitations in measurement precision arising from the photon shot noise, the main challenge of measurement-based squeezing is to get the largest possible amount of information about the collective state per photon.

The measurement-based setups typically rely on dispersive atom-light interactions—where the atoms cause a state-dependent phase shift on the light. In order to get significant information about the collective state, we would want a large optical depth—each photon should go through a large number of atoms, or through the same atoms many times, letting the incurred phase shift per atom add linearly. Different methods have been used to get the large optical depth necessary for QND measurements of atomic states, such as using large numbers of room temperature atoms or trapping cold atoms in special geometries. The optical cavity was a natural technology to facilitate enhancement of optical depth, as it allows light to travel through cold atomic clouds tens of thousands of times. As a result, cavity measurement-based setups enabled larger amounts of squeezing in much larger ensembles of thermal atoms [40–44].

Past squeezing experiments have been mainly limited by the difficulty in performing precise QND measurements of the collective state of the atoms while maintaining coherence. In this thesis I present some key improvements to these measurements. The QND measurements are purely photon shot noise limited, enabling quantum-limited measurements of the collective state. Additionally, a homodyne detection scheme was used instead of a heterodyne detection scheme, avoiding the mixing in of additional quantum noise. Finally, the cavity used for measurements featured a significantly

higher finesse and more atoms were trapped, allowing higher amounts of squeezing. Through these improvements, the state of the art squeezing in any physical system was surpassed by at least a factor of four [44]. This work is presented in Chapter 4.

An important limitation of cavity-based systems was inhomogeneous coupling—the atoms were trapped in an optical lattice with an incommensurate relationship to the cavity mode used to probe the atoms. Consequently, each atom contributed differently to the measurement and the squeezing could only be utilized if the final readout of the precision measurement was done in the cavity. The squeezed states were then incompatible with the resonant fluorescence-based readout techniques commonly used in atomic sensors. To address this limitation, the experiment described in this thesis uses a dual-wavelength cavity with a commensurate relationship between the cavity mode and optical lattice. The homogeneous coupling of this scheme produces states which can be released into free space for metrology.

The entanglement contained in the squeezed states was quantified both using the entanglement depth criterion and by demonstrating nonlocal Bell correlations. The work concerning Bell correlations is described in Chapter 5.

While the results described in the previous paragraphs allow for significantly more squeezing to be generated using precise measurements, a method was developed that allow squeezed state metrology without detection sensitivity below the quantum projection noise limit. This method is described in Chapter 6. Here, cavity-mediated collective interactions were used to generate unconditional squeezing [45, 46]. The squeezed states were then magnified through further collective interaction prior to a fluorescence measurement.

The experimental work in this thesis was all done in collaboration with my fellow graduate student Rajiv Krishnakumar and postdoc Onur Hosten. In Chapter 2, I will outline some of the concepts behind squeezing in a cavity system and show some techniques used to characterize entanglement in squeezed states. This is followed by Chapter 3, which describes the apparatus used for the experiments performed in Chapters 4, 5 and 6.

# Chapter 2

## Atoms, cavities, and spin-squeezing

This chapter gives a brief introduction to the concepts of spin-squeezing. I will outline some cavity QED principles used to perform cavity-based measurements and generate collective interactions. The goal is to show and justify some of the mathematical tools used in the spin-squeezing experiments described as well as establish definitions for quantities used in the rest of the thesis. I will show what limits squeezing in both measurement- and interaction-based methods and discuss the effect of coupling inhomogeneity in a cavity system. Furthermore, I will also outline different entanglement measures that can be applied to squeezed states.

## 2.1 Introduction to squeezing

### 2.1.1 The Bloch sphere model

It is useful to model an ensemble of  $N$  two-level atoms as a spin- $J$  system, where  $J = N/2$ . The collective state of the system can then be pictorially represented on the Bloch sphere. In this thesis, the  $^{87}\text{Rb}$  hyperfine clock states  $|F = 2, m_F = 0\rangle \equiv |\uparrow\rangle$  and  $|F = 1, m_F = 0\rangle \equiv |\downarrow\rangle$  will be labeled as the spin-up and spin-down states respectively. We can now define collective spin operators in terms of single spin operators as

$$J_i = \sum_{n=1}^N j_i^{(n)} \quad (2.1)$$

where  $j_i$  are single spin operators in the  $i = x, y, z$ -direction. The  $z$ -component of the spin,  $J_z$ , represents the population difference while the orientation of the state in the  $J_x - J_y$  plane represents the phase difference between the two states. I will also define normalized spin operators as

$$\mathcal{J}_i = \frac{1}{N/2} J_i. \quad (2.2)$$

The Cartesian spin components  $J_{x,y,z}$  are conjugate observables with the corresponding uncertainty relation,

$$\Delta J_z \times \Delta J_y \geq |\langle J_x \rangle / 2|. \quad (2.3)$$

A minimum uncertainty state is one where the above inequality is saturated. The most trivial example of such a state is the coherent spin state (CSS), where  $\langle J_x \rangle = N/2$  and  $\langle J_y \rangle = \langle J_z \rangle = 0$ . The uncertainties are then given by  $\Delta J_z = \Delta J_y = \sqrt{N}/2 \equiv \Delta_{\text{CSS}}$ . The CSS noise establishes the standard quantum limit on resolvable phase or population difference. From the uncertainty relation, we can see that for any minimum uncertainty state, a reduction in uncertainty (squeezing) in one component, *e.g.*  $J_z$ , must be accompanied by an increased uncertainty (antisqueezing) in the conjugate observable, here  $J_y$ .

I will use  $\xi$  and  $\xi'$  to describe squeezed states. Here  $\xi$  and  $\xi'$  are parameters for

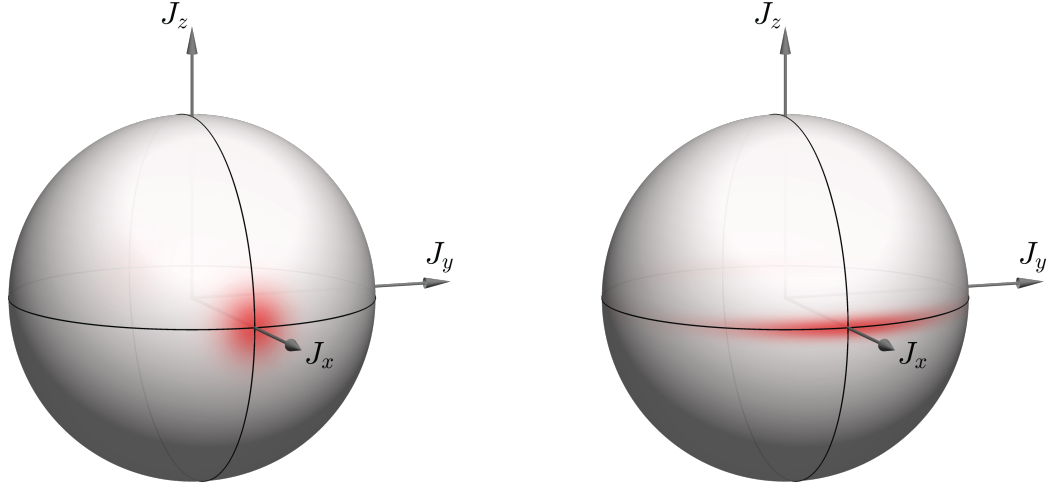


Figure 2.1: Left: Coherent state of 30 atoms shown on the Bloch sphere. Right: 10 dB minimum uncertainty squeezed state of 30 atoms. Here  $\xi = 1/\sqrt{10}$  and  $\xi' = \sqrt{10}$ . Both states are Gaussian and their Wigner distribution is plotted on the sphere.

the amount of squeezing and antisqueezing respectively, such that for a state with  $J_x \sim N/2$

$$\Delta J_z = \xi \Delta_{\text{CSS}} \quad (2.4)$$

$$\Delta J_y = \xi' \Delta_{\text{CSS}} \quad (2.5)$$

For a minimum uncertainty squeezed state,  $\xi \times \xi' = 1$ , which means the state is at the Heisenberg limit. In general the equality will not hold and  $\xi \times \xi' > 1$  due to inefficiencies in the squeezing process. The quantity  $\xi$  is often referred to as the spin noise reduction, as it is not necessarily an accurate representation of the metrological capability of the state since it does not take decoherence into account.

The metrological enhancement by the Wineland criterion [17] provided by a squeezed state with uncertainty  $\Delta J_z$ , is given by

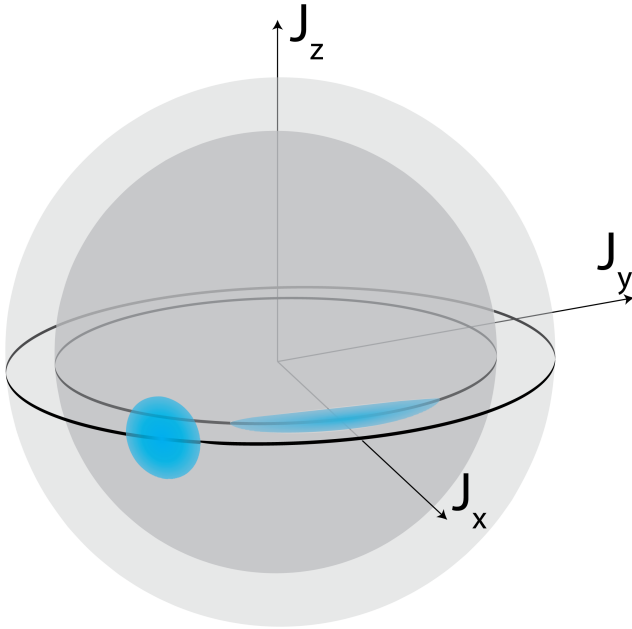


Figure 2.2: The figure illustrates the change from a coherent state to a squeezed state. The coherent state shows the same uncertainty in all directions while the squeezed state has reduced uncertainty in  $J_z$ . The decoherence is shown by the shrinking of the Bloch sphere.

$$\chi^2 = \left( \frac{\sqrt{N}/2}{\Delta J_z} \times \frac{|J_x|}{N/2} \right)^2 \quad (2.6)$$

where the first factor represents the noise reduction and the second represents the loss of coherence. The coherence of a state can be thought of as the state's Bloch vector length, where a reduction of length leads to lower sensitivity to small rotations. The metrological enhancement directly translates into the reduction in resources needed to perform a specific measurement. The improvement in precision at  $\chi^2 = 100$  is equivalent to that achieved by increasing the atom number or the averaging time by a factor of 100.

## 2.2 The optical cavity

The enabling technology of this experiment is a dual-wavelength optical cavity. In order to make the non-demolition measurements necessary for squeezing, we used a highly reflective optical cavity allowing the light to pass through the atoms tens of thousands of times. The increased optical depth of the cavity is what allows highly squeezed states to be generated [47, 48]. Here I will discuss some of the basic properties of the optical cavity and how different cavity parameters relate to spin-squeezing experiments. A more formal treatment can be found in quantum optics textbooks such as [49, 50].

### 2.2.1 The dispersive signal

In Appendix A, the transmission and reflection coefficients of a high-finesse cavity are derived. These results are shown below, and the full derivation can be found in the appendix. For a cavity with linewidth  $\kappa$  and decay rate per mirror of  $\kappa_M$ , we find that for a detuning from cavity resonance of  $\delta$ , the cavity power transmission coefficient is

$$T = \left(\frac{\kappa_M}{\kappa}\right)^2 \frac{1}{1 + \left(\frac{\delta}{\kappa/2}\right)^2}. \quad (2.7)$$

Similarly the reflection coefficient is

$$R = \frac{\left(\frac{\kappa_L}{\kappa}\right)^2 + \left(\frac{\delta}{\kappa/2}\right)^2}{1 + \left(\frac{\delta}{\kappa/2}\right)^2} \quad (2.8)$$

where  $\kappa_L$  is the rate of loss from the cavity mode, encompassing both loss due to absorption in the mirror and scattering into free space due to the medium. I will later label  $2\kappa_M/\kappa$  the cavity efficiency. The cavity efficiency can be thought of as the chance that a photon that enters the cavity is not lost. We can also find the phase shift on the reflected and transmitted light when tuned close to resonance, i.e.  $\delta/\kappa \ll 1$ , to be

$$\tan \phi_r = \frac{\kappa_M}{\kappa_L} \frac{\delta}{\kappa/2} \quad (2.9)$$

$$\tan \phi_t = \frac{\delta}{\kappa/2}. \quad (2.10)$$

The homodyne setup used to measure the cavity resonance in this experiment measures the real or imaginary parts of the electric field of the reflected light, we will be predominantly interested in these quantities. I will here provide the real and imaginary parts of the reflection coefficients for the incident electric field on the cavity.

$$\Re [r_{\text{cav}}] = \frac{\kappa_L}{\kappa} \frac{1}{1 + \left(\frac{\delta}{\kappa/2}\right)^2} \quad (2.11)$$

$$\Im [r_{\text{cav}}] = - \frac{\kappa_0}{\kappa} \frac{\frac{\delta}{\kappa/2}}{1 + \left(\frac{\delta}{\kappa/2}\right)^2} \quad (2.12)$$

Note that the real part of the reflection coefficient to first order in  $\delta/(\kappa/2)$  is zero when there is no loss. For the transmission coefficients, we obtain

$$\Re [t_{\text{cav}}] = \frac{\kappa_0}{\kappa} \frac{1}{1 + \left(\frac{\delta}{\kappa/2}\right)^2} \quad (2.13)$$

$$\Im [t_{\text{cav}}] = \frac{\kappa_0}{\kappa} \frac{\frac{\delta}{\kappa/2}}{1 + \left(\frac{\delta}{\kappa/2}\right)^2} \quad (2.14)$$

In the experiments shown later, the imaginary part of the reflected electric field is measured using a homodyne setup. This signal is then used to measure the cavity resonance. When close to resonance, the frequency discriminator, or the

frequency derivative of the imaginary part of the reflection coefficient, scales as  $(\kappa_0/\kappa)^2$ , meaning that losses in the mirrors or the medium cause a double hit in the frequency discriminator.

### 2.2.2 Cavity QED for spin-squeezing

The finesse is an important parameter for describing the quality of optical cavities. Mathematically, it is defined as

$$\mathcal{F} = \frac{\pi\sqrt{R}}{1-R} \approx \frac{\pi}{1-R} \quad (2.15)$$

where  $R$  is the reflectivity of the mirrors and the approximation holds when  $R$  is close to 1, as will be the case here.  $\mathcal{F}/\pi$  is the average number of roundtrips a photon entering the cavity makes. The cavity thereby enhances the optical depth of the atomic cloud by  $2\mathcal{F}/\pi$ . When making a photon shot noise limited measurement, this allows significant enhancement of the measurement, as the amount of phase shift accumulated by a single photon due to the atomic cloud increases linearly with the finesse. A single photon probing the cavity gets the same signal to noise ratio as  $(2\mathcal{F}/\pi)^2$  photons probing the same cloud in free space. This enhancement is the main reason for the success of cavities in measurement-based spin-squeezing.

A cavity is characterized by regularly spaced resonances, as the resonance condition is met every time an integer number of half-wavelengths can fit between the two cavity mirrors. The resonance spacing is known as the free spectral range (FSR) and is given by

$$\nu_{\text{FSR}} = \frac{c}{2L} \quad (2.16)$$

where  $c$  is the speed of light and  $L$  is the length of the cavity. The linewidth of the cavity resonance determines the rate of decay of the intracavity photon number,  $n$ , such that when there is no incident field

$$\frac{dn}{dt} = \kappa n \quad (2.17)$$

where  $\kappa$  is the full cavity linewidth. The relation above lets us measure the cavity linewidth accurately through ringdown spectroscopy, where the cavity is excited with an incident field, which is then turned off instantaneously. By looking at the decay rate of the transmitted power afterwards, the linewidth can be found. It should now be clear that a connection can be made between the finesse, the cavity linewidth and the free spectral range, as the linewidth describes the decay rate inside the cavity and the free spectral range the roundtrip time. As the lifetime of a photon in the cavity is given by  $1/\kappa$  and the roundtrip time is  $1/\nu_{\text{FSR}}$ , we can see that the finesse is given by

$$\mathcal{F} = \frac{\nu_{\text{FSR}}}{\Delta\nu} \quad (2.18)$$

where  $\Delta\nu = \kappa/2\pi$ . For a more rigorous proof of this relation, see § 2.2.1. The above equation provides the most easily experimentally accessible route to measure the finesse. As mentioned above, the linewidth can be measured to high accuracy using ringdown spectroscopy. The FSR can be measured by placing sidebands of known frequency on the light and sending both sidebands in on resonance.

In a cavity with vacuum as its medium, the decay rate is dominated by the light leaking out through the mirrors, which I will denote as  $\kappa_M$ , and loss in the mirrors,  $\kappa_L$ , such that  $\kappa = \kappa_L + 2\kappa_M$ . While the leakage light is what allows measurement of the cavity resonance, the loss in the mirrors is detrimental, as it reduces the amount of information gained for a given amount of light sent onto the cavity. For some incident power,  $P_{\text{in}}$ , the intracavity photon number is given by

$$n = T(\omega) \frac{P_{\text{in}}}{\hbar\omega} \frac{1}{\kappa_M} \quad (2.19)$$

where  $T(\omega)$  is the transmission of the cavity as a function of incident frequency  $\omega$  (see Equation 2.7). This relation is useful experimentally, as most atom-cavity interactions are easily calculated in terms of the intracavity photon number, but usually only the incident power is known.

We can now consider interactions between atoms and the cavity. The atoms in the cavity will interact with the standing wave cavity mode. The strength of interaction will depend on the intensity of the cavity mode at the atom's position, which also

depends on the geometry of the cavity. We will first consider only the peak interaction strength, where the atom is positioned at the point of maximum intensity in the cavity mode. The atom-cavity interaction strength is most commonly expressed through the single-photon Rabi frequency,  $g_0$ . It is given by

$$g_0 = \frac{\mu}{\hbar} \sqrt{\frac{\hbar\omega}{2\epsilon_0 V_m}} \quad (2.20)$$

where  $\mu$  is the dipole matrix element of the transition,  $\omega$  is the angular frequency of the electric field (which we assume is equal to the atomic transition frequency, *i.e.* the atom-cavity detuning is zero) and  $V$  is the mode volume given by

$$V_m = \frac{\iiint_V |\mathbf{E}(\mathbf{r})|^2}{\max(|\mathbf{E}(\mathbf{r})|^2)}. \quad (2.21)$$

With a single atom in the cavity,  $2g_0$  is the frequency of the Rabi oscillation on a specific atomic transition when the intracavity photon number is 1. This atom-cavity interaction parameter therefore gives the rate of photon exchange between the atomic two-level system and the cavity field. Note that this parameter does not depend on the reflectivity of the mirrors (the finesse), but instead only on properties of the mode of the cavity and the atomic transition. A simple way to understand this is that the single photon Rabi frequency is agnostic to how the cavity mode was excited with one photon. The finesse instead determines how much input light is necessary to excite one photon in the cavity mode. To understand the square root scaling with frequency, we can simply think of how the amount of energy stored in an electric field is proportional to  $E^2$ , hence as the energy of the photon increases the field increases with the square root of frequency.

For an arbitrary position in the cavity, the single-photon Rabi frequency is given by  $g = g_0 \sin(kx)$ , where  $x$  is the position of the atom along the cavity axis. If the atoms are not trapped in a trap with the same periodicity as the excitation field, each atom will undergo Rabi oscillations at different frequencies, leading to rapid decoherence. This can be counteracted by a spin-echo. However, we will see in § 2.3.4 that the prepared squeezed states are different when each atom is coupled identically

to the cavity.  $g$  also varies as a function of position due to the intensity profile of the particular cavity mode. For experiments with many atoms, it is therefore beneficial to sacrifice some peak coupling strength to gain homogeneity of coupling strength across the cloud of atoms.

While the single-photon Rabi frequency parametrizes some aspects of atom-cavity interactions well, the atom-cavity cooperativity,  $C$ , allows comparison of the coupling to the cavity with the coupling to the rest of the environment through a single number given by

$$C = \frac{4g_0^2}{\kappa\Gamma} \quad (2.22)$$

where  $\Gamma$  is the linewidth of the relevant atomic transition. The atom-cavity cooperativity is the ratio of the number of photons scattered into the cavity to the number of photons scattered into free space for a single atom. The number thus directly tells you something about the strength of coupling between a single atom and the cavity. This is the parameter where the cavity finesse enters—the reflectivity of the mirrors determines  $\kappa$ , we can thereby see that a higher finesse leads to higher cooperativity. The length of the cavity does not affect the cooperativity for fixed reflectivity, as  $g_0 \propto 1/\sqrt{V_m} \propto 1/\sqrt{L}$  and  $\kappa \propto 1/L$ . For near-confocal cavities, it is therefore beneficial to have a longer cavity such that the atom-cavity coupling in the center is more homogeneous, as a shorter cavity will have a more rapidly diverging cavity mode. The increased homogeneity in the center allows trapping of a larger number of atoms in the homogeneous region. However, a longer cavity and thus a narrower linewidth does require lower frequency noise to achieve photon shot noise limited resonance measurement, hence increasing the technical requirements. Additionally, a narrower linewidth cavity responds more slowly to change in incident intensity, thus complicating pulsed measurement of the cavity resonance, which will be explored in § 3.2.7.

The so-called strong coupling regime where  $C \gg 1$  is where a single atom significantly shifts the cavity resonance (*i.e.* a shift of order  $\kappa$ ) and a single photon causes significant excitation of the atom. When there are  $N$  atoms interacting with the cavity

mode, there is a collective enhancement of the atom-cavity interaction—the Rabi frequency due to a single photon is enhanced by  $\sqrt{N}$  to  $2\sqrt{N}g_0$ . For the purpose of describing interactions with a large number of atoms it is therefore useful to define a collective cooperativity,

$$C_N = NC = \frac{Ng_0^2}{\kappa\Gamma}. \quad (2.23)$$

We will see in § 2.3 that for a system of many atoms in a cavity, this is the relevant parameter for describing the strength of their interaction with the cavity [26, 48]. By decreasing the mode volume,  $V_m$ , we can increase  $g^2$ . However, since the atom number is also proportional to the mode volume in the density limited case, this would not increase the collective cooperativity. For the purposes of metrology, it is therefore beneficial to have a larger mode volume, to have more atoms and thus better overall sensitivity [51].

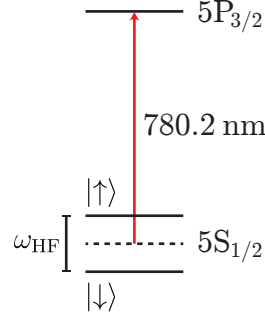


Figure 2.3: The figure shows the detuning of the probe light (shown in red) relative to the hyperfine clock states of  $^{87}\text{Rb}$ , here labeled as  $|\uparrow\rangle$  and  $|\downarrow\rangle$ . The light is detuned halfway between the  $^{87}\text{Rb}$  clock states, such that an atom in the ‘up’ state gives rise to the same resonance shift as an atom in the ‘down’ state.

## 2.3 Spin-squeezing methods and limits

In this section I will give a framework to understand spin squeezing by QND measurement. While most of the material has been covered in other references such as [48, 52–55], I will attempt to put it in context of this experiment. The simplest description of the experiment is to think of the atoms as a medium of a refractive index proportional to their internal state which causes a dispersive shift on the cavity resonance allowing QND measurement of said internal state. The cavity here serves to strongly enhance the interaction of the light with the atoms. While I will elaborate on this simple picture, it captures all the essentials.

### 2.3.1 Cavity-aided quantum non-demolition measurement

In the early theoretical work on spin-squeezing using a QND measurement, the suggested system was a cavity where every atom is coupled identically to the cavity mode and the cavity-atom detuning is large compared to the atomic and cavity linewidths [26, 56]. The setup used in this thesis is an experimental realization of such a system. In [52] it is shown that in the low excitation limit ( $ng^2/\Delta^2 \ll 1$ ) the relevant Hamiltonian is

$$H = \hbar \frac{g^2}{\Delta} a^\dagger a J_z \quad (2.24)$$

where  $a$  and  $a^\dagger$  are the creation and annihilation operators for the cavity mode and we assume that the detuning for the two states is equal and opposite. Specifically in this thesis we will be detuned halfway between the hyperfine clock states of Rubidium as shown in Figure 2.3. This Hamiltonian does not include spontaneous emission, which I will get back to in §2.3.2 and §2.3.6. The coupling of the cavity to the atoms induces a differential ac-Stark shift on the  $|\uparrow\rangle$  and  $|\downarrow\rangle$  states proportional to the intra-cavity photon number,  $n = a^\dagger a$ . This ac-Stark shift gives rise to antisqueezing, where the photon shot noise of the probe leads to quantum noise on  $J_y$ . The ac-Stark shift will later be used as an experimentally measurable probe of  $n$ . The coupling of the atoms to the cavity enables the QND measurement of the state: the atoms cause a cavity resonance frequency shift proportional to  $J_z$  with proportionality constant  $g^2/\Delta$ . This reduces the problem of generating spin-squeezing to measuring the cavity resonance to the accuracy of the desired level of squeezing and has been used to great effect in many squeezing experiments [41–44].

### 2.3.2 Atomic scattering into free space

When atoms are in the cavity mode, their spontaneous emission leads to additional loss from the cavity mode, manifesting as a broadened cavity linewidth. If the empty cavity linewidth is  $\kappa_0$ , we can model the atomic scattering as an additional loss term  $\kappa_s$  such that the new cavity linewidth is

$$\kappa = \kappa_0 + \kappa_s. \quad (2.25)$$

To find an expression for  $\kappa_s$  consider  $N$  atoms in a superposition of two hyperfine states  $|\uparrow\rangle$  and  $|\downarrow\rangle$  split by  $\omega_{\text{HF}}$ . The excited state has a linewidth  $\Gamma$ . The cavity-atom detuning for the two states is given by  $\Delta_\uparrow = \omega_{\text{HF}}/2$  and  $\Delta_\downarrow = -\omega_{\text{HF}}/2$ . At low intra-cavity photon numbers, the excited state population is  $ng^2/\Delta^2$  where  $n$  is the intra-cavity photon number and  $g$  is the atom-cavity coupling rate. We then have that the atomic scattering rate is

$$\Gamma_s = Nn \frac{g^2}{\Delta^2} \Gamma. \quad (2.26)$$

and thus

$$\kappa_s = N \frac{g^2}{\Delta^2} \Gamma = NC \left( \frac{\Gamma}{\omega_{\text{HF}}} \right)^2 \quad (2.27)$$

where  $C$  is the single-atom cooperativity. As will be shown in § 2.3.3, the atomic scattering places a limit on the amount of squeezing that can be achieved. We will see that this simple model for the atomic scattering is in good agreement with experimental data (see § 3.3.4).

### 2.3.3 Limits on measurement-induced squeezing

The limit on the maximum attainable squeezing is imposed by the competition between measurement noise and spin-flip noise [41, 44, 48, 57]. The spin-flip noise arises from photon scattering events causing atoms to change hyperfine state, which leads to a random walk in  $J_z$ . Of the photon scattering events, the most important process is the one which changes the state of an atom from one clock state to the other. The measurement noise is dominated by photon shot noise. A stronger measurement, using more photons, is less affected by photon shot noise, but will cause additional spin-flips. When probing the  $^{87}\text{Rb}$  clock states, the probability,  $p$ , that a scattering event leads to a change of hyperfine state is  $1/6$  [48]. In the derivation of the squeezing limits, we will use the induced ac-Stark shift on the clock states, given by

$$\phi_{\text{AC}} = \frac{2g^2}{\Delta} \int dt n_c(t) \quad (2.28)$$

where  $g$  is the atom-cavity coupling,  $\Delta$  is the atom-cavity detuning and  $n_c$  is the intra-cavity photon number. The probe-induced ac-Stark shift will be used as a parameter for the interaction strength of light in the cavity throughout the thesis. For a cavity-atom detuning  $\Delta = \omega_{\text{HF}}/2$ , where  $\omega_{\text{HF}}$  is the hyperfine splitting of  $^{87}\text{Rb}$ , the number of scattered photons per atom is given by

$$m_s = \phi_{\text{AC}} \frac{\Gamma}{\omega_{\text{HF}}} \quad (2.29)$$

where  $\Gamma$  is the linewidth of the  $^{87}\text{Rb}$  D<sub>2</sub> line (see § 2.3.2). The scattered photons give rise to a random walk on  $J_z$ , with a variance given by

$$\delta_{\text{flip}}^2 = Npm_s = \frac{N}{6} \frac{\Gamma}{\omega_{\text{HF}}} \phi_{\text{AC}}. \quad (2.30)$$

This is a Poissonian process with a variance equal to the mean. We now have an expression for the spin-flip noise, and continue to examine the measurement noise. For the measurement noise, consider the information imprinted on the light transmitted from the cavity. The total decay rate of the cavity,  $\kappa$ , is given by

$$\kappa = 2\kappa_M + \kappa_L + \kappa_S \quad (2.31)$$

where  $\kappa_M$  is the mirror out-coupling,  $\kappa_L$  is due to optical losses in the mirrors and  $\kappa_S$  is the atomic scattering into free space. From Equation 2.27, the atomic scattering can be expressed as

$$\frac{\kappa_S}{\kappa_0} = NC \left( \frac{\Gamma}{\omega_{\text{HF}}} \right)^2 \quad (2.32)$$

where  $\kappa_0 = \kappa_L + 2\kappa_M$  and  $C$  is the cavity cooperativity. When the probe is on resonance, the number of photons transmitted through the cavity is

$$n_T = \frac{\epsilon_C}{2C} \frac{\Gamma}{\omega_{\text{HF}}} \phi_{\text{AC}} \quad (2.33)$$

where  $\epsilon_C = 2\kappa_M/\kappa_0$  is the cavity efficiency. The atoms shift the cavity resonance frequency by

$$\delta_{\text{atoms}} = \frac{2g^2}{\Delta} J_z. \quad (2.34)$$

For a small cavity resonance frequency shift,  $\delta_{\text{atoms}} \ll \kappa$ , the phase shift,  $\psi$ , on the transmitted light (see Equation 2.10) is given by

$$\psi = \frac{\delta_{\text{atoms}}}{\kappa/2} = \frac{2C(\Gamma/\omega_{\text{HF}})}{1 + NC(\Gamma/\omega_{\text{HF}})^2} J_z. \quad (2.35)$$

For a coherent photon state, the quantum phase noise is given by

$$\Delta\psi_{\text{PSN}} = \frac{1}{2\sqrt{n_T}}. \quad (2.36)$$

The noise equivalent  $J_z$  resolution of a measurement with strength  $\phi_{\text{AC}}$  is then

$$\Delta J_{z,\text{meas}} = \frac{\Delta\psi_{\text{PSN}}}{\psi/J_z} = \frac{1 + NC(\Gamma/\omega_{\text{HF}})^2}{\sqrt{8\epsilon_C C(\Gamma/\omega_{\text{HF}})}} \frac{1}{\sqrt{\phi_{\text{AC}}}}. \quad (2.37)$$

For a symmetric cavity, equal amounts of information come out in transmission and reflection. So far we have only considered the transmitted light. If we assume we collect light from both sides of the cavity, the variance of the measurement is reduced by a factor of two. We then bundle efficiency factors (photon loss and detection efficiency) into  $\epsilon$  and obtain an expression for the measurement noise,

$$\delta_{\text{meas}}^2 = \frac{(1 + NC(\Gamma/\omega_{\text{HF}})^2)^2}{16\epsilon C(\Gamma/\omega_{\text{HF}})} \frac{1}{\phi_{\text{AC}}}. \quad (2.38)$$

If we now add up our two sources of noise (spin-flips and measurement noise) and minimize the noise with respect to  $\phi_{\text{AC}}$  we obtain

$$\delta_{\text{opt}}^2 = \frac{\sqrt{N}(1 + NC(\Gamma/\omega_{\text{HF}})^2)}{\sqrt{24\epsilon C}} \quad (2.39)$$

at an optimal probe induced ac-Stark shift of

$$\phi_{\text{AC,opt}} = \frac{1 + NC(\Gamma/\omega_{\text{HF}})^2}{\sqrt{8/3\epsilon NC}} \frac{\omega_{\text{HF}}}{\Gamma}. \quad (2.40)$$

At this ac-Stark shift,  $\delta_{\text{meas}} = \delta_{\text{flip}} = \delta_{\text{opt}}/\sqrt{2}$ . Inserting  $\delta_{\text{opt}}$  for  $\Delta J_z$  in Equation 2.6 and assuming negligible loss of coherence we obtain

$$\chi_{\text{opt}}^2 = \frac{\sqrt{3/2\epsilon NC}}{1 + NC(\Gamma/\omega_{\text{HF}})^2}. \quad (2.41)$$

There are two interesting regimes for this equation. For low atom numbers,

$$\chi^2 \approx \sqrt{3/2\epsilon NC} \quad (2.42)$$

*i.e.* the metrological enhancement scales with  $\sqrt{NC}$ . However, the enhancement reaches a maximum of

$$\chi_{\text{opt}}^2 = \frac{\omega_{\text{HF}}}{\Gamma} \sqrt{3\epsilon/8} \quad (2.43)$$

at an optimal atom number of

$$N_{\text{opt}} = \frac{\omega_{\text{HF}}^2}{\Gamma^2 C}. \quad (2.44)$$

After this optimal atom number, we enter the saturated regime where atomic scattering starts to dominate. In this regime, the metrological enhancement is given by

$$\chi^2 \approx \sqrt{\frac{3\epsilon}{2NC}} \left( \frac{\omega_{\text{HF}}}{\Gamma} \right)^2. \quad (2.45)$$

Here, the metrological enhancement decreases weakly with increased atom number. Equation 2.43 places a limit on the achievable squeezing for the  $^{87}\text{Rb}$  clock states of 28 dB for  $\epsilon = 1$  when using the scheme described here. Here, the limit is set by the atomic structure of  $^{87}\text{Rb}$  as it depends only on  $\omega_{\text{HF}}$  and  $\Gamma$ . For a different squeezing scheme or a different atom, the particulars of the derivation and therefore also the limit, will change.

The saturation effect can be traced back to the linewidth broadening effect of atomic absorption. It occurs when the loss of photons due to atomic scattering approaches the cavity linewidth. This means that the light sent into the cavity is now likely to be lost due to atomic scattering into free space, thereby causing spin-flips without giving extra information. This squeezing limit could be bypassed by probing with squeezed light, as the contribution of photon shot noise would then be reduced.

The optimum atom number for a cavity of given cooperativity scales as  $1/C$ . Therefore the choice of cavity parameters for a squeezing experiment is not as simple as choosing the highest cooperativity, but rather one has to choose a cooperativity

compatible with the target atom number of the experiment. While the spin-flip noise increases linearly with atom number, the measurement noise does not change. Therefore, at atom numbers below the optimal atom number, the amount of ac-Stark shift required for optimal squeezing decreases with increasing atom numbers (see Equation 2.40). Any cavity will have residual inhomogeneities, meaning that any amount of ac-Stark shift will cause decoherence. Hence it is easier to make a coherence-preserving measurement at higher atom numbers, as less ac-Stark shift is required. While the cavity used in this work is a symmetric cavity as treated here, a single-sided cavity could be beneficial, assuming one can still achieve a high enough finesse or atom number to operate near the optimal atom number for the cavity. In this case the photon collection efficiency could be increased by a factor of two without complicating the measurement scheme by trying to collect light from both sides of the cavity.

### 2.3.4 Atom-cavity coupling inhomogeneity

So far I have assumed we are measuring the collective observable

$$J_z = \sum_{n=1}^N j_z^{(n)} \quad (2.46)$$

where  $N$  is the number of atoms and  $j_z^{(n)} = (1/2)\sigma_z^{(n)}$  is the z-component for atom  $n$ . However, due to the residual inhomogeneity in the atom-cavity coupling, a slightly different collective observable is measured,  $S_z$ , which is a weighted sum of  $j_z^{(n)}$ , given by

$$S_z = \frac{1}{Z} \sum_{n=1}^N (1 - \epsilon_n) j_z^{(n)} \quad (2.47)$$

where  $Z$  is a normalization constant and  $\epsilon_n \ll 1$  is the fractional deviation from uniform coupling for the  $n$ th atom. For uniform coupling, we expect a total cavity shift of  $\Delta_c = \delta_0 J_z$ , where  $\delta_0 = g_0^2/\Delta$ . When taking into account the inhomogeneity, we obtain instead

$$\Delta_c = \sum_n \delta_0 (1 - \epsilon_n) j_z^{(n)} = (\delta_0 Z) \left( \frac{1}{Z} (1 - \epsilon_n) j_z^{(n)} \right) = \delta_{\text{eff}} S_z \quad (2.48)$$

where  $\delta_{\text{eff}}$  is the effective cavity shift per spin-flip. To decide on a normalization, we utilize two properties of  $S_z$ : its maximum

$$S_{z,\max} = \frac{N}{2} \frac{1}{Z} \langle 1 - \epsilon \rangle_e \quad (2.49)$$

and its projection noise

$$\text{Var}S_{z,\text{proj}} = \frac{N}{4} \frac{1}{Z^2} \langle (1 - \epsilon)^2 \rangle_e \quad (2.50)$$

where  $\langle \cdot \rangle_e$  indicates an ensemble average over the phase space of the atoms. We now choose  $Z$  such that the condition

$$\frac{\text{Var}J_z}{J_{z,\max}} = \frac{1}{2} \quad (2.51)$$

satisfied by  $J_z$  is also satisfied by  $S_z$ . Then

$$Z = \frac{\langle (1 - \epsilon)^2 \rangle_e}{\langle 1 - \epsilon \rangle_e} \quad (2.52)$$

and thus

$$S_z = \frac{\langle 1 - \epsilon \rangle_e}{\langle (1 - \epsilon)^2 \rangle_e} \sum_n ((1 - \epsilon_n) j_z^{(n)}) \quad (2.53)$$

Hence a non-uniformly coupled system of  $N$  atoms can be modeled as a uniformly coupled system of

$$N_{\text{eff}} = N \frac{\langle 1 - \epsilon \rangle_e^2}{\langle (1 - \epsilon)^2 \rangle_e} \quad (2.54)$$

effective atoms with an effective cavity shift of

$$\delta_{\text{eff}} = \delta_0 \frac{\langle (1 - \epsilon)^2 \rangle_e}{\langle 1 - \epsilon \rangle_e} \quad (2.55)$$

per spin-flip. We can now quantify the inhomogeneity of the probing, which is what causes the nonsymmetry. First we consider the density of atoms as a function of transverse displacement from the center of the optical lattice,

$$\rho(x, y) \propto \exp\left(-\frac{x^2 + y^2}{2\sigma_r^2}\right) \quad (2.56)$$

where  $\sigma_r = 15.2(3)\text{ }\mu\text{m}$  is the waist of the atoms in the trap calculated from the temperature measurements and  $x$  and  $y$  are position axes perpendicular to the trap. In our case, we are probing and trapping the atoms with cavity modes. The center of the cloud and the center of the probe beam are therefore well aligned. The probe has a waist of  $w_{780} = 111\text{ }\mu\text{m}$  and its intensity governs the cavity coupling coefficients for atoms. We can now consider  $\eta_i = 1 - \epsilon_i$  as the coupling coefficient for the  $i$ th atom. For  $x = y = 0$ ,  $\eta = 1$  and we therefore have maximal coupling. Utilizing Equation 2.56, we then have that for the Gaussian TEM00 mode of the cavity,

$$\eta(x, y) = \exp\left(\frac{-2(x^2 + y^2)}{w_{780}^2}\right). \quad (2.57)$$

For the system described here,  $N_{\text{eff}} = 0.995N$  and  $\delta_{\text{eff}} = 0.93\delta_0$  where  $\delta_0$  is the cavity shift averaged over the longitudinal distribution. In the thesis I will take  $N = N_{\text{eff}}$ . By averaging over the longitudinal distribution, one can obtain that  $\delta_{\text{eff}} = 0.83\delta_{\text{max}} = 5.5\text{ Hz}$ , where  $\delta_{\text{max}}$  is the maximum atom-cavity coupling when an atom is on the maximum intensity of the standing wave in both the transverse and longitudinal direction.

### 2.3.5 Squeezing through collective interactions

So far I have focused on squeezing through QND measurement. An alternate method first demonstrated in [45] is to use a so-called one-axis twisting Hamiltonian to generate squeezing [56, 58–60]. This has the advantage that it generates unconditional squeezing [61] and does not necessarily require good detection sensitivity. As we will later see there are alternative methods to exploit the metrological gain from squeezed states without having to make measurements of the atomic state below the CSS noise level.

The relevant Hamiltonian is here

$$H = \hbar\chi J_z^2 \quad (2.58)$$

where  $\chi$  is a parameter for the strength of the shearing interaction. To enable such an interaction in a cavity system, light can be sent in detuned from the atom-dressed cavity resonance. Since the detuning of the light is then set by  $J_z$  (see § 2.3.1), the intra-cavity photon number,  $n$ , is now proportional to  $J_z$ . The state is then ac-Stark shifted by an amount proportional to  $J_z$ . The interaction thus leads to the state being ‘sheared’ out on the Bloch sphere as illustrated in Figure 2.4. The squeezing and antisqueezing is here along an axis that is determined by the amount of shearing done. The sheared out states can be converted to  $J_z$ -squeezed states through a small microwave rotation that varies depending on the shearing strength. The fundamental limit of squeezing by this method is again imposed by atomic scattering [62], and hence the limit  $\xi_{min} \propto (\Gamma/\omega_{HF})^2$ .

### 2.3.6 Introduction to quantum phase magnification

The shearing interaction shown in § 2.3.5 can be used to ‘magnify’ squeezed atomic states to read them out with a detection system detecting at significantly above the CSS noise level. The idea of using cavity-mediated interactions to perform quantum metrology without low-noise detection was first presented in [63]. The method presented here are a generalization of that method. In Figure 2.5 I show an illustration of the protocol used.

To provide a theoretical framework for understanding this procedure, I will here show a derivation of the relevant equations of motion starting from the atom-cavity-reservoir Hamiltonian. Through the derivation, we will see that the method described pictorially in Figure 2.5 allows magnification by a factor  $M$ , where  $M$  is given by

$$M = N \frac{\delta_0 \delta_c}{|\delta_0 + i\kappa/2|^2} \phi_{AC}. \quad (2.59)$$

We start with the interaction picture Hamiltonian for the full atom-cavity system

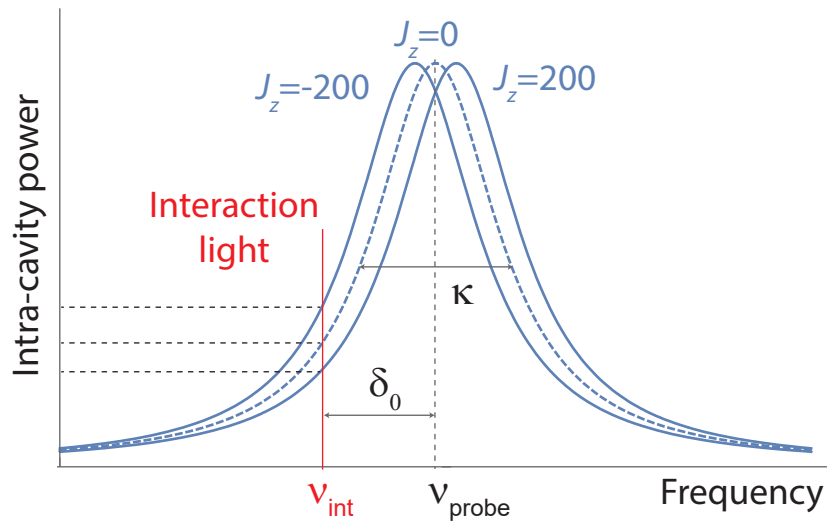


Figure 2.4: The mechanism leading to the collective atomic interactions that enables shearing. The intracavity power is linked to  $J_z$ , due to the dispersive shift of the cavity from the atomic state. The detuning of the interaction light then depends on  $J_z$ , thus producing a  $J_z$ -dependent ac-Stark shift. The frequencies of the interaction beam  $\nu_{\text{int}}$  and probe beam  $\nu_{\text{probe}}$  are indicated. The shifted cavity resonances for  $J_z = \pm 200$  illustrate how a change in  $J_z$  changes the intensity of the interaction light entering the cavity at a detuning  $\delta_0$ .

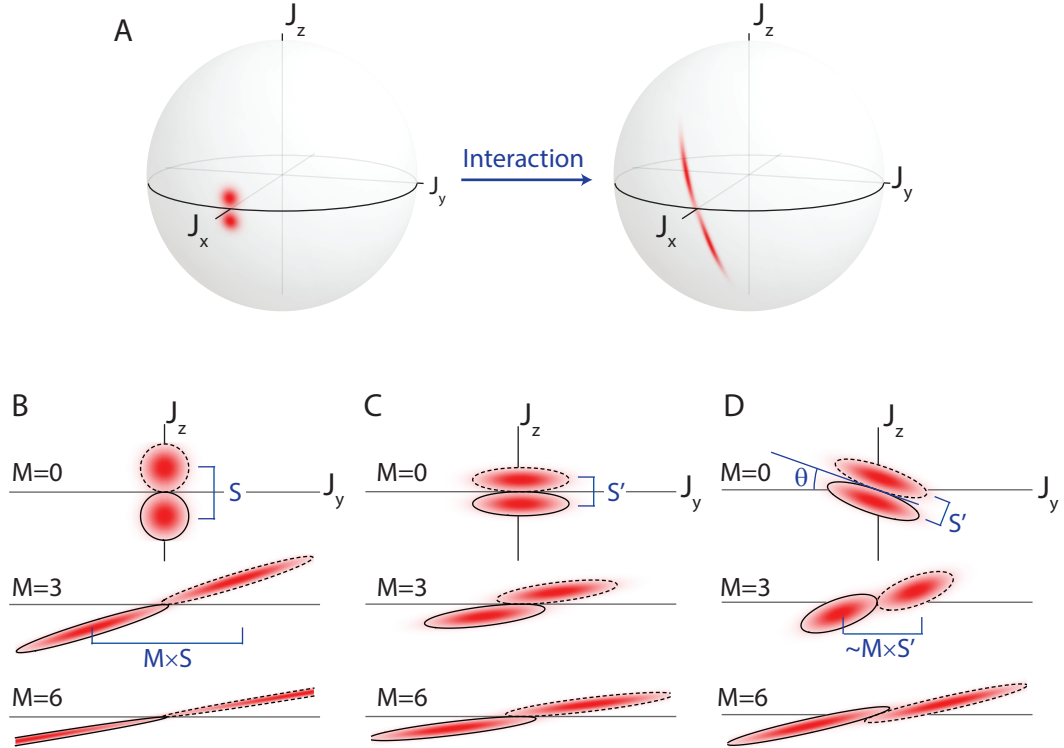


Figure 2.5: Conceptual description of quantum phase magnification. **(A)** Illustration of the phase magnification protocol on the Bloch sphere. The Wigner quasi-probability distributions are shown for two separated initial CSSs (left), and after the states are magnified through collective interactions (right). Here this is shown with  $N = 900$  atoms and a magnification of  $M = 3$  for pictorial clarity. Experimentally we use up to  $N = 5 \times 10^5$  and  $M = 100$ , permitting us to concentrate on a planar patch of the Bloch sphere. **(B-C)** Effect of the  $J_z^2$  (shearing) interaction used for mapping  $J_z$  onto  $J_y$  for a pair of different initial states with separations  $S$  and  $S' = S/2$ ; each panel shows three different magnification factors. A  $\pi/2$  rotation about the  $J_x$  needs to follow to complete the protocol by rotating the states into the measurable  $J_z$  quadrature before fluorescence detection. **(B)** shows CSSs and **(C)** shows 6 dB squeezed states, together illustrating the requirement of larger magnifications to separate two initially squeezed states. **(D)** A small rotation  $\theta$  before the shearing step is added, eliminating the requirement of larger magnifications for squeezed states by giving rise to a re-focusing of the  $J_y$  noise. At an optimal magnification (here  $M = 3$ ), the noise re-focusing scheme maps the initial  $J_z$  onto  $J_y$  with the separation-to-noise ratio of the two initial states preserved.

including spontaneous emission, which is given by

$$\begin{aligned} H^I = & \hbar \delta_c J_z a^\dagger a - \hbar \delta_c J_z |\alpha(0, t)|^2 \\ & - \hbar (\beta^*(t) e^{i\delta_0 t} a + \beta(t) e^{-i\delta_0 t} a^\dagger) \\ & - \hbar \sum_k \sqrt{\frac{\kappa c}{2L}} (a_k^\dagger a_e^{i(\omega_k - \omega_c)t} + a_k a_e^{i(\omega_k - \omega_c)t}) \end{aligned} \quad (2.60)$$

The first term is simply the Hamiltonian shown in § 2.3.1. This gives rise to a cavity shift of  $\delta_c$  per spin-flip and generates a differential ac-Stark shift on the clock states of  $\delta_c$  per intra-cavity photon. The second term is a choice of rotating frame, taking out the mean precession on the Bloch sphere, where  $|\alpha(0, t)|^2$  is the time-dependent intra-cavity photon number for  $J_z = 0$ . The third term accounts for the excitation of the cavity mode with an incident laser, where  $\beta(t)$  is the driving amplitude and  $\delta_0$  is the cavity-light detuning referenced to the empty cavity resonance frequency. The last term phenomenologically introduces decay of the cavity modes at a rate  $\kappa$  to a continuum of modes with dispersion relation  $\omega_k = ck$  in a 1D-space extending from  $-L/2$  to  $L/2$  ( $L \rightarrow \infty$  limit is taken) where  $a_k$  are the decay mode annihilation operators and  $\omega_c$  is the cavity resonance frequency. The loss to atomic scattering is also included in this term by using the atom-broadened linewidth,  $\kappa = \kappa_0(1 + NC(\Gamma/\omega_{HF})^2)$ , where  $\kappa_0$  is the empty cavity decay rate and the second term in the parentheses is due to atomic scattering with cavity-atom detuning  $\Delta = \pm\omega_{HF}/2$ . For more details on the atomic scattering see § 2.3.2.

From this Hamiltonian we can find the Heisenberg equations of motions using the Heisenberg-Langevin approach shown in [49].

$$J_z(t) = J_z(0) \quad (2.61)$$

$$\dot{a} = \left( -i\delta_c J_z - \frac{\kappa}{2} \right) a + i\beta(t) e^{i\delta_0 t} + f_a \quad (2.62)$$

$$\dot{J}_y = -\delta_c |\alpha(0, t)|^2 J_x + \delta_c a^\dagger J_x a \quad (2.63)$$

Here

$$f_a = i \sum_k \sqrt{\frac{\kappa c}{2L}} a_k(0) e^{-i(\omega_k - \omega_c)t} \quad (2.64)$$

is a noise operator. This operator and the decay term in the second equation show the effects of the reservoir.

Now I will show that the intra-cavity field amplitude becomes linked to  $J_z$  in the limit of slowly varying amplitude  $|\dot{\beta}(t)/\beta(t)| \ll |\delta_c J_z - i\kappa/2|$ . By integrating  $\dot{a}$  by parts, assuming  $\beta(0) = 0$ , dropping the term involving  $\dot{\beta}(t)$  and taking the long time limit  $t \gg 1/\kappa$  we obtain

$$a(t) = -\alpha(J_z, t) - f'_a(J_z, t) \quad (2.65)$$

where

$$\alpha(J_z, t) = \frac{\beta(t) e^{-i\delta t}}{\delta_0 - \delta_c J_z(0) + i\kappa/2}. \quad (2.66)$$

Taylor expanding  $\alpha(J_z, t)$  around  $J_z = 0$ , we obtain

$$\alpha(J_z, t) \sim \alpha(0, t) \left( 1 + \frac{\delta_c}{\delta_0 + i\kappa/2} J_z \right) \quad (2.67)$$

which incorporates the lowest order field amplitude correction due to atoms.  $f'_a(J_z, t)$  is a noise operator proportional to  $a_k(0)$ . Since the decay modes are assumed to be initially in the vacuum state, this noise operator will vanish when acting upon the initial state of the reservoir. I will now assume we are on a planar patch of the Bloch sphere, where  $J_x = J = N/2$  and  $J_y \in [-0.2, 0.2]$ , which covers the experimentally relevant range. Now, substituting the lowest order equation for  $a(t)$  into the equation for  $\dot{J}_y$ , we obtain

$$\dot{J}_y = -J\delta_c |\alpha(0, t)|^2 + J\delta_c [\alpha^*(J_z, t) + f_a'^\dagger(J_z, t)] [\alpha(J_z, t) + f'_a(J_z, t)] \quad (2.68)$$

then take the expectation value over the decay modes, denoted as  $\langle \cdot \rangle_a$ , and as previously

mentioned we assume  $\langle f_a(J_z, t) \rangle_a = 0$ ,

$$\begin{aligned} \langle J_y \rangle_a &\approx J\delta_c |\alpha(0, t)|^2 \left\langle J_z \left( \frac{\delta_c}{\delta_0 - i\kappa/2} + \frac{\delta_c}{\delta_0 + i\kappa/2} \right) \right\rangle_a \\ &= 2J \frac{|\alpha(0, t)|^2 \delta_c^2 \delta_0}{|\delta_0 + i\kappa/2|^2} \langle J_z \rangle_a \end{aligned} \quad (2.69)$$

I will now define a quantity  $m = M/N$ —the magnification factor divided by the atom number for an ac-Stark shift  $\phi_{\text{AC}}$ . It is given by

$$m = M/N = \int_{t_0}^t dt' \frac{|\alpha(0, t)|^2 \delta_c^2 \delta_0}{|\delta_0 + i\kappa/2|^2} = \frac{\delta_0 \delta_c}{|\delta_0 + i\kappa/2|^2} \phi_{\text{AC}} \quad (2.70)$$

where  $\phi_{\text{AC}}$  is found according to Equation 2.28. By integrating Equation 2.69 with respect to time, we obtain

$$\langle J_y \rangle_a \approx \langle J_y(0) \rangle_a + 2Jm \langle J_z(0) \rangle_a \quad (2.71)$$

We can now calculate

$$\langle J_z J_y + J_y J_z \rangle_a \approx \langle J_z J_y(0) + J_y J_z(0) \rangle_a + 4Jm \langle J_z^2(0) \rangle_a \quad (2.72)$$

by inserting for  $J_y$ . This quantity will be useful during the derivation later. We can now also find  $\dot{J}_y^2$  from the Hamiltonian as

$$\begin{aligned} \dot{J}_y^2 &= -\delta_c |\alpha(0, t)|^2 (J_x J_y + J_y J_x) + \delta_c a^\dagger (J_x J_y + J_y J_x) a \\ &= -2J\delta_c |\alpha(0, t)|^2 J_y + 2J\delta_c [\alpha^*(J_z, t) + f'^\dagger(J_z, t)] J_y [\alpha(J_z, t) + f'_a(J_z, t)]. \end{aligned} \quad (2.73)$$

Then we again take the expectation value over the decay modes to find

$$\langle \dot{J}_y^2 \rangle_a \approx 2J\delta_c |\alpha(0, t)|^2 \left\langle \frac{\delta_c}{\delta_0 - i\kappa/2} J_z J_y + J_y J_z \frac{\delta_c}{\delta_0 + i\kappa/2} \right\rangle_a \quad (2.74)$$

$$= 2J\dot{m} \left\langle J_z J_y + J_y J_z - \frac{i\kappa/2}{\delta_0} [J_z, J_y] \right\rangle_a \quad (2.75)$$

We now use the commutation relation  $[J_z, J_y] = iJ_x$ , then take  $\langle J_x \rangle \approx J$  to obtain

$$\begin{aligned} \langle \dot{J}_y^2 \rangle_a &\approx 2J \frac{\delta_c |\alpha(0, t)|^2 \delta_c \delta_0}{|\delta_0 + i\kappa/2|^2} \langle J_z J_y + J_y J_z \rangle_a + 2J^2 \frac{\delta_c |\alpha(0, t)|^2 \delta_c \kappa/2}{|\delta_0 + i\kappa/2|^2} \\ &= 2J\dot{m} \langle J_z J_y + J_y J_z \rangle_a + 2J^2 \dot{m} \frac{\kappa/2}{\delta_0} \end{aligned} \quad (2.76)$$

Inserting for  $\langle J_z J_y + J_y J_z \rangle$  using Equation 2.72 we obtain

$$\langle \dot{J}_y^2 \rangle_a = 2J\dot{m} \langle J_z J_y(0) + J_y J_z(0) \rangle_a + 4J^2 \partial_t m^2 \langle J_z^2(0) \rangle_a + 2J^2 \dot{m} \frac{\kappa/2}{\delta_0} \quad (2.77)$$

then integrate with respect to time to obtain

$$\langle J_y^2 \rangle_a = \langle J_y^2(0) \rangle_a + 2Jm \langle J_z J_y(0) + J_y J_z(0) \rangle_a + 4J^2 m^2 \langle J_z^2(0) \rangle_a + 2J^2 m \frac{\kappa/2}{\delta_0} \quad (2.78)$$

We can now assume that the amount of decoherence is small to insert  $J = N/2$  and use total magnification factors to find the desired quantities  $\langle J_y \rangle$  and  $\langle J_y^2 \rangle$  as

$$\langle J_y \rangle = \langle J_y(0) \rangle + M \langle J_z(0) \rangle \quad (2.79)$$

$$\langle J_y^2 \rangle = \langle J_y^2(0) \rangle + M \langle J_z J_y(0) + J_y J_z(0) \rangle + M^2 \langle J_z^2(0) \rangle + \frac{N}{4} M \frac{\kappa}{\delta_0} \quad (2.80)$$

These equations allow the calculation of the mean and variance of  $J_y$  after magnification. From the above equations, we can find  $\text{Var}[J_y] = \langle J_y^2 \rangle - \langle J_y \rangle^2$  as

$$\text{Var}[J_y] = \text{Var}[J_y(0)] + \text{Cov}[J_y(0), J_z(0)]_{\text{sym}} + M^2 \text{Var}[J_z(0)] + \frac{N}{4} M \frac{\kappa}{\delta_0}. \quad (2.81)$$

Here the last term is the only term that would not be present under the action of a pure one-axis twisting Hamiltonian. It represents the effect of measurement back-action due to cavity decay. For quantum phase magnification, this term is negligible, but we will see that we can use it to estimate the antisqueezing due to measurement in §2.3.8. We can now insert the appropriate variances and covariances for a tilted  $J_z$ -squeezed state to attain a formula for  $\text{Var}[J_y]$  using the noise re-focusing protocol. Expressing the variances and covariances in terms of the initial  $J'_y$  and  $J'_z$  of the unrotated squeezed state, we obtain

$$\text{Var}[J_y(0)] = \sin^2 \theta \text{Var}[J'_z] + \cos^2 \theta \text{Var}[J'_y] \quad (2.82)$$

$$\text{Var}[J_z(0)] = \cos^2 \theta \text{Var}[J'_z] + \sin^2 \theta \text{Var}[J'_y] \quad (2.83)$$

$$\text{Cov}[J_y(0), J_z(0)] = -\frac{1}{2} \sin 2\theta (\text{Var}[J'_y] - \text{Var}[J'_z]) \quad (2.84)$$

where  $\theta$  is the angle the state is rotated by. If we insert these into our previous formula for  $\text{Var}[J_y]$  after magnification and assume  $\theta$  is a small angle, we obtain

$$\text{Var}[J_y] = M^2 \text{Var}[J'_z] + (1 - M\theta)^2 \text{Var}[J'_y]. \quad (2.85)$$

This means for any given magnification  $M$  there exists a  $\theta_0 = 1/M$  for which the second term is zero and we magnify only the squeezed initial  $J_z$  noise. To see how the ordinary magnification scheme performs, we can set  $\theta$  to 0. For a squeezed state characterized by  $\xi$  and  $\xi'$  such that  $\text{Var}[J'_z] = \xi^2 \Delta_{CSS}^2$  and  $\text{Var}[J'_y] = \xi'^2 \Delta_{CSS}^2$ , where  $\xi \times \xi' \geq 1$ , the formula reduces to

$$\text{Var}[J_y] = M^2 \xi^2 \Delta_{CSS}^2 + \xi'^2 \Delta_{CSS}^2. \quad (2.86)$$

Thereby, to set the noise contribution of the first term to some fractional contribution

$1 - \epsilon$  we would need to magnify by

$$M = \frac{1}{\sqrt{2\epsilon}} \frac{\xi'}{\xi} \quad (2.87)$$

which grows at least quadratically with the squeezing factor  $\xi$ . Therefore for highly squeezed states, very large magnifications would be needed to utilize this basic scheme, leading to decoherence or to regimes where the measurement back-action would enter. The noise re-focusing protocol avoids this problem by allowing faithful reproduction of the initial squeezed state at an arbitrarily chosen magnification.

### 2.3.7 Magnification limits

In this subsection I will show that the quantum state magnification scheme described in the previous section has a similar limit to its performance as the regular squeezing scheme. It is important to note that the squeezed states must be generated in some other way, and this scheme is purely meant to read out states that have already been squeezed. In [63] it is shown that the quantum state magnification scheme described in this thesis will be limited due to atomic and cavity decay to a metrological gain scaling with  $\sim \sqrt{NC}$ . To analyze the limit of the protocol, I will use a similar method to that in § 2.3.3.

Considering an initial state with  $\Delta J_z(0) = \xi\sqrt{N}/2$  and working at the optimal magnification point  $M = 1/\theta$  where  $\theta \ll 1$  the  $J_y$  variance after magnification from Equation 2.81 is given by

$$\text{Var}[J_y] = \frac{N}{4} M^2 \xi^2 + \frac{N}{4} M \frac{\kappa}{\delta_0}. \quad (2.88)$$

The first term is again purely from the initial  $J_z$  noise and the second term from cavity decay can be limited by detuning further from cavity resonance (increasing  $\delta_0$ ). Increasing the detuning comes at the expense of needing to send in more light for the same magnification. We therefore again need to consider the effect of spin-flips due to spontaneous emission, so recalling Equation 2.30, we have

$$\delta_{\text{flip}}^2 = \frac{N}{6} \frac{\Gamma}{\omega_{\text{HF}}} \phi_{AC} = \frac{1}{6C} M \frac{\delta_0}{\kappa_0} \quad (2.89)$$

where the second equality holds only if  $\delta_0 \gg \kappa/2$ . If we assume the state magnification protocol will work properly only when the noise due to spin-flips is less than the initial  $J_z$  noise (*i.e.* our readout method should not induce more noise than what is in the initial state), we can set a limit to the maximum usable detuning by asserting that

$$\delta_{\text{flip}}^2 \leq \xi^2 \frac{N}{4} \quad (2.90)$$

and thus by assuming the equality

$$\delta_{0,\text{max}} = \frac{3}{2} \frac{NC\kappa_0\xi^2}{M}. \quad (2.91)$$

Inserting this back into Equation 2.88 we obtain

$$\text{Var}[J_y] = \frac{N}{4} M^2 \xi^2 + M^2 \frac{1}{\xi^2} \frac{1 + NC(\Gamma/\omega_{\text{HF}})^2}{6C} \quad (2.92)$$

where in the second term I have utilized Equation 2.27. Assuming that the initial state is no longer resolvable when the second term becomes equal to the first one, we can get an estimate of the resolving power of the magnification scheme:

$$\xi_{\text{min}}^2 = \sqrt{\frac{1 + NC(\Gamma/\omega_{\text{HF}})^2}{\frac{3}{2}NC}} \quad (2.93)$$

which has similar features to the limit placed on squeezing by QND measurement in § 2.3.3. In this case, the resolving power is

$$\xi_{\text{min}}^2 = \sqrt{\frac{1 + NC(\Gamma/\omega_{\text{HF}})^2}{\frac{3}{2}NC}}. \quad (2.94)$$

For low atom numbers,  $\xi_{\text{min}}^2$  decreases proportionally to  $1/\sqrt{3/2(NC)}$ , then as  $N \rightarrow \infty$  saturates at  $\xi_{\text{sat}}^2 = \sqrt{2/3}(\omega_{\text{HF}}/\Gamma) \sim -31 \text{ dB}$  due to the effects of atomic scattering. Unlike squeezing due to measurement, the method does not have a specific optimal atom number—the achievable resolution gets asymptotes to  $\xi_{\text{sat}}^2$  as the atom

number increases. The achievable resolution limit does not depend on  $M$  as long as one operates at the optimal point of the re-focusing.

### 2.3.8 Antisqueezing from QND measurement

As mentioned in §2.1.1 and §2.3.1, a QND measurement of  $J_z$  below the coherent state noise limit necessarily leads to antisqueezing in  $J_y$ . In the case of QND measurement in a cavity, the antisqueezing is caused by the quantum noise in the probing field. The treatment in §2.3.6 includes the antisqueezing due to measurement, so we can use it as a starting point. Using the intermediate results in Equations 2.71, 2.72, and 2.78, we can take  $\langle J_y \rangle = \langle J_z \rangle = \langle J_y J_z + J_z J_y \rangle = 0$  and  $\langle J_y^2 \rangle = \langle J_z^2 \rangle = J/2$  to obtain

$$\begin{aligned} \langle J_y^2 \rangle &= \frac{J}{2} + 2J^3m^2 + 2J^2m\frac{\kappa/2}{\delta_0} \\ &= \frac{1}{2}J \left( 1 + (2Jm)^2 + 2Jm\frac{\kappa}{\delta_0} \right) \end{aligned} \quad (2.95)$$

We can now again assume that the amount of decoherence is small and insert  $J = N/2$  and use total magnification factors to find the desired quantity  $\langle J_y^2 \rangle$  as

$$\langle J_y \rangle^2 = \frac{N}{4} \left( 1 + M^2 + M\frac{\kappa}{\delta_0} \right). \quad (2.96)$$

If we assume the probe to be on resonance, *i.e.*  $\delta_0 = 0$ , we can obtain that

$$\langle J_y \rangle^2 = N^2 \frac{\delta_c}{\kappa} \phi_{\text{AC}}. \quad (2.97)$$

This means that the increased variance due to measurement increases linearly with measurement strength. We can also show using Equation 2.38 that when spin-flips are ignored,

$$\Delta J_y \times \Delta J_z = \frac{N}{4} \frac{1}{\sqrt{\epsilon\kappa_0/\kappa}} \quad (2.98)$$

which means that the squeezing is area conserved up to a factor of the losses due to

nonidealities.  $\epsilon$  here represents all the coupling efficiencies of the light and  $\kappa_0/\kappa$  are the losses due to atomic scattering. In a full treatment of antisqueezing spin-flips will play a role, and in combination with technical noise these two factors will mean that the shearing terms cannot be neglected. However, I will here stick with this simplified model.

## 2.4 Entanglement measures

Quantifying entanglement in many-body systems has been a theoretical challenge for several decades and significant advances have been made in the area. While the metrological enhancement shown in Equation 2.6 shows readily how the entanglement can be useful, in order to compare between different systems it can be helpful to use other measures of entanglement. The Wineland criterion itself does guarantee entanglement for symmetric states, but does not quantify it in a way that is readily comparable to *e.g.* Dicke states, where there is clearly entanglement but the Wineland criterion cannot be used.

### 2.4.1 Entanglement depth in symmetric states

A commonly used method of quantifying entanglement is to establish the least entangled state the system can be reduced to [64, 65]. A non-entangled system can be reduced to product states, while a system of entanglement depth  $k$  can be reduced to product states where each state is an entangled state of at least  $k$  particles. This metric of entanglement can be quantified through only collective measurements and is therefore readily accessible experimentally. As seen in [64] this metric can also be used on Dicke states. The entanglement depth is calculated by considering the maximum  $J^2 = \langle J_x^2 + J_y^2 \rangle$  and minimum  $(\Delta J_z)^2$  possible with a state of entanglement depth  $k$ .

I will here give a brief outline of the derivation of the entanglement depth criterion shown in [65]. The following does not produce an optimal bound for all entangled states, but shows some of the general concepts employed in these entanglement criteria. For the actual calculations of entanglement depth, I will use the more optimal criterion shown in [64]. The boundaries are calculated by considering the inequality

$$\langle J_x^2 \rangle + \langle J_y^2 \rangle + \langle J_z^2 \rangle \leq J(J+1) \quad (2.99)$$

in combination with Heisenberg's uncertainty relation

$$\Delta J_y \times \Delta J_z \geq \frac{|\langle J_x \rangle|}{2} \quad (2.100)$$

and utilizing the above to find the maximally squeezed states as a function of  $\langle J_x \rangle$ . For states where  $\langle J_x \rangle$  is close to  $J$ , one can find the maximally squeezed states variationally by minimizing  $\text{Var}J_z + \mu \langle J_x \rangle$  where  $\mu$  is a Lagrange multiplier constraining  $\langle J_x \rangle$ . This allows us to find the minimum variance as a function of  $\langle J_x \rangle$  for a given  $J$ . I will label this bound as  $F_J(\langle J_x \rangle / J)$ . Then considering a separable state of  $N$  spin- $J$  particles as a weighted sum of products of density matrices,

$$\rho = \sum_i p_i \rho_1^{(i)} \otimes \rho_2^{(i)} \dots \otimes \rho_N^{(i)} \quad (2.101)$$

where  $p_i$  is the weight of the  $i$ th set of density matrices and  $\rho_n^{(i)}$  is the density matrix of the  $n$ th particle in the  $i$ th term of the weighted sum. The variance of such a state will obey the inequality

$$\text{Var}J_z \geq \sum_i p_i \sum_{j=1}^N (\Delta J_z^2)_j^{(i)} \geq \sum_i p_i \sum_{j=1}^N J F_J \left( \frac{\langle J_x \rangle_i^{(i)}}{J} \right). \quad (2.102)$$

where the second inequality comes from considering the bound on maximal squeezing found from the variational argument shown previously. Now, using that the function  $F_J$  is convex, it can be shown that for spin-1/2 particles,

$$\text{Var}J_z \geq \frac{N}{2} F_J \left( \frac{\langle J_x \rangle}{N/2} \right). \quad (2.103)$$

This is the entanglement criterion found in [65] and the entanglement depth for a system of spin-1/2 particles can be found by considering  $J = k/2$  where  $k$  is the entanglement depth. The criterion was improved upon in [64] where it is shown that using a different argument for the  $F_J$  function, the criterion can be generalized to treat Dicke states and states with significant antisqueezing. This more optimal criterion is given by

$$\text{Var}J_z \geq \frac{N}{2} F_J \left( \frac{\sqrt{\langle J_x^2 + J_y^2 \rangle}}{N/2} \right). \quad (2.104)$$

The above assumes that  $k \ll N$  and that  $N \gg 1$ . Essentially the use of  $\sqrt{\langle J_x^2 + J_y^2 \rangle}$

in place of  $\langle J_x \rangle$  allows nonzero values of entanglement depth to be found for states that are wrapped around the Bloch sphere or otherwise have a nontrivial Wigner distribution.

### 2.4.2 Entanglement depth in nonsymmetric states

The method of quantifying entanglement outlined in the previous section works for symmetric states, which in our case would mean the atoms are probed symmetrically and couple identically to the cavity. While our system is close to this ideal case, there is still some residual inhomogeneity as seen in § 2.3.4. Fortunately, as seen in [66], a modification can be made to the entanglement inequalities in order to find the entanglement depth in nonsymmetric states.

As shown in [66, 67], we can put tighter bounds on the entanglement depth of our slightly nonsymmetric states. The main message from this section is that for the level of inhomogeneities we are dealing with, the full non-symmetric calculation and the symmetric calculation ignoring the inhomogeneities in our system give virtually the same entanglement depths. The predictions of the full calculation is in fact  $\sim 1\%$  lower. These results imply that the boundaries quantifying quantum correlations are smooth functions of the inhomogeneity. For more details on how the inhomogeneity in this system is modeled, see § 2.3.4.

In order to generate entanglement boundaries for our particular nonsymmetric probing, we first generate random positions distributed according to Equation 2.56 and calculate individual coupling coefficients from Equation 2.57. Following the procedure in [66], we consider  $n$  ensembles of  $k$  particles, where each ensemble indexed by  $i$  has the same coupling coefficient  $\eta_i$ . It is shown in [66] that ensembles of  $k$  entangled atoms with identical coupling coefficients minimize the variance of the ensemble thus this is a suitable assumption to place entanglement boundaries. In the following treatment of the inhomogeneity we will consider

$$s_v^{(i)} = \eta_i j_v^{(i)} \quad (2.105)$$

the inhomogeneous spin operator on the  $i$ th atom in the  $v$  direction with coupling

coefficient  $\eta_i$ . We can then define full collective inhomogeneous operators as

$$S_v = \frac{1}{Z} \sum_i s_v^{(i)} \quad (2.106)$$

where

$$Z = \frac{\sum_i \eta_i}{\sum_i \eta_i^2}. \quad (2.107)$$

$Z$  is chosen such that  $\text{Var } S_z / \langle S_x \rangle_{\text{CSS}} = 1/2$ , as used previously in § 2.3.4. We then have the following two equations for the normalized coherence

$$\frac{\langle S_x \rangle}{\langle S_x \rangle_{\text{CSS}}} = \frac{1}{\langle S_x \rangle_{\text{CSS}}} \sum_{i=1}^n \langle S_x^{(i)} \rangle_{\text{CSS}} \frac{\langle S_x^{(i)} \rangle}{\langle S_x^{(i)} \rangle_{\text{CSS}}} \quad (2.108)$$

and variance

$$\frac{(\Delta S_z)^2}{(\Delta S_z)_{\text{CSS}}^2} = \frac{1}{(\Delta S_z)_{\text{CSS}}^2} \sum_{i=1}^n (\Delta S_z^{(i)})_{\text{CSS}}^2 \frac{(\Delta S_z^{(i)})^2}{(\Delta S_z^{(i)})_{\text{CSS}}^2} \quad (2.109)$$

of the collective state. Here, for an inhomogeneously coupled ensemble we have defined

$$\langle S_x \rangle_{\text{CSS}} = \frac{1}{Z} \sum_i \frac{\eta_i}{2} \quad (2.110)$$

$$(\Delta S_x)_{\text{CSS}}^2 = \frac{1}{Z^2} \sum_i \frac{\eta_i^2}{4} \quad (2.111)$$

Since each ensemble of  $k$  atoms has the same coupling coefficient  $\eta_i$ , we can place entanglement depth boundaries based on previous work in uniformly coupled ensembles [64, 65]. We can now minimize  $\Gamma$  defined as follows

$$\Gamma \left( \{(\Delta S_z^{(i)})^2\}, \{\langle S_x^{(i)} \rangle\}, \mu \right) = \sum_{i=1}^n \left[ \frac{k\eta_i^2}{4} \frac{(\Delta S_z^{(i)})^2}{(\Delta S_z^{(i)})_{\text{CSS}}^2} - \mu \frac{\langle S_x \rangle}{\langle S_x \rangle_{\text{CSS}}} \right] \quad (2.112)$$

where  $\mu$  is a Lagrange multiplier to enforce the constraint of coherence and  $\Gamma$  is the variance of the full collective state, subject to the constraint. From [65], we also have that

$$(\Delta S_z)^2 \geq \frac{k}{2} F_{k/2} \left( \frac{\langle S_x \rangle}{k/2} \right) \quad (2.113)$$

for each ensemble of  $k$  atoms. We use the numerical method described in [64] to find this upper bound on  $(\Delta J_z)^2$  for each ensemble of  $k$  atoms. We minimize  $\Gamma$  with respect to  $\langle S_x \rangle$  for each individual ensemble using the numerically calculated entanglement bounds. We insert the minimized variance and the corresponding coherence into Equation 2.108 and Equation 2.109 to find the bounds on entanglement for our inhomogeneity. Now, we sample coupling strengths calculated from randomly generated positions within the distribution in Equation 2.57, and use the bounds on the individual ensembles along with the coupling coefficients to produce an overall bound from Equation 2.109 and Equation 2.108. To produce conservative bounds we use  $\sigma_r = 20\mu\text{m}$ . We use  $\sqrt{\langle J_x^2 + J_y^2 \rangle}$  in place of  $\langle S_x \rangle$  paralleling the procedures outlined in [64] and [68] since it places a tighter bound on the entanglement depth of states with large antisqueezing. The validity of this procedure is shown in the following two sections § 2.4.3 and § 2.4.4. The calculated bounds are presented with experimental data in § 4.3.2.

### 2.4.3 Coherence for entanglement bounds

In [64] and [68] it was shown that for the calculation of entanglement depth in symmetric states,  $\langle J_x^2 + J_y^2 \rangle$  can be used in place of  $\langle J_x \rangle$  when  $N \gg k$ . Here, I follow the same general procedure to show that this also works in the nonsymmetric case. We will consider groups of  $k_i$  particles and use the inhomogeneous operators. Using the standard definition of the variances in the  $x$  and  $y$  direction and the fact that the variance of the entire ensemble is the sum of the variances of the subensembles, we obtain

$$\begin{aligned}
\langle (\Delta S_x)^2 \rangle + \langle (\Delta S_y)^2 \rangle &= \frac{1}{Z^2} \sum_i (\Delta s_x^{(i)})^2 + (\Delta s_y^{(i)})^2 \\
&\leq \frac{1}{Z^2} \sum_i \frac{k_i \eta_i^2}{2} \left( \frac{k_i}{2} + 1 \right) - \langle (s_z^{(i)})^2 \rangle - \langle s_x^{(i)} \rangle^2 - \langle s_y^{(i)} \rangle^2.
\end{aligned} \tag{2.114}$$

The inequality holds as

$$\begin{aligned}
&(\Delta s_x^{(i)})^2 + (\Delta s_y^{(i)})^2 \\
&= \eta_i^2 \left[ (\Delta j_x^{(i)})^2 + (\Delta j_y^{(i)})^2 \right] \\
&\leq \eta_i^2 \left[ \frac{k_i}{2} \left( \frac{k_i}{2} + 1 \right) - \langle (j_z^{(i)})^2 \rangle - \langle j_x^{(i)} \rangle^2 - \langle j_y^{(i)} \rangle^2 \right]
\end{aligned} \tag{2.115}$$

Since  $\langle (j_z^{(i)})^2 \rangle \geq 0$  we neglect it. We now expand the variances and move the squared means to the RHS and obtain

$$\langle S_x^2 + S_y^2 \rangle \leq \langle S_x \rangle^2 + \langle S_y \rangle^2 + \frac{1}{Z^2} \sum_i \frac{k_i \eta_i^2}{2} \left[ \left( \frac{k_i}{2} + 1 \right) - \frac{k_i}{2} \frac{\langle j_x^{(i)} \rangle^2 + \langle j_y^{(i)} \rangle^2}{k_i^2/4} \right] \tag{2.116}$$

We now define  $\zeta = (1/Z^2) \sum_i k_i \eta_i^2$ , then set the term inside the square bracket to its maximum, where  $k_i = k$  for all  $i$ .

$$\langle S_x^2 + S_y^2 \rangle \leq \langle S_x \rangle^2 + \langle S_y \rangle^2 + \frac{\zeta}{2} + \frac{1}{Z^2} \sum_i \frac{k_i \eta_i^2}{2} \left[ \frac{k}{2} \left( 1 - \frac{\langle j_x^{(i)} \rangle^2 + \langle j_y^{(i)} \rangle^2}{k^2/4} \right) \right] \tag{2.117}$$

We can now use Jensen's inequality to show that

$$-\sum_i k_i \left( \frac{\langle s_v^{(i)} \rangle}{k_i} \right)^2 \leq -\frac{1}{N} \left( \sum_i k_i \frac{\langle s_v^{(i)} \rangle}{k_i} \right)^2 = -\frac{Z^2}{N} \langle S_v \rangle^2 \quad (2.118)$$

for  $v = x, y, z$ , where we used that  $\sum_i k_i = N$ . Applying this inequality on Equation 2.117, we obtain

$$\langle S_x^2 + S_y^2 \rangle - \frac{\zeta}{2} \left( \frac{k}{2} + 1 \right) \leq \left( 1 - \frac{k}{N} \right) (\langle S_x \rangle^2 + \langle S_y \rangle^2). \quad (2.119)$$

Now we choose to consider states polarized in the  $x$ -direction and, without loss of generality, set  $\langle S_y \rangle = 0$ . If we then divide by  $(1 - k/N)$  and take the square root, we obtain

$$\left\{ \frac{1}{1 - k/N} \left[ \langle S_x^2 + S_y^2 \rangle - \frac{\zeta}{2} \left( \frac{k}{2} + 1 \right) \right] \right\}^{1/2} \leq \langle S_x \rangle \quad (2.120)$$

For the inhomogeneity of our experiment,  $\zeta \sim 0.995N$ . As  $\langle S_x^2 + S_y^2 \rangle \sim \zeta^2$  is large compared to  $(\zeta/2)(k/2 + 1)$  we neglect  $(\zeta/2)(k/2 + 1)$  and take  $(1 - k/N) \sim 1$ . We can then use  $\sqrt{\langle S_x^2 + S_y^2 \rangle}$  in place of  $\langle S_x \rangle$  to calculate our entanglement depth.

#### 2.4.4 Symmetric and nonsymmetric coherence

In the experiment described in this thesis, we actually measure the symmetric coherence instead of the nonsymmetric coherence. Using a similar method to that shown in § 2.4.2 we can model our decoherence. In this section I will show that these coherence measurements give a lower bound on the coherence associated with the nonsymmetric collective observables which go into the entanglement depth calculations in the nonsymmetric case. We choose states polarized in the  $x$ -direction. Consider the Heisenberg picture operators for  $J_x$ ,  $J_y$ ,  $S_x$  and  $S_y$ :

$$J_x = \sum_i (\cos \theta_n j_x^{(n)} + \sin \theta_n j_y^{(n)}) \quad (2.121)$$

$$J_y = \sum_i (\cos \theta_n j_x^{(n)} + \sin \theta_n j_y^{(n)}) \quad (2.122)$$

$$S_x = \frac{1}{Z} \sum_n \eta_i (\cos \theta_n j_x^{(n)} + \sin \theta_n j_y^{(n)}) \quad (2.123)$$

$$S_y = \frac{1}{Z} \sum_n \eta_i (\cos \theta_n j_x^{(n)} + \sin \theta_n j_y^{(n)}) \quad (2.124)$$

Here  $\theta_n$  parametrizes the amount of decoherence, essentially modeling the decoherence as a mixing in of the orthogonal operator  $j_y^{(n)}$ . The origin of this is the inhomogeneous ac-Stark shifts from the probe beam. Thus the model adopts Equation 2.57 to define a  $\theta_n = \beta r_n^2$  where  $r_n = (x_n^2 + y_n^2)^{1/2}$  is the  $n$ th particle's distance from the center of the probe beam. Using this model and inserting positions sampled from the same distribution used earlier, we calculated numerically that

$$\frac{\sqrt{J_x^2 + J_y^2}}{N/2} \leq \frac{\sqrt{S_x^2 + S_y^2}}{(1/Z) \sum_i \eta_i / 2}. \quad (2.125)$$

We are therefore justified in using the LHS of Equation 2.125 as a lower bound on the coherence for entanglement depth calculations in the nonsymmetric case.

# Chapter 3

## Experimental apparatus

The generation of spin-squeezing is well understood theoretically—many schemes are capable of generating large amounts of spin-squeezing—the measurement and characterization of the states’ noise properties is challenging. The cavity measurement-based system used in this thesis was carefully engineered to make photon shot noise limited measurements of the collective atomic state of  $^{87}\text{Rb}$ . This Chapter discusses the steps taken to reach this performance limit.

Some parts of the apparatus have been described previously in references [53, 69, 70]. Nevertheless, I will describe the key elements of the apparatus. This chapter is divided into three parts where first, we focus on the atom source and discuss the preparation of cold atoms in the correct hyperfine state. Next, I will describe the optical cavity and the measurement of its resonance. The final section describes the interaction between the atoms and the cavity.

## 3.1 Cold atom source

The tools of laser cooling were developed in the 1980s and described in seminal papers such as [71–78]. Laser cooling enabled Bose-Einstein condensation [79, 80] and was followed by a new wave of atomic physics experiments for the purposes of precision measurement [10, 11, 81–85], quantum information technology [86–88] and investigation of fundamental physics [13, 89–92]. In this experiment, we employ laser cooling to prepare a cold atomic cloud which is then loaded into the optical lattice generated in the cavity. In this section I will describe the apparatus and experimental sequences used as well as the characterization of the atom source. The techniques used are explained in atomic physics textbooks such as [93–96] or in the review paper [97].

### 3.1.1 Vacuum chamber

The vacuum chamber is a compact setup with a box around it for mounting optics. The MOT setup uses retroreflected cooling and repump beams. The beams are not exactly retroreflected, as at large densities, the optical density of the cloud gets large and creates a shadow in the beam. In order to get effective cooling, the retroreflected beam must therefore be slightly displaced. An ion pump is attached to maintain vacuum. Below the center of the cavity there is a vertical region the atoms can be dropped through to do *e.g.* atom interferometry experiments. An overview of the chamber with its most important features is shown in Figure 3.1 and two pictures in Figure 3.2.

### 3.1.2 Laser setup

Two distributed feedback laser diodes are used to generate the cooling and the repump light. Each laser uses two optical isolators to avoid optical feedback. The error signals for locking are generated using frequency modulated saturated absorption spectroscopy. The frequency modulation is done by modulating the laser current. The lasers are then locked to the crossover transitions, as they are stronger than the other transitions.

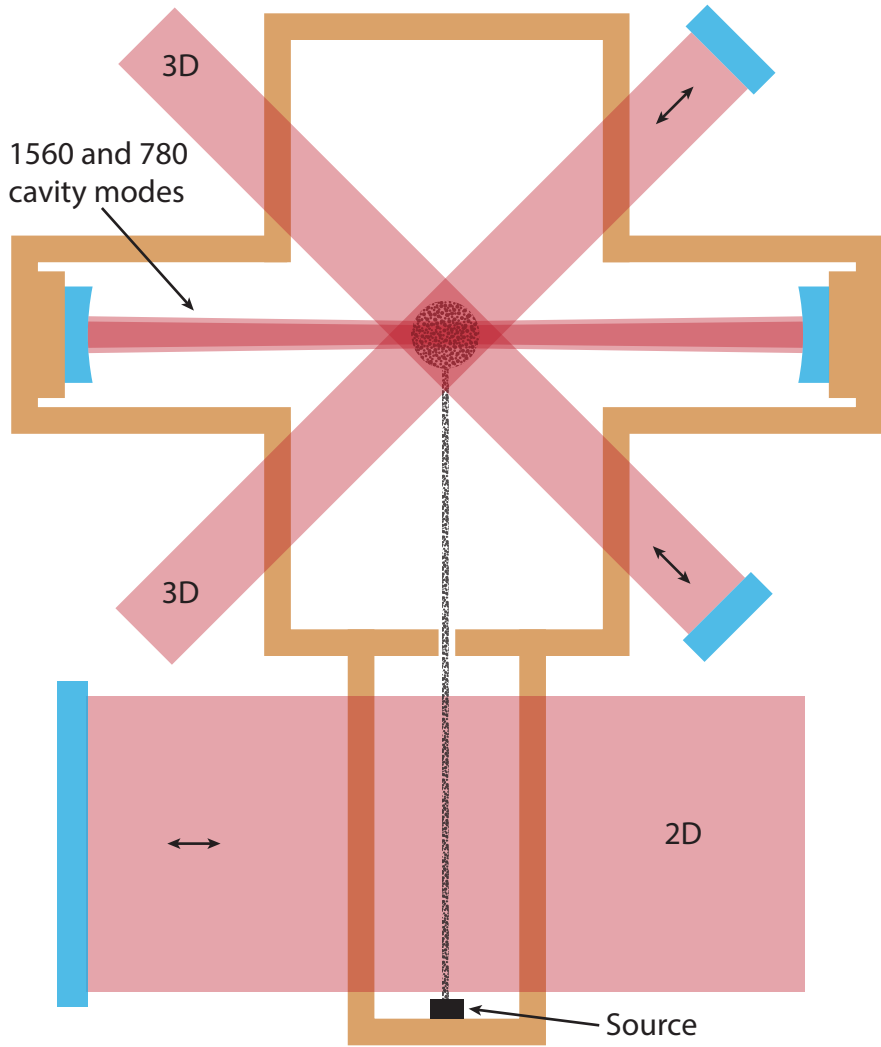


Figure 3.1: The figure shows the geometry of the chamber. The black part illustrates how the atoms go from the source to the 2D MOT then through a pinhole to load the 3D MOT in the center of the cavity. The cooling beams are retroreflected. The repump light is overlapped with the cooling light. There are  $\lambda/4$  waveplates in front of the retroreflecting mirrors to set the beams in the right circular polarization. The third beam pair in the z-direction for the 3D MOT is not drawn. The chamber is made out of low thermal expansion zerodur glass for stability.

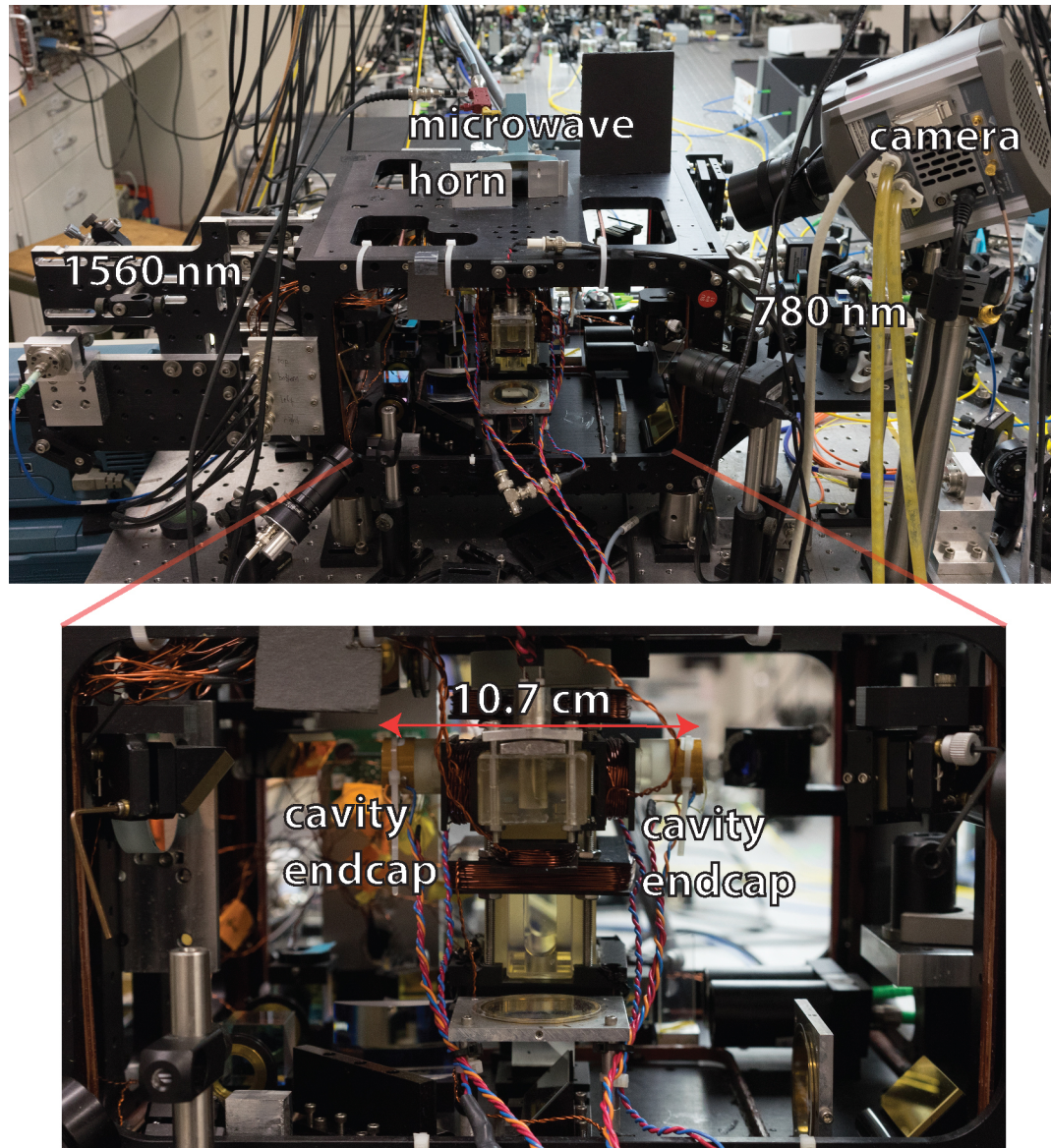


Figure 3.2: The picture shows an overview of the vacuum chamber setup with an inset showing a zoom-in on the chamber itself. The paths where the light at 780 nm and 1560 nm is coupled in are labeled, in addition to the camera for fluorescence imaging and the microwave horn. The closeup shows the cavity and some of the MOT optics.

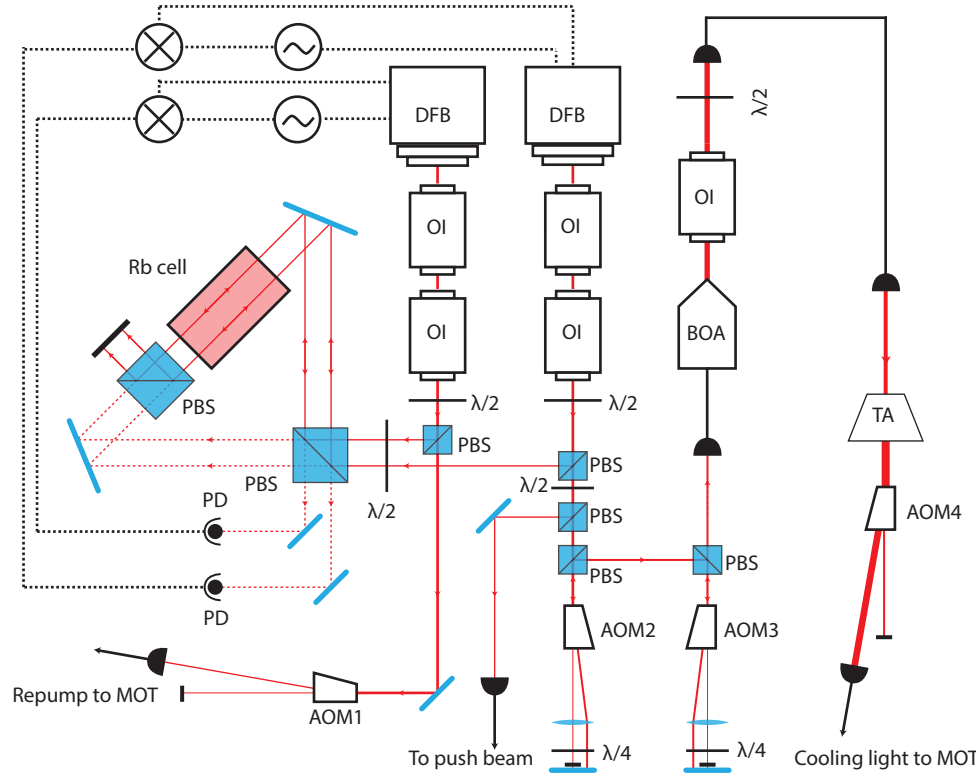


Figure 3.3: Laser setup to generate cooling and repump light. Red lines show laser light paths. Thicker lines indicate higher powers. Arrows indicate direction of propagation, in some cases there is light going both ways. The dashed line in the saturated absorption setup is the spectroscopy probe beam, going in the opposite direction of the pump beam which is filtered out by the PBS. DFB: Distributed feedback laser diode. OI: Optical isolator. PBS: Polarizing beamsplitter.  $\lambda/2$ : Half-wave plate.  $\lambda/4$ : Quarter-wave plate. AOM: Acousto-optic modulator. BOA: Booster amplifier. TA: Tapered amplifier.

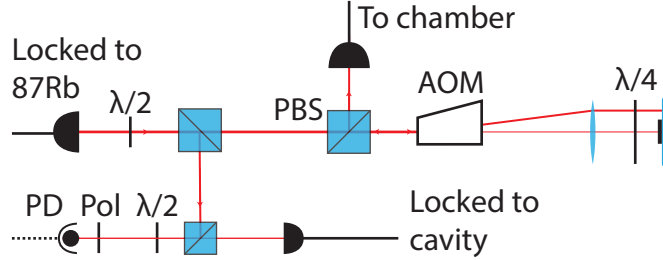


Figure 3.4: The figure shows the setup used to frequency shift the push beam to resonance and how some of the light is split off to go to the beatnote setup. After the double-pass AOM, the push beam light is resonant with the  $|F = 2\rangle \rightarrow |F' = 3\rangle$  transition. The light that generates the beatnote is resonant with the  $|F = 2\rangle \rightarrow |F' = 2, 3\rangle$  crossover transition.

The cooling laser is locked to the  $|F = 2\rangle \rightarrow |F' = 2, 3\rangle$  crossover transition and the repump laser is locked to the  $|F = 1\rangle \rightarrow |F' = 1, 2\rangle$  crossover transition. The repump laser is then shifted up by 78.5 MHz using an AOM (AOM1 in Figure 3.3) to be resonant with the  $|F = 1\rangle \rightarrow |F' = 2\rangle$  transition. This AOM also works as a switch for the repump beam and controls the repump power. The frequency shifted light is fiber coupled and sent to the MOT setup. The cooling light is passed through two double pass AOMs (AOM2 and AOM3 in Figure 3.3) to enable control of the laser-atom detuning during the cooling stages. The conditioned light is then amplified using a booster amplifier and a tapered amplifier. The booster amplifier is here a single-pass, traveling-wave amplifier. It takes input through an optical fiber and amplifies the light using a semiconductor-based gain medium. The final AOM (AOM4 in Figure 3.3) is used to switch the cooling light on and off and regulate its power. Before the fiber to the MOT setup, there is 140 mW of light when the detuning is set to  $2\Gamma$ . Coupled at 50 % efficiency, there is about 70 mW of light to be distributed between the 2D and 3D MOT. About 4 mW of the cooling light is picked off before it passes through any AOMs to generate both the push beam and a beat note with the cavity probe beam.

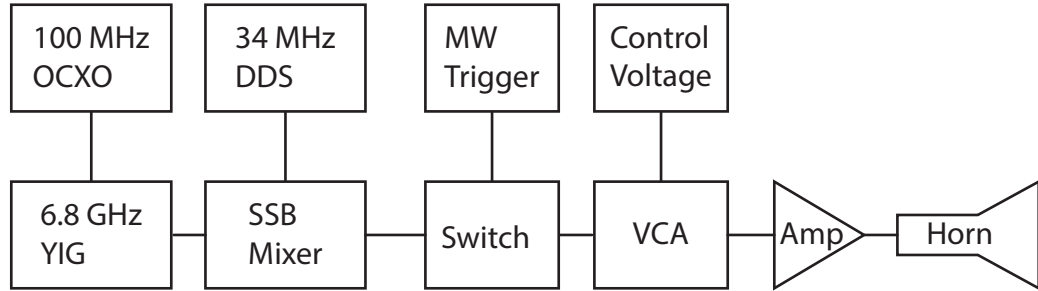


Figure 3.5: Block diagram of microwave chain. The master oscillator is a 6.8 GHz YIG oscillator, which is stabilized by a 100 MHz oven controlled oscillator (OCXO). The 34 MHz DDS is used to do fine control of the microwave frequency and mixes in with the 6.8 GHz source at the single-sideband mixer (SSB) mixer. The DDS also allows for frequency shift keying (FSK) during the cycle, which is used to change the microwave rotation axis in cycle. The switch is used for fast turn on/off of the microwaves. The voltage control attenuator enables attenuation of the microwave amplitude. The amplifier brings the power up to 0.5 W and the horn couples the microwaves to free space about 10 cm above the center of the cavity.

### 3.1.3 Microwave source

For driving Rabi oscillations between the  $^{87}\text{Rb}$  hyperfine ground states we use a microwave horn driven by a low-noise frequency tunable microwave source. The system is capable of  $\pi$ -pulse times of 150  $\mu\text{s}$  at  $|B| = 100 \text{ mG}$ , when driving the microwave horn with 0.5 W of power. The phase of the microwave pulses relative to the atoms is controlled using frequency shift keying, triggered by the experimental control system. For the experiments shown in this thesis, the FSK was chosen to be  $\delta\nu = 1/72 \mu\text{s}$ . This was chosen because 72 has many factors, allowing easy phase shifts of most common fractions of  $\pi$ . To generate very short microwave pulses for small rotations, a SRS DG535 pulser can be used to trigger the microwave switch.

The microwave source was also used for microwave spectroscopy of the magnetically sensitive Zeeman states to zero the magnetic fields and set the bias field in the chamber. For zeroing the magnetic fields, the microwave frequency was scanned to find all 7 microwave transitions possible in the  $^{87}\text{Rb}$  hyperfine manifold. The Zeeman shifts of these transitions were then minimized to get the lowest possible magnetic field

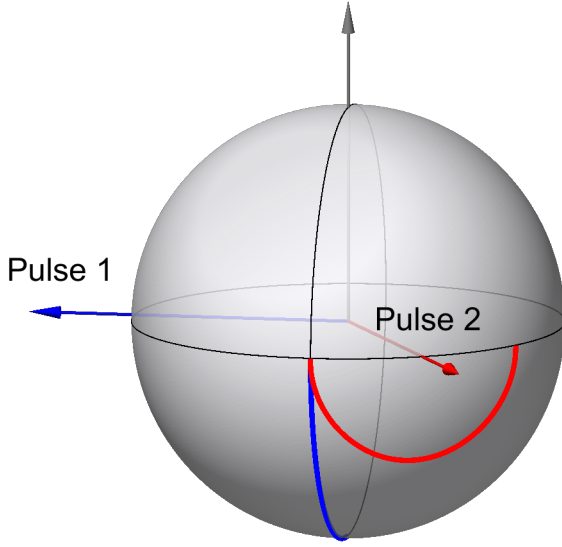


Figure 3.6: The figure shows state trajectory on the Bloch sphere. The first pulse is shown in blue and is simply a  $\pi/2$  rotation around the  $J_y$ -axis in blue. This is followed by a  $2\pi/3$  FSK before a  $\pi$  rotation around the new axis, shown in red. This sequence removes the first order sensitivity to amplitude noise, assuming that the fractional amplitude difference is the same for Pulse 1 and Pulse 2.

during the optical molasses cooling stage.  $|F = 1, -1\rangle \rightarrow |F' = 2, -2\rangle$  has the lowest frequency transition and  $|F = 1, 1\rangle \rightarrow |F' = 2, 2\rangle$  has the highest frequency transition in a finite magnetic field.

It is crucial that the microwave drive brings the atoms to the  $\langle J_z \rangle = 0$  state with as little cycle-to-cycle fluctuation as possible. We found that the amplitude of the microwave drive varied from cycle to cycle. We therefore employ a composite  $\pi/2$  pulse with the aim of reducing the impact of microwave amplitude noise. The composite pulse shown on Figure 3.6 is insensitive to amplitude noise to the first order. The offset from  $J_z=0$ ,  $\Delta J_z$ , using the composite  $\pi/2$  is given by

$$\Delta J_z = \frac{\sqrt{3}}{2} \delta\theta - \frac{\sqrt{3}\pi}{4} \delta A \delta\theta + \frac{\pi^3}{16} \delta A^3 \quad (3.1)$$

where  $\delta A$  is the fractional microwave pulse area error and  $\delta\theta$  is the microwave axis offset given by  $\Delta/\Omega$  where  $\Delta$  is the microwave frequency offset and  $\Omega$  is the microwave

Rabi frequency. The above equation can be found by considering a small  $\delta A$  and  $\delta\theta$  on the microwave pulse sequence described. To put an upper bound on this error in our experiment, we measured that the lattice intensity and pulse area fluctuate at most 1%. The lattice intensity gives rise to a detuning fluctuation of at most  $\Delta = 6$  Hz. Given the Rabi frequency of 3 kHz we find that the first term is dominant and obtain  $\Delta\mathcal{J}_z = \Delta/\Omega = 1.7 \times 10^{-3}$ . We will see later (Figure 4.3 in § 4.1.1) that the actual noise is substantially lower than this at approximately  $3.4 \times 10^{-4}$ . The composite pulse allows us to prepare  $\langle \mathcal{J}_z \rangle = 0$  states limited only by coherent state noise at atom numbers as high as  $2 \times 10^5$ .

### 3.1.4 State preparation

It is important to get the atoms into the  $|F = 1, m_F = 0\rangle$  state with very high fidelity prior to starting the squeezing experiments. The first approach was to simply start with all the atoms repumped into the  $|F = 2\rangle$  manifold then performing a microwave  $\pi$ -pulse to bring the  $|F = 2, m_F = 0\rangle$  atoms into the  $|F = 1, m_F = 0\rangle$  state, then blast away all  $|F = 2\rangle$  atoms using the push beam. However, a significant number of atoms were depumped into the  $|F = 1\rangle$  manifold and also not all atoms in the  $|F = 2\rangle$  were removed. The  $|F = 2\rangle$  and  $|F = 1, m_F \neq 0\rangle$  atoms reduce the amount of possible squeezing and make it more difficult to bring the probe on cavity resonance in cycle due to their interaction with the cavity probe. Additionally this simple state preparation method loses at least 80% of the atoms. We therefore employed a sequence of repump and depump stages combined with microwave transitions (see Figure 3.8 for more details). Improving the state preparation more than doubled the final number of atoms in the lattice by increasing the number of atoms in the  $|F = 1, m_F = 0\rangle$  state when the final blast happens. The new sequence also decreased the number of atoms left in the  $|F = 2\rangle$  manifold by a factor of 10.

### 3.1.5 Fluorescence imaging

The atoms are fluorescence imaged using an Andor IXUS camera. The MOT cooling and repump beams are used as imaging beams. For atomic state tomography a push

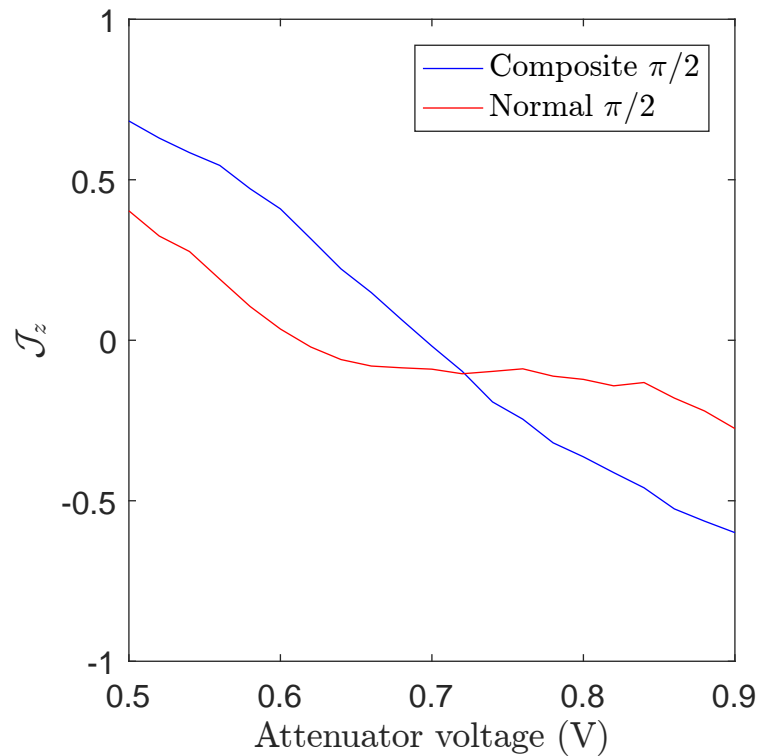


Figure 3.7: The figure shows  $\mathcal{J}_z$  as a function of microwave attenuator voltage for a normal and a composite  $\pi/2$ -pulse. The range of amplitudes shown here is approximately a factor of 3 from 90% of maximum amplitude at 0.5 V to 30% of maximum amplitude at 0.9 V. The composite pulse clearly shows reduced sensitivity to microwave amplitude. Note that the  $\mathcal{J}_z$  shown here is uncalibrated for losses in the imaging process, the true  $\mathcal{J}_z = 0$  is around -0.1.

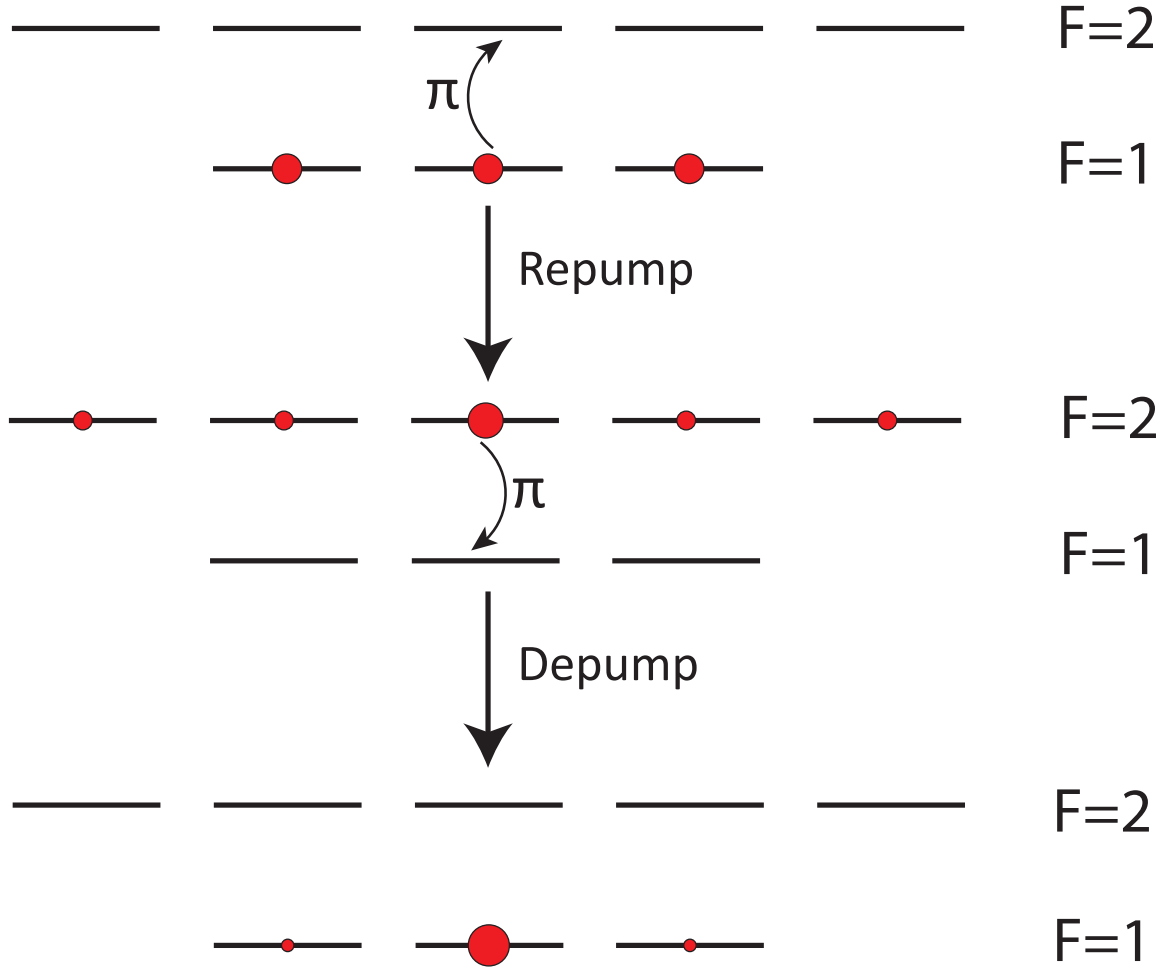


Figure 3.8: The state preparation begins with the atoms evenly distributed in the  $|F = 1\rangle$  manifold. The atoms in the  $|F = 1, m_F = 0\rangle$  state are then brought to the  $|F = 2, m_F = 0\rangle$  state by a microwave  $\pi$ -pulse. The remaining atoms in the  $|F = 1, m_F \neq 0\rangle$  state are now optically repumped into the  $|F = 2\rangle$  manifold. The sequence is then performed in reverse, the atoms in the  $|F = 2, m_F = 0\rangle$  state are brought to the  $|F = 1, m_F = 0\rangle$  state followed by depumping the remaining atoms in the  $|F = 2, m_F \neq 0\rangle$  states. There is now a significant accumulation of atoms in the  $|F = 1, m_F = 0\rangle$  state. The sequence is then repeated two more times. In the final repeat, the depump step is left out and the  $|F = 2, m_F \neq 0\rangle$  atoms are blasted away using the push beam. The area of the circles correspond to the relative atom numbers in each state.

beam resonant with the  $|F = 2\rangle \rightarrow |F' = 3\rangle$  transition is used to spatially separate the two hyperfine ground states. The push beam is turned on for 7  $\mu\text{s}$ , giving the atoms in the  $|F = 2, m_F = 0\rangle$  state downwards momentum. After a 1.2 ms time of flight, the separated clouds are imaged simultaneously with an exposure time of 2 ms, determining  $\mathcal{J}_z$  within a factor of three above the atomic projection noise. Figure 3.9 shows the images after this procedure.

Approximately 20% of the pushed atoms are lost, so to estimate the true  $\mathcal{J}_z$  we performed calibration measurements as shown in Figure 3.10. The calibration procedure uses a short Ramsey sequence to avoid decoherence due to the optical lattice. An initial microwave  $\pi/2$ -pulse prepares the atoms in the  $\mathcal{J}_z = 0$  state, then a timed FSK is inserted to phase shift the microwave before a second  $\pi/2$ -pulse. The second  $\pi/2$ -pulse converts the FSK-induced phase shift into a known population difference. The population difference is then measured and plotted on Figure 3.10. We then fit a 10th order polynomial to the data (chosen to minimize fit error in the relevant parameter range). The data does not conform to a simple sinewave. Based on the minimum of the polynomial fit, we extract the phase of a sinewave with fixed amplitude to 0.997 and fixed frequency according to the known FSK frequency. The amplitude of 0.997 is the measured coherence at the bottom of the fringe with a 20% loss in the pushed atoms taken into account. To find the true  $\mathcal{J}_z$  value, we can then interpolate on the polynomial fit (from the first minimum to first maximum) and adjust from the measured raw  $\mathcal{J}_{z,\text{raw}}$  to a loss-adjusted  $\mathcal{J}_z$ . We use this procedure to account for lost atoms in later coherence measurements and for processing full-fringe Rabi oscillation data. The calibration procedure adds an error of approximately  $\Delta\mathcal{J}_z = 1.7 \times 10^{-3}$  to the measurements of  $\mathcal{J}_z$ .

When performing cavity measurements, no push beam is used and the atoms are imaged for 2 ms to count the atom number and adjust for cavity linewidth broadening due to atomic scattering (see §2.3.2).

For time-of-flight temperature measurements, the exposure time is reduced to 100  $\mu\text{s}$  to preserve the shape of the atom cloud. In the initial cooling stages prior to loading the optical lattice it is sufficient to fit an isotropic 2D Gaussian to the cloud as it is spherically symmetric. However, after loading the atoms into the lattice,

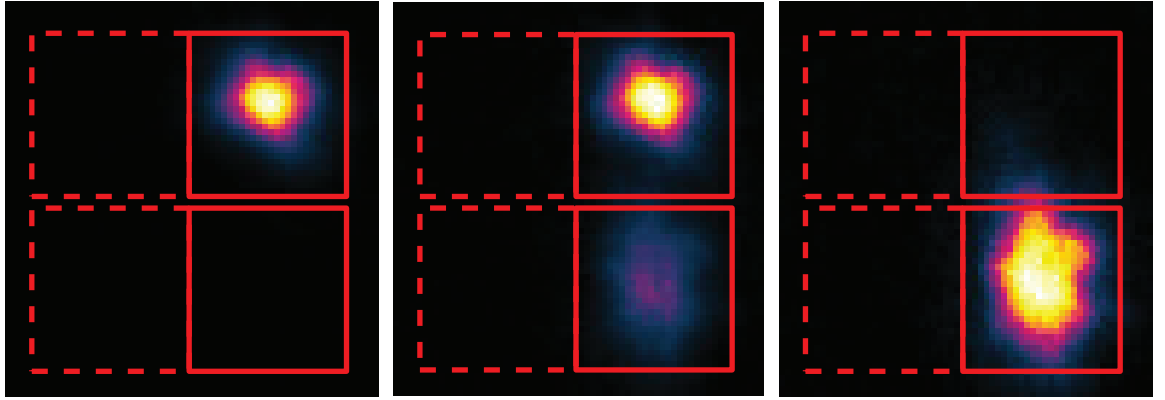


Figure 3.9: Images of different  $\mathcal{J}_z$  states using fluorescence detection. The images were taken by using a  $7\text{ }\mu\text{s}$  push on the  $|F = 2\rangle \rightarrow |F' = 3\rangle$  transition, followed by a  $1.2\text{ ms}$  time of flight before  $2\text{ ms}$  of fluorescence imaging. From left to right we see  $\mathcal{J}_z = -1$ ,  $\mathcal{J}_z = 0$  and  $\mathcal{J}_z = +1$ . Note that the bottom cloud appears fainter both because it is less dense and because there is some loss in the push process. The colormap used here and throughout the rest of the thesis is ‘morgenstemning’ from [98]. The maximum of the colormap is scaled according to the highest intensity pixel in each image.

the atoms experience different confinement in the axial and the transverse axis. The overall cloud now have a cigar-like shape, where its axial length depends on the size of the cloud loaded into the lattice and the transverse size depends on the strength of transverse confinement, the temperature and the atom number. The atoms are distributed over approximately 1000 lattice sites. In each site, the atoms have a highly anisotropic, pancake-like density profile. The anisotropy can be quantified through the ratio of the trap frequency in the two directions, which is approximately 1:450, where the axial confinement is stronger.

As the camera is imaging on an axis not perpendicular to any of the characteristic axes of the cigar-shaped atom cloud, we fit a rotated 2D Gaussian to the cloud in order to extract the transverse and axial temperatures of the atoms. We assume the density of the cloud will have the form of a 3-dimensional Gaussian, symmetric in the  $x$  and  $z$ -axes. We can then apply the appropriate rotation matrices to this density distribution to arrive at the appropriate fit function to extract the parameters

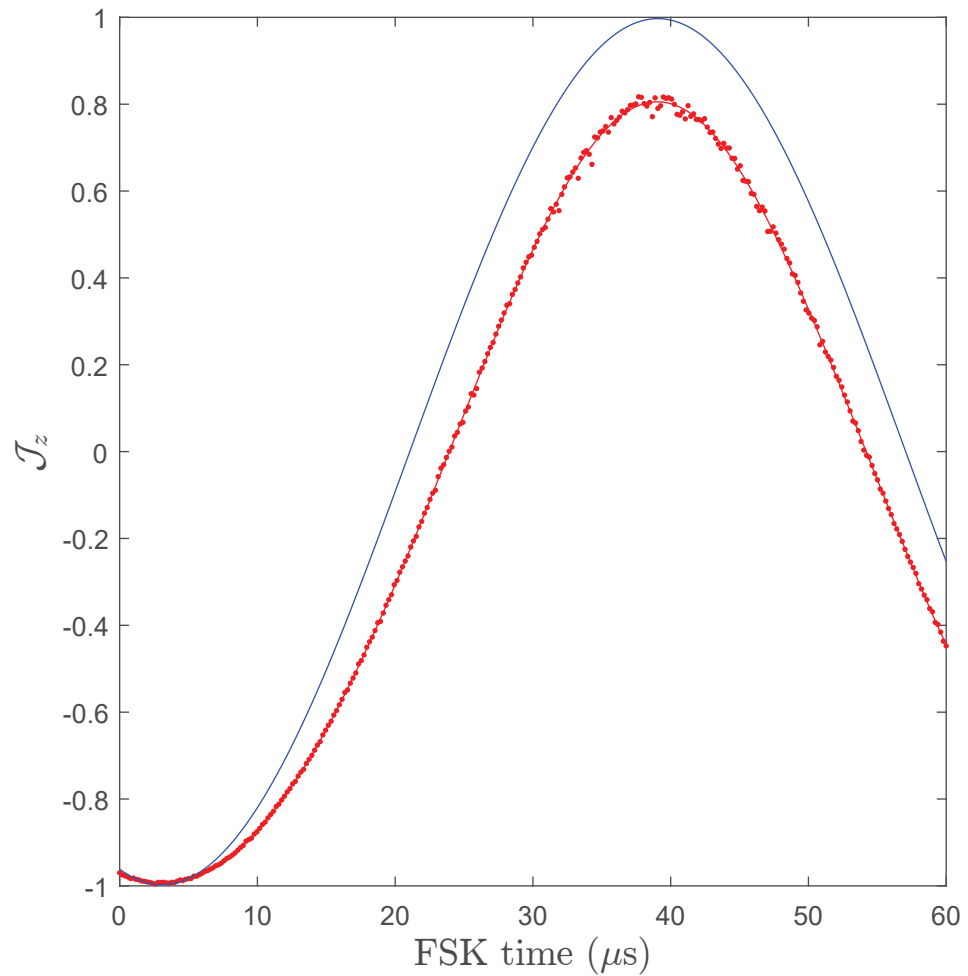


Figure 3.10: The data points show the measured  $\mathcal{J}_{z,\text{raw}}$ . The blue line is a 10th order polynomial fit. The red line is the true  $\mathcal{J}_z$  value. The data points are a mean of three runs, consisting of 300 uniformly spaced data points. Experimental data points are adjusted from the raw value on the red curve to the corresponding value on the blue curve.

necessary to estimate the temperatures in the transverse and axial direction. We start with a 3-dimensional Gaussian given by

$$a \exp \left[ \frac{(x - x_0)^2 + (y - y_0)^2}{w_t^2} + \frac{(z - z_0)^2}{w_a^2} \right] \quad (3.2)$$

where  $a$  corresponds to the peak intensity of the cloud,  $w_t$  the transverse width of the cloud,  $w_a$  the axial width of the cloud,  $x_0$ ,  $y_0$  and  $z_0$  are the centers of the cloud in all three dimensions. We then measured the azimuthal and polar angle the camera was imaging from, here labeled as  $\phi$  and  $\theta$  respectively. By applying the appropriate rotation matrices, one can obtain that the appropriate fit function for a Gaussian distribution imaged from angles  $\theta$  and  $\phi$  is

$$a \exp \left\{ - \frac{[(x - x_0) \sin \phi + (y - y_0) \sin \theta \cos \phi]^2}{2w_{mod}^2} - \frac{[(y - y_0) \cos \theta]^2 + [-(x - x_0) \cos \phi + (y - y_0) \sin \theta \sin \phi]^2}{2w_t^2} \right\} \quad (3.3)$$

where

$$w_{mod}^2 = w_t^2 \frac{w_t^2 + w_a^2 (\sec^2 \theta \sec^2 \phi - 1)}{w_t^2 (\sec^2 \theta \sec^2 \phi + 1) - w_a^2} \quad (3.4)$$

is a modified width. The  $x$  and  $y$  coordinates are the coordinates of the image taken from the new position. The  $z$  direction is here the imaging axis, so its dependence will simply amount to an amplitude factor when integrated out. Using this fit function we were able to extract the longitudinal and transverse temperatures of the cloud following lattice release.

### 3.1.6 Atom cooling

The cooling of the atoms starts with a 2D MOT loading a 3D MOT. We then bring the atoms through several cooling stages with increasingly large detunings and lowered intensities in order to cool to lower temperatures [97]. The atoms are then loaded

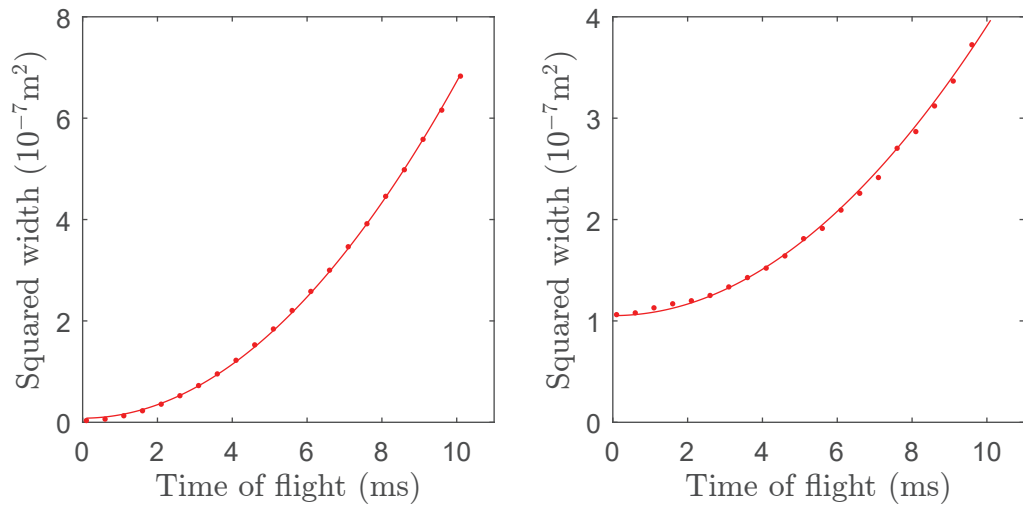


Figure 3.11: The figures show the squared transverse (left) and longitudinal (right) widths of the cloud as a function of time of flight. The fits are of form  $at^2 + c$ . The temperature can then be found by  $T = (m/k_B)a$  where  $m$  is the mass of  $^{87}\text{Rb}$  and  $k_B$  is Boltzmann's constant. Here the temperature was found to be  $30\,\mu\text{K}$  in the longitudinal direction and  $70\,\mu\text{K}$  in the transverse direction.

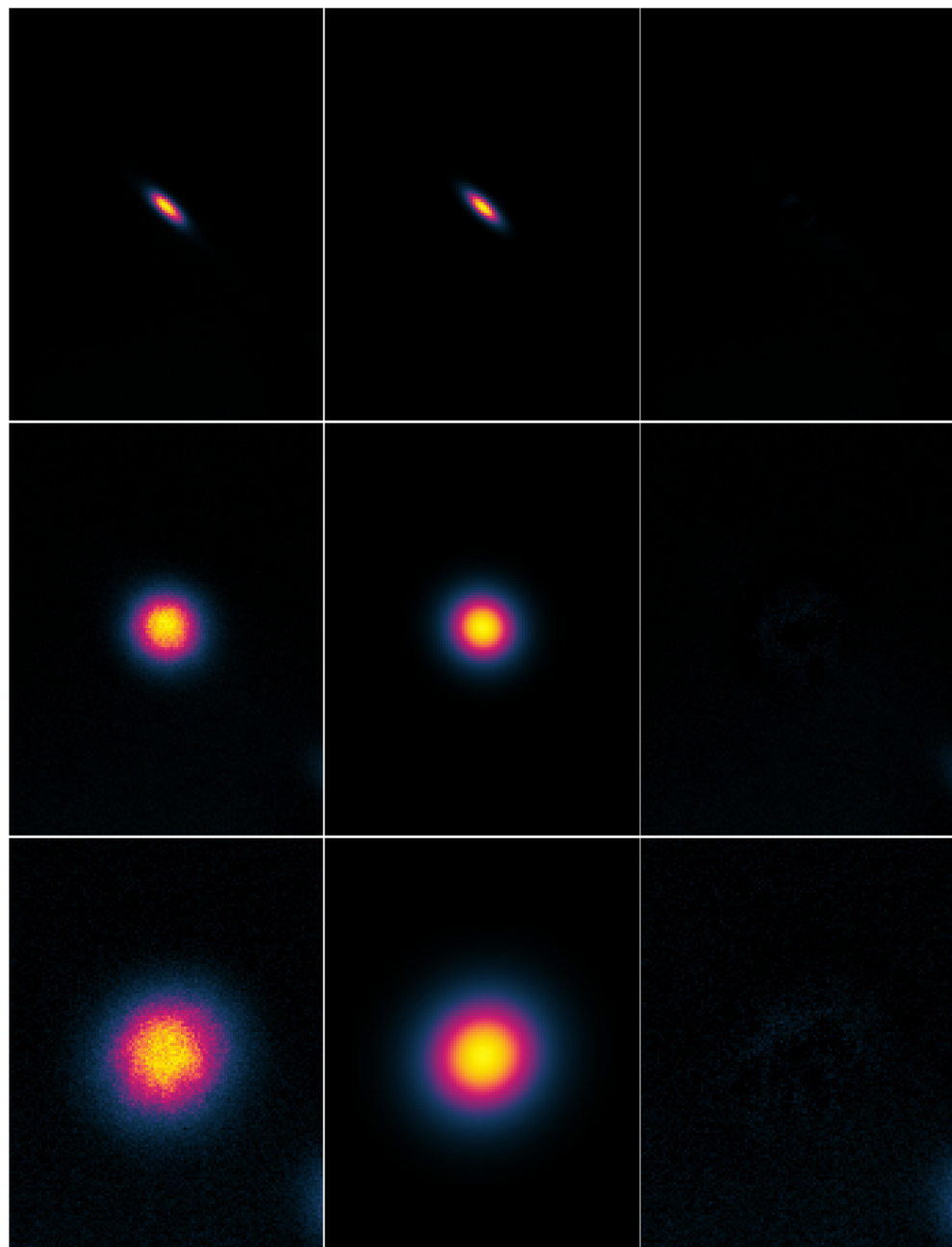


Figure 3.12: Sample images from the same run as Figure 3.11. **Left column:** Images of atom cloud as it expand from the lattice. Time of flight from top to bottom: 0.6 ms, 4.1 ms, 7.6 ms. **Middle column:** 2D Gaussian fits of the form given in Equation 3.3. **Right column:** Small residuals of the fits normalized to the maximum value in the leftmost image. Residuals appear black due to small values. Imaging time: 100  $\mu$ s.

Stage	Duration	Detuning		Cooling intensity		2D	3D
Units	ms	MHz	$\times \Gamma$	$\text{mW/cm}^2$	$\times I_{\text{sat}}$		
MOT	600	12	2	32	19	On	On
FDMOT1	20	35	6	29	17	Off	On
FDMOT2	10	49	8	29	17	Off	On
FDMOT3	20	63	10	24	14	Off	On
FDMOT4	10	104	17	19	11	Off	On
Molasses1	0.3	125	21	14	8	Off	Off
Molasses2	1.2	125	21	9	5	Off	Off
Molasses3	1.2	125	21	7	4	Off	Off
Molasses4	1.2	125	21	5	3	Off	Off

Table 3.1: List of parameters for the different cooling stages. Note that the detuning is increased and the intensity decreased in order to cool to lower temperatures. FDMOT: Far-detuned MOT. The 2D and 3D columns indicate whether the 2D and 3D magnetic coils are on during that stage. The 2D coils are only on during loading of the 3D MOT and are turned off for the subsequent cooling stages. The saturation intensity of the  $|F = 2, m_F = 2\rangle \rightarrow |F' = 3, m_F = 3\rangle$  transition is used to calculate the values in the 6<sup>th</sup> column. The cooling light intensity is the sum of the intensity in each of the three arms multiplied by two to account for retroreflection. During Molasses1-4 the detuning remains unchanged to avoid unwanted cavity-enhanced heating processes. In Molasses3-4 the lattice is ramped up to 10% of its maximum value such as to cool into the lattice. Following Molasses4, the lattice is kept at 10% of its maximum value to let the hotter atoms escape. The lattice is then ramped up to its final value.

into the lattice. The parameters and durations of the different stages are shown in Table 3.1. After the atoms loaded in the lattice and the MOT coils are off, we perform a ‘sloshing’ stage (Molasses1-2), where the lattice is rapidly lowered before a few hundred microseconds of optical molasses (Molasses1) and then rapidly raised back up. The lattice lowering and raising is done as fast as the cavity allows, hence having a timescale of  $1/\kappa \sim 20\text{ }\mu\text{s}$ . This is adiabatic in the longitudinal direction of the lattice but essentially instant in the transverse direction. The atoms are then held in the lattice for a quarter of a transverse oscillation period before being released for another millisecond of optical molasses. The idea is that the atoms ‘roll downhill’ to the center of the lattice, thus having maximum kinetic energy when the second stage of optical molasses occurs.

The magnetic field felt by the atoms during molasses was zeroed to within 5 mG using microwave spectroscopy of the magnetically sensitive Zeeman states of the  $^{87}\text{Rb}$   $|F = 2\rangle$  manifold. By scanning the microwave frequency it was possible to address the different Zeeman sublevels of the manifold, then change the magnetic field such as to minimize the frequency separation between the sublevels. The low magnetic field allows polarization gradient cooling during molasses. After molasses the bias fields are ramped to 100 mG in the  $x$ -direction (perpendicular to the cavity, along the direction of the 2D MOT in Figure 3.1). The 100 mG field sets the quantization axis during experiments such that we can send in a  $\pi$ -polarized probe beam.

When optimizing the various cooling stages of the experiment we found that the final atom temperatures varied greatly depending on the cavity-atom detuning. These temperature fluctuations manifested themselves as atom number fluctuations after loading into the lattice and would also potentially lead to variations in coupling to the cavity mode due to the atoms’ spatial extent in the lattice. The different processes were characterized by measuring the width of the cloud in the longitudinal and transverse direction at a fixed time of flight. This is essentially a single-shot temperature measurement. By then changing the cavity-atom detuning (as per §3.2.3) and measuring the single-shot temperature as a function of cavity-atom detuning, we characterized the different processes occurring. It turned out that the atoms were Raman lasing and Rayleigh scattering into the various transverse cavity modes, leading

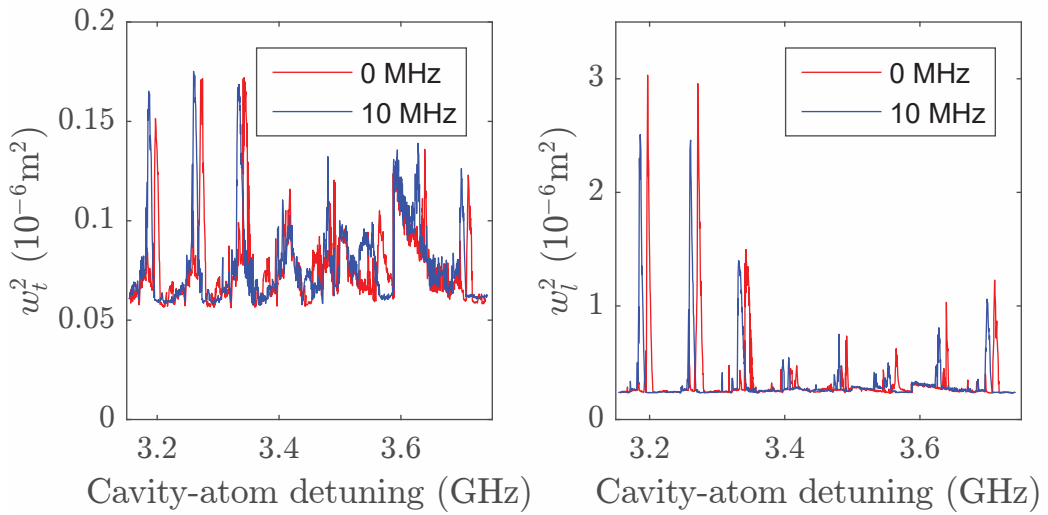


Figure 3.13: The figure shows the longitudinal and transverse widths of the cloud after a fixed time of flight as a function of cavity-atom detuning. The data shows that the heating effect is most pronounced in the longitudinal direction, *i.e.* along the cavity axis, which points strongly towards a cavity-enhanced heating process. Additionally, the sharp peaks are separated by approximately 75 MHz, which is the cavity transverse mode spacing. For the data in blue, the cooling laser was red-detuned an additional 10 MHz during the final cooling stage. The sharp peaks that are especially prominent are indeed shifted by the same amount.

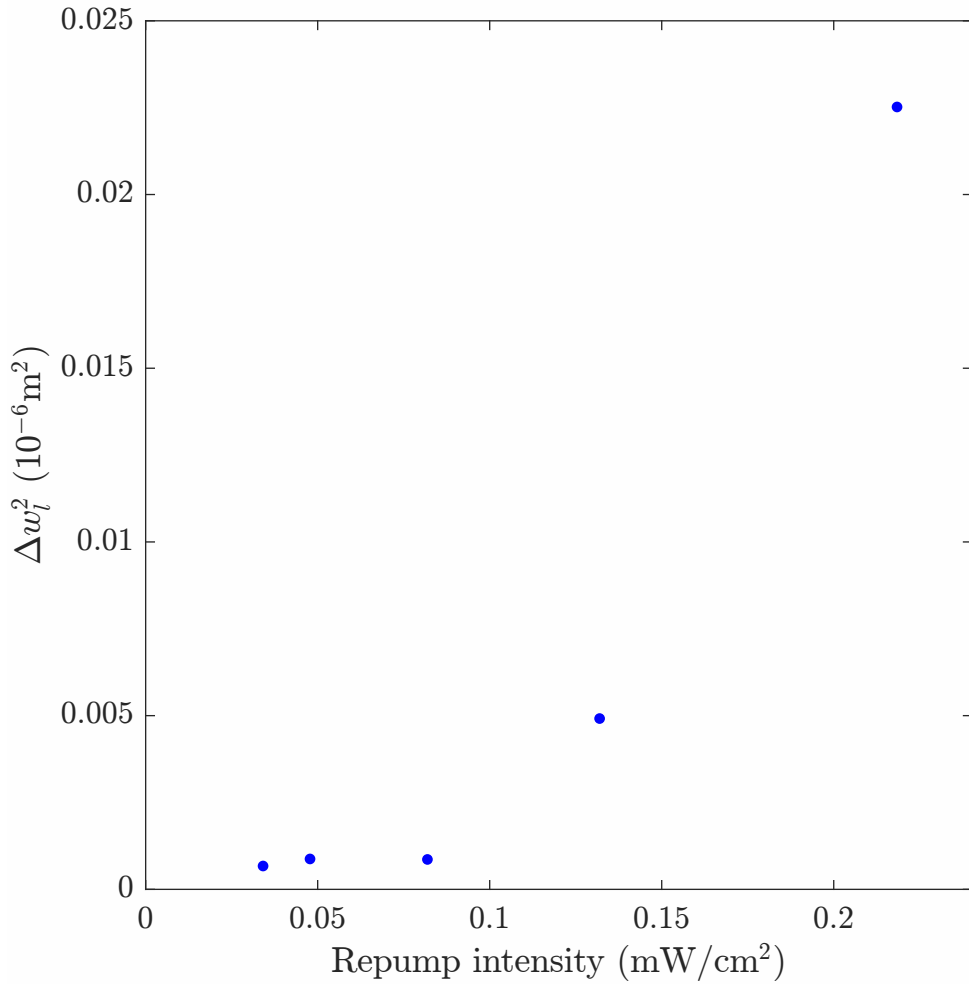


Figure 3.14: Here we did peak fitting to a peak in the longitudinal width at a cavity-atom detuning of approximately 3.34 GHz. We then varied the repump power during the final cooling stage. The peak showed distinct lasing behavior, strongly indicating that some kind of cavity-enhanced raman lasing. The cooling laser would then be one arm of the Raman laser, and the atoms scatter into the cavity mode. The repump allows the lasing to continue by pumping the atoms back to the  $|F = 2\rangle$  state.

to resonant behavior as a function of cavity-atom detuning. The evidence of Raman lasing is shown in Figure 3.13 and Figure 3.14. In addition to the features shown there, we also observed features that shifted with the cooling laser frequency but were not affected by the repump power. We believed these to be due to Rayleigh scattering into the cavity, where the cooling light is resonant with some transverse cavity resonance and thus undergoes cavity-enhanced scattering off the atoms.

We wanted to operate the experiment at a specific cavity-atom detuning, and therefore needed the region around this detuning to be devoid of these deleterious processes. The heating effects should perhaps not be surprising, since in the past the setup was used to make a Raman laser [99]. By carefully choosing our atom-laser detunings and lowering the repump power by approximately a factor of 100, we managed to largely eliminate these processes during the cooling stages at our chosen cavity-atom detuning. Following this optimization, our atom numbers went up by a factor of 10 compared to previous. The region of stability was also expanded as shown in Figure 3.15.

Prior to cavity measurements, we performed velocity filtering. The lattice was lowered to approximately 10% of its maximum intensity, losing a bit over half the atoms. Following the velocity filtering, the lattice was adiabatically ramped up to its maximum power before cavity measurements occur. The final result of the cooling and state preparation techniques is that there are up to  $7 \times 10^5$  atoms at approximately 25  $\mu\text{K}$  in the ramped up lattice. The atom number fluctuations are limited to approximately 2%. The state prepared atom number is limited to  $7 \times 10^5$  as the homodyne path length stabilization sidebands (see §3.2.5) would go on resonance during state preparation.

### 3.1.7 Timing sequence

The timing and control of the experiment was performed using a DSP-based control system. The generalized timing sequence is shown in the table below. All experiments done in this thesis had the same general sequence, with changes only during the part labeled ‘measurement sequence’ below. Much like the case of a typical graduate

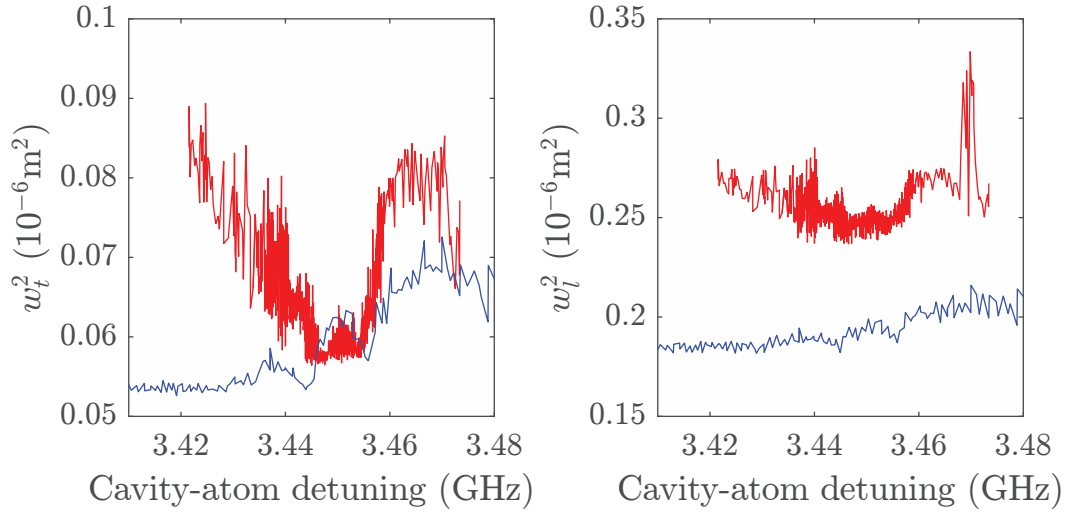


Figure 3.15: The figures show the squared width as a function of cavity-atom detuning before (in red) and after (in blue) optimization of the chosen detunings. To go from red to blue, we set the cooling laser frequency to be the same during all molasses stages such that the lasing would happen at the same cavity-atom detuning for all stages. Additionally, we greatly reduced the repump power to be below the Raman lasing threshold during cooling. During experiments, the cavity-atom detuning was kept as near  $\omega_{\text{HF}}/2 = 3.417$  GHz as possible. The cooling was optimized to make the atoms as cold as possible and the temperature as stable as possible at this point such as to minimize atom number fluctuations.

Stage	Duration (ms)
Cooling	715
Lattice hold 1	15
State preparation	15
Lattice hold 2	115
Measurement sequence	5
Fluorescence	5
Empty cavity measurement	120
Total	990

Table 3.2: The above shows a general sequence used for the experiments detailed in this thesis. The MOT load time is varied from 10 ms to 600 ms to change the atom number. For the shorter load times, time is added at the start of the sequence to maintain identical thermal conditions throughout the sequence. Lattice hold 1 is used to let hotter atoms fall from the cavity prior to the next stage. The state preparation stage is described in § 3.1.4. Lattice hold 2 provides the long hold time required to minimize thermal drifts of the cavity during the measurement sequence as described in § 3.2.4. The long empty cavity measurement time in the last stage is used to do the calibration described in § 3.2.6. The lattice ramp during this stage replicates that used in the main sequence such that the cavity will be put at the same frequency.

student, only 1% (10 ms) of the time is spent taking data.

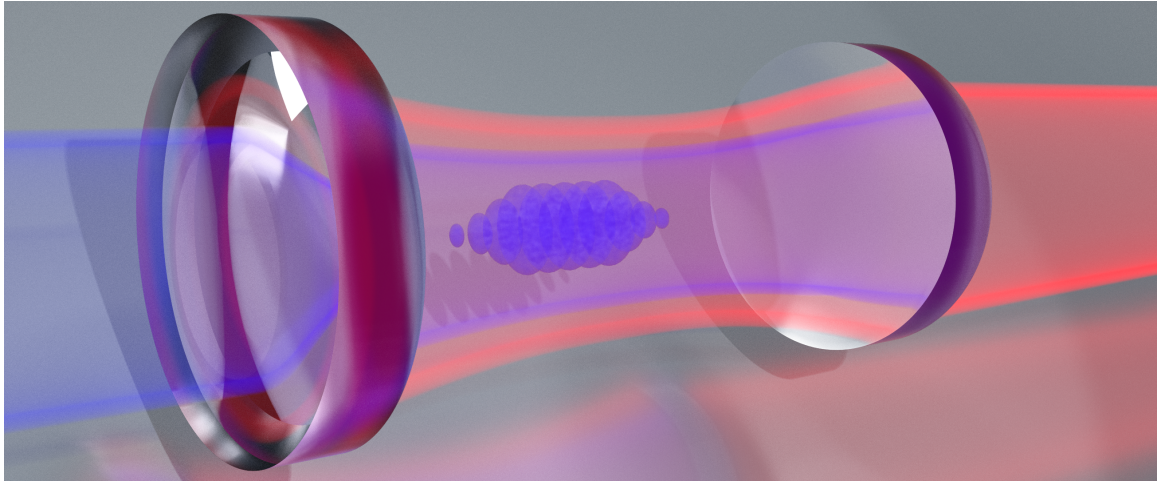


Figure 3.16: Render of cavity with pancakes of atoms shown in blue. The blue cavity mode is here meant to illustrate the probing 780 nm light and the red cavity mode the 1560 nm light. The transmitted beams are omitted for clarity. Artist credit: Brannon Klopfer.

## 3.2 Dual-wavelength optical cavity

The cavity used in this work is near confocal and symmetric. It is also a dual wavelength cavity with very high finesse at both 780 and 1560 nm. The commensurate optical lattice allows trapping the atoms with maximal and uniform coupling to the 780 nm cavity probe (see Figure 3.17). Using a dual wavelength cavity also allows locking the laser at 1560 nm and simply doubling the light to generate the 780 nm probe. This eliminates the need for a locking sideband at 780 nm. Additionally, this commensurate wavelength scheme means there is no first-order optomechanical coupling of the probe to the atoms, which could limit the amount of achievable squeezing [43]. The cavity-atom detuning is stabilized using heating pads on the cavity tube. The cavity resonance frequency is measured using a homodyne detection setup. A stylized 3D render of the cavity is shown in Figure 3.16.

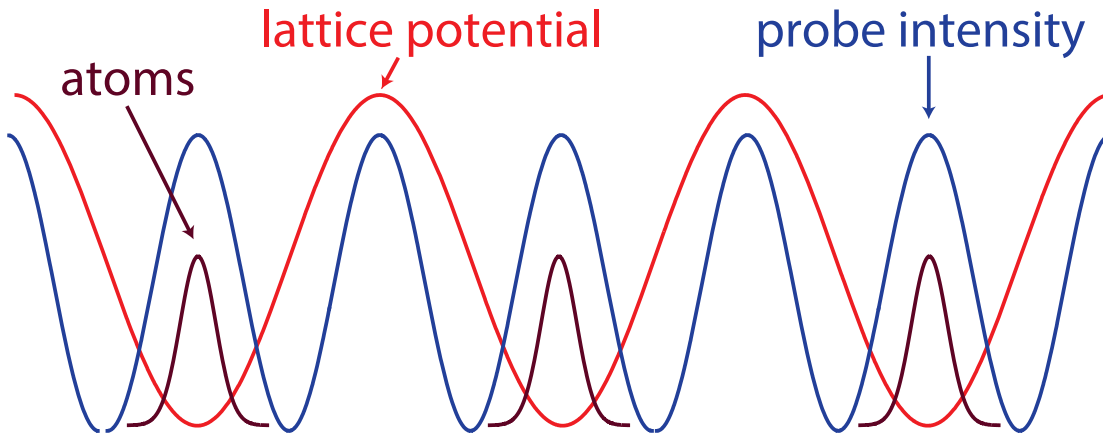


Figure 3.17: The figure shows the commensurate relationship between the probe and lattice. The figure shows the lattice potential generated by the 1560 nm light, trapping the atoms at the peak intensity of the 1560 nm cavity mode. The probe intensity peaks are overlapped with the lattice intensity peaks for maximal and uniform coupling of the atoms to the cavity mode.

Parameter	Symbol	Values		Units
Wavelength	$\lambda$	780	1560	nm
Free Spectral Range	$\nu_{\text{FSR}}$		1.396	GHz
Mirror Radius	$R$		9.9	cm
Length	$L$		10.73	cm
Finesse	$\mathcal{F}$	175 000	113 000	
Linewidth	$\kappa/2\pi$	7.98	11.96	kHz
Mode Waist	$w_0$	111	157	$\mu\text{m}$
Atom-cavity coupling	$g_0/2\pi$	142		kHz
Single-atom cooperativity	$C = 4g_0^2/\kappa\Gamma$	1.14		

Table 3.3: List of important cavity parameters. Note that the values quoted for the cooperativity,  $C$ , and atom-cavity coupling,  $g_0$ , here are the values calculated from cavity parameters before adjusting for any coupling inhomogeneity due to for example thermal motion. Some values taken from [53, 70].

### 3.2.1 Cavity parameters

The main feature of the cavity and experiment is the high finesse of the cavity combined with its large mode volume to accommodate a large number of atoms. As we will later see, this enables large amounts of squeezing on the clock states. The high finesse combined with the relatively long cavity length gives rise to a narrow linewidth, necessitating good frequency stabilization to make precise cavity resonance measurements. A list of important cavity parameters can be found in Table 3.3.

### 3.2.2 Cavity laser stabilization

All light going into the cavity originates from a RIO 1560 nm laser. The laser has an approximately 10 kHz linewidth and is then narrowed down by locking to a ‘scrubbing’ cavity using the standard Pound-Drever-Hall (PDH) locking technique [100, 101]. The locking scheme is similar to that described in [102]. There is a slow feedback to the RIO laser current and a fast feedback to the fiber EOM. The fast feedback extends the locking bandwidth out to a few megahertz. The scrubbing cavity is a copy of the science cavity that is not kept under vacuum but is equipped with a piezo. The piezo is used to make the scrubbing cavity follow the science cavity. The scrubbing cavity filters out high frequency optical noise and the transmission is passed through a double pass AOM (used for high bandwidth feedback) to then inject a 1560 nm diode. The 1560 nm injection diode works as a saturated amplifier, getting rid of the inevitable amplitude noise from passing through the scrubbing cavity. Additionally, this laser diode ensures that the fiber amplifier is always injected, regardless of the status of the cavity lock. Following the fiber amplifier, the amplified output is split into two paths, about 200 mW is passed through a frequency doubling crystal to generate the 780 nm light and about 40 mW is locked to the science cavity using a modified PDH scheme described in Figure 3.19. The 780 nm light generated from the frequency doubling injects a distributed feedback laser diode. The light from this diode is used both to generate a beatnote to measure the cavity-atom detuning and for probing the cavity.

The scheme eliminates the need for any locking light at 780 nm. This is crucial for limiting decoherence or additional noise due to extra light interacting with the

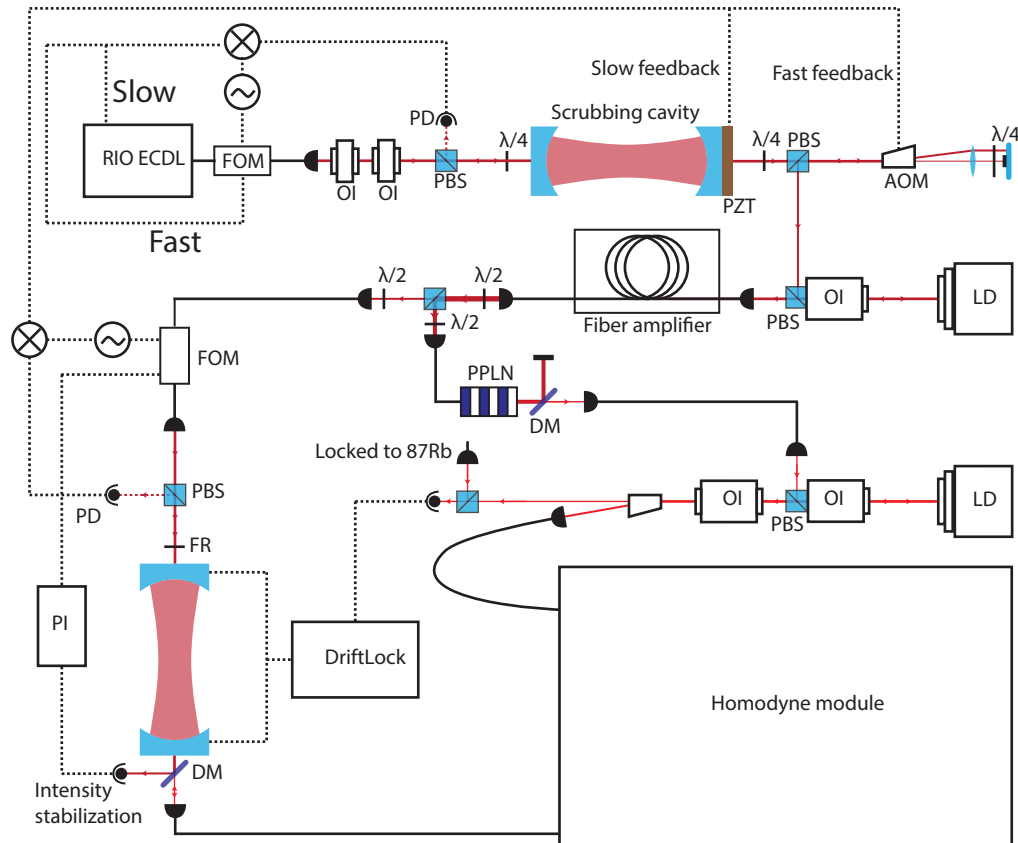


Figure 3.18: The figure shows the cavity laser stabilization setup used in this experiment to generate both the 1560 nm lattice and 780 nm probe light. Red lines show laser light paths. Dark red is 1560 nm, red is 780 nm. Arrows indicate direction of propagation, in some cases there is light going both ways. Thicker lines indicate higher powers. Solid black lines are optical fibers. Dotted black lines show electronic paths. FOM: Fiber-optic modulator. OI: Optical isolator. PBS: Polarizing beamsplitter.  $\lambda/4$ : Quarter-wave plate.  $\lambda/2$ : half-wave plate. LD: Laser diode. PD: Photodiode. AOM: Acousto-optic modulator. PZT: Piezoelectric transducer. PPLN: Periodically poled lithium niobate (frequency doubling crystal). FR: Faraday rotator. PI: Proportional-integral feedback controller. DM: Dichroic Mirror reflecting 1560 nm and transmitting 780 nm.

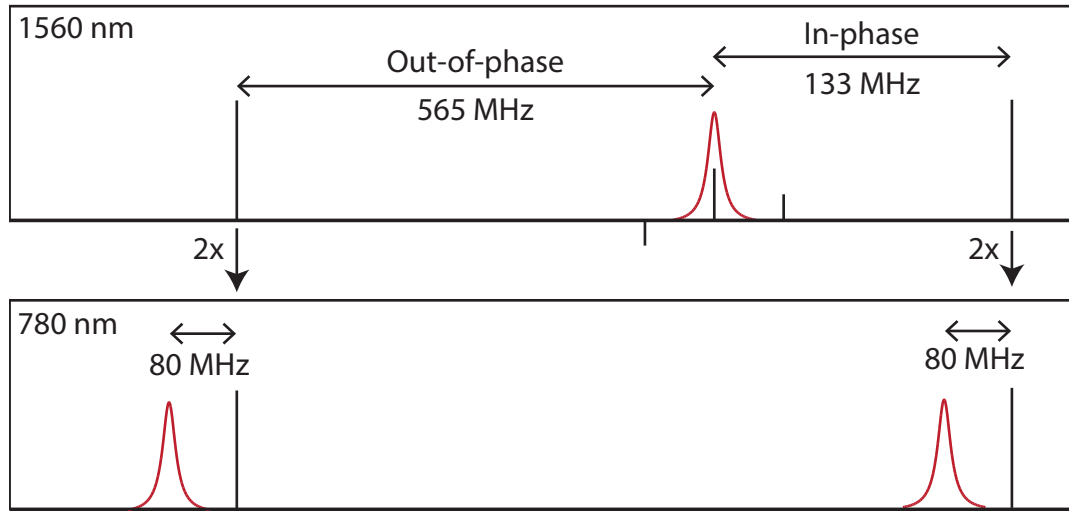


Figure 3.19: Using a fiber modulator, we put a Pound-Drever-Hall structure on the 1560 nm at an offset. The offset doubles during frequency doubling. The diagram shows both the configurations the locking scheme can be in. While it is always the carrier that is frequency doubled, by locking with different lock offsets we can shift the doubled light at 780 nm by exactly one  $\nu_{\text{FSR}} = 1.396 \text{ GHz}$  without changing which 1560 nm resonance we are locked to. The 133 MHz offset sets the registration in phase and the 565 MHz offset sets the registration out of phase. On the 780 nm side, we use an AOM to shift the frequency down by 80 MHz. The sidebands generated on the other side of the carrier for the two configurations are not shown as they are not relevant.

atoms. In addition to the previously mentioned science benefits, the dual wavelength cavity scheme has a number of advantages that lower the implementation complexity compared to the alternatives. The use of only one master laser means that only one frequency stabilization system is needed and only one laser must be locked to the cavity, which increases reliability. There are also cost benefits, as only one narrow linewidth master laser is needed and frequency doubling crystals are relatively cheap compared to the cost of building an additional stable laser system at 780 nm.

If the cavity length was equal for both wavelengths, ie  $L_{780} = L_{1560}$  and we simply frequency doubled light locked to a 1560 nm resonance, it would be directly on resonance at 780 nm. However, the cavity length is slightly different, such that the resonances at 780 nm are 186 MHz above the corresponding 1560 nm resonance.

Additionally, we need to be able to shift the frequency of the light on the 780 nm side relative to the light at 1560 nm by an entire  $\nu_{\text{FSR}}$  in order to switch between in-phase and out-of-phase registration. Here, in-phase registration is taken to mean the condition where the intensity peaks of the 780 nm cavity mode in the cavity overlap with the intensity peaks of the 1560 nm cavity mode, and out-of-phase registration the opposite. We therefore employ a modified locking scheme showed in Figure 3.19. The modified locking scheme allows independent control of the 780 nm light by changing the frequency of the lock offset. The lock offset can also be changed between two conditions—one using a 133 MHz offset and one using a 565 MHz offset. This facilitates switching between in-phase and out-of-phase registration.

We also have complete control of the transmitted 1560 nm power through a voltage controlled attenuator, which allows us to change the lattice depth for the atoms. While the lock performance is degraded at low powers, the 1560 nm light stays locked through a large dynamic range (approximately a factor of 100 in intensity). At full power, the frequency noise of the 1560 nm light is approximately  $40 \text{ mHz}/\sqrt{\text{Hz}}$  in the 0.2-0.4 kHz band, giving a r.m.s stability of 4 Hz relative to the cavity. The locking scheme ensures short-term stability of both the 1560 nm light and the 780 nm light.

### 3.2.3 Cavity-atom detuning stabilization

The cavity-atom detuning had to be stabilized to within a few MHz to perform most of the experiments in this thesis. The stabilization was done using a digital feedback system acting on heating pads on the cavity. The cavity-atom detuning was measured with a beatnote between a laser locked to the  ${}^{87}\text{Rb} |F = 2\rangle \rightarrow |F' = 2, 3\rangle$  crossover transition and the resonant cavity probe laser. This beatnote is read out using a frequency counter every cycle ( $\sim 1 \text{ s}$ ) and the appropriate feedback is applied to the cavity heating pads to keep the beatnote stabilized, thus stabilizing the cavity atom detuning. The stabilized atom-cavity detuning allowed us to tune the cavity to a detuning where the  $|F = 2, m_F = 0\rangle$  and  $|F = 1, m_F = 0\rangle$  states have equal and opposite cavity shift. This condition occurs at a detuning of roughly

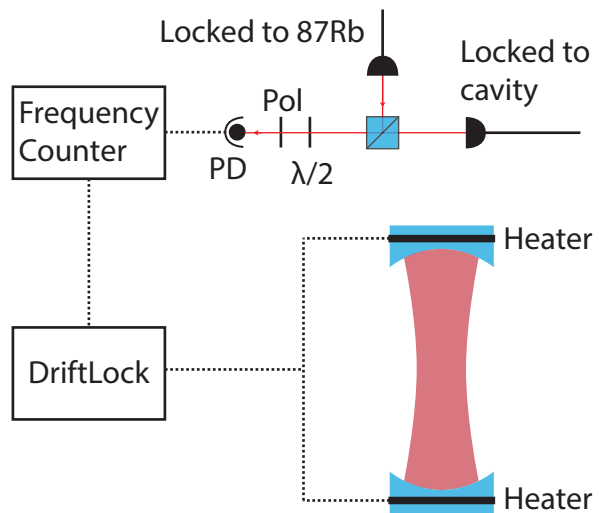


Figure 3.20: A beatnote between light locked to the  $^{87}\text{Rb} |F = 2\rangle \rightarrow |F' = 2, 3\rangle$  and light locked to the cavity is generated on a high frequency photodiode. The beatnote frequency is read out once per second using a frequency counter and feedback is then applied to the heating pads on the cavity to keep the beatnote frequency at the setpoint.

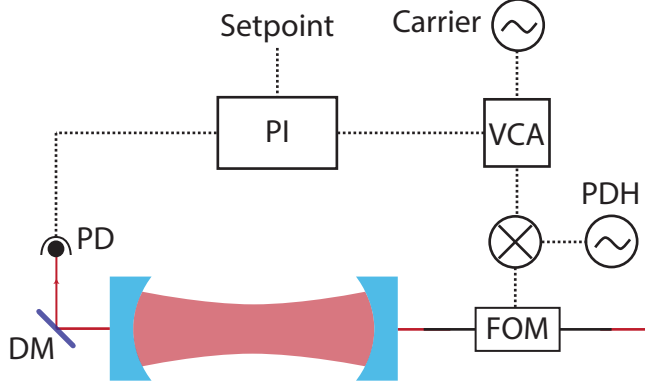


Figure 3.21: The transmitted 1560 nm power is measured with a photodiode after filtering out the reflected 780 nm light with a dichroic mirror. The proportional-integral circuit is then used to stabilize the measured intensity to a setpoint by feeding back on a voltage-controlled attenuator in the electronics path generating the frequency modulation for the 1560 nm lock.

$\Delta = \omega_{\text{HF}}/2 \sim 3.417 \text{ GHz}$ . At this detuning, for a  $|J_z = 0\rangle$  state the dressed atom-cavity resonance is at the same frequency as the empty cavity resonance and is thus insensitive to fluctuations in the atom number. The probe beam can therefore be preset to the empty cavity resonance at the end of every cycle and hit the dressed atom-cavity resonance in cycle. The stabilization of cavity-atom detuning also allows for better cooling of the atoms, as explained in § 3.1.6. Without stabilizing the cavity-atom detuning, it would not be possible to avoid all the transverse cavity modes causing heating during the cooling stages.

### 3.2.4 Lattice intensity stabilization

To have precise and repeatable control of the 1560 nm lattice intensity a stabilization system was made. The system allows stabilizing the intensity to an arbitrary set point given by our DSP control and timing system. Controlling the lattice intensity allows for specific ramp up and down sequences for maximal cooling and trapping of the atoms. Additionally, changing the lattice intensity has a large thermal effect on the cavity resonance. It takes hundreds of milliseconds for the 780 nm cavity resonance

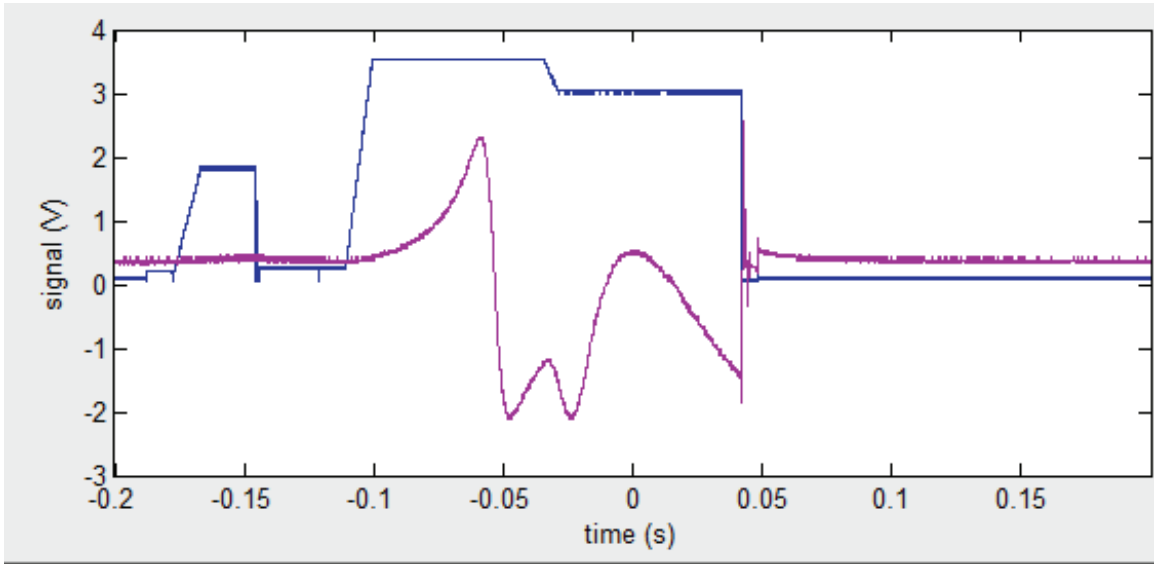


Figure 3.22: The blue trace shows the 1560 nm lattice transmission while the purple trace shows the measured 780 nm resonance. The probe is on in the time between  $t \sim -0.12$  s and  $t \sim 0.04$  s. A full cavity resonance is traced through (a few tens of kHz in frequency) before the frequency drift reverses when the lattice is lowered at around  $t = -0.03$  s. The frequency drift then reverses a second time when the cavity is almost exactly on resonance at  $t = 0$ . This is where cavity measurements are performed in the cycle, as the drift was limited to 4.0(4) Hz/ms. Alternate strategies such as waiting 100 ms for the cavity resonance to stabilize lead to drifts as high as 180(7) Hz/ms. The strategy of overshooting the target lattice intensity and then ramping down allowed for minimal hold times in the lattice while achieving good noise performance.

to reach equilibrium after changing the lattice intensity. We therefore ramped the lattice intensity up and then down again to allow the probing of the cavity resonance to happen at a point where the cavity resonance is at a turning point. Without this sequence it would not be possible to bring the cavity resonance to a repeatable and stable point when the science probing and the empty cavity probing happens. The total effect of the lattice AC Stark shift on the cavity-atom detuning is approximately 700 MHz, so in order to keep the detuning within 1 MHz of the desired value the intensity must be stabilized to at least one part in thousand.

### 3.2.5 Homodyne detection module

A homodyne detection scheme was used to perform cavity resonance measurements. Homodyne detection offers several advantages for achieving large spin squeezing at the cost of some technical challenges. The scheme used in these experiments allowed for exquisite control of probe powers on the order of picowatts while minimizing any additional unwanted on-resonance light. A homodyne detection scheme also allows for an additional 3 dB of squeezing as opposed to a heterodyne scheme where one sends an optical sideband into the cavity. One way to rationalize this gain is that the heterodyne scheme would lose information as amplitude modulation, thus requiring twice as many photons to make the same measurement. However, a homodyne setup requires path length stabilization, implemented here with sidebands 2 MHz detuned from the cavity resonance. The sidebands generate an error signal using a heterodyne scheme. The error signal is then fed back on the AOM in the local oscillator path such as not to affect the frequency of the probe light incident on the cavity. The path length is stabilized to the theoretical limit imposed by the amount of power in the 2 MHz sidebands. The homodyne measurements of the cavity resonance are thus limited only by the photon shot noise. The path length stabilization sidebands can be turned off during the cycle, such that the sidebands will not be on resonance with the atom-dressed cavity resonance. A diagram of the homodyne setup can be seen in Figure 3.23 and a picture in Figure 3.24.

We characterized the homodyne noise performance by making cavity measurements of the empty cavity at different powers. 100 ms time traces were recorded and then analyzed by taking the Allan deviation with different averaging times. To compute the Allan deviation, I divide the time trace into segments of length equal to the averaging time. I then compute the estimate of the cavity resonance frequency for each segment by taking the mean of the signal and multiplying by a frequency discriminator. We will denote the frequency estimate from the  $n$ th segment as  $\nu_n$ . We can then find the Allan variance for an averaging time  $\tau$  as

$$\sigma_A^2(\tau) = \frac{1}{N} \sum_{n=1}^N (\nu_{n+1} - \nu_n)^2 \quad (3.5)$$

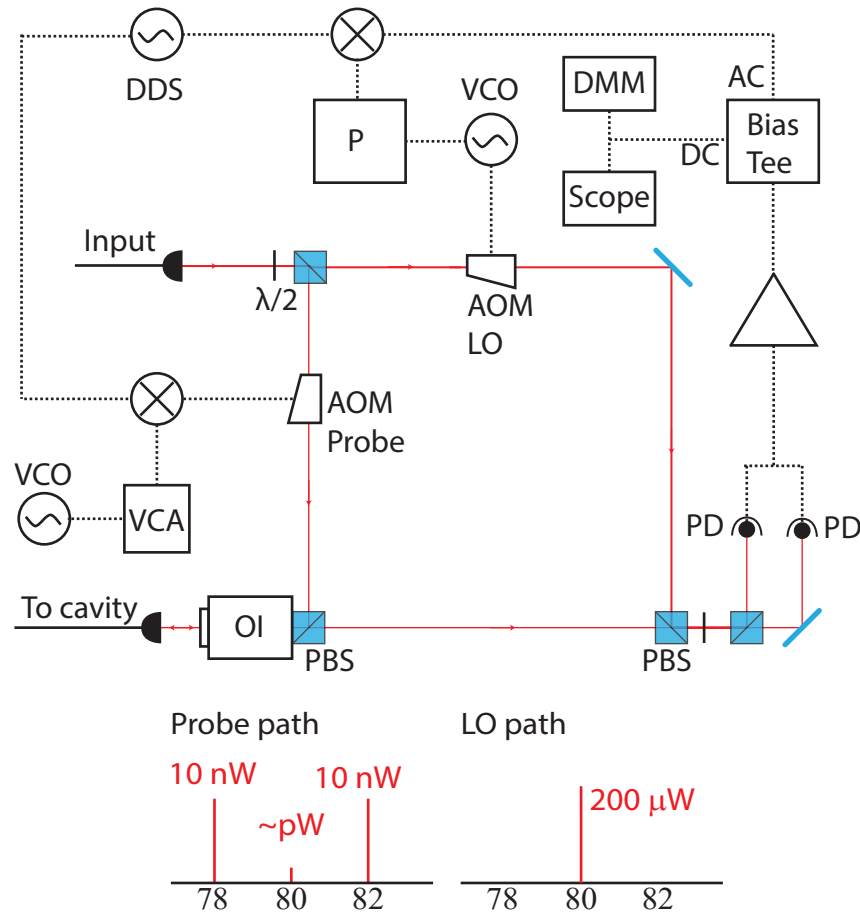


Figure 3.23: Diagram shows the homodyne system with electronics. The input light is split in two paths, one going to the cavity and one acting as the local oscillator. The AOMs are used to shift the cavity light the final 80 MHz onto resonance and enable control of the power of the resonant light. The AOM on the probe path also adds the 10 nW 2 MHz sidebands used for pathlength stabilization. The imaginary part of the electric field is then found by beating the probe with the local oscillator. Using a bias tee on the final photodiode readout allows us to separate the AC component (for pathlength stabilization) and the DC component (for cavity resonance detection). The DC component can be recorded on both a scope and a digital multimeter (DMM). The DMM is used to do the readout at the end of the cycle used to stabilize the probe on the empty cavity resonance. The scope is used for squeezing measurements.

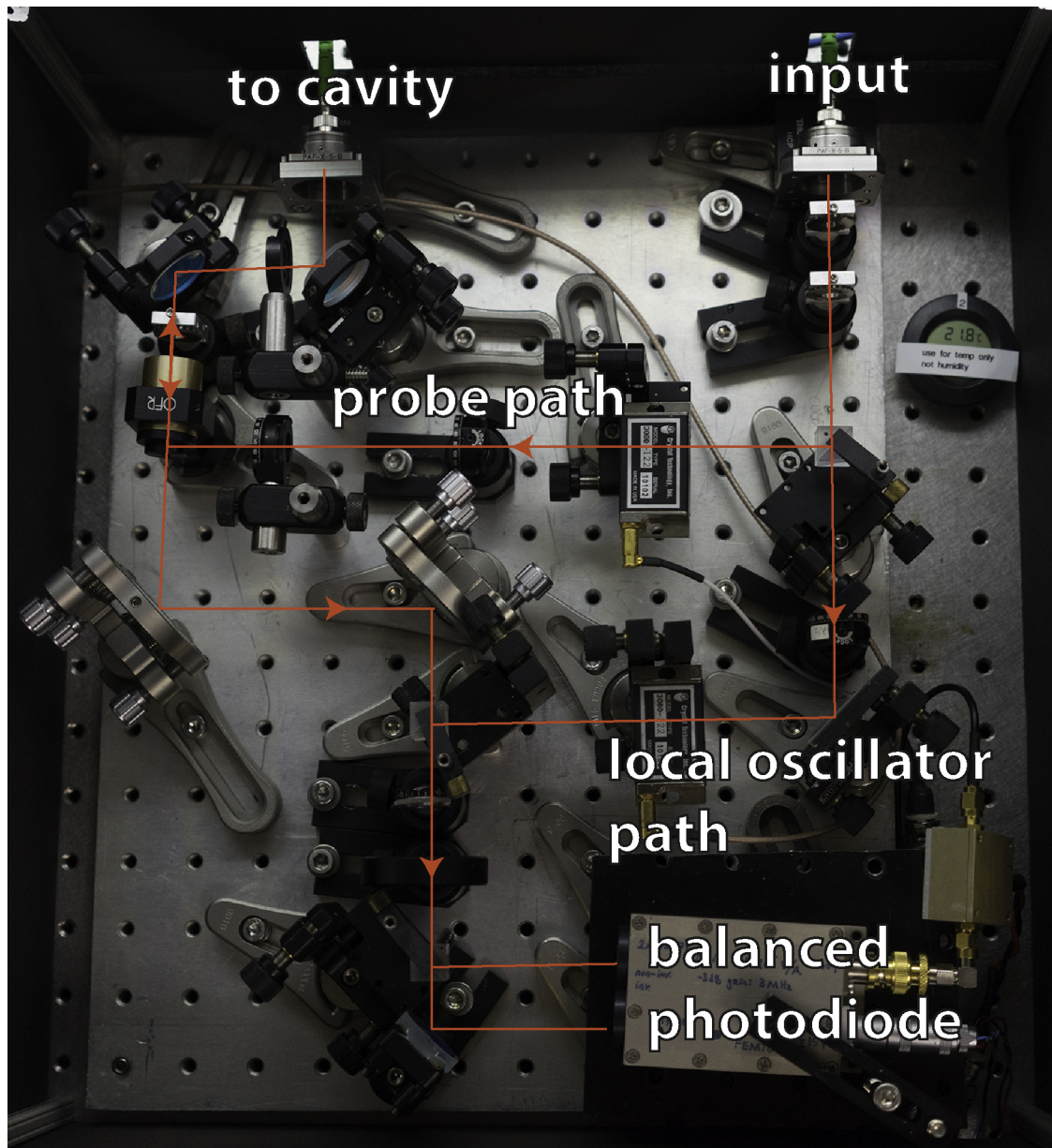


Figure 3.24: The figure shows a picture of the homodyne module. The red lines show the beam paths of the probe and local oscillator path.

where  $N = T/\tau$  and  $T$  is the length of the time trace. The results of this procedure can be seen in Figure 3.25.

The detection efficiency of our system, which dictates the achievable squeezing as per Equation 2.43, is  $\epsilon = 0.16$ , limiting the achievable squeezing to 24 dB. The breakdown is as follows: a factor of 0.50 as we only detect from one cavity mirror, a factor of 0.57 due to loss in the cavity mirrors, 0.80 from the backwards fiber coupling efficiency, a factor of 0.85 from loss in the optical isolator and other optics in the homodyne module and finally a factor of 0.85 from interferometer mode matching efficiency.

### 3.2.6 Probe detuning stabilization

The frequency stabilization of the 1560 nm light guarantees short-term stability for the 780 nm probe light. The frequency noise is approximately double that of the 1560 nm light, *i.e.*  $80 \text{ mHz}/\sqrt{\text{Hz}}$  in the 0.2-0.4 kHz band, giving a r.m.s stability of 12 Hz. However, thermal drifts can cause the 780 nm probe light to go off resonance, as the cavity length at 780 nm and 1560 nm differs by a small amount. As noted in [53], the difference between the frequency doubled 1560 nm lattice light and the 780 nm probe light is 186 MHz. This implies a length difference of  $\delta L = 51 \text{ nm} + n \times 390 \text{ nm}$  where  $n$  is an integer. This length difference is likely due to the different thicknesses of the reflective coatings on the cavity mirror, where the 1560 nm coatings are thicker. The difference in free spectral range at 1560 nm and 780 nm was found to be approximately 7 kHz, which sets a value of  $n = 1$ . The difference in cavity lengths was additionally investigated experimentally by changing the cavity temperature and measuring the differential shift of the 1560 nm cavity resonance and the 780 nm resonance. Here, the beatnote between the probe light and cooling light was used to measure the overall shift of the cavity resonance, while the differential shift was measured by recording how much the probe frequency needed to be changed to stay on resonance. The results are plotted in Figure 3.26. As the vacuum chamber is made of Zerodur, the cavity actually contracts when heated. Most of the cavity length change therefore comes from the expansion of the mirror substrate.

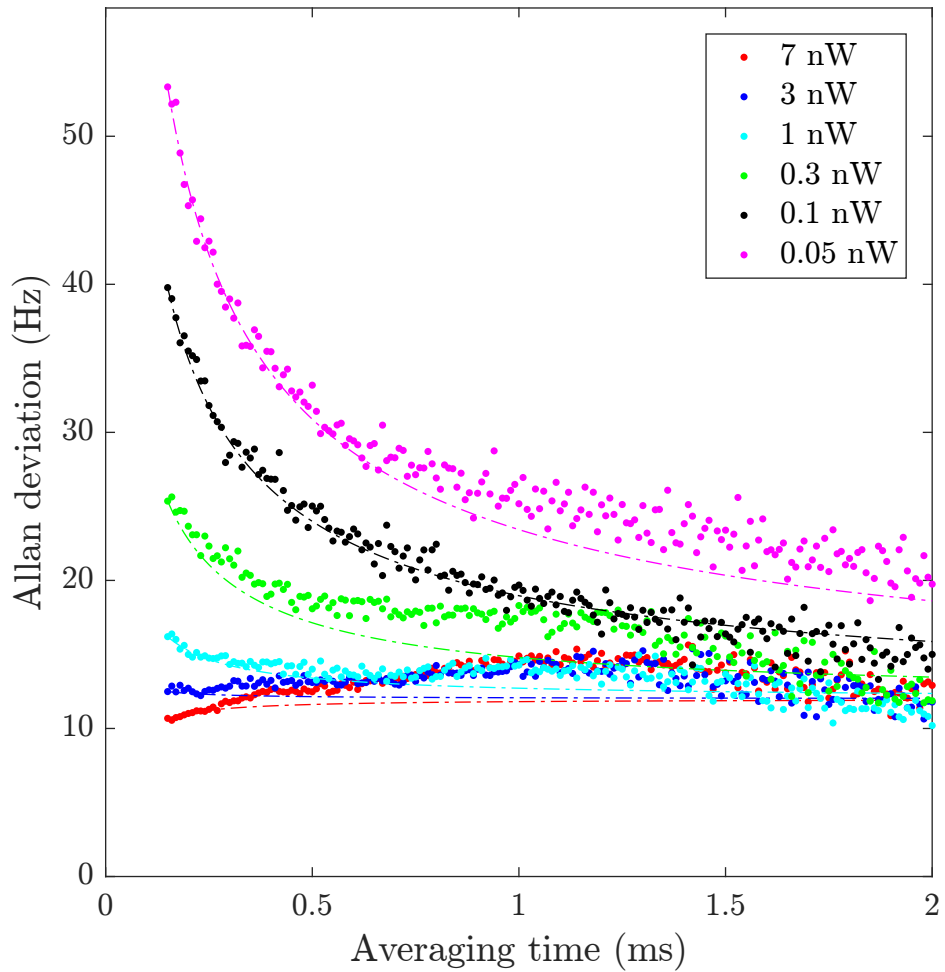


Figure 3.25: The figure shows the Allan deviation as a function of averaging time for different probe powers. The dashed lines are showing the ideal behavior if the first point of the trace averages down as white noise, *i.e.* as  $t^{-1/2}$  where  $t$  is the averaging time. At low powers and low averaging times, the noise mostly follows white noise, but at higher powers and higher averaging times we hit the technical noise limit of approximately 12 Hz.

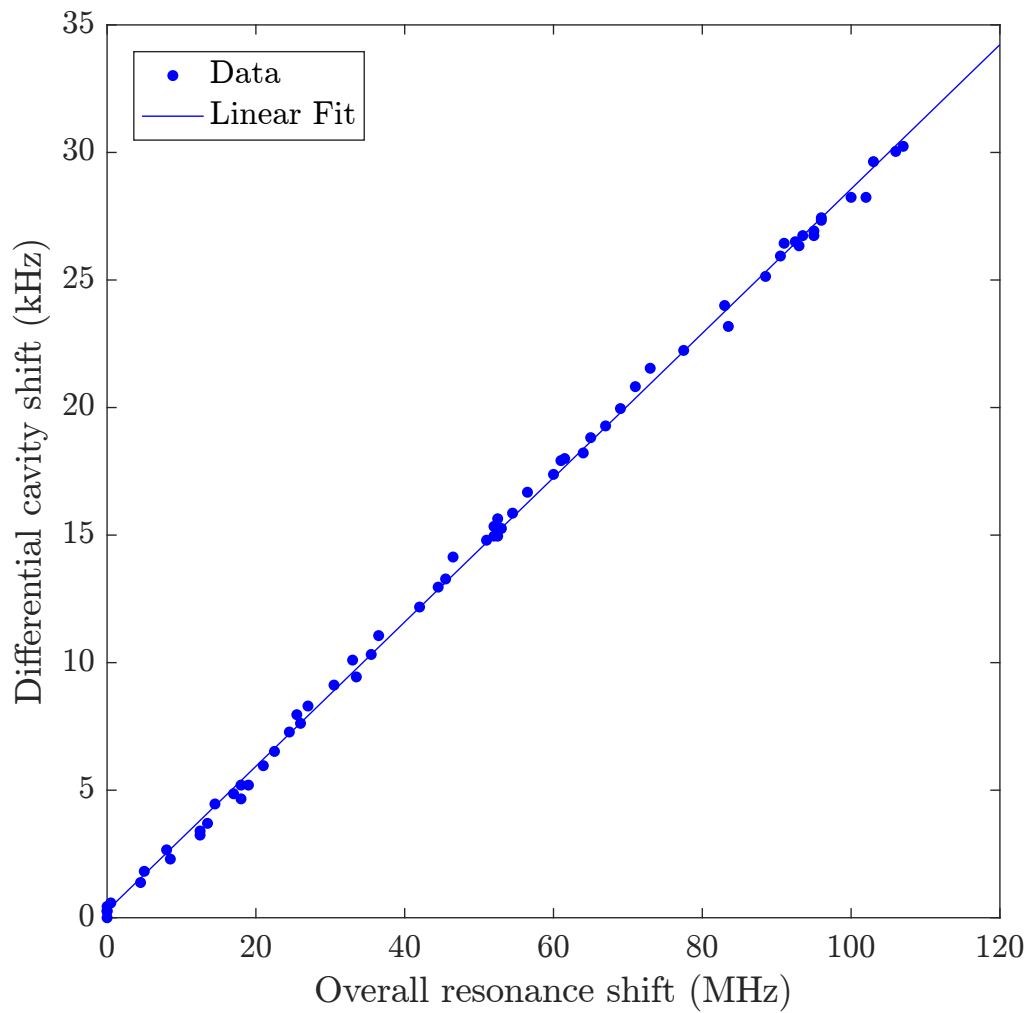


Figure 3.26: The figure shows the differential shift between the doubled 1560 nm light and the 780 nm cavity resonance plotted against the overall cavity resonance shift. The data shows a linear dependence as expected for small changes in length. The fit coefficient is 283 Hz/MHz.

Due to the unequal lengths, a drift in overall cavity length can cause the 780 nm probe to drift off resonance by order of 1 kHz on a timescale of minutes. The drifts can have a significant impact on our experiment due to the narrow linewidth of our cavity. In order to keep the 780 nm probe on resonance, we used a digital feedback system programmed in MATLAB. At the end of every experimental cycle ( $\sim 1$  s), a measurement is made of the empty cavity resonance. The measurement uses the homodyne system, but is read out with a digital multimeter instead of the scope (see Figure 3.23). The software automatically calibrates the frequency discriminator of this measurement by doing an automatic initial calibration where measurements are made at known frequency offsets. Prior to this measurement, the lattice is ramped in the same way as in the cycle such as to put the empty cavity resonance in this reference measurement at exactly the same point as during the cycle. The reference measurement is then used to feed back on the probe frequency through the RF synthesizer that sets the offset of the 1560 nm lock (see §3.2.2). The feedback system keeps the probe within 100 Hz of resonance every cycle. The empty cavity measurement at the end of the cycle is also used to correct the probe measurement made during the cycle.

### 3.2.7 Cavity frequency measurement

When performing a cavity frequency measurement, we ramp up the intensity adiabatically compared to the cavity linewidth. We use 200  $\mu$ s pulse length - the shortest possible pulse length while avoiding ringing in the homodyne measurement. The homodyne signal discriminator is time-dependent, we therefore apply a time-dependent weighting function when analyzing the time traces generated from the homodyne detection module. This method achieves the same signal and photon shot noise values for any pulse shape given that the pulse area is conserved. The weighting function is found by tuning the probe  $\kappa/8 = 1$  kHz off cavity resonance and averaging traces with an empty cavity. We then use the measured normalized weighting function,  $\rho(t)$ , to calculate the cavity shift,  $\Delta\nu$ , measured with homodyne signal  $s(t)$  as follows:

$$\Delta\nu = D \frac{\int dt s(t)\rho(t)}{\int dt \rho^2(t)}. \quad (3.6)$$

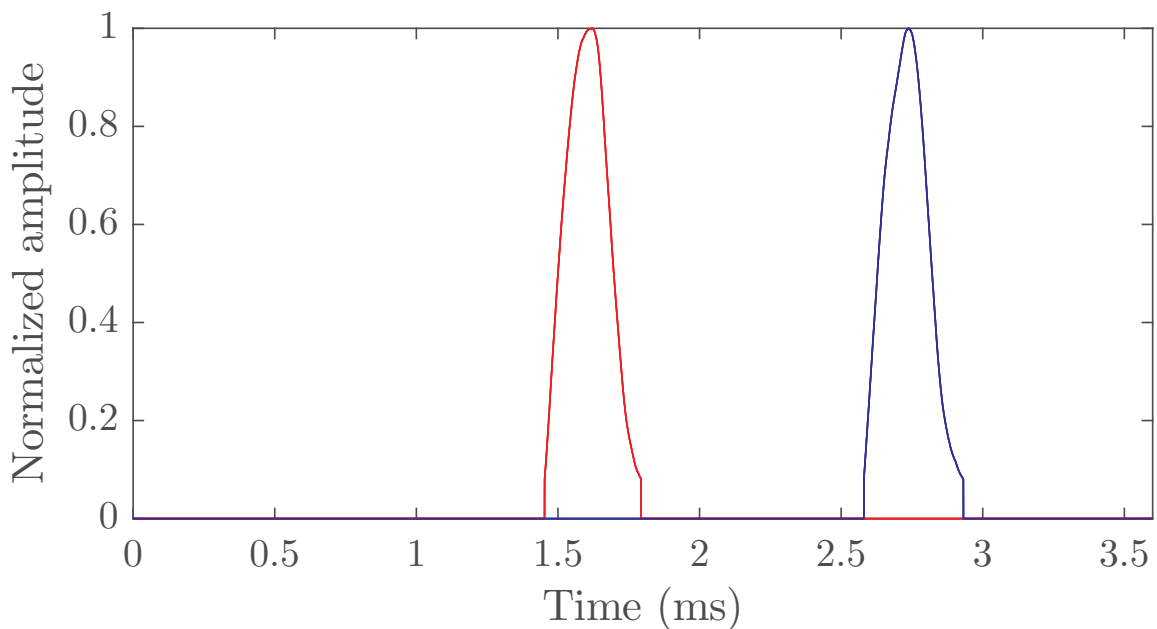


Figure 3.27: Templates for a measurement strength of  $\phi_{AC} = \pi$ , taken at a 1 kHz offset from the cavity resonance and averaged over 300 traces. The templates are inserted for  $\rho(t)$  in Equation 3.6 to calculate the frequency deviation from cavity resonance in a pulsed measurement. Values under 8% of the maximum are set to 0 to avoid noise in the template.

where  $D$  is the frequency discriminator in units of Hz/V at the peak probe power. This method calculates the correct cavity shift as long as the dressed cavity-probe detuning is in the linear regime. When outside the linear regime, an additional correction factor is applied. This correction factor is calibrated by detuning to a known value and measuring the discrepancy between the known detuning and inferred detuning. The correction factor is of particular importance when measuring the CSS noise levels, as at large atom numbers the CSS noise approaches  $\kappa/2$  and is thus outside the linear regime.

Using the method outlined above, we characterized the r.m.s noise between back-to-back cavity measurements during the cycle. The results are shown in Figure 3.29. We found that after properly accounting for the number of photons used in the measurement, the measurements taken during the cycle replicated the noise performance of those in steady state and again follows the expected photon shot noise scaling.

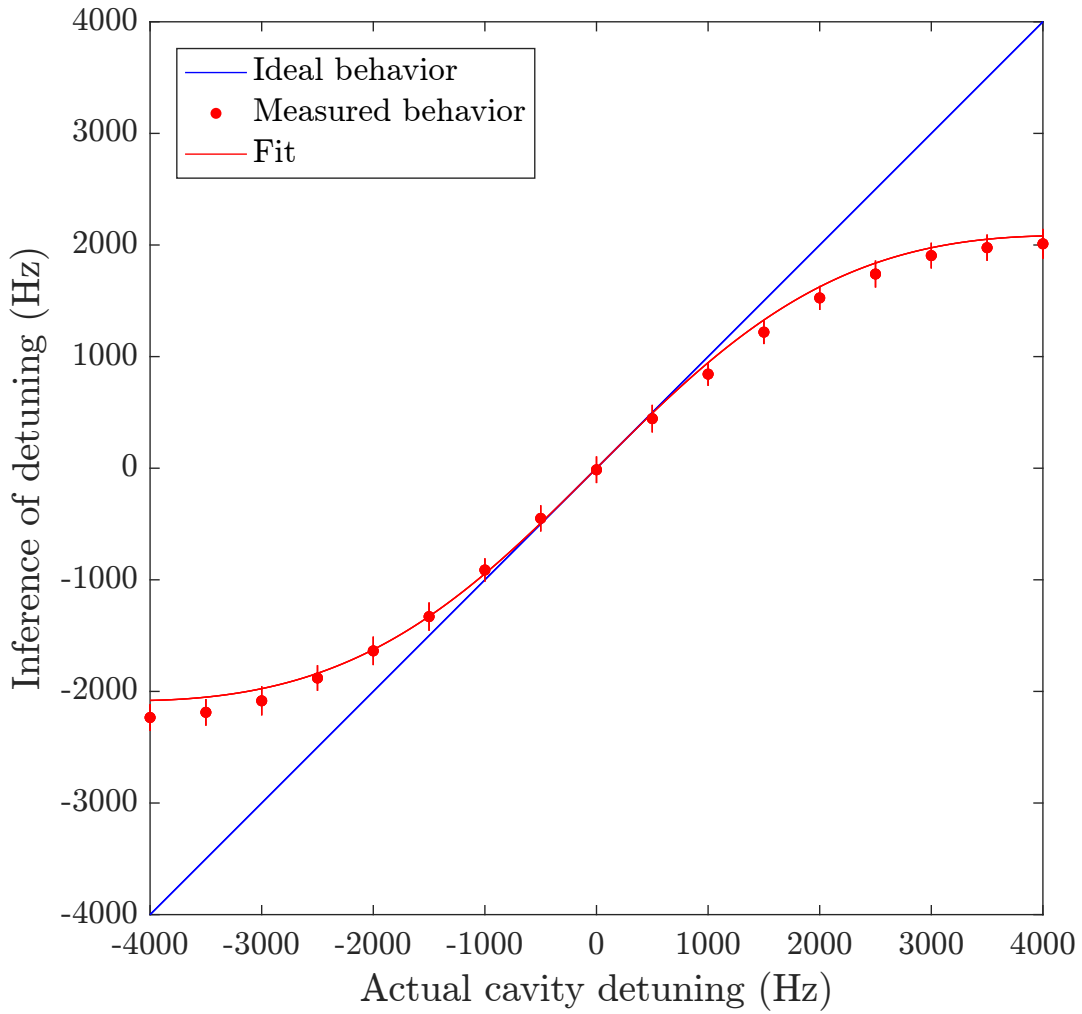


Figure 3.28: Blue line shows the ideal behavior, assuming a linear relationship between the measured homodyne signal and frequency. Red data points show the inferred cavity detuning based on the ideal assumption. The fit is a dispersive curve with the given cavity linewidth.

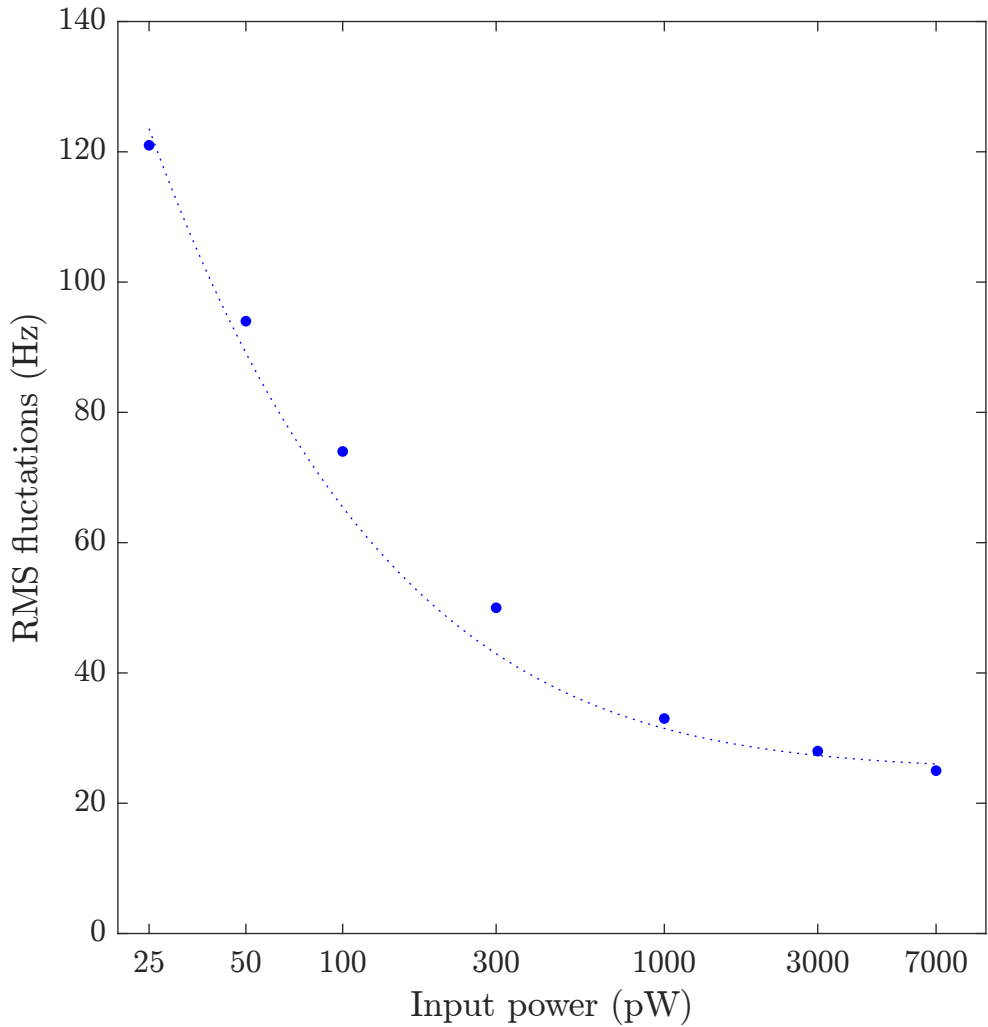


Figure 3.29: The plot shows rms fluctuations between two  $200\text{ }\mu\text{s}$  measurements of the empty cavity resonance. The data is taken during the experimental cycle with the lattice ramped to minimize thermal drifts (described in §3.2.4). The dotted line shows the expected square root scaling based on the measured fluctuations in the first point. The  $x$ -axis is shown on a log scale.

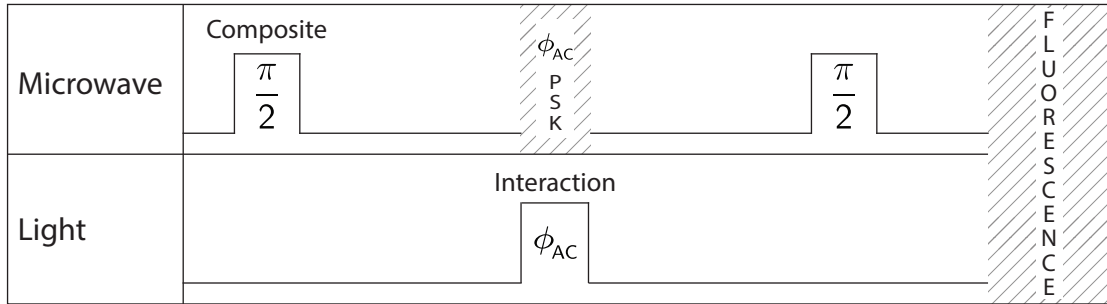


Figure 3.30: The sequence shown is used to calibrate the incurred ac-Stark shift of all kinds of atom-cavity interactions. By first setting the PSK to the desired ac-Stark shift value, we can tune the interaction or measurement strength until it is at the desired ac-Stark shift. The microwave rotation axes are set such that the final value of  $J_z$  is 0, maximizing sensitivity to ac-Stark shifts. The fluorescence imaging here uses the push beam to do state tomography. The time axis is not to scale.

### 3.3 Characterization of atom-cavity interactions

#### 3.3.1 ac-Stark shift measurements

Throughout the thesis, measurement strengths and other atom-cavity interactions are characterized in terms of the incurred ac-Stark shift on the atoms. In general, these are measured through a simple Ramsey-like sequence shown in Figure 3.30. While other methods could be used to infer the intracavity photon number, the most direct measurement of the interaction between atoms and light is through the ac-Stark shift. This method therefore allows for precise tuning of the relevant interactions.

#### 3.3.2 Atom-cavity coupling measurement

The atom-cavity coupling parameter,  $g_0$ , can be accurately calculated from cavity parameters. By taking into account the temperature of the atoms and thus their spatial extent in the lattice,  $g_{\text{eff}}$  can also be found such that the per spin-flip cavity shift,  $\delta_c = 2g_{\text{eff}}/\Delta$ , can be found as per § 2.3.4. The value for  $\delta_c$  does not enter into measurements of spin noise reduction for squeezing, however we use the cavity to calibrate our atom number. In order to verify the calculation, a simple experiment

was performed. We sent 800 nW of light 500 kHz off cavity resonance into the cavity and measured an ac-Stark shift of  $\phi_{\text{AC}} = 4\pi$  in  $\delta t = 800 \mu\text{s}$ . From Equation 2.19 we can then find the intracavity photon number,  $n = 496$ . We can then use the relation between ac-Stark shift and intracavity photon number,

$$\phi_{\text{AC}} = \delta\omega\delta t = n \frac{2g_{\text{eff}}^2}{\Delta} \delta t = 4\pi \quad (3.7)$$

to find that  $\delta_c = 2\pi \times 5(1) \text{ Hz}$  which is in good agreement with the calculated value of  $\delta_c = 2\pi \times 5.5 \text{ Hz}$ . I assume here that the intracavity photon number has no time dependence, *i.e.* that when the light is turned on the steady state intracavity photon number is reached instantaneously. Since in this case  $1/\Delta \gg \delta t$  this assumption holds well.

### 3.3.3 Lattice characterization

It is well known that far-detuned light traps atoms through the ac-Stark shift [103]. The trapping potential is given by

$$V = \frac{1}{2\epsilon_0 c} \Re[\alpha(\omega)] I(\mathbf{r}) \quad (3.8)$$

where  $\epsilon_0$  is the permittivity of free space,  $\alpha$  is the polarizability of the atom which depends on  $\omega$ , the frequency of the far-detuned light and finally  $I(\mathbf{r})$  is the intensity of the trapping light. In the cavity, the standing wave of the 1560 nm light forms an optical lattice trapping the atoms in lattice sites spaced by 780 nm, exactly commensurate with the probe beam.

In order to first find the intensity of light inside the cavity, we can infer the intracavity photon number from the measured transmission. We expect that

$$n = \frac{P_t}{\hbar\omega} \frac{1}{\kappa_M} \quad (3.9)$$

where  $P_t$  is the measured transmitted power and  $\kappa_M$  is the single mirror decay rate. The intensity in the cavity can then be found by first calculating the electric field of the cavity TEM00 mode, for some mode of wavevector  $k_0$  is given by

$$E(\mathbf{r}) = E_0 \exp\left(-\frac{r^2}{4\sigma^2}\right) \cos k_0 z \quad (3.10)$$

where

$$E_0 = \sqrt{\frac{n\hbar\omega}{2\pi\epsilon_0\sigma^2 L}} \quad (3.11)$$

and  $\sigma$  is half the waist and  $L$  is the length of the cavity. We will assume that the atoms are trapped at the waist of the cavity mode and at the peak electric field. We can now simply find the intensity by combining the two previous equations as follows

$$I = 2\epsilon_0 c E_0^2 = \frac{P_t c}{\pi\sigma^2 L \kappa_M} = \frac{2P_t \nu_{FSR}}{\pi\sigma^2 \kappa_M} \quad (3.12)$$

where  $\nu_{FSR} = c/2L$  is the free spectral range of the cavity. For a 1560 nm driving field the semiclassical approximation gives a good estimate of the polarizability of Rubidium, but I will use the more accurate calculated value from [104], which is different by approximately 5 %. Nevertheless, it is instructive to look at the semiclassical approximation to get some ideas of the parametric dependencies of the lattice potential,  $V$ ,

$$V(\mathbf{r}) = -\frac{3\pi c^2 \Gamma}{2\omega_0} \left( \frac{1}{\omega_0 - \omega} + \frac{1}{\omega_0 + \omega} \right) I(\mathbf{r}) \quad (3.13)$$

where  $\Gamma$  is the width of the  $D_2$  line,  $\omega_0$  is the frequency of the  $D_2$  line,  $\omega$  is the frequency of the driving field (in this case, 1560 nm) and  $I(\mathbf{r})$  is the light intensity. For less far-detuned traps, it is often appropriate to take the rotating wave approximation and ignore the second term, but for 1560 nm traps the rotating wave approximation does not hold. The terms outside the parentheses are a classical approximation for the dipole matrix element, and thus all the frequency dependence is contained in the co-rotating and counter-rotating term inside the parentheses. In the experiment, the lattice potential was measured by measuring the transverse trap frequency and then calculating the trap depth using the known waist of the lattice beam. The trap frequency is found by expanding the Gaussian potential to second order, then finding the frequency of this harmonic term by setting it equal to  $(1/2)m\omega_{\text{trap}}^2$ . The trap

depth is then given by

$$V_0 = m\omega_{\text{trap}}^2 \sigma^2 \quad (3.14)$$

where  $m$  is the mass of  $^{87}\text{Rb}$  and  $\omega_{\text{trap}}$  is the trap frequency. We can then combine Equation 3.8 and Equation 3.14 to find that

$$\omega_{\text{trap}} = \sqrt{\frac{P_t \nu_{\text{FSR}} \Re[\alpha(\omega)]}{\pi \sigma^4 \kappa_M \epsilon_0 m}} \quad (3.15)$$

which predicts the coefficient of the square-root fit to the experiment shown in Figure 3.32. The trap frequency was measured by trapping the atoms in the lattice, then rapidly lowering the potential for approximately 200  $\mu\text{s}$  then rapidly raising lattice back up again. The purpose of this procedure was to excite the atoms' motion in the harmonic trap. The atoms were then held in the lattice for a variable duration before being released. After release the width and center of mass of the cloud was measured. The final width and center of mass of the cloud showed a decaying sinusoidal dependence on the variable hold time in the lattice.

A sample plot of the width and center of mass oscillation for a given lattice intensity is shown in Figure 3.31. The frequency of the oscillation in width was twice the frequency of the center of mass oscillation, indicating that the oscillation in width is a breathing mode as expected. This oscillation frequency was taken to be the trap frequency and measured as a function of the transmitted lattice power. Due to the location of the camera, the transverse trap frequency could only be measured on the vertical  $z$ -axis, and there was therefore distortion of the potential due to gravity. Gravity modifies the Gaussian potential to

$$V(\mathbf{r}) = mgz - V_0 \exp\left(\frac{-z^2}{2\sigma^2}\right). \quad (3.16)$$

For the beam waist of the 1560 nm cavity mode and the mass of  $^{87}\text{Rb}$ , the lattice no longer traps at trap depths of 13  $\mu\text{K}$ , where the atoms fall out of the trap.

Despite the large detuning, the lattice light will induce a small but measurable differential ac-Stark shift on the clock states. We can calculate the differential shift

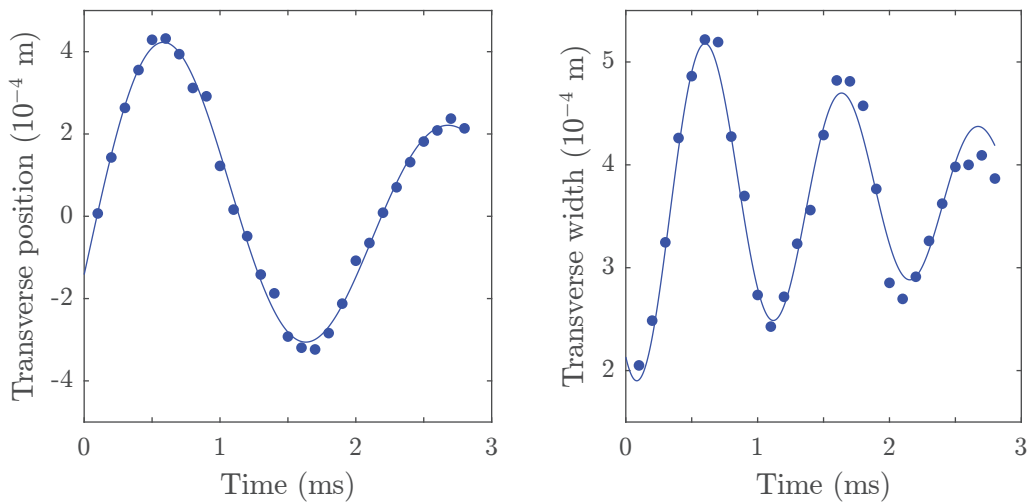


Figure 3.31: The figure shows the transverse width and position as a function of hold time in the lattice. The fits are of form  $a \sin(bt + c)e^{-dt} + e$ , i.e. exponentially decaying sinusoids. The width oscillation happens at twice the position oscillation frequency. Both the width and position parameters are extracted from the rotated 2D Gaussian fit shown in Equation 3.3. Both fits give a trap frequency of 480 Hz but in general the position oscillation was found to have lower error bars.

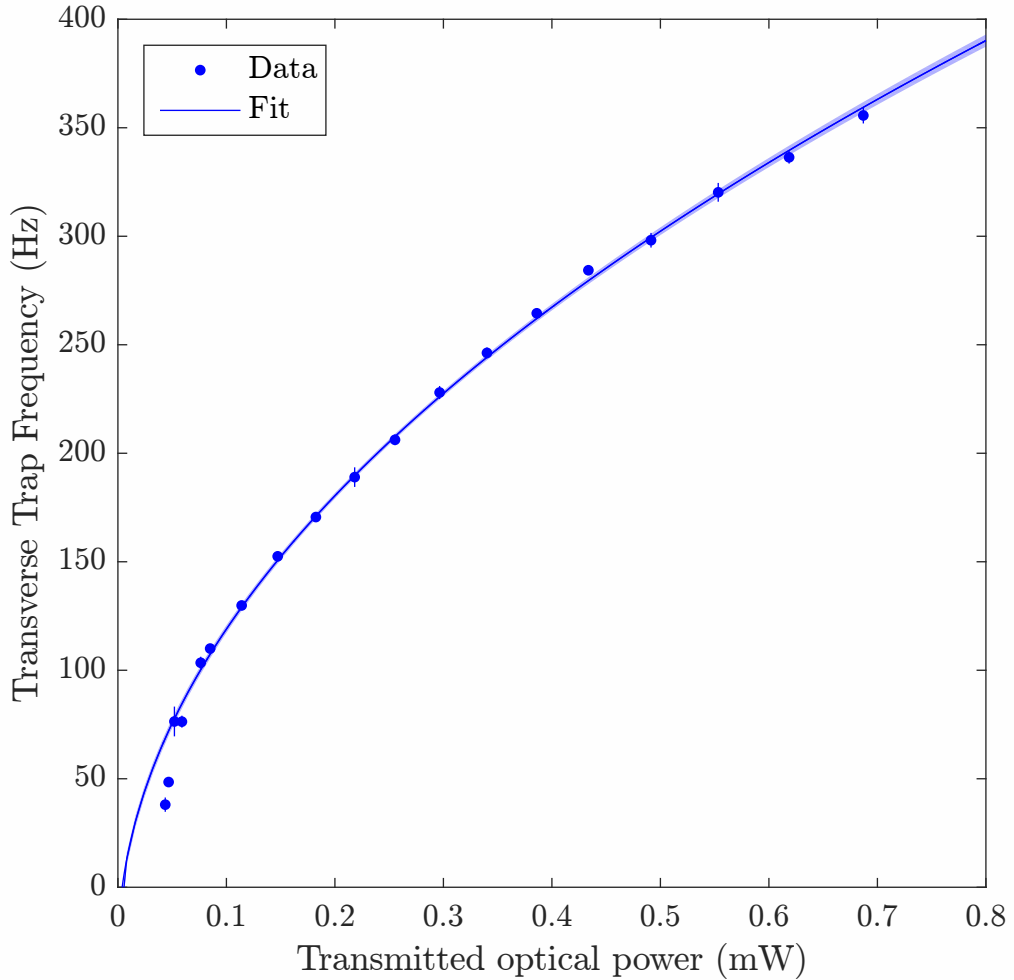


Figure 3.32: The figure shows a plot of trap frequency against transmitted power. The fit is of form  $\sqrt{ax} + b$ . The offset was added as the lattice becomes non-trapping at a finite depth due to gravity. For the purposes of the fit, the first two points were ignored, as the distortion due to gravity is especially significant here. The fit coefficient  $a$  was found to be  $446(10)\text{ Hz mW}^{-1}$ , agreeing well with the expected value of  $440\text{ Hz mW}^{-1}$  from Equation 3.15. Error bars and shaded regions are 68% confidence intervals.

induced on the clock state by calculating the induced shift for  $\omega_0 \rightarrow \omega_0 \pm \omega_{\text{HF}}/2$  using the frequency dependence inside the parentheses in Equation 3.13 and find that if the overall frequency shift of the hyperfine states is  $\omega_{\text{AC}} = V/h$ , the differential shift is given by

$$\delta_{\text{diff}} = \frac{5\omega_{\text{HF}}}{3\omega_0} \omega_{\text{AC}} \quad (3.17)$$

assuming  $\omega_0 \sim 2\omega$  and that  $\omega_{\text{HF}} \ll \omega_0$ . We found the differential shift experimentally by measuring the shift of the  $|1, 0\rangle \rightarrow |2, 0\rangle$  microwave transition as a function of lattice intensity. The shift was measured by scanning the microwave frequency with a 3.3 ms  $\pi$ -pulse time and finding the frequency at which most atoms were transferred from the  $|1, 0\rangle$  to the  $|2, 0\rangle$  state. The measured differential shift shows good agreement with the expected result from theory as seen in Figure 3.33.

Additionally, the lattice will cause a downward shift of the excited state predominantly due to the accessible transitions from the  ${}^5\text{P}_{3/2}$  state to the  ${}^6\text{S}_{1/2}$  (1366 nm,  ${}^4\text{D}_{5/2}$  and  ${}^4\text{D}_{3/2}$  (both 1529 nm) states [105]. We can calculate the relevant polarizability by summing the contributions of the transitions from and to the  ${}^5\text{P}_{3/2}$  state. Here, I summed all transitions up to the  ${}^{10}\text{S}_{1/2}$  at 530 nm using dipole matrix element values from [106] and [107]. From this summation I find that the excited state should be shifted down 45.8 times more than the ground state, meaning the  $D_2$  line is shifted by 44.8 times more than the ground state shift. The excited state shift was found by measuring the cavity shift per atom in the  $|F = 2\rangle$  state for varying detunings in varying lattice depths. The measurement was performed for three different lattice depths and the results are shown in Figure 3.34. The result of this large excited state shift is that the cavity-atom detuning (for the lattice powers used in later experiments) must be set to approximately 2.81 GHz instead of the expected 3.418 GHz for the chosen lattice intensity. Note that the cavity-atom detuning is determined as described in Figure 3.4, by beating light locked to the  $|F = 2\rangle \rightarrow |F' = 2, 3\rangle$  crossover with light resonant with the 780 nm cavity mode. The excited state shift turns out to be a beneficial effect, as the cavity resonance is now tuned away from the thermal Rubidium atoms in the chamber, that would otherwise cause extra noise and broadened cavity

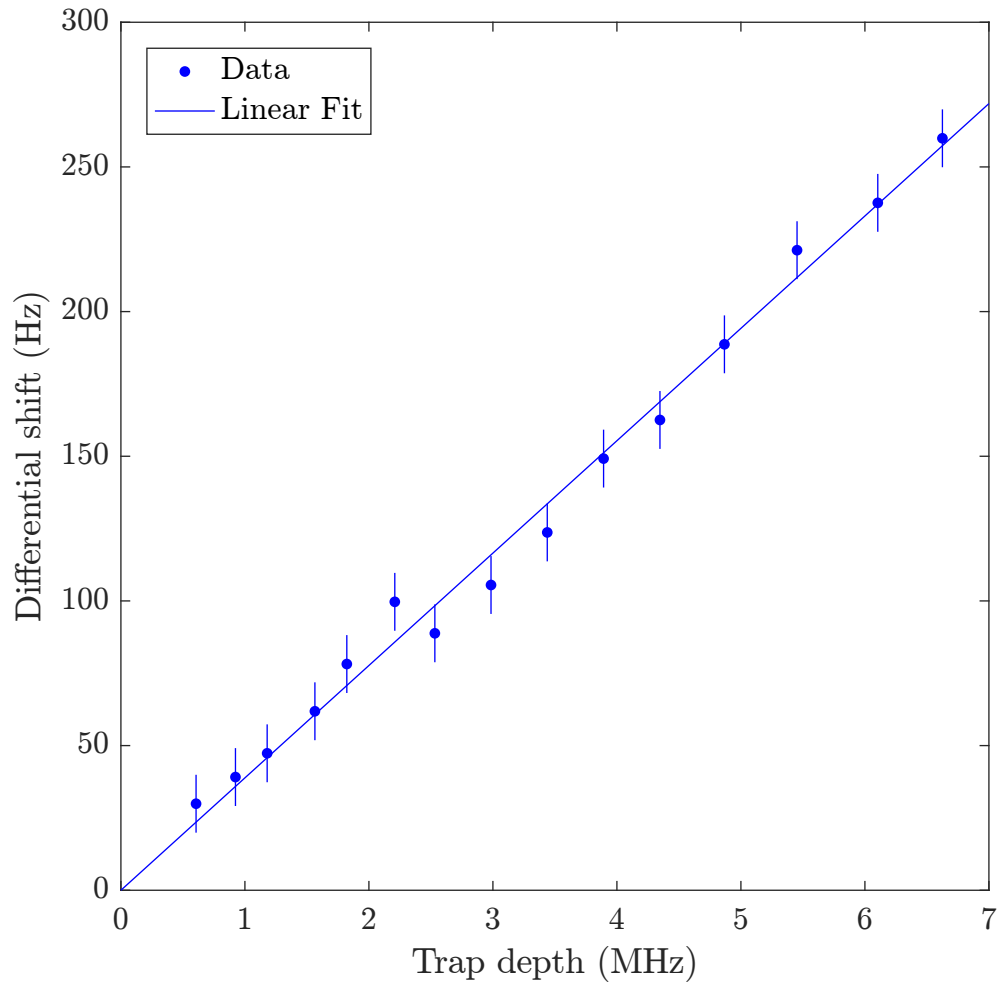


Figure 3.33: The plot shows the shift in  $\omega_{\text{HF}}$  as a function of transmitted power. The fit is of form  $a * x$ . The coefficient is about 20 % higher than expected at  $400 \text{ Hz mW}^{-1}$ . Error bars are 68% confidence intervals.

linewidths. The effect of these thermal atoms is described in §3.3.5.

### 3.3.4 Measurement of atom-broadened linewidth

Atomic scattering broadens the cavity linewidth at large atom numbers. To make accurate measurements, a modified linewidth must be used. The broadening is given by

$$\kappa = \kappa_0 (1 + NC (\Gamma/\omega_{\text{HF}})^2) \quad (3.18)$$

as per Equation 2.27. To take this into account, an atom number dependent correction factor is applied to the frequency measurements. The correction factor amounts to modifying the frequency discriminator,  $D$ , as follows

$$D_{\text{atom}} = D (1 + NC (\Gamma/\omega_{\text{HF}})^2)^2 \quad (3.19)$$

where  $N$  is here the atom number measured by fluorescence at the end of each cycle. To correct the frequency discriminator, the scale factor,  $1 + NC (\Gamma/\omega_{\text{HF}})^2$ , enters twice: once due to the broadening of the linewidth and once due to the reduced amplitude of the dispersive signal due to increased loss (see § 2.2.1). The scale factor was experimentally verified by shifting the cavity measurement away from the quadratic region of thermally induced cavity frequency shift, such that a  $\sim 1$  kHz shift was induced between cavity measurements. The atom number was then varied, to verify that the correction factor was correct over a range of atom numbers. The calibration is shown in Figure 3.35. The correction factor was applied to these measurements, and we found that the difference between having the thermal drift on and off was close to  $\sim 1$  kHz for a wide range of atom numbers. Without applying the linewidth correction, the difference between the fits would change by up to 20% from 450 000 atoms to 650 000 atoms. The experimental verification of the linewidth broadening was actually the first measurement utilizing squeezing in our lab. The measurement took 10 minutes - it would have taken 11 hours without squeezing.

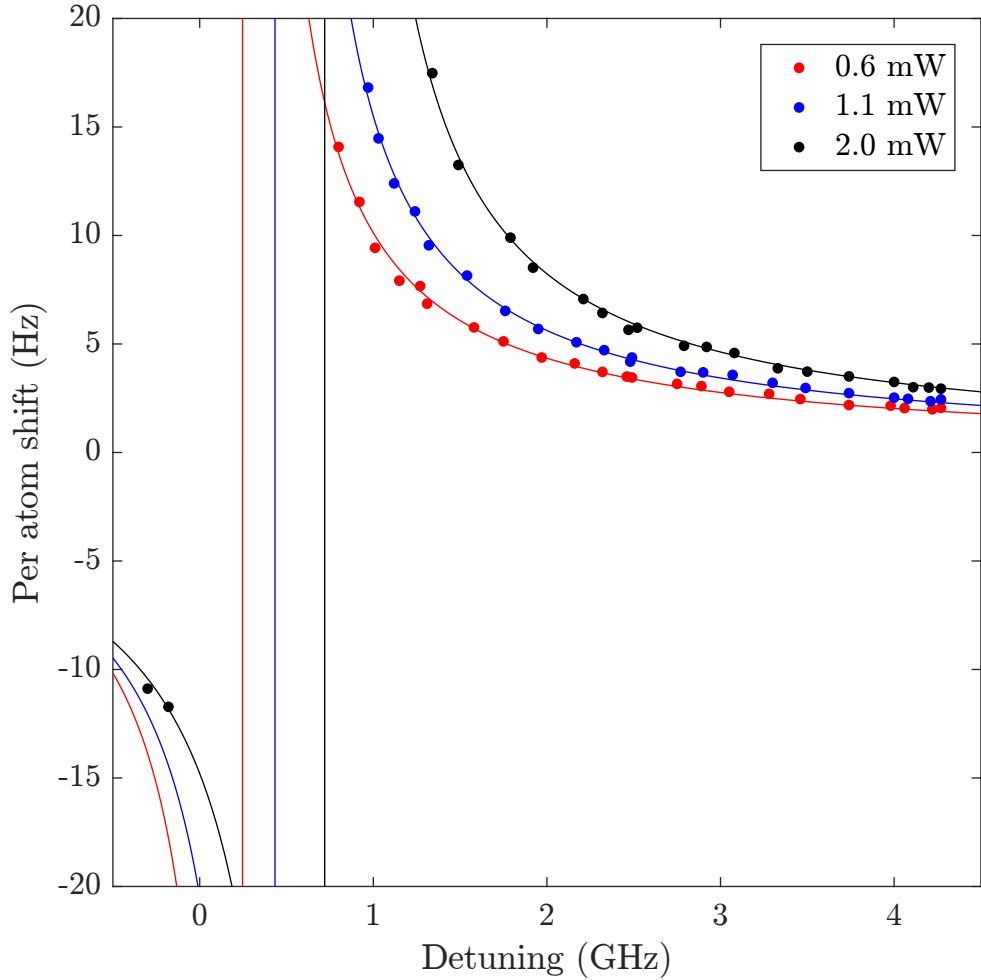


Figure 3.34: The figure shows a plot of the shift per atom in the  $|F = 2\rangle$  state as a function of the beatnote between the crossover line and the cavity resonance. The fits are of form  $\frac{a}{\Delta-b}$  where  $\Delta$  is the detuning. The centers of the fits are shifted approximately as a function of lattice power as expected. As the trap frequencies were measured only at low powers, I will limit my comparison of theory and experiment to the low power point at 0.6 mW where we can find the ground state shift based on the measured trap frequency and compare this to the measured excited state shift. At this point the excited state shift is approximately 47 times the ground state shift, which agrees well with the theoretical expectation.

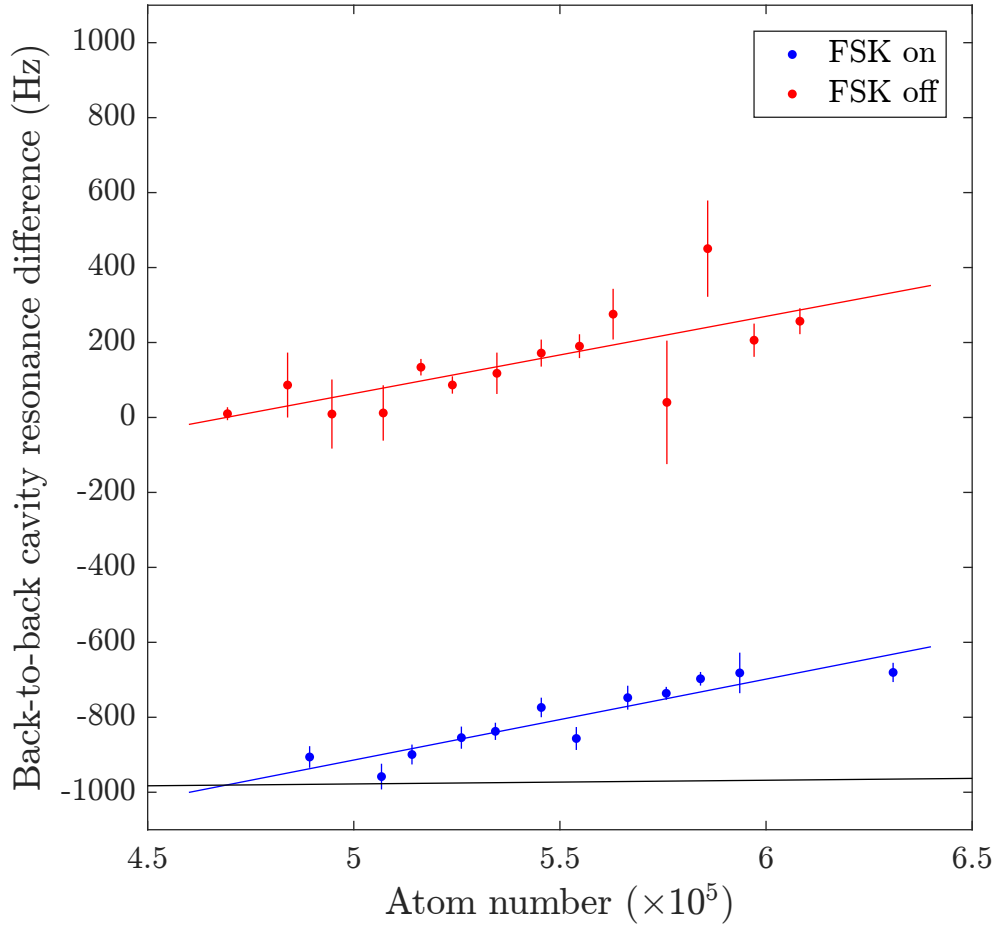


Figure 3.35: The figure shows a plot of the difference in frequency for back-to-back measurements of the cavity with atoms. The measurements were binned according to their atom number in bins of  $10^4$  atoms. The points shown are mean values with the 68% confidence interval of the mean indicated. Points in blue have an intentional thermal drift of the cavity between measurements that was calibrated to be  $\sim 1$  kHz. The red points do not have this thermal drift. The red and blue lines are linear fits to the data and the black line is the difference between the linear fits. The linear relationship between back-to-back cavity resonance difference and atom number is due to the effect of spin-flips.

### 3.3.5 Effect of thermal atoms

The vacuum chamber is set up such that the vapor pressure of Rubidium should be higher in the region of the 2D MOT and lower in the 3D MOT region. However, the background gas does still significantly interact with the cavity. When scanning through cavity-atom detunings, we found significant absorption at both  $^{85}\text{Rb}$  and  $^{87}\text{Rb}$  cooling and repump transitions. The amount of absorption depends on the amount of background Rubidium gas in the chamber. Under normal operating conditions where the  $^{87}\text{Rb}$  atom source had been kept hot for long enough to stabilize the background Rubidium gas pressure, up to 95% of the light sent into the cavity was absorbed by the background atoms. At the frequency corresponding to the  $^{85}\text{Rb}$  cooling transition for example the cavity linewidth was broadened by almost a factor of 5. By probing the cavity with low and high powers we inferred the cavity resonance shift due to the background atoms. At high powers the atoms are saturated and thus do not cause significant shifts, while at low powers their effect can be seen. By doing both these measurements we could infer the total shift. The total shift served as a proxy for the absorption from the background atoms. The background atom shift behaved as expected and showed broad resonances at expected frequencies. Additionally the natural abundance of  $^{85}\text{Rb}$  is about 2.5 times higher than  $^{87}\text{Rb}$ , which meant  $^{85}\text{Rb}$  resonances were substantially larger. To additionally characterize the resonances we observed the peak-to-peak dispersive signal as a function of cavity-atom detuning, as well as the r.m.s. noise on the homodyne signal when the cavity is put on resonance. A sample resonance is shown in Figure 3.36.

In the squeezing experiment we operate at a beatnote frequency of approximately 2.8 GHz between the cavity probe and the atomic resonance frequency. The excited state shift due to the lattice sets the detuning of the cold atoms to the appropriate  $\Delta = \pm\omega_{\text{HF}}/2$ . This particular lattice depth has the benefit that we can operate at the point where the background atoms have a minimal effect. We additionally characterized the additional frequency noise due to the thermal atoms at this cavity-atom detuning and found that for a bandwidth of 0.2-0.4 kHz r.m.s. frequency noise goes from 8 Hz to 20 Hz at the chosen cavity-atom detuning. For the atom numbers used in these experiments, this extra noise is insignificant in comparison to the squeezed state noise

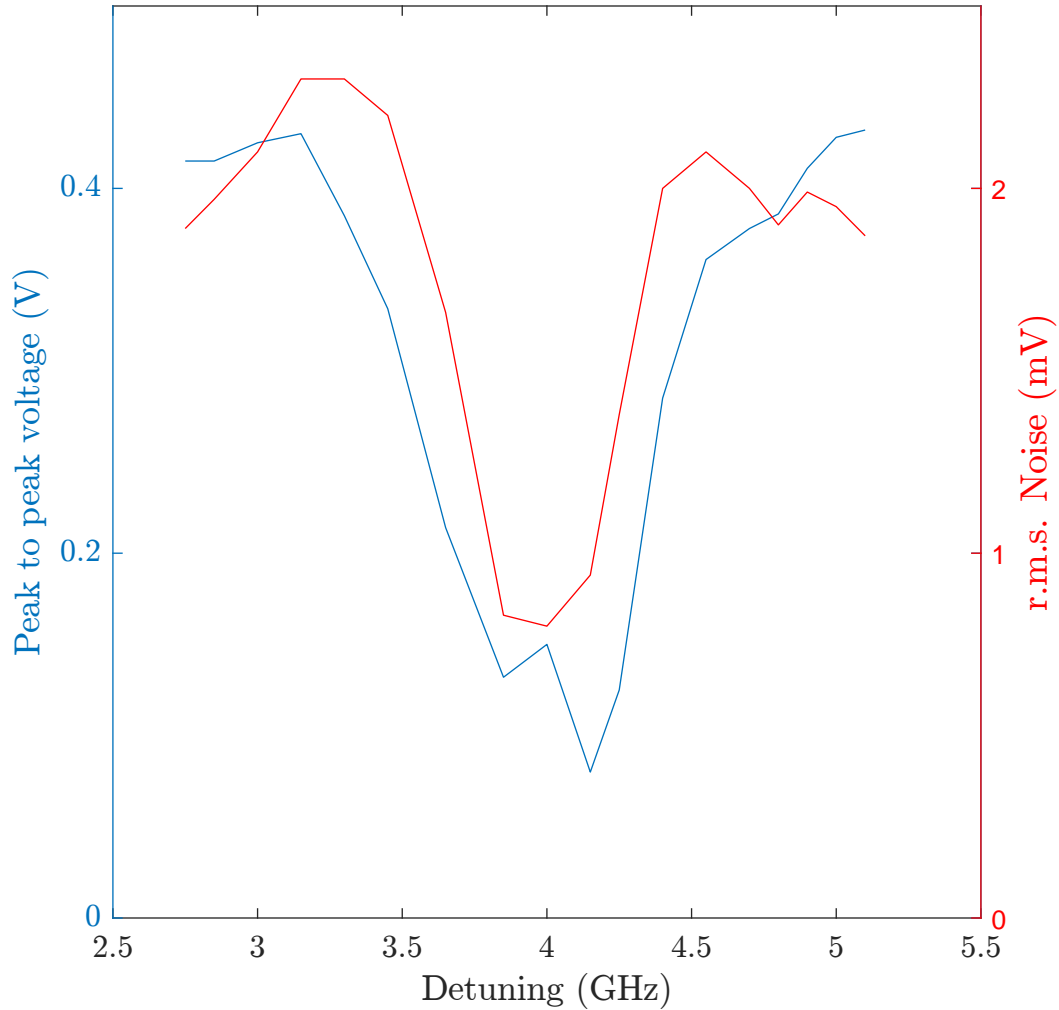


Figure 3.36: The peak-to-peak voltage of the dispersive signal was recorded for a wide range of cavity-atom detunings. The peak-to-peak voltage of the dispersive signal is proportional to the square root of the probe power returning from the cavity. Here we are scanning over the  $^{85}\text{Rb}$  transitions out of the  $|F = 2\rangle$  state. On the atomic resonance there is significant absorption leading to a reduction in peak to peak voltage. The r.m.s noise also goes down, but is actually greatly increased in frequency terms, reaching a peak of hundreds of Hertz at the point of greatest absorption.

and thus does not significantly impact the performance of the measurement.

### 3.3.6 Cavity-atom coupling as a function of atom number

The atom-cavity coupling changes as a function of atom number. By preparing the atoms in a  $\langle J_z \rangle = 0$  state and then causing a  $\pi$  ac-Stark shift with light detuned by 350 kHz we measured this effect. From the fit shown in Figure 3.37 we can conclude for  $N = 5 \times 10^5$ ,  $g(N)^2/g_0^2 \approx 0.983$ . One might expect that the effect is due to atomic scattering. However, for fixed incident power and detuning, the ac-Stark shift is proportional to the transmission coefficient. Therefore we can calculate, using Equation 2.7, that the contribution of the linewidth broadening will be approximately 3 parts in  $10^4$  which is not enough to explain the experimentally observed effect. The linewidth broadening accounts for all kinds of scattering losses in the cavity and has been measured experimentally. We can therefore rule out scattering losses as a cause of the effect. The exact mechanism of the change in coupling is therefore unclear. It is possible that the spatial extent of the cloud inside the lattice increases with increasing atom number thus leading to a decrease in average coupling to the cavity. For example, we know that more lattice sites are occupied further from the center of the cavity at higher atom number, which would lead to a decrease in coupling at higher atom numbers. There are also more atoms per lattice site, which could support some kind of collisional interaction causing the reduction in coupling.

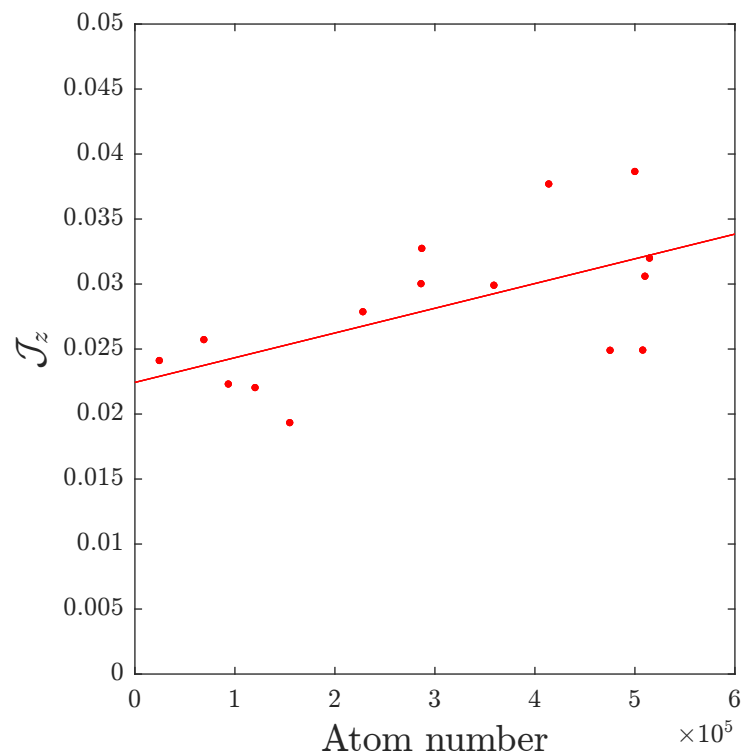


Figure 3.37: The plot shows the change in  $\mathcal{J}_z$  as a function of atom number at the end of an ac-Stark shift measurement cycle with a nominal  $\pi$  ac-Stark shift. The fit is linear and is used to extract the change in coupling for different atom numbers.

# Chapter 4

## Spin-squeezing through measurement

This Chapter describes the use of QND measurement to generate highly spin-squeezed states. The main results in this chapter were published in [44]. The observed 20.1(3) dB of squeezing is the largest observed in any system [108] and has the best directly measured phase resolution (147  $\mu$ rad rms, 18.5(3) dB below CSS noise) of any atomic sensor. The phase resolution was demonstrated on the  $^{87}\text{Rb}$  clock transition of 6.834 GHz by performing a small rotation of collective state. Due to the uniform coupling of the cavity, the generated states are compatible with free-space release. An atomic clock operating at 10.5(3) dB below the CSS noise was also demonstrated. Furthermore, we inferred that the states contain ensembles of at least 1590(130) entangled particles.

### 4.1 Squeezed state characterization

#### 4.1.1 Coherent state noise

Before performing any squeezing measurement, it must first be shown that the system can measure CSS noise according to theoretical expectation. In order to make this measurement, the atoms were prepared in a  $\langle J_z \rangle = 0$  state using the previously

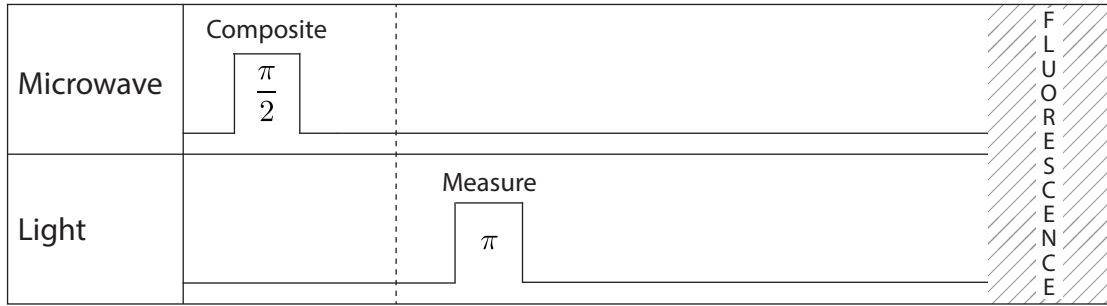


Figure 4.1: The figure shows the sequence used to measure coherent state noise. The part left of the dashed line is the state preparation. The measurement strength was  $\pi$ . The fluorescence imaging indicated at the end of the sequence is used to find the atom number and to calibrate the scattering-induced increase in linewidth as explained in § 2.3.2. The time axis is not to scale.

described composite  $\pi/2$  microwave pulse. A cavity resonance measurement was then made with  $\pi$  probe-induced ac-Stark shift. The measurement sequence is shown in Figure 4.1. The sequences shown in this chapter will detail only the measurement sequence. For more details on the rest of the timing sequence, see § 3.1.7. The data showed the expected square-root scaling, with microwave noise entering at higher atom numbers. The microwave rotation noise is due to fluctuations in the lattice intensity leading to noise in the microwave detuning, which manifests as rotation noise in the composite  $\pi/2$ -pulse (see § 3.1.3). As we operate at  $\langle J_z \rangle = 0$  with atom-cavity detuning of  $\Delta = \pm\omega_{\text{HF}}/2$ , atom number fluctuations do not enter into the measurement of CSS noise. Figure 4.2 shows a sample histogram of the coherent state noise of  $2 \times 10^5$  atoms.

### 4.1.2 Pre-squeezing

As seen in the previous section, the CSS noise at higher atom numbers exceeds the linewidth of the cavity. The probe would then go in at different detunings in each realization of the experiment, and measure at lowered strength away from the linear region of the homodyne signal. We therefore implemented a pre-squeezing procedure

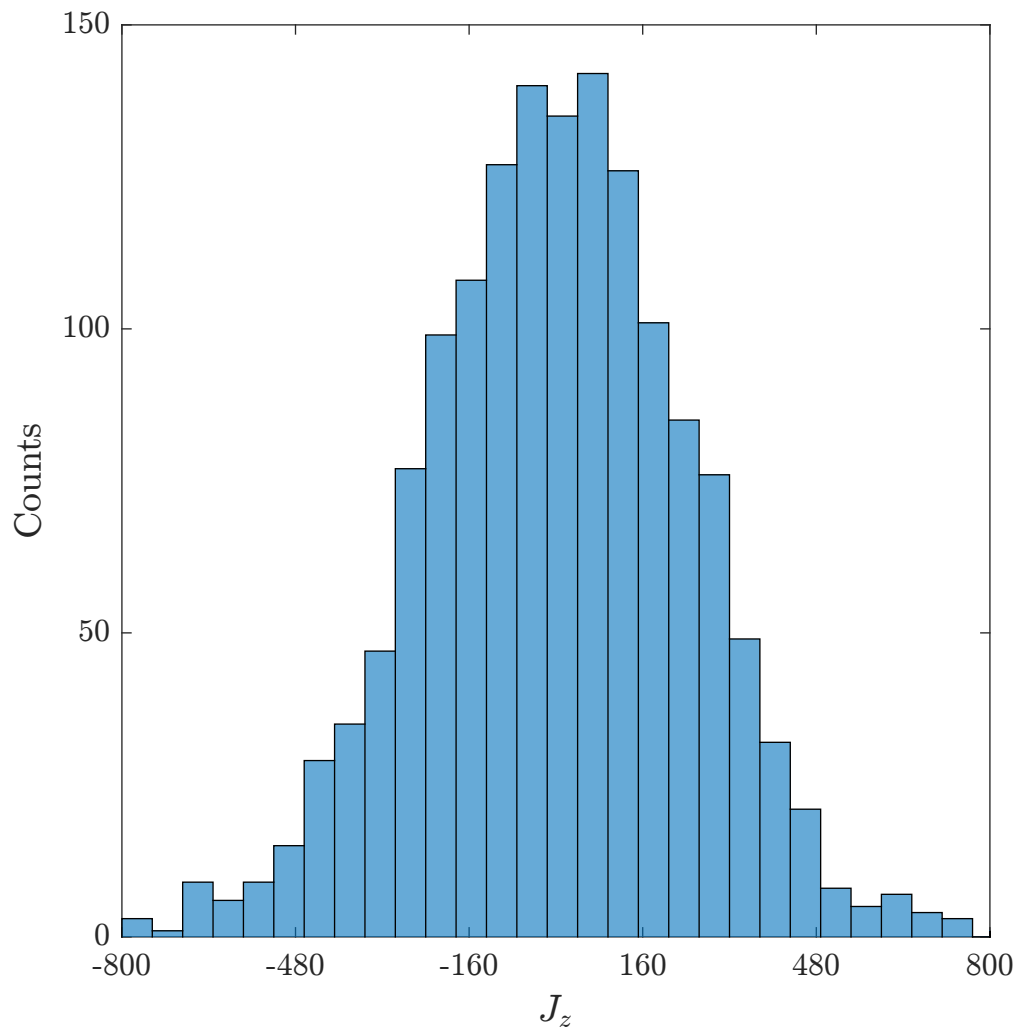


Figure 4.2: The histogram shows the CSS noise of  $2 \times 10^5$  atoms. The data is from 1500 experimental runs. The atom number was chosen such that the noise was still smaller than the cavity linewidth and the microwave rotation noise did not significantly enter to the measurement.

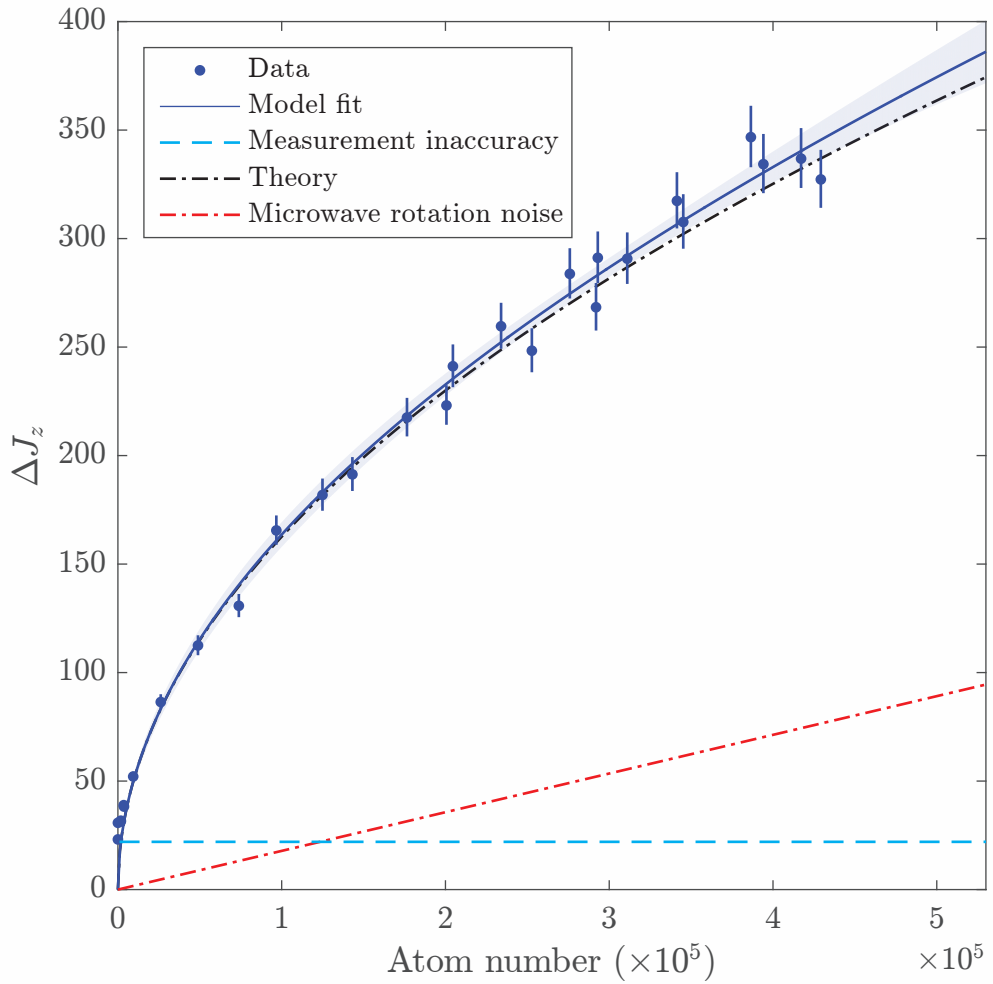


Figure 4.3: The graph shows a measurement of the CSS noise as a function of atom number up to an atom number of  $\sim 4 \times 10^5$  where the CSS noise gets close to  $\kappa/2$  and it is no longer possible to make a reliable measurement of the CSS noise using this cavity. The black dot-dashed curve is the theoretical expectation of  $\Delta_{\text{CSS}} = \sqrt{N}/2$ . The solid line fit has an added linear component to account for rotation noise from the composite microwave pulse, which is shown in red. The cyan dot-dashed line shows the resolution of a  $\pi$ -strength measurement, which was subtracted in quadrature from the data. The error bars and ribbons show a 68 % confidence interval on the data and the fit.

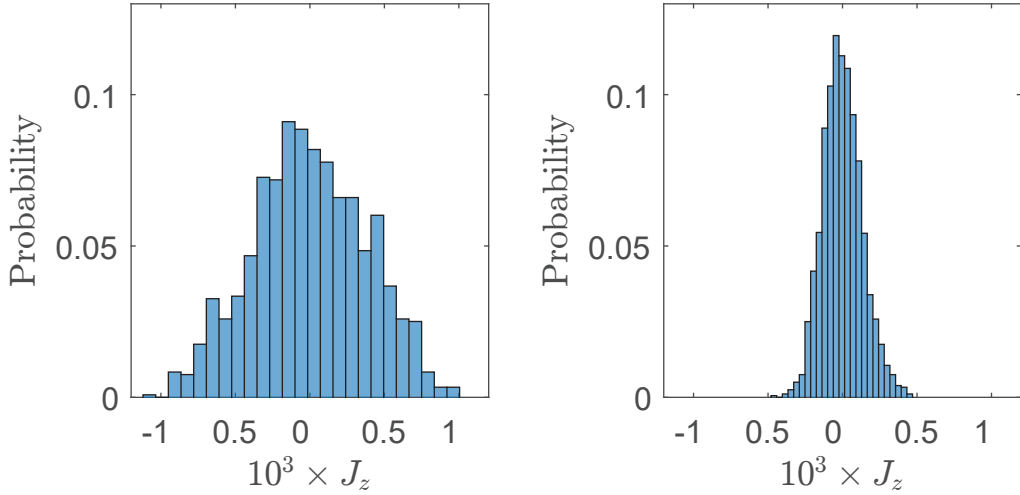


Figure 4.4: The histograms show spin states of  $5 \times 10^5$  atoms. The left histogram shows the  $J_z$  distribution of 1197 shots of a coherent spin state. The right histogram shows the  $J_z$  distribution of 3598 shots of a state pre-squeezed according to the above procedure. In this case we achieved approximately 8.5 dB of unconditional squeezing. At this atom number,  $\kappa/2$  is equivalent to approximately  $10^3$  spin-flips of cavity resonance shift. The time axis is not to scale.

using a small microwave rotation and  $J_z^2$  interaction, allowing unconditional pre-squeezing of the state prior to QND measurement. To pre-squeeze the state, 100 nW of light was sent in at  $6.25\kappa_0$  detuning, simultaneous with a 400  $\mu$ s  $\pi/12$  microwave pulse. The combined action led to 7 dB of unconditional squeezing while retaining 99 % coherence. While the pre-squeezing procedure helps the robustness and efficiency of the squeezing measurement, it does not alter the final squeezing results. The same amount of squeezing was attained by post-selecting on the first measurement being in the linear region of the homodyne signal, but with pre-squeezing this happens more than twice as often (approximately 2/3 of the time) at the largest atom numbers used here.

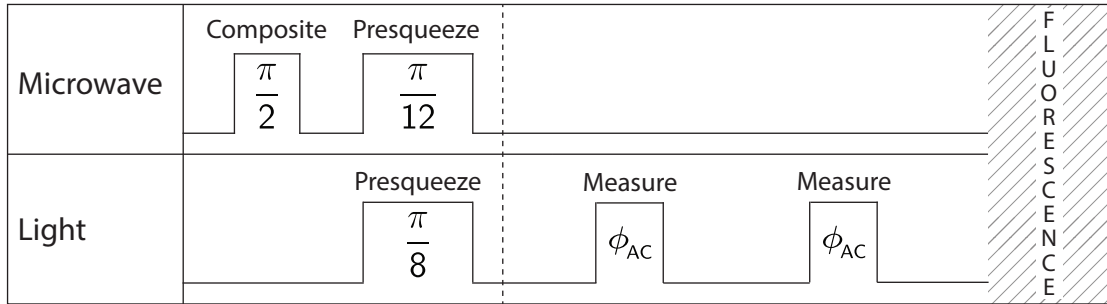


Figure 4.5: The figure shows the sequence used to measure squeezing as a function of measurement strength. The pre-squeezing sequence shown here is described in § 4.1.2. The measurement strength is indicated by  $\phi_{AC}$  and is calibrated in advance using the method described in § 3.3.1. The fluorescence imaging is again used for measuring the atom number. The time axis is not to scale.

### 4.1.3 Squeezing as a function of measurement strength

To investigate the theoretical dependencies expected for squeezing as shown in § 2.3.3 we performed identical strength back-to-back measurements for varying atom numbers. The experimental sequence is shown in Figure 4.5. Figure 4.6 shows the results with fits. We found that the spin-noise reduction saturates earlier than expected, suggesting unknown sources of additional noise. For identical strength measurements, the prepared states contain 3 dB more squeezing than directly observed due to the uncorrelated noise from the second measurement. The idea here is that one makes the first (squeezing) measurement, then follow with a procedure that measures the quantity of interest using atoms such as atom interferometry or an atomic clock. The final readout of the procedure is a stronger or more optimal measurement that exploits the full metrological enhancement of the squeezed state. At  $\pi$  measurement strength with  $5 \times 10^5$  atoms we found our highest inferred enhancement capability of  $20.1(3)$  dB, including a 0.6 dB loss due to the measured  $93.2(2)\%$  coherence. In § 4.2.1 I will show that we in fact recover some of this inferred enhancement capability by increasing the strength of the second measurement.

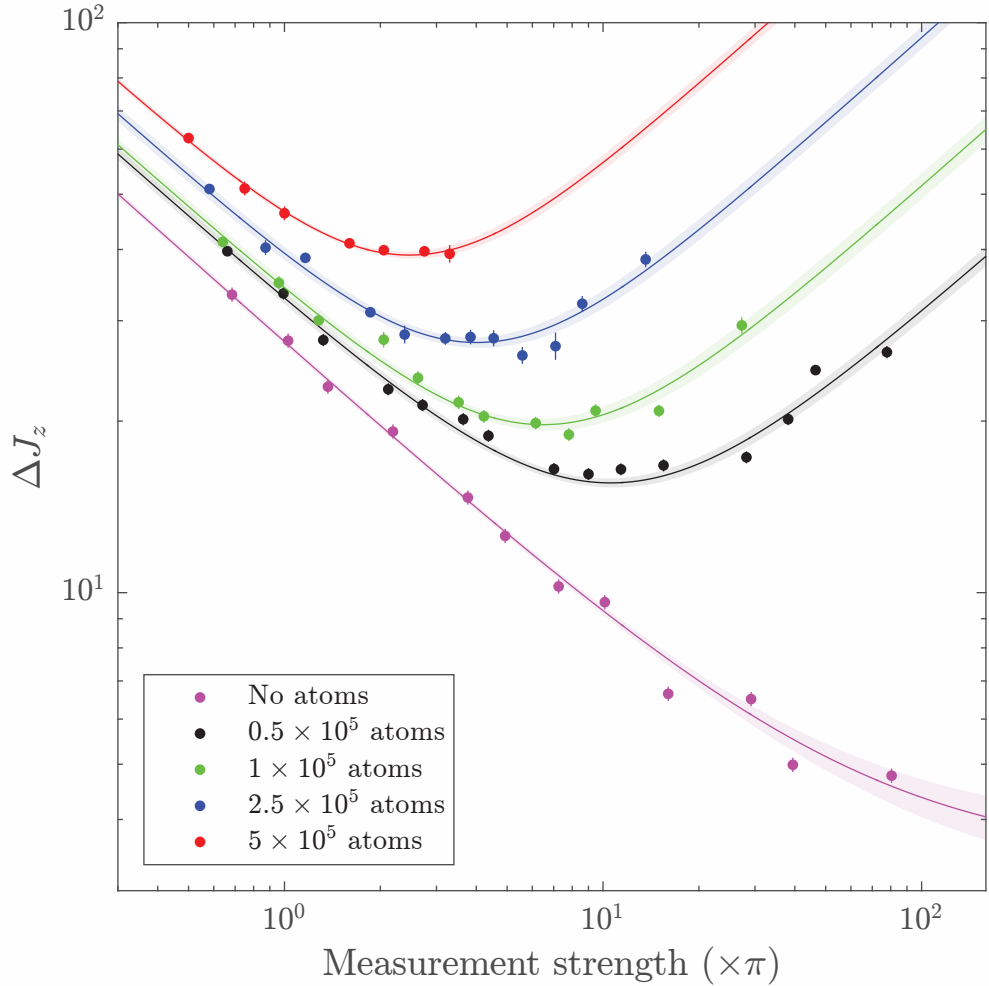


Figure 4.6: The back-to-back  $J_z$  noise for varying measurement strength is shown for different atom numbers. This is a spin noise reduction measurement where loss of coherence is not taken into account. The magenta line and data points show the empty cavity noise, displaying characteristic photon shot noise scaling. The fits for the data with atoms are of form  $\delta J_z^2 = \frac{\alpha}{\phi_{AC}} + \beta\phi_{AC} + \delta_{\text{meas}}^2$  where  $\alpha$  and  $\beta$  are fit parameters and  $\delta_{\text{meas}}$  is the technical measurement noise of 7 spin-flips. The fit follows the expected dependencies of theory, but are not in exact agreement. In particular, the  $\alpha$  coefficient is proportional to the atom number as expected. The error bars and ribbons show a 68 % confidence interval on the data and the fits.

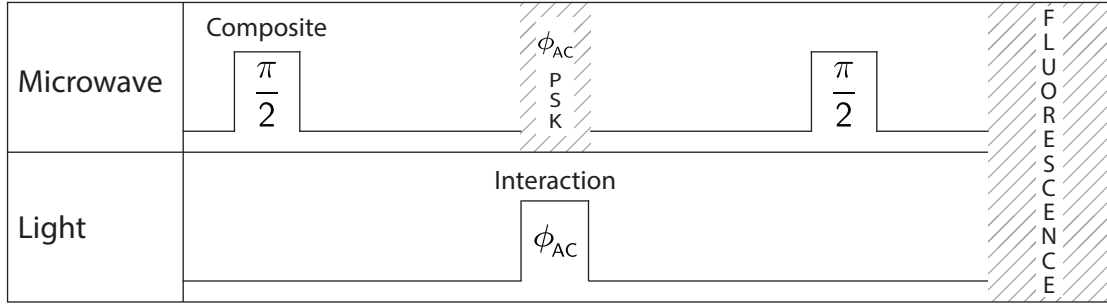


Figure 4.7: The sequence used to characterize antisqueezing. The camera is used to measure the  $J_z$  variance as the width of the antisqueezed state is far larger than the cavity linewidth. The push beam is used for state tomography here. The time axis is not to scale.

#### 4.1.4 Characterization of anti-squeezing

The cavity measurements, while projecting the atomic ensemble onto a state with reduced  $J_z$  noise, also act back onto the conjugate observable  $J_y$  and increase its noise. This backaction happens due to the photon shot noise of the probe beam. In the ideal case a measurement would preserve the area of the uncertainty ellipse, that is, the reduction and the increase in the noises of  $J_z$  and  $J_y$  respectively would be through the same factor. However owing to photon losses, inefficiencies in extracting the information in the read-out, and the additional spin-flip noise in  $J_z$ , the balance is expected to be broken. Experimentally, the variance of  $J_y$  scales linearly with measurement strength, reaching 39 dB above CSS noise at the  $\pi$  measurement strength accompanying the quoted 20.7(3) dB spin noise reduction in  $J_z$ . This corresponds to a factor of 8.8 increase in the uncertainty ellipse area (defining area as  $\Delta J_y^2 \times \Delta J_z^2$ ). We expect a factor of 8.1 increase in ellipse area due to the detection efficiency of  $\epsilon = 0.16$  and the loss due to atoms of  $\kappa_0/\kappa = 0.77$ .

Note that the model for antisqueezing did not take into account spin flips. The spin flip random walk would lead to additional shearing due to the probe walking off resonance during the measurement. The uncertainty area could also be increased due to technical effects - the probe does not always hit exactly on resonance, which leads to a different ac-Stark shift, which directly causes extra noise on  $J_y$ .

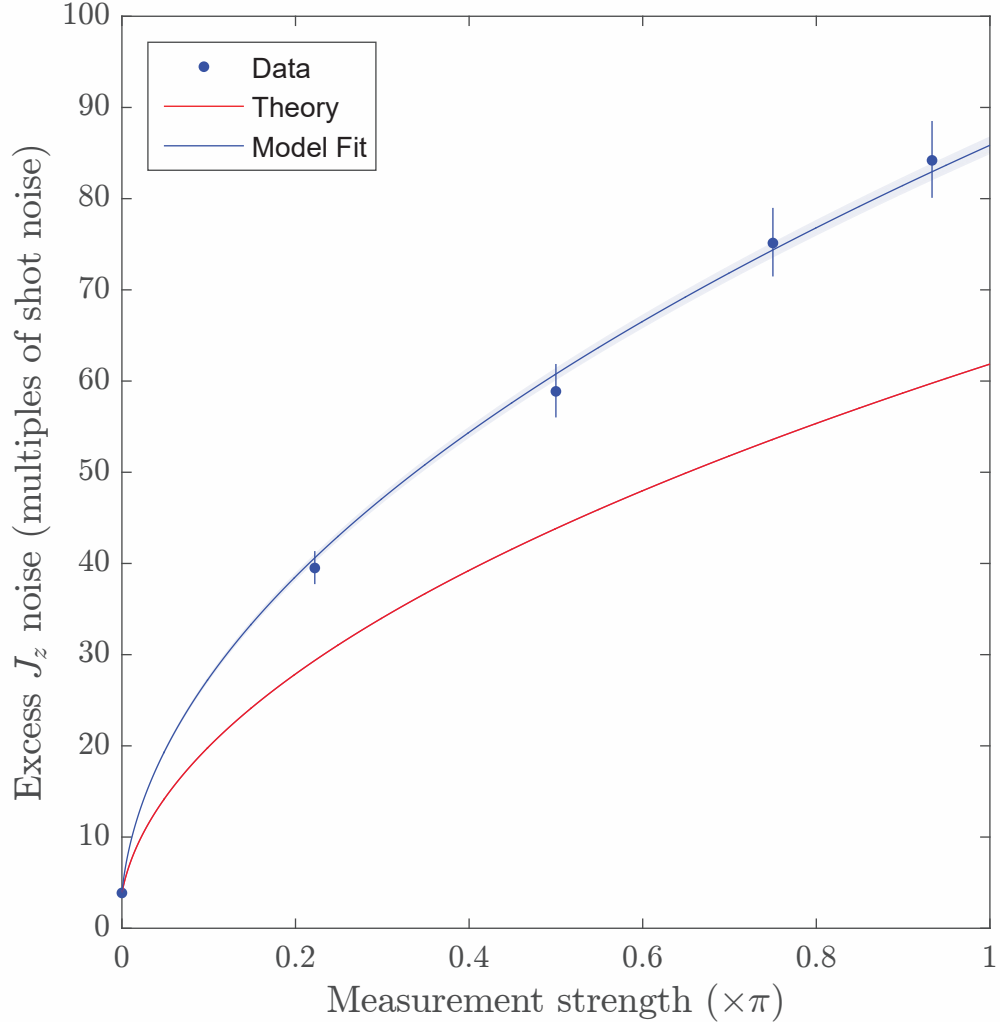


Figure 4.8: The figure shows the antisqueezing as a function of measurement strength. Shown in red is the theoretical expectation from Equation 2.97. The blue is a fit of form  $\sqrt{a^2 + b\phi_{AC}}$ . Here,  $a$  is the measurement uncertainty of the fluorescence measurement added in quadrature.  $b$  is a fit coefficient that fits to approximately two times the theoretical expectation. The amount of antisqueezing follows the expected scaling. The error bars are the 68% confidence intervals.

### 4.1.5 Coherence measurements

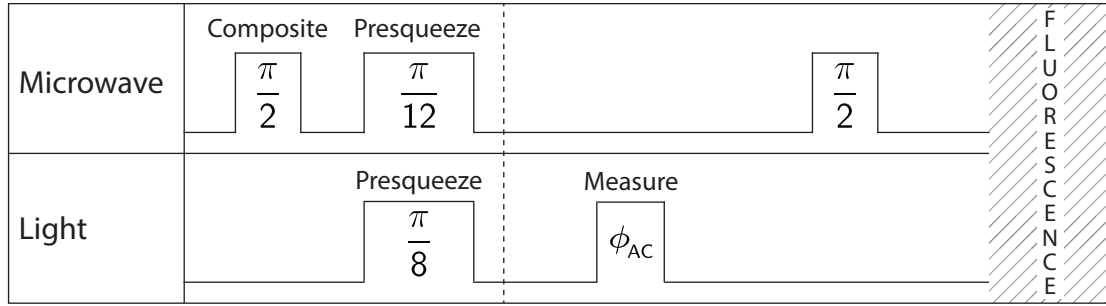


Figure 4.9: The figure shows the sequence used to measure the coherence of the squeezed state as a function of measurement strength. The measurement strength is labeled as  $\phi_{AC}$ . The  $\pi/2$ -pulse is used to rotate the state to the bottom of the Bloch sphere before the fluorescence imaging is used to measure the length of the Bloch vector. The time axis is not to scale.

To establish the metrological enhancement conferred by squeezing, the coherence of the states must be measured. As previously discussed, despite having a dual-wavelength cavity the coupling is not completely uniform and there is therefore some decoherence associated with probing. Some of the coherence could be recovered through the use of a spin-echo, but our microwave pulses are too noisy for such a procedure to be implemented. The pulse area noise on the microwave pulse would have to be less than one part in  $10^4$  to be used for a spin-echo on 20 dB squeezed states of  $5 \times 10^5$  atoms. Fortunately, the amount of ac-Stark shift needed for optimally squeezed states decreases with increasing atom numbers, allowing us to operate at relatively weak measurement strengths with little decoherence. It is also possible to recover some coherence by recohering the states with the 1560 nm lattice beam. Simply holding the squeezed state in the lattice undoes some of the inhomogeneity-induced decoherence, due to the 1560 nm light inducing the opposite differential ac-Stark shift on the clock states from the 780 nm probe and the atoms being in the harmonic region of the intensity profile of both beams. For estimating the metrological enhancement, coherence was measured using a simple Ramsey sequence where the probe pulse is applied between two  $\pi/2$  microwave pulses. The sequence is shown in Figure 4.9. The

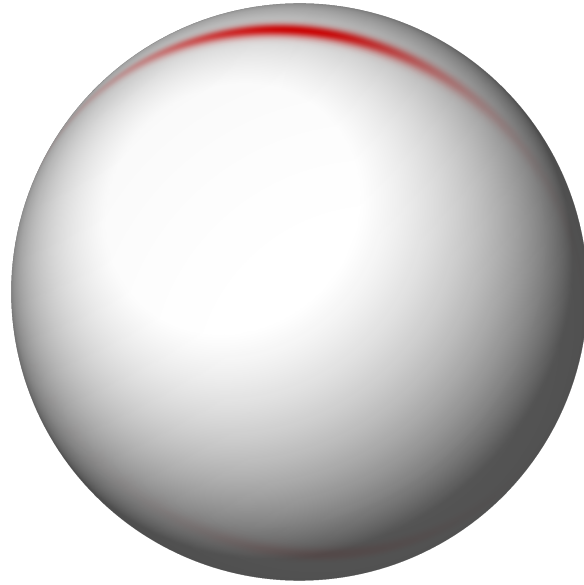


Figure 4.10: The figure shows a squeezed state rotated to the top of the Bloch sphere. As can be seen the antisqueezing causes the state to partially wrap around the curvature of the sphere. This was observed in Figure 4.12. The effect slightly degrades the metrological enhancement of the squeezed states.

results are shown in Figure 4.11. In Figure 4.12 the distribution of  $J_z$  measurements from fluorescence detection is shown in a histogram both for the squeezed and coherent state. The broadened and skewed distribution is due to antisqueezing, as illustrated in Figure 4.10. To calculate the coherence,  $\mathcal{J}$ , we use the mean of  $J_z$  and divide this by  $N/2$ .

#### 4.1.6 Saturation of squeezing with atom number

In § 2.3.3 I showed a simple model of the squeezing limits of the clock states of Rubidium. In Figure 4.13 I show the maximum attainable spin noise reduction as a function of atom number, with a model fit taken from the theory shown previously. While the theory does not give exact agreement, the experiment shows the same general features of squeezing saturating at high atom numbers.

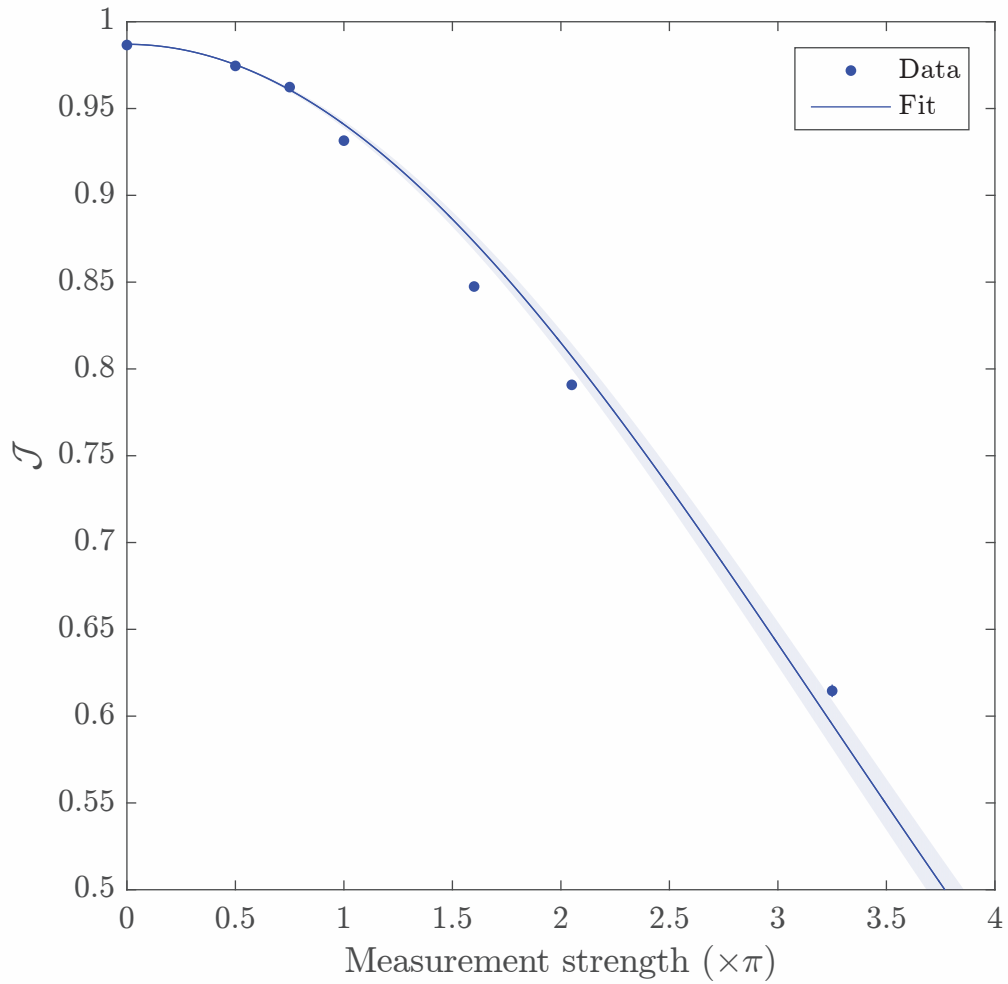


Figure 4.11: The figure shows coherence as a function of measurement strength with a fit of form  $\mathcal{J}_0 e^{-\beta \phi_{\text{AC}}^2}$  where  $\mathcal{J}_0 = 0.987$  is the initial coherence after pre-squeezing,  $\beta$  is a fit parameter and  $\phi_{\text{AC}}$  is the probe-induced ac-Stark shift. The coherence rapidly degrades at measurement strengths higher than  $\pi$ . The error bars and ribbons show the 68 % confidence intervals.

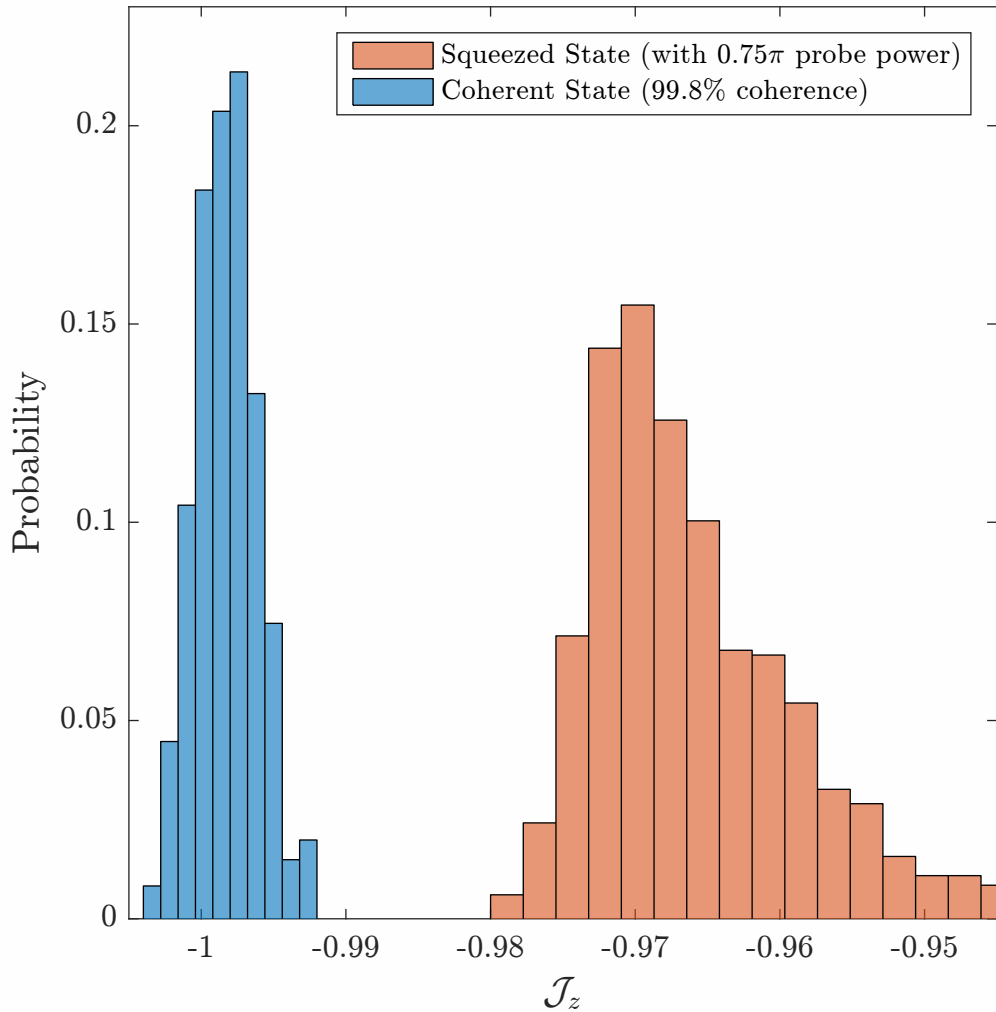


Figure 4.12: The histograms shows the distributions of a coherent and a squeezed state at the minimum of the fringe. The width of the coherent state is limited by camera noise. The squeezed state is showing anti-squeezing as illustrated in the Bloch sphere in Figure 4.10.

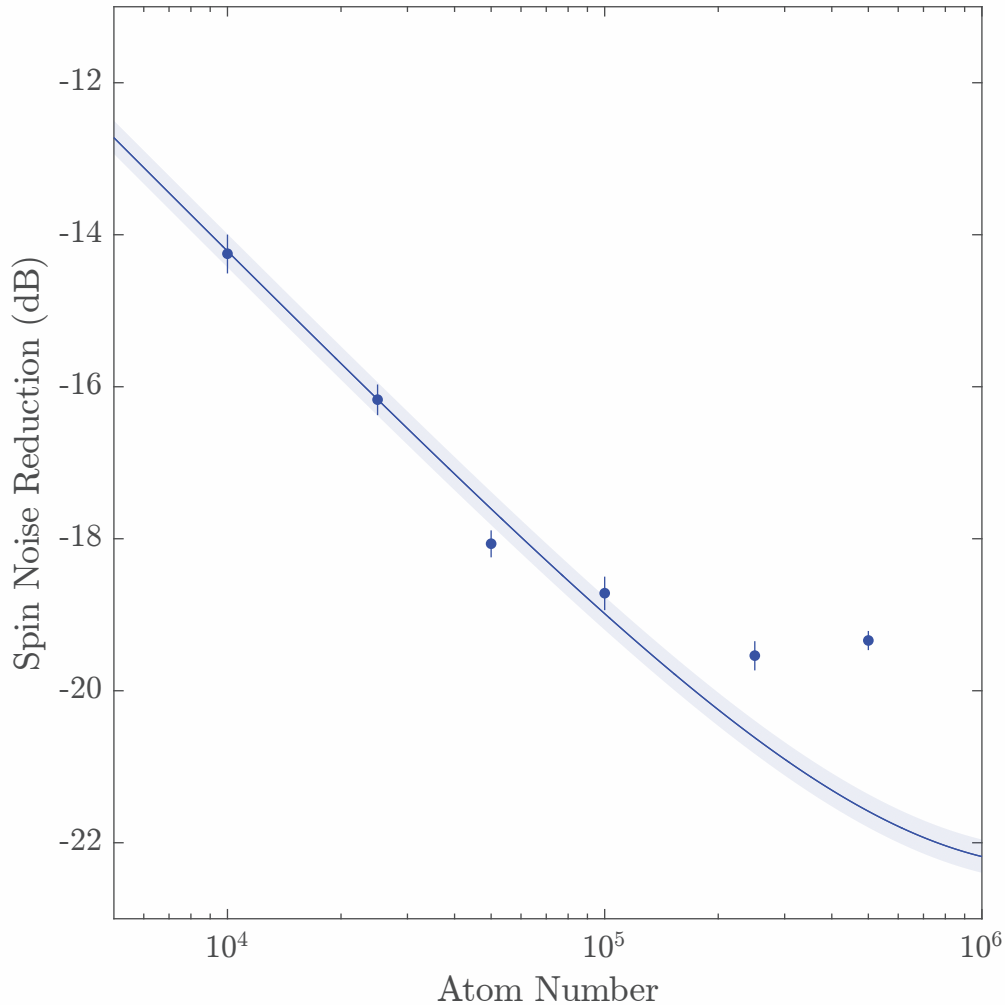


Figure 4.13: The plot shows the atom number dependence of the maximum attainable spin noise reduction. Solid line is a model fit of form  $\chi_{\text{opt}}^2 = \alpha \frac{\sqrt{NC}}{1+NC(\Gamma/\omega_{\text{HF}})^2}$  where  $\alpha$  is a fit parameter (see § 2.3.3). The spin noise reduction clearly saturates earlier than expected from theory. The error bars and shaded areas show a 68 % confidence interval.

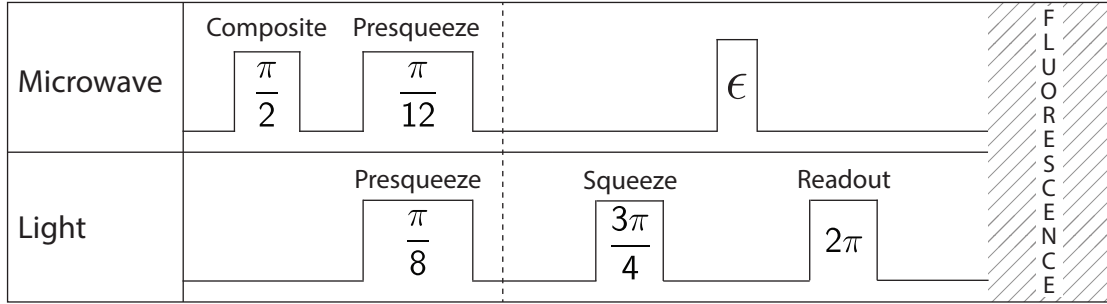


Figure 4.14: The figure shows the sequence used for the metrology example. For Figure 4.17, the second measurement pulse was not used and a longer microwave pulse replaced the  $\epsilon$  microwave rotation. The time axis is not to scale.

## 4.2 Quantum metrology demonstrations

### 4.2.1 Measurement of a small rotation

In order to demonstrate the squeezed state phase measurement performance, we performed a measurement of the rotation induced by a weak microwave pulse ( $660 \mu\text{rad}$ ). For this measurement, we reduced the measurement strength of the first pulse to  $0.75\pi$  and increased the second to  $2.0\pi$ , in order to increase the coherence after the first measurement to  $96.2(2)\%$ . The sequence used is shown in Figure 4.14. The initial measurement scatters only  $2 \times 10^{-3}$  photons per atom. Increasing the strength of the second measurement allows one to recover more information, by utilizing some of the inferred enhancement capability. For this configuration, using  $6.5 \times 10^5$  atoms, the directly measured metrological improvement was  $18.5(3)$  dB, corresponding to a single-shot phase sensitivity (r.m.s) of  $147 \mu\text{rad}$ . This phase resolution exceeds the sensitivity of the best engineered unentangled cold atoms sensors while using fewer atoms [109, 110]. The measured histograms of the displaced and undisplaced squeezed states are shown overlaid with a coherent state in Figure 4.16. We showed full-fringe Rabi oscillations using these squeezed states in Figure 4.17 by inserting a variable time microwave pulse after the first measurement then reading out with fluorescence imaging.

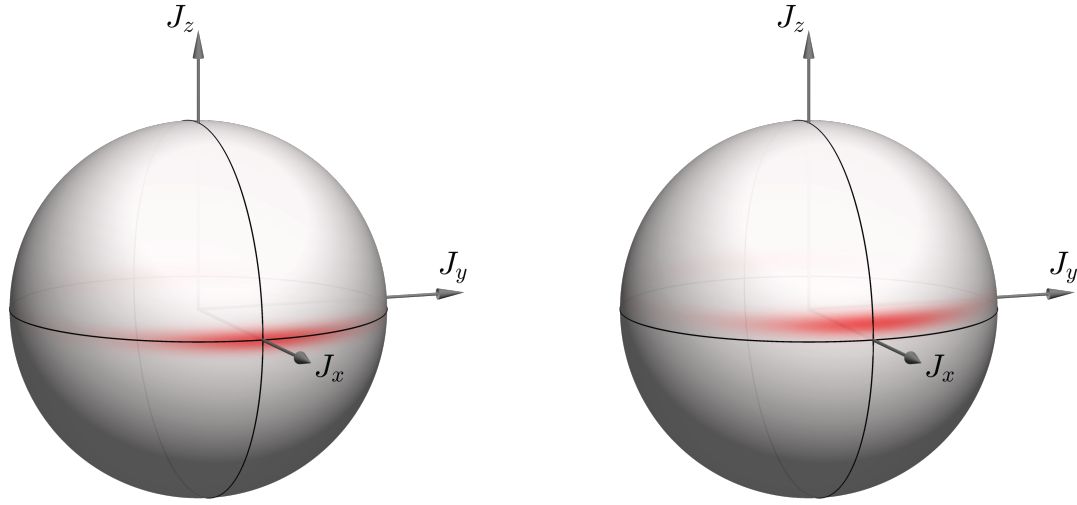


Figure 4.15: Left: 10 dB squeezed state of 30 atoms. Right: The same squeezed state after a small rotation around the  $J_y$  axis.

#### 4.2.2 Squeezed atomic clock demonstration

An atomic clock measurement using squeezed states was demonstrated. The sequence used is shown in Figure 4.18. An illustration of the sequence on the Bloch sphere is shown in Figure 4.19. The measurement precision was limited by high frequency microwave phase noise during the interrogation time. Both inhomogeneous ac-Stark shifts from the lattice and lattice intensity fluctuations were ruled out as dominant noise sources. To get better phase noise performance, we utilized a PhaseMatrix QuickSyn FSW-0010 (these products are now sold by National Instruments) to generate the 6.8 GHz tone in place of the setup shown in § 3.1.3. The PhaseMatrix was stabilized by a 10 MHz OscilloQuartz oscillator. Nevertheless, the microwave local oscillator was still the limiting factor. We reduced the atom number to  $1 \times 10^5$  to demonstrate below shot noise performance. With this reduced atom number and relatively short interrogation time of 228  $\mu$ s we demonstrated an atomic clock operating at 10.5(3) dB below shot noise. In principle, high-frequency local oscillator noise can be circumvented using interleaved clocks [111], in which case the squeezed states can be fully utilized using adaptive measurements [112]. In this experiment, the short interrogation time

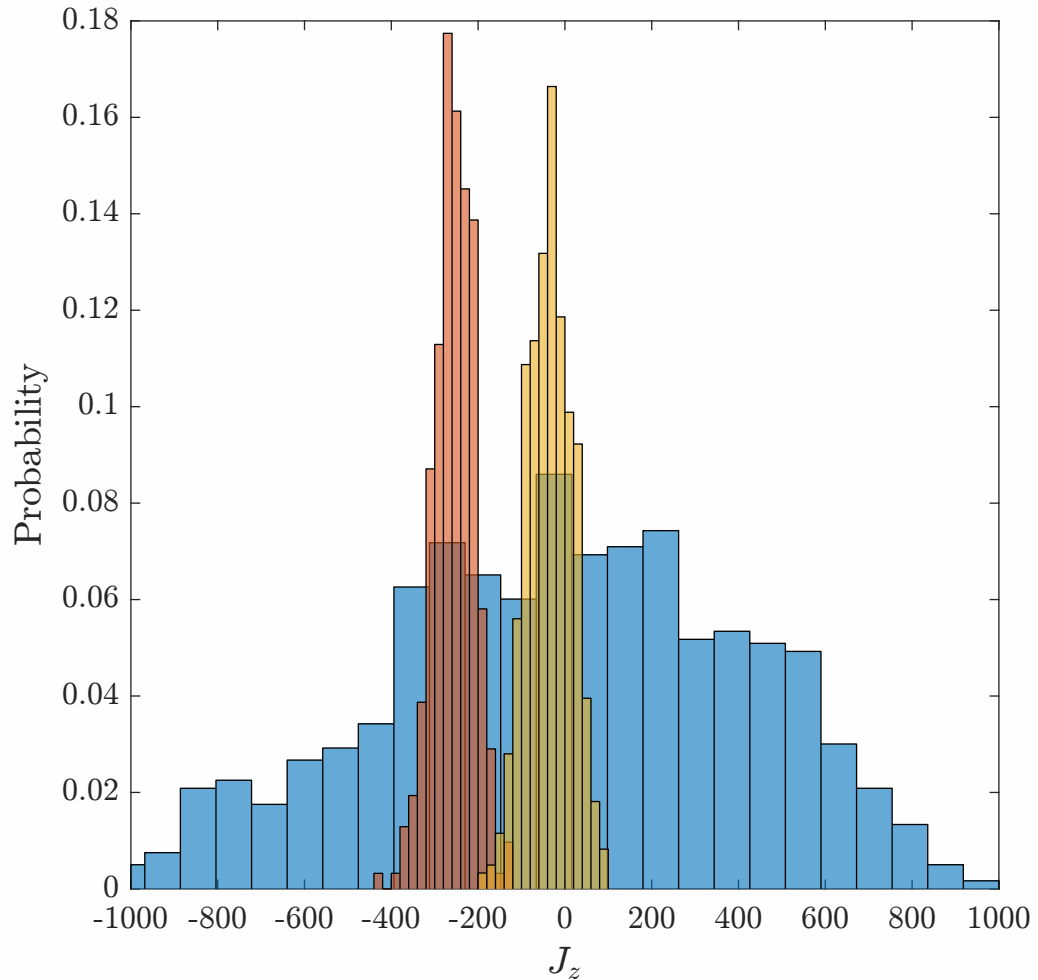


Figure 4.16: The figure shows two squeezed state distributions, one (yellow) rotated by  $660 \mu\text{rad}$  relative to the other (red). The  $x$ -axis is here the difference in  $J_z$  between the two measurements. The squeezed state distributions are overlaid on a coherent state distribution (blue). All measurements were done using  $6.5 \times 10^5$  atoms.

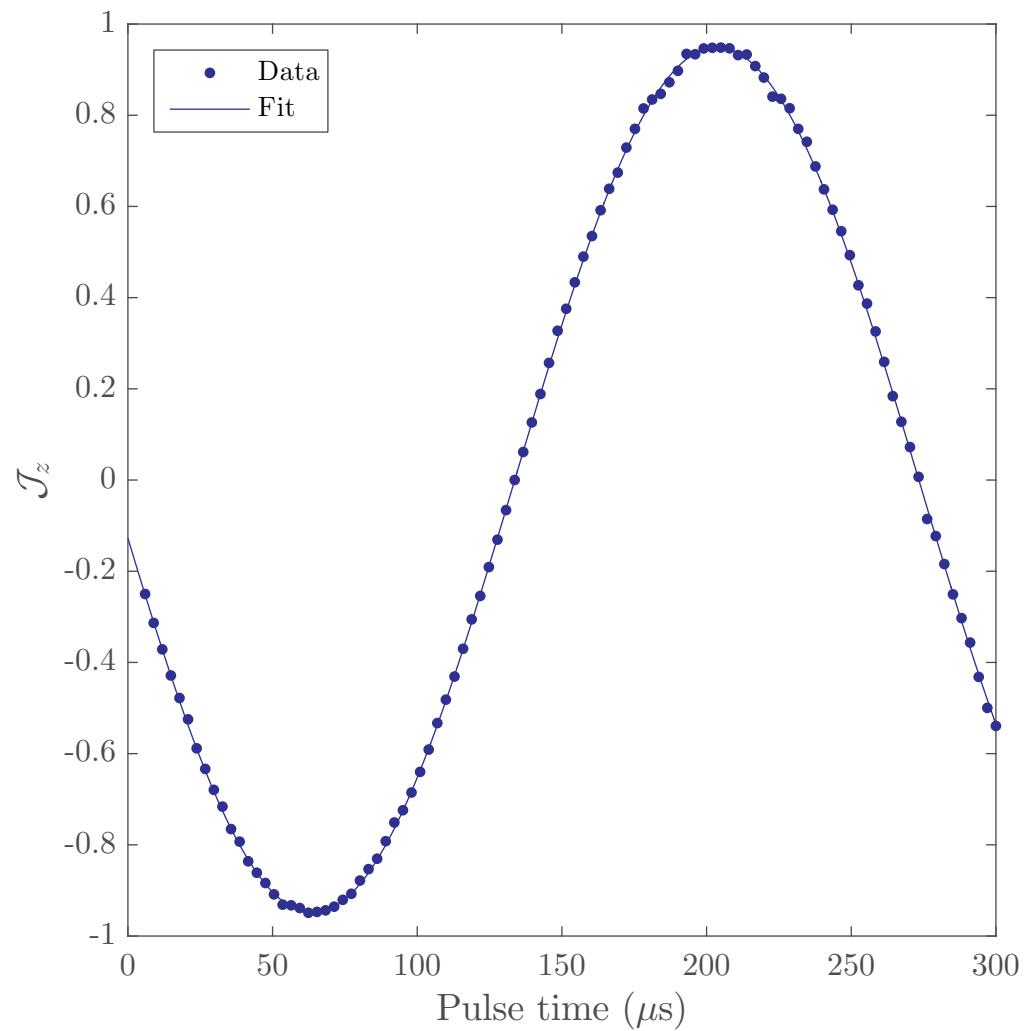


Figure 4.17: The figure shows full-fringe Rabi oscillations by a squeezed state of  $6.5 \times 10^5$  atoms with a sinusoidal fit. The contrast is 96 %. The squeezed state was prepared using a  $0.75\pi$ -strength measurement.

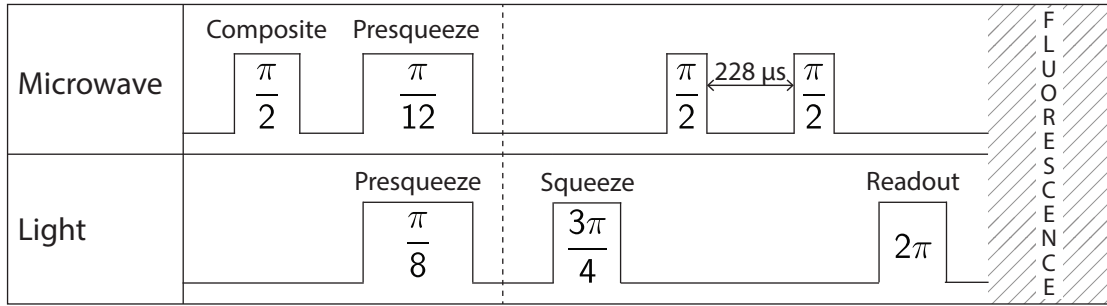


Figure 4.18: The figure shows the sequence used for the clock example. Here the interrogation time is  $228 \mu s$ . We use an imbalanced measurement strength in order to maximize coherence during the clock measurement. The accumulated phase during the interrogation time is turned into a population difference before the population difference is read out with the cavity. The time axis is not to scale.

was chosen to demonstrate the largest quantum enhancement. For the performance at higher interrogation times, see Figure 4.21.

## 4.3 Free-space release and entanglement

### 4.3.1 Inhomogeneity analysis for free-space release

As previously discussed in § 2.3.4, despite the commensurate optical lattice and cavity probe beam, there are still residual inhomogeneities in the cavity. While the fluorescence measurement is made in a different basis than the cavity, this effect is small compared to the limitations imposed by thermal motion of the atoms in the cavity. The thermal motion limits how much of the squeezing enhancement can be recovered when making the first measurement with the cavity and the second with fluorescence imaging. To evaluate the effect of thermal motion, consider that the atom-cavity coupling of an individual atom depends on the transverse position of the atom in the probe beam (the longitudinal motion is averaged out over the  $200 \mu s$  cavity measurement). The fluorescence imaging would see no such effect. Hence there will be an additional noise entering from the statistical fluctuations of the initial phase-space distribution of the

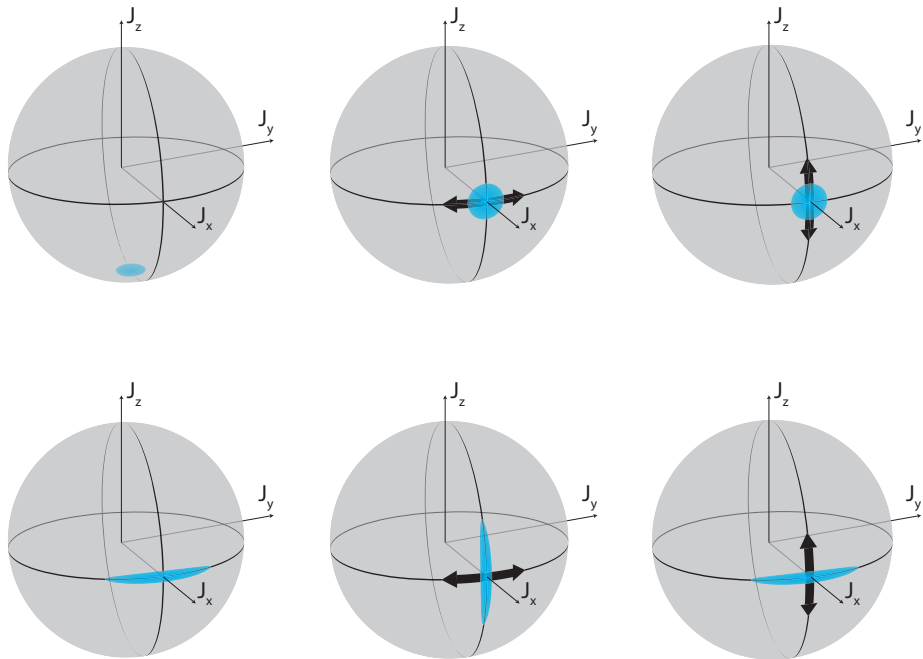


Figure 4.19: Visualization of a coherent state clock sequence and a squeezed state clock sequence. For a sequence using coherent states, the sequence starts with bringing the atoms from  $\langle J_z \rangle = -N/2$  to  $\langle J_z \rangle = 0$  using a microwave drive. This starts the phase accumulation if there is any difference between the microwave frequency and  $\omega_{\text{HF}}$ . The second microwave rotation turns this phase difference into a population difference before readout. For the squeezed state, we start with a number-squeezed state at  $\langle J_z \rangle = 0$  then rotate the state into a phase-squeezed state. After the interrogation time, the second microwave rotation again turns the accumulated phase into a population difference.

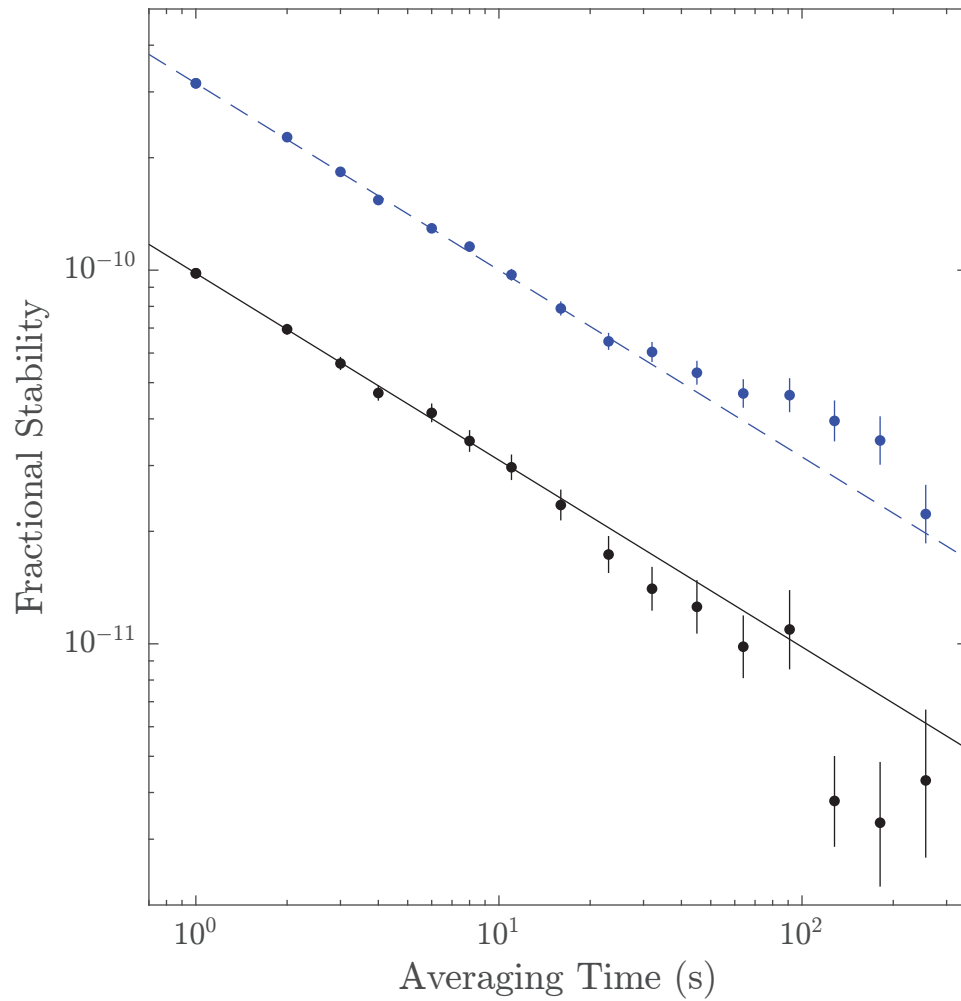


Figure 4.20: Plot of Allan deviation (a measure of clock stability) for a squeezed atomic clock using  $1 \times 10^5$  atoms, 228  $\mu$ s interrogation time and 1 Hz repetition rate (filled circles). The dashed blue line shows the theoretical expectation for a coherent state clock. Open circles show the measured CSS noise with the same interrogation time. The solid line is  $9.7 \times 10^{-11} s^{1/2}/\sqrt{\tau}$ , the performance of the squeezed state clock. The Allan deviation was calculated over a 900 s time trace, consisting of 900 data points. Error bars show a 68 % confidence interval.

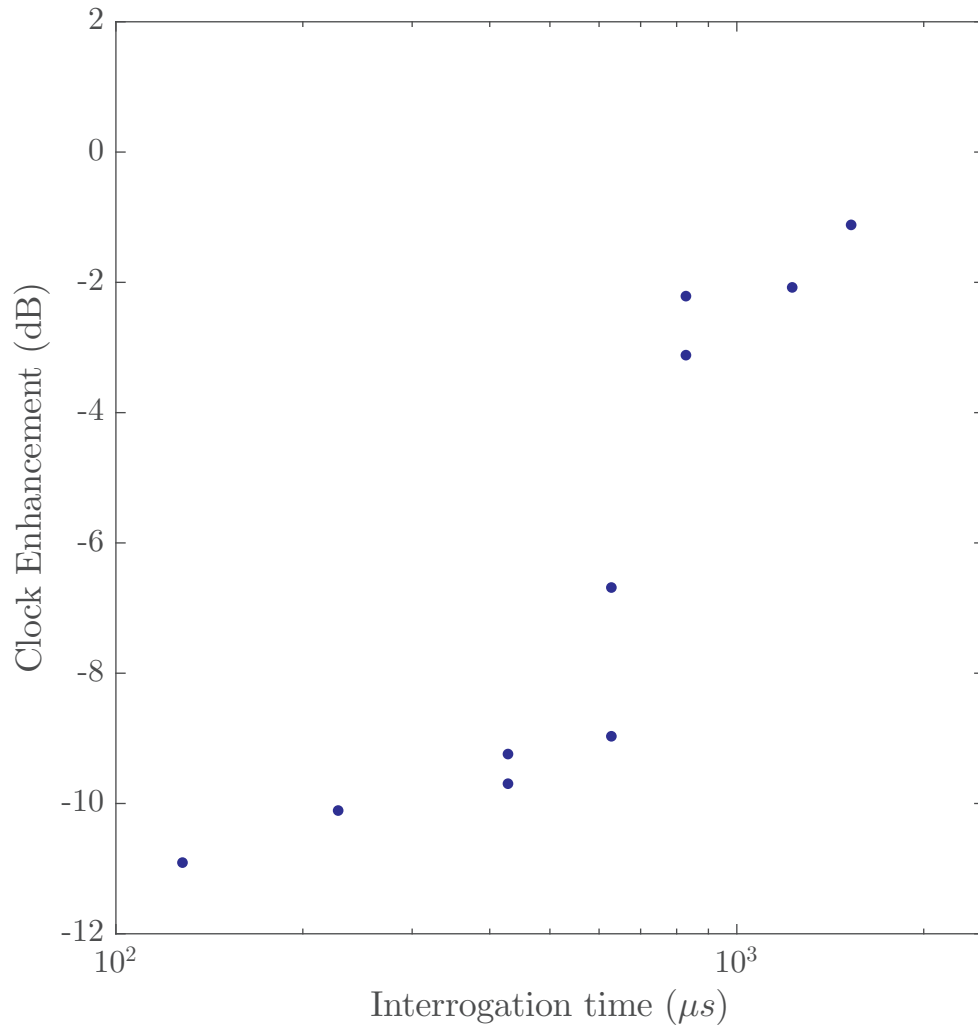


Figure 4.21: The plot shows the measured clock enhancement as a function of interrogation time. The reduced enhancement as a function of increased interrogation time is due to a combination of microwave phase noise and small amounts of spurious, cavity resonant 780 nm light coming from the homodyne setup.

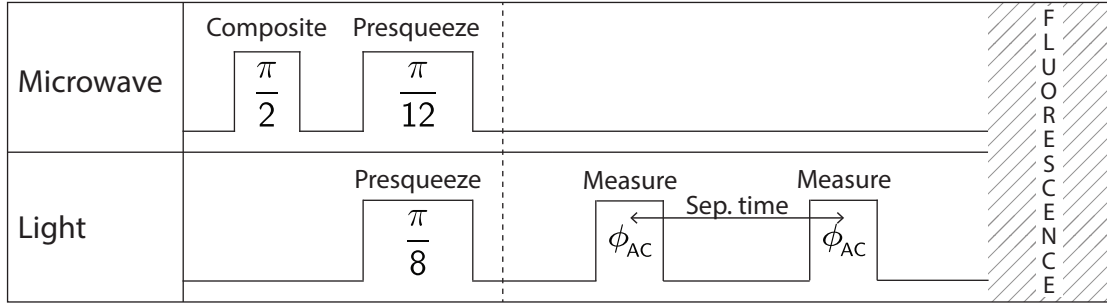


Figure 4.22: The figure shows the sequence used for the cavity inhomogeneity characterization. The separation time is the ‘center-to-center’ separation of the measurement pulses. The measurement strength indicated by  $\phi_{AC}$  was varied for different atom numbers. The time axis is not to scale.

atoms during the cavity measurement.

In order to measure the effect of the thermal motion, we made two cavity measurements with varying separation time and measured the standard deviation of the difference. See Figure 4.22 for details on the experimental sequence. Figure 4.23 shows the measured noise as a function of separation time with a theoretical prediction. The prediction was made using classical trajectory analysis of the atoms in a harmonic trap. Given the initial phase-space distribution of the atoms during the first measurement, the location of the atoms in the second measurement and hence their frequency difference, can be deterministically predicted. However, each time the experiment is repeated, the atoms will start at a different configuration in phase space giving rise to a slightly different cavity frequency difference. We calculate this additional noise assuming a thermal distribution for the atoms. The resulting prediction is

$$\sqrt{\langle \Delta J_z^2 \rangle} = \sqrt{N} (1 + \alpha^2) f(\omega t, \alpha) \quad (4.1)$$

where  $\omega$  is the transverse oscillation frequency,  $\alpha = 2\sigma_r/w_{780}$  with  $\sigma_r$  the transverse size of the atomic cloud,  $w_{780}$  the waist of the probe beam and  $f(\omega t, \alpha)$  is a function containing the time dependence, given by

$$f(\omega t, \alpha) = \sqrt{\frac{1}{1+2\alpha^2} + \frac{1}{1+2\alpha^2 + \alpha^4(1-\cos^4\omega t)} - \frac{2}{1+2\alpha^2 + \alpha^4 \sin^2 \omega t}}. \quad (4.2)$$

For our experiment,  $\alpha^2 = 0.0762$ . The theory curves in Figure 4.23 is this prediction added in quadrature with the baseline. Given the good agreement of the theory with the data, we can make a prediction for the additional noise in a free-space measurement as

$$\sqrt{\langle \Delta J_z^2 \rangle} = \frac{\sqrt{N}\alpha^2}{\sqrt{1+2\alpha^2}} \quad (4.3)$$

giving an additional noise of 17 dB below CSS noise. This noise would be added in quadrature with the squeezed state noise to make a prediction of the squeezing measured in free-space. For the 18.5 dB squeezed state measured previously, we could retrieve at most 14.6 dB in a free-space measurement.

### 4.3.2 Calculation of entanglement depth

Following the procedure outlined in §2.4, the entanglement boundaries for our slightly nonsymmetric squeezed states can be calculated. I choose to use  $\sigma_r = 20 \mu\text{m}$  (corresponding to  $\alpha^2 = 0.130$ ) to compute the boundaries. This is an overestimate of the inhomogeneity in our system. Using these boundaries, we can infer an entanglement depth of 1590(130). The data is plotted in Figure 4.24. The point with the highest metrological gain gives an entanglement depth of 1140(80). This exemplifies that entanglement depth is itself not a direct predictor for metrological improvement.

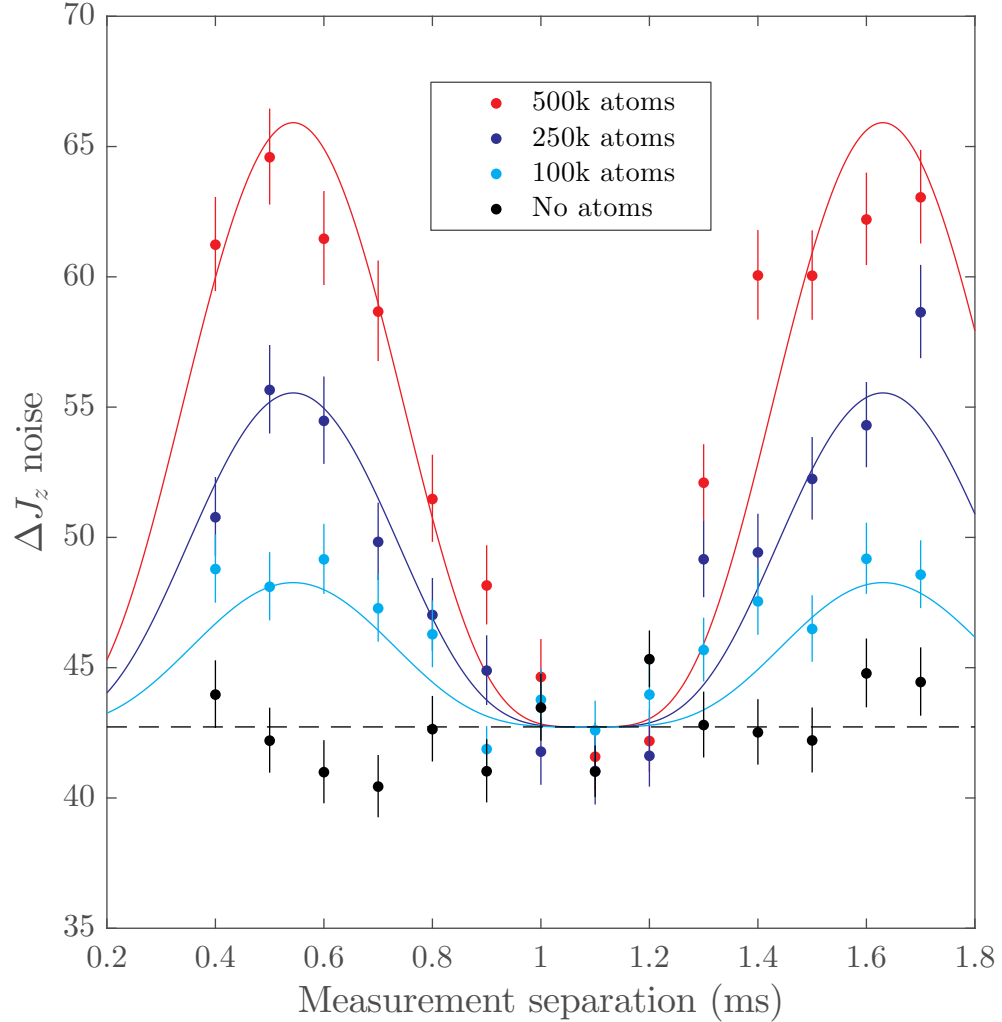


Figure 4.23: The figure shows back-to-back measurement noise as a function of separation time. No matching pattern in mean  $J_z$  difference was found, only the noise is modulated. Measurement strengths were chosen to make the minima identical for each atom number. The solid lines are theory predictions with no free parameters. The black dashed line is the measured r.m.s. error (black point) with no atoms in the cavity. The error bars are 68 % confidence intervals.

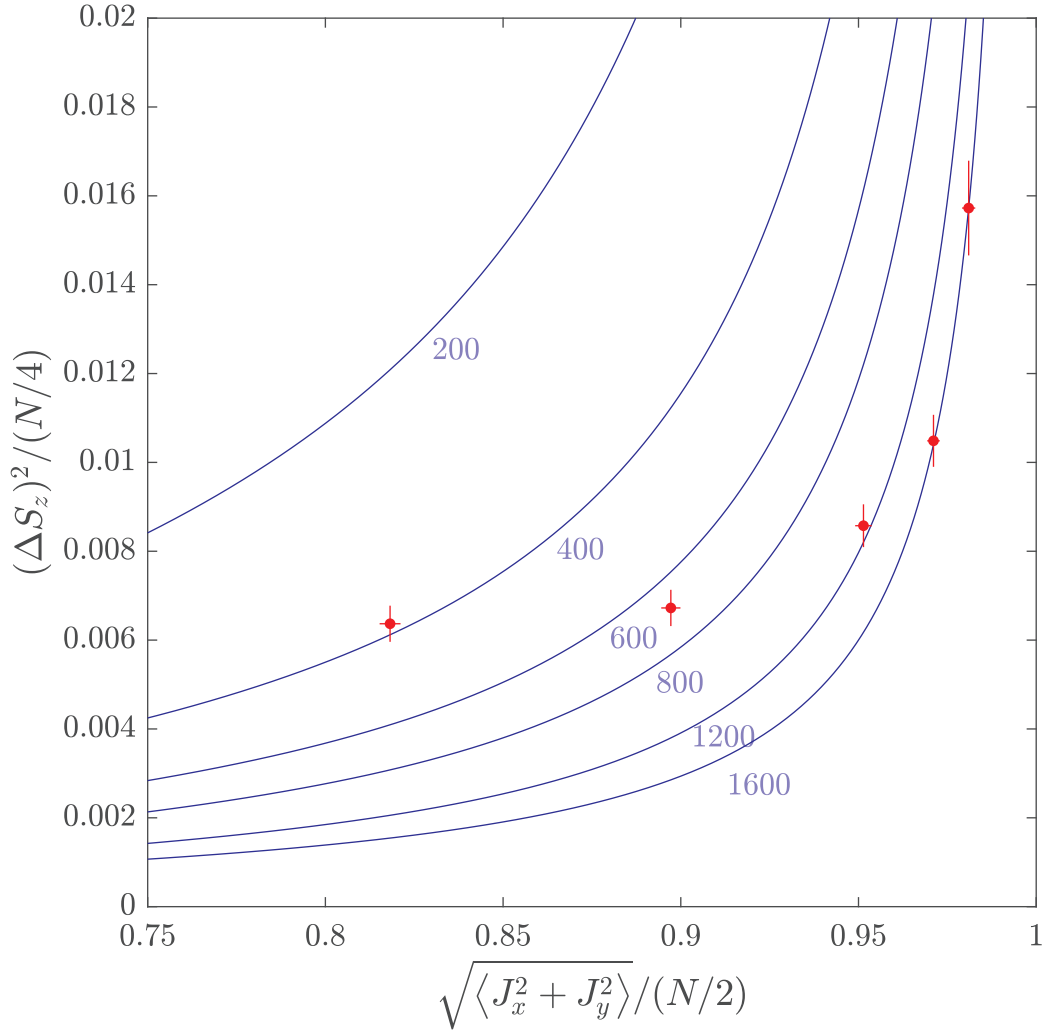


Figure 4.24: The normalized spin noise variance ( $y$ -axis) and the mean-square Bloch vector lengths ( $x$ -axis) are plotted for the  $5 \times 10^5$  atom data set. Note that the measurement strength decreases from left to right. The  $x$ -axis values are conservatively chosen to be the most probable value of the measured Bloch vector length distributions (see Figure 4.12). Note that this is subtly different to the value previously quoted as the coherence, which is the mean of the distribution shown in the referenced figure. Here we use the best estimate of the actual value of  $\sqrt{\langle J_x^2 + J_y^2 \rangle}$ . On the plot, a state below a  $k$ -particle boundary (blue lines labeled with particle numbers) is guaranteed to contain at least groups of  $k$  particles whose quantum states are non-separable. The error bars correspond to the 68% statistical confidence intervals on the quoted values. The third data point the dataset shows the largest metrological improvement.

# Chapter 5

## Bell Correlations in squeezed states

The progress in the control of quantum systems has been accompanied by the development of metrics quantifying quantum correlations in many-body systems [113–116]. A widely adopted measure for systems with large numbers of particles is the depth of entanglement [64, 65, 117] (see also § 2.4). This measure characterizes the minimal number of particles that are mutually entangled in a system. However, not all types of quantum correlations can be classified using the concept of entanglement alone [118]<sup>1</sup>. An example is the Bell-type correlations which are exhibited by quantum systems violating Bell’s inequalities [119].

The detection of Bell correlations is of fundamental interest as a different means of characterizing correlations in many-body states. There have also been suggested practical uses of Bell correlations in quantum information science [120], such as quantum key distribution [121–123] or randomness generation [124, 125]. Recent experiments have shown large spatial separation of quantum superpositions of atomic wavepackets [126]. Combining the ideas of spin squeezing with spatially separated superpositions, the Bell correlations discussed in this Chapter could perhaps be used to test quantum mechanics in new ways.

Demonstrating nonlocal Bell correlations was restricted to small systems where

---

<sup>1</sup>A set of examples is displayed in the Werner states, which are mixed states defined by the density matrix  $\rho = p |\phi_+\rangle\langle\phi_+| + (1 - p)I/4$ . Here,  $|\phi_+\rangle = \frac{1}{\sqrt{2}}(|\uparrow\uparrow\rangle + |\downarrow\downarrow\rangle)$  is a Bell state and the identity matrix  $I$  represents a maximally mixed state. For  $1/3 < p < 1/2$  these states are entangled but do not violate any Bell inequalities. For more details see [118]

the individual components of a composite quantum system can be measured directly. Bell correlations have been shown with photons [127–130], ions [131], atoms [132], solid state spins [133] and NV centers [134]. To extend the investigation of Bell correlations to larger systems, a new framework was developed in [120] that enables observation of Bell correlations without accessing individual components of a system. This framework provides a method to witness whether a quantum many-body system features nonlocality, as evidenced by Bell correlations. The method was employed in [35] with measurements that access only the collective observables of a Bose-Einstein condensate of 480  $^{87}\text{Rb}$  atoms to demonstrate Bell correlations with a statistical significance of 3.8 standard deviations. In this Chapter, I show Bell correlations in spin-squeezed states in a thermal ensemble of  $5 \times 10^5$   $^{87}\text{Rb}$  atoms at  $25\,\mu\text{K}$  which are statistically significant to 124 standard deviations. While this result establishes the existence of Bell correlations, it cannot be used to perform loophole free tests of Bell’s inequalities, as the measurement duration is longer than the time of flight for light across the sample (the no-communication loophole [118]).

This Chapter has been submitted for publication.

## 5.1 Witnesses of Bell correlations

The most commonly used Bell inequality for two particles is the Clauser-Horne-Shimony-Holt (CHSH) inequality. The experiment considered in this inequality is one where two observers measure two spin-1/2 particles on axes **a** and **b** respectively. We now define  $N_{\uparrow\downarrow}$  as the number of outcomes where the measurement of particle 1 on axis **a** finds  $\uparrow$  and the measurement of particle 2 on axis **b** finds  $\downarrow$ .  $N_{\uparrow\uparrow}$ ,  $N_{\downarrow\uparrow}$ , and  $N_{\downarrow\downarrow}$  are defined analogously. We can then define experimental correlations between the two spin-1/2 particles as

$$C_e(\mathbf{a}, \mathbf{b}) = \frac{N_{\uparrow\uparrow} + N_{\downarrow\downarrow} - N_{\downarrow\uparrow} - N_{\uparrow\downarrow}}{N_{\uparrow\uparrow} + N_{\downarrow\downarrow} + N_{\downarrow\uparrow} + N_{\uparrow\downarrow}} \quad (5.1)$$

when the two observers measure on axes **a** and **b**. The CHSH inequality is then

$$C_e(\mathbf{a}, \mathbf{b}) + C_e(\mathbf{a}, \mathbf{b}') + C_e(\mathbf{a}', \mathbf{b}) - C_e(\mathbf{a}', \mathbf{b}') \leq 2. \quad (5.2)$$

This inequality is satisfied in local hidden variable theories of physics. This is a class of theories that assume locality, i.e. no interactions travel faster than the speed of light, and realism, meaning that all observables are determined prior to measurement. A violation of the inequality shows that quantum physics violate either locality or realism. In this chapter, I will take Bell correlations to mean correlations strong enough to violate this assumption of local realism.

While the CHSH inequality shown above is strict—no two-particle system that obey the inequality contain Bell correlations and all two-particle systems that violate it do—the witness functions used for many-body systems are not strict in this sense. A witness is a metric that guarantees Bell correlations if fulfilled, but does not necessarily exclude the possibility of Bell correlations in states that do not satisfy the witness inequality. In this section, I will show two different witnesses of Bell correlations. The witness functions shown here are not meant to do tests of local realism, but instead to characterize the correlations shown in the spin-squeezed states treated here.

We can model the atomic ensemble as a system of  $N$  spin-1/2 particles (see § 2.1.1). We again utilize the clock states of  $^{87}\text{Rb}$  and define  $|F = 2, m_F = 0\rangle \equiv |\uparrow\rangle$  and  $|F = 1, m_F = 0\rangle \equiv |\downarrow\rangle$  as our pseudo-spin states. For a measurement of the  $i$ th spin on a given axis  $\mathbf{m}$  only two measurement outcomes are possible,  $j_{\mathbf{m}}^{(i)} = \pm 1/2$ . Considering two possible axis choices, defined by the unit vectors  $\mathbf{m}$  and  $\mathbf{n}$ , the quantities relevant for constructing a Bell inequality are the expectation values  $\langle j_{\mathbf{m}}^{(i)} \rangle$ , and the correlations  $\langle j_{\mathbf{m}}^{(i)} j_{\mathbf{m}}^{(k)} \rangle$ ,  $\langle j_{\mathbf{m}}^{(i)} j_{\mathbf{n}}^{(k)} \rangle$ ,  $\langle j_{\mathbf{n}}^{(i)} j_{\mathbf{n}}^{(k)} \rangle$ . Simple algebraic combinations of these one- and two-body correlators, such as,  $\mathcal{S}_{\mathbf{m}} = 2 \sum_{i=1}^N \langle j_{\mathbf{m}}^{(i)} \rangle$  and  $\mathcal{S}_{\mathbf{mn}} = 4 \sum_{i,k=1, i \neq k}^N \langle j_{\mathbf{m}}^{(i)} j_{\mathbf{n}}^{(k)} \rangle$  lead to a Bell inequality under the assumption of permutation symmetry of the spins in the system [120]:

$$2\mathcal{S}_{\mathbf{m}} + \mathcal{S}_{\mathbf{mm}}/2 + \mathcal{S}_{\mathbf{nm}} + \mathcal{S}_{\mathbf{nn}}/2 + 2N \geq 0. \quad (5.3)$$

A violation of this inequality is a witness for Bell correlations between the spins in the system. Since the inequality can be written in terms of the components of

the collective spin vector  $\mathbf{J} \equiv \sum_{i=1}^N \mathbf{j}^{(i)}$  where  $\mathbf{j}^{(i)} = [j_x^{(i)}, j_y^{(i)}, j_z^{(i)}]$ , its violation can be probed with measurements of these collective observables alone [35, 135]. This is analogous to the widely adopted entanglement depth measure for characterizing entanglement in systems with large numbers of particles [64, 65, 117], which makes an inference on the size of entangled clusters from measurements of collective observables. Note that these kinds of inferences require repeated observations of identically prepared states of the system.

A particular class of collective states that can violate Equation 5.3 are spin-squeezed states [14]. For a symmetric collective state of  $N$  spins, assuming a mean polarization along the  $x$ -direction, the uncertainty of two orthogonal components of  $\mathbf{J}$  is limited by the relation  $\Delta J_z \times \Delta J_y \geq N/4$ . Spins that are each independently polarized along the  $x$ -direction comprise a coherent spin state (CSS), an unentangled minimum uncertainty state where  $\Delta J_z = \Delta J_y = \sqrt{N}/2$  define the CSS noise. Spin-squeezing redistributes the uncertainty from one conjugate variable to the other, generating entanglement between the spins in the process. As a consequence of the uncertainty principle, reduction in uncertainty in one conjugate variable (squeezing) comes at the expense of a corresponding increase in the uncertainty for the other conjugate variable (antisqueezing). As I will demonstrate, for sufficient amounts of squeezing, the squeezed states may also contain Bell correlations.

Choosing a specific set of measurement axes determined by two unit vectors  $\mathbf{z}$  and  $\mathbf{n}$  (Figure 5.1), the witness function can be expressed in terms of the expectation values of the normalized collective spin operators  $\mathcal{J}_{1,\mathbf{n}} \equiv \langle 2J_{\mathbf{n}}/N \rangle$  and  $\mathcal{J}_{2,\mathbf{z}} \equiv \langle 4J_{\mathbf{z}}^2/N \rangle$ , where  $J_{\mathbf{z}} \equiv \mathbf{z} \cdot \mathbf{J}$  and  $J_{\mathbf{n}} \equiv \mathbf{n} \cdot \mathbf{J}$ . The witness inequality then reads [35]

$$\langle W \rangle = -|\mathcal{J}_{1,\mathbf{n}}| + (\mathbf{z} \cdot \mathbf{n})^2 \mathcal{J}_{2,\mathbf{z}} + 1 - (\mathbf{z} \cdot \mathbf{n})^2 \geq 0 \quad (5.4)$$

In this expression, the total particle number  $N$  inside the expectation values is allowed to be a fluctuating random variable, which in our experiment has a 3% standard deviation from one realization to the next. The first term can be measured by rotating the collective spin state, which amounts to changing the angle between  $\mathbf{z}$  and  $\mathbf{n}$ .  $\mathcal{J}_{1,\mathbf{n}}$  can then be found by measuring the projection of the state on the  $z$ -direction after

the rotation. The second term, when  $\langle J_z \rangle = 0$ , is simply proportional to the variance of  $J_{\mathbf{z}}$  normalized to the CSS noise. Equation 5.4 is the first criterion that we will use to demonstrate Bell correlations. From Equation 5.4 it follows that the inequality

$$\mathcal{J}_{2,\mathbf{z}} < \frac{1}{2} \left[ 1 - (1 - \mathcal{J}_{1,\mathbf{x}}^2)^{1/2} \right] \quad (5.5)$$

also guarantees Bell correlations (a full derivation can be found in the supplementary material of [35]). Here, assuming a squeezed state with  $\langle J_z \rangle = 0$ , the quantity  $\mathcal{J}_{1,\mathbf{x}}$  is simply the coherence of the state. This second criterion is more robust to experimental noise [35] and it is with this criterion we get the most statistically significant violation. Similarly to the entanglement depth criterion the Bell violation witness function is fully parametrized by the coherence (the length of the Bloch vector) and the amount of squeezing in the state [64, 65].

## 5.2 Experimental demonstration of Bell correlations

The squeezed states utilized for demonstrating Bell correlations are prepared utilizing QND measurements as described in Chapter 4. The dual wavelength cavity enabling uniform coupling of the atoms to the probe is essential for satisfying the permutation symmetry assumption implicit in the derivation of Equation 5.3. Nevertheless, any experimental preparation of collective states has a residual level of departure from perfect permutation symmetry for the correlators. In our setup, although small, we expect the  $\sim 5 \times 10^{-3}$  fractional variance in the atom-probe coupling to determine the finite level of departure from perfect permutation symmetry in the prepared states. Assuming a smooth dependence of the Bell violation boundaries on the deviations from perfect symmetry, which has explicitly been shown for the case of entanglement depth boundaries (see §2.4) [66], we will proceed using the above inequalities.

For the purposes of showing Bell correlations, we seek to measure the symmetric collective observable  $J_{\mathbf{z}} = \sum_{i=1}^N j_z^{(i)}$ . A cavity where each atom is identically coupled to the probe mode would measure this observable. However, the residual inhomogeneity

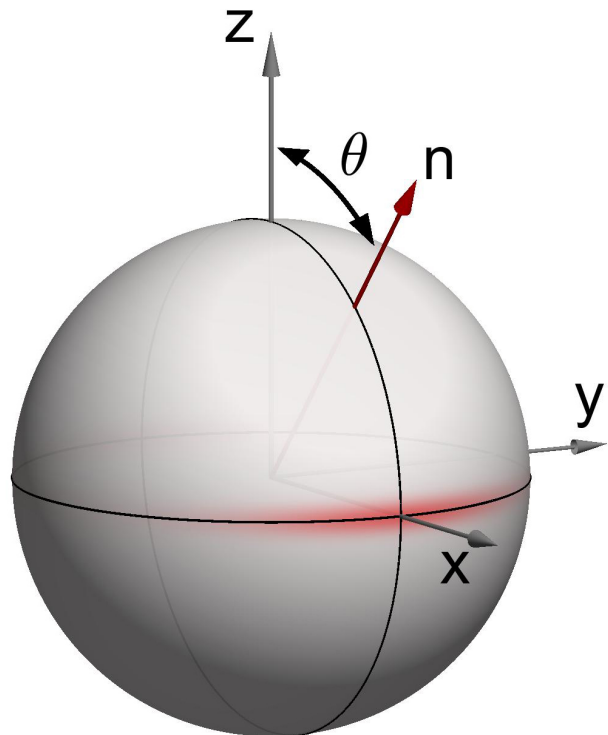


Figure 5.1: Illustration of a squeezed spin state. An example Wigner distribution of a 10 dB squeezed state with 30 atoms, polarized along the  $x$ -axis. Squeezing is along the  $z$ -direction, antisqueezing is along the  $y$ -direction. Also shown is the axis  $\mathbf{n}$  used to calculate the Bell witness in Equation 5.4.

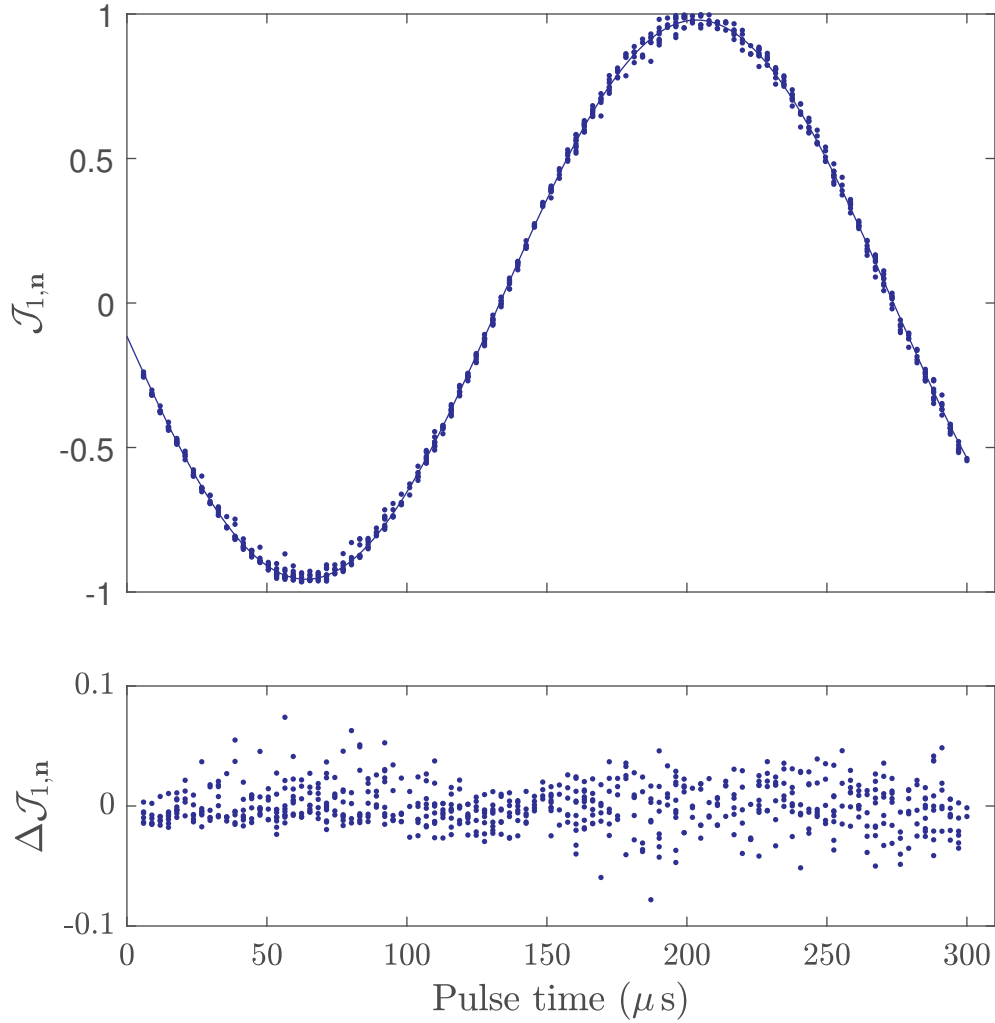


Figure 5.2: Rabi oscillations of squeezed states of  $6.5 \times 10^5$  atoms. Upper panel:  $\mathcal{J}_{1,n}$  as a function of the microwave pulse time. The fit is sinusoidal and is used to extract the angle for the witness function in Figure 5.3. The fit shows a contrast of  $94.9(1)\%$ . Lower panel: Residuals from subtracting the sine fit from the data points. The increased noise at the  $\mathcal{J}_{1,n} \approx \pm 1$  points is due to antisqueezing. While fluorescence detection noise dominates at low pulse times, microwave amplitude noise takes over at larger times. Pulse times below  $5\text{ }\mu\text{s}$  were not achievable due to control system limitations.

due to the finite temperature of the atoms allows us to measure only the collective observable  $S_{\mathbf{z}} = (1/Z) \sum_{i=1}^N (1 - \epsilon_i) j_z^{(i)}$  where  $Z$  is a normalization constant and  $\epsilon_i$  is a small quantity parametrizing the reduction from unity in coupling of atom  $i$  (see § 2.3.4 for more details on the inhomogeneous coupling of this cavity).

We generate up to 20 dB of squeezing following the procedure described in Chapter 4. Following the first measurement generating the squeezing, we can choose to drive Rabi oscillations using microwaves, amounting to rotation of the collective spin state about the  $y$ -axis. This way, a subsequent measurement of  $S_{\mathbf{z}}$  allows us to determine  $S_{\mathbf{n}}$  for any chosen angle  $\theta$  between  $\mathbf{z}$  and  $\mathbf{n}$ . Since the squeezing is conditional on the outcome of the QND measurement, the inferred  $\langle S_z \rangle$  for the prepared squeezed states is different in each realization. In order to show Bell correlations, we therefore choose an axis  $\mathbf{z}'$  at each realization such that the inferred  $\langle S_{\mathbf{z}'} \rangle = 0$ . The shot-to-shot variation in the chosen axis can be accounted for as noise in  $\theta$  in Equation 5.4. For our parameters, this noise is small compared to the noise added by microwave rotation noise.

To relate the measured  $S_{\mathbf{z}}$  observable to the properties of  $J_{\mathbf{z}}$ , we use a conservative procedure based on a model that was verified experimentally (see § 2.3.4 and § 4.3.1). In this model  $\epsilon_i$  depends on the specific position of the atom, and is randomized in each experimental run. The randomization of the position can be modeled as an additive noise that would appear in a measurement of the uniform observable  $J_{\mathbf{z}}$ . In our setup, this additive noise is 16.8(70) dB below the CSS noise. The error on this quantity is estimated from the additive noises found at three different atom numbers (see § 4.3.1). According to this model, the squeezed state utilized for the metrology demonstration in § 4.2.1 for example, which is 18.5 dB squeezed in  $S_{\mathbf{z}}$  is guaranteed to be squeezed by at least 14.5 dB in  $J_{\mathbf{z}}$ . For all Bell correlation data presented below, we calculate  $\mathcal{J}_{2,\mathbf{z}}$  according to this model. The error on this quantity is obtained by adding in quadrature the error in squeezing measurements and the error from the  $J_z$  estimation model.

While we measure the squeezing levels using the cavity probe, the Rabi oscillations needed to determine  $\mathcal{J}_{1,\mathbf{n}}$  are characterized using fluorescence imaging since the cavity does not have the dynamic range to make these measurements. The fluorescence

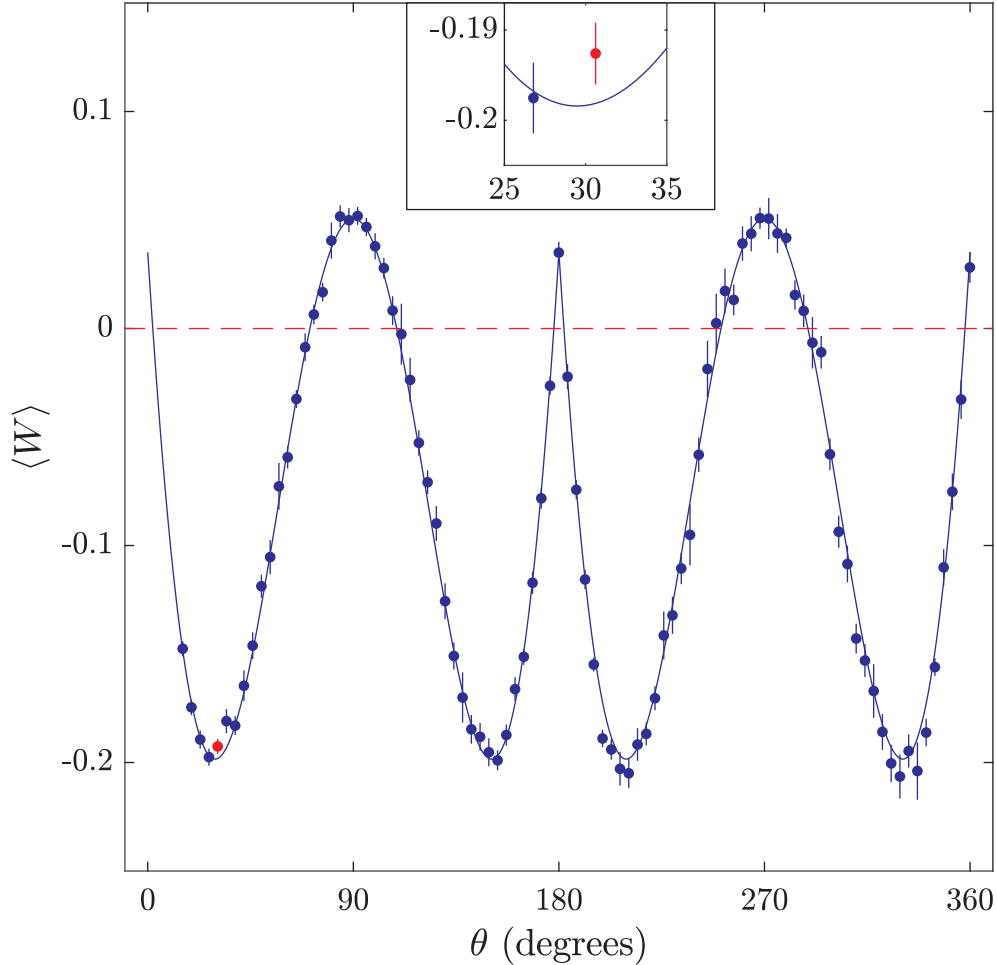


Figure 5.3: The data points show the Bell correlation witness  $\langle W \rangle$  as a function of  $\theta$ . The  $\theta$  values are extracted from the fit in Figure 5.2. The error bars show the combined statistical error from the measured  $\mathcal{J}_{1,n}$  and the total error in the estimated  $\mathcal{J}_{2,z}$  value. Points below the dashed red line show violation of the inequality in Equation 5.4. The highest violation is from the point shown in red (also in inset) which is 56 standard deviations from the boundary. The solid blue line is calculated from the contrast of the fit to the Rabi fringe and the squeezing level. For a maximally squeezed state with 100% coherence, the minimum of the witness function would approach -0.25.

imaging is done by first releasing the atoms from the optical lattice then pushing the atoms in the  $|\uparrow\rangle$  state with a laser resonant with the  $|F=2\rangle \rightarrow |F'=3\rangle$  transition. After a 1.2 ms time of flight the spatially separated states are imaged for 2 ms with resonance fluorescence. The signal from the pushed  $|\uparrow\rangle$  atoms is 20% lower due to lower fluorescence beam intensity at their location. We performed a calibration to correct for this and applied it to the raw data (see §3.1.5). The error in the calibration procedure is insignificant compared to statistical errors for the presented data.

For a data set containing 15.0(70) dB inferred squeezing in  $J_z$ , we plot the observed Rabi oscillations in Figure 5.2. Combining the Rabi oscillation data with the squeezing level, we plot the witness function  $\langle W \rangle$  in Figure 5.3. All data points below the dashed line indicate nonlocal correlations in the prepared squeezed states. The dominant contribution to the error bars is the noise of the microwave rotation which amounts to an uncertainty in the angle  $\theta$  between  $\mathbf{z}$  and  $\mathbf{n}$ . This leads to increasing uncertainties with increasing microwave drive time.

In Figure 5.4 the data is plotted with the Bell correlation boundary and entanglement depth boundaries on the  $\mathcal{J}_{1,\mathbf{x}}^2$ - $\mathcal{J}_{2,\mathbf{z}}$  plane. Here, the  $\mathcal{J}_{1,\mathbf{x}}$  values of the states were determined by first performing the squeezing measurement, then making a microwave  $\pi/2$ -rotation about the y-axis to turn  $J_{\mathbf{x}}$  into  $J_{\mathbf{z}}$ . The observable  $J_{\mathbf{z}}$  was then measured using fluorescence imaging in 200 repetitions. For error estimation, the fluorescence calibration errors as well as the statistical errors are taken into account. In Figure 5.4, I also show a dataset that was unconditionally squeezed by 8.5 dB. These states were prepared using a similar method to that in [46]. The best conditionally squeezed data is 124 standard deviations from the boundary; the corresponding number for unconditional squeezing is 33. The largest entanglement depth obtained in this analysis is approximately 500. However, using a more optimal entanglement depth criterion tailored for nonsymmetric probing [66], the best entanglement depth becomes 1590(130) as described in §4.3.2.

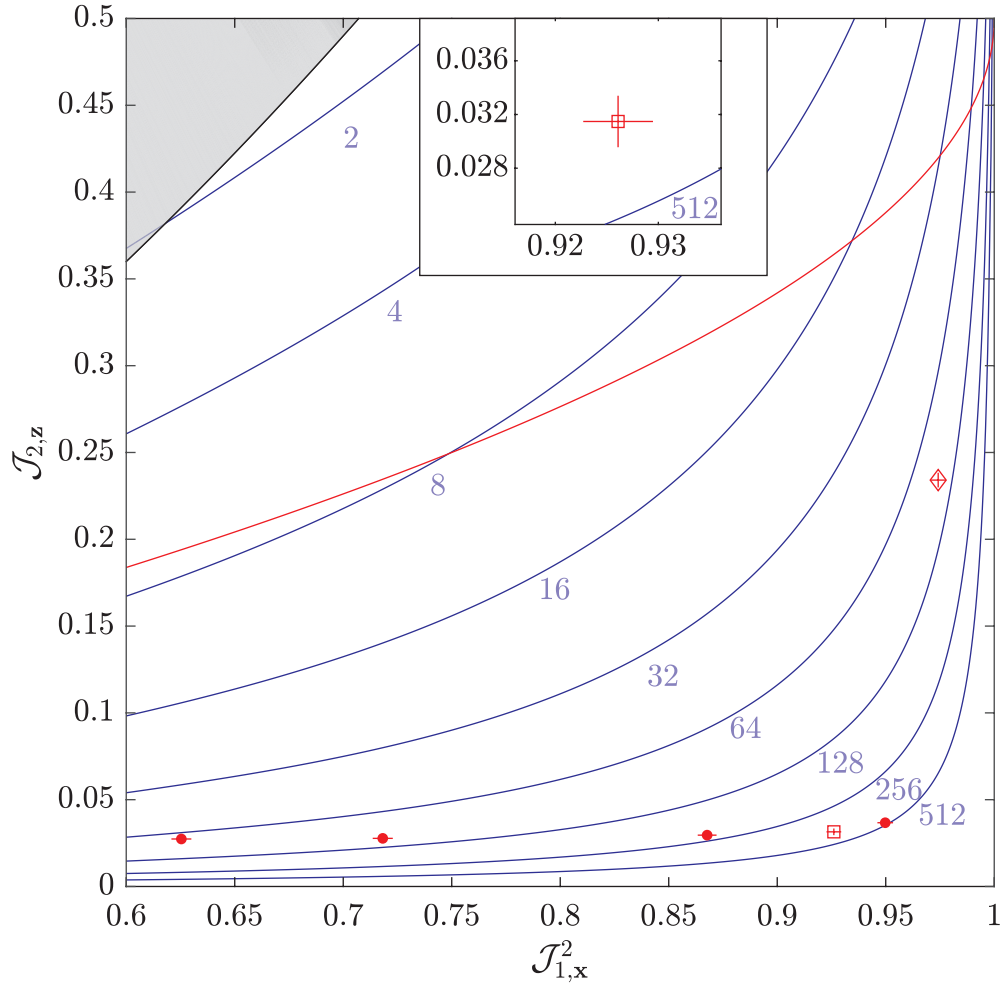


Figure 5.4: Entanglement depth and Bell correlation boundaries. Red line shows the Bell violation boundary according to Equation 5.5. Blue lines show the boundary for  $k = 2^n$  entanglement depth for  $n = 1 \dots 9$  (labeled below each line). The gray area bounded by the black line contain unentangled states according to the Wineland criterion for entanglement. The data points, taken with  $5 \times 10^5$  atoms and approximately 450 measurements each, have measurement strengths going from higher on the left to lower on the right. The error bars represent 68% confidence intervals. The open-square data point shows the most statistically significant violation of Bell's inequality (the inset is a zoomed in version of this data point). The open-diamond data point shows the result from a data set of 3286 runs with unconditional squeezing.

### 5.2.1 Conditionally squeezed states in Bell inequalities

The Bell inequality stated in Equation 5.4 utilizes the scaled second moment of  $J_z$  as opposed to its variance, which is the quantity we typically calculate since we generate conditionally squeezed states. From one realization of squeezing to the next, the mean  $J_z$  value of the prepared squeezed states can vary as much as the CSS noise, since this is the width of  $J_z$  distribution prior to the first measurement. For the  $i$ th realization of the squeezing, we infer a mean  $J_z$  value following the first measurement. Instead of choosing the  $\mathbf{z}$  unit vector for Equation 5.4 at each realization, we choose a specific unit vector  $\mathbf{z}'_i$  that differs slightly at each realization. This unit vector is chosen such that  $\langle J_{\mathbf{z}'_i} \rangle = 0$ . Since the angle between  $\mathbf{z}$  and  $\mathbf{z}'_i$  is of order 1 mrad rad, the squeezing level associated with this new direction remains essentially the same, i.e.,  $\text{Var } J_{\mathbf{z}'_i} \sim \text{Var } J_z$ . This procedure allows us to use the variance associated with the squeezed states instead of the second moment. However, choosing an arbitrary axis contributes to the uncertainty in the angle  $\theta$  between the two unit vectors that go into Equation 5.4, since the other axis which we called  $\mathbf{n}$  is fixed. To account for this we add  $\delta\theta = 1/\sqrt{N}$  to our error budget for the data plotted in Figure 5.3. A similar argument can be applied to the violations shown according to 5.5, but here  $\delta\theta$  is much smaller than the uncertainty due to the microwave rotation to the top of the Bloch sphere to measure the coherence. No such considerations apply for the unconditionally squeezed case which was also shown in Figure 5.4, where we directly measure the squeezed second moment of  $J_z$ .

## 5.3 Error calculations and statistical significance

In order to characterize the statistical significance of our results, we compute the minimum number of standard deviations the point is from the Bell violation boundary. This amounts to minimizing  $r$ , defined as

$$r = \left[ \left( \frac{\mathcal{J}_{1,\mathbf{x}} - x_{\text{bell}}}{\Delta \mathcal{J}_{1,\mathbf{x}}} \right)^2 + \left( \frac{\mathcal{J}_{2,\mathbf{z}} - y_{\text{bell}}}{\Delta \mathcal{J}_{2,\mathbf{z}}} \right)^2 \right]^{1/2} \quad (5.6)$$

where  $x_{\text{bell}}$  and  $y_{\text{bell}}$  describe the line that forms the boundary and  $\Delta X$  denotes the empirically determined standard deviation of the quantity  $X$ .  $r$  is then the number of standard deviations from the point on the boundary described by  $(x_{\text{bell}}, y_{\text{bell}})$ . We use Equation 5.5 to describe the boundary such that

$$y_{\text{bell}} = \frac{1}{2} \left( 1 - \sqrt{1 - x_{\text{bell}}^2} \right). \quad (5.7)$$

The variance of the empirical second moment for the unconditional squeezing was computed using the formula

$$\text{Var}(\langle J_z^2 \rangle) = \frac{2(\Delta J_z)^4 + 4\langle J_z \rangle^2 (\Delta J_z)^2}{n} \quad (5.8)$$

where  $n$  is the number of samples. The variance of the empirical second moment for the conditional squeezing was computed using the usual chi-squared distribution for the variance of a sample variance, just as in the rest of the thesis.

To estimate the statistical probability of the reported results being produced without containing Bell correlations, we first assume that  $\mathcal{J}_{1,\mathbf{x}}$  is  $\beta$ -distributed on the interval  $[-1, 1]$  and  $\mathcal{J}_{2,\mathbf{z}}$  is  $\Gamma$ -distributed on the interval  $[0, \infty]$ . The probability density function of these distributions is calculated using the experimentally determined mean and variance. We can then integrate the overlap of their joint probability distribution with the area outside the Bell violation boundary, computing the following integral:

$$p = \int_0^1 dx \int_{y_{\text{bell}}(x)}^{\infty} dy \Gamma(y; \mathcal{J}_{2,\mathbf{z}}, \Delta \mathcal{J}_{2,\mathbf{z}}) \beta(x; \mathcal{J}_{1,\mathbf{x}}, \Delta \mathcal{J}_{1,\mathbf{x}}) \quad (5.9)$$

where  $\Gamma$  and  $\beta$  denote the relevant probability density functions as determined by the mean and standard deviations. The integrals were calculated using the variable precision array package in MATLAB and the results are presented in Table 5.1.

## 5.4 Conclusion

In conclusion we have shown Bell correlations in a large, thermal ensemble of  $^{87}\text{Rb}$  atoms to 124 standard deviations. These Bell correlations measure the amount

Measurement strength ( $\times \pi$ )	$p$	$r$
0.5	$8.6 \times 10^{-740}$	116
0.75	$9.9 \times 10^{-819}$	124
1	$2.1 \times 10^{-681}$	106
1.6	$5.9 \times 10^{-463}$	82
2.05	$3.2 \times 10^{-354}$	68
Unconditional	$2.1 \times 10^{-139}$	34

Table 5.1: The table shows the overlap  $p$  of the probability distributions associated with different data points with the area above the Bell violation boundary. The measurement strength is parametrized in units of  $\pi$  radians of differential ac-Stark shift incurred on the clock states by the measurement pulse.

of nonlocality contained in the state which can be used as a resource in quantum information. Bell correlations in many-body systems might also find applications in tests of quantum mechanics. For tests of quantum mechanics, one would want to spatially separate the atoms in the spin-squeezed states and then perform measurements of the individual degrees of freedom. While this task is challenging experimentally, this work has shown it is possible to generate Bell-correlated states of large atom numbers that could be used in this way.

# Chapter 6

## Quantum phase magnification

Quantum metrology exploits entangled states of particles to improve sensing precision beyond the limit achievable with uncorrelated particles. All previous methods required detection noise levels below the standard quantum limit to realize the benefits of the intrinsic sensitivity provided by squeezed states [23, 30–32, 34, 37–39, 41–44, 136, 137], Dicke states [64, 138, 139] and other states with negative wigner functions [140]. Detection noise has been the bottleneck of performance for quantum metrology. The largest metrological enhancement seen for spin-squeezed atoms used measurement-based techniques [43, 44]. As described in the earlier chapters of the thesis, these methods require extensive engineering. This Chapter shows a widely applicable method for entanglement-enhanced measurements without low-noise detection; it is a generalization of a proposal [63] for approaching the Heisenberg limit without single-particle detection noise. The method was used to perform squeezed-state metrology 8 dB below the standard quantum limit with a detection system that has a noise floor 10 dB above the standard quantum limit.

The main results in this chapter were published in [46].

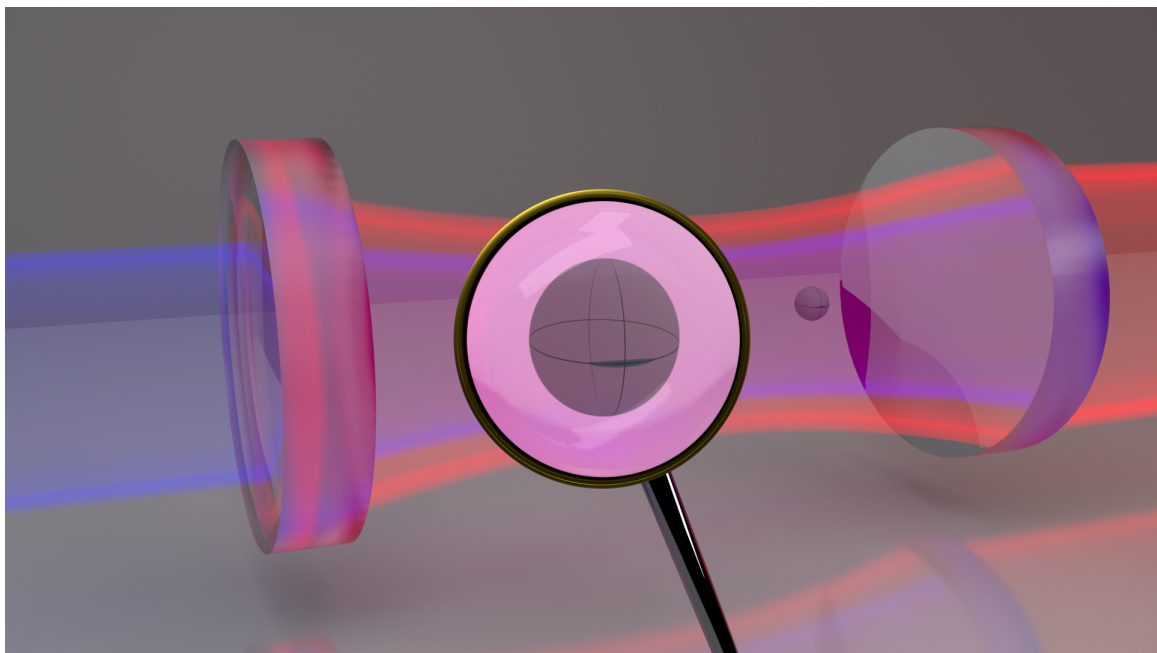


Figure 6.1: Artist rendering of quantum phase magnification. Artist credit: Brannon Klopfer.

## 6.1 Squeezed state generation through collective interactions

To generate squeezed states, we use the same shearing interaction used for magnification (see §2.3.5 for background). The manner in which a state becomes squeezed due to the shearing interaction can be seen in Figure 2.5. In the following, we will again consider states polarized along the  $J_x$ -axis. Starting from a CSS, the Wigner distribution becomes narrower in a particular direction as the shearing is increased. To obtain  $J_z$ -squeezing, a small final microwave rotation about the  $J_x$ -axis needs to be applied. The cavity probe was used to verify faithful production of the squeezed state variance and  $J_z$  mean.

This method for generating squeezed states has previously been used in [136]. The difference here is the combination of a higher cooperativity and larger cavity-light detuning. Light was sent in to the cavity at a detuning of  $\delta_0 = 36 \text{ kHz} \approx 4\kappa$  instead of at  $\delta_0 \approx \kappa/2$  in [136]. The purpose of this larger detuning was to ensure a linear dependence of intracavity photon number on  $J_z$ . Additionally, in this further detuned regime, the measurement backaction on  $J_y$  is reduced at the expense of reduced shearing strength for a given amount of input light. In principle, this makes the interaction more ideal in terms of noise-area preservation for a given target squeezing level, until the point at which the spin-flips due to spontaneous emission become the limiting factor to the achievable squeezing. Although the shearing interaction should be near-area preserving for our range of parameters, as is evident from the generated squeezed states with 8 dB squeezing and 32 dB anti-squeezing, there is apparent area non-preservation. This area non-preservation is a result of statistical ensemble averaging in presence of technical noise, effectively giving rise to mixed states. There are two main contributions. The first contribution is from the technical pulse area noise of the light generating the shearing. The  $J_y$  noise increases with pulse power due to increasing absolute ac-Stark shift precession noise. The second contribution is from the microwave phase noise. The mean  $J_z$  value of the generated squeezed states after the microwave rotation that concludes state preparation is crucially dependent on the location of the rotation axis. For  $5 \times 10^5$  atoms, we observe 10 dB to 15 dB

above CSS noise uncertainty in the rotation axis location due to microwave phase noise. Because of these effects, at low shearing powers we do not observe noise levels below the CSS noise, and at higher levels ( $\phi_{AC} = \pi/8$ ) squeezing saturates around 8 dB.

## 6.2 Basic magnification scheme

To verify correct operation of the magnification scheme we first mapped out the dependencies of the basic magnification scheme shown in Figure 2.5A-B. Here, the  $J_z^2$  interaction maps a population difference ( $J_z$ ) into a phase difference ( $J_y$ ). A  $\pi/2$ -pulse then rotates the phase difference into a population difference for readout. We expect the magnitude of the magnification to follow Equation 2.59. To verify this we used the sequence shown in the bottom of Figure 6.2. The sequences shown in this chapter will detail only the measurement sequence. For more details on the rest of the timing sequence, see §3.1.7. A CSS of  $2 \times 10^5$  atoms was prepared with a  $J_z$  expectation value of  $\pm 200$ . The lower atom number was used such that the CSS noise of the state would be significantly lower than the linewidth of the cavity (at this atom number,  $\Delta_{CSS} \approx \kappa/4$ ). The prepared states were characterized using the cavity probe to verify the correct  $J_z$ -displacement.

We then magnified the states while varying the ac-Stark shift (top of Figure 6.4) or the detuning (bottom of Figure 6.4). The measured magnification was calculated by comparing the initial separation of the centroid of the distributions as measured with the cavity to the separation measured with fluorescence after magnification. To estimate the centroids we take approximately 800 measurements before and after the magnification procedure. We observed that the magnification depends linearly on the ac-Stark shift and is proportional to the inverse of the detuning squared as expected.

In the large M limit, the signal-to-noise ratio (SNR) associated with the two states after magnification approaches the value measured by the cavity (Figure 6.5), set by the intrinsic sensitivity of the quantum state. Here, SNR is defined as the separation between the centroids of the two  $J_z$  distributions divided by the RMS width of their distributions.

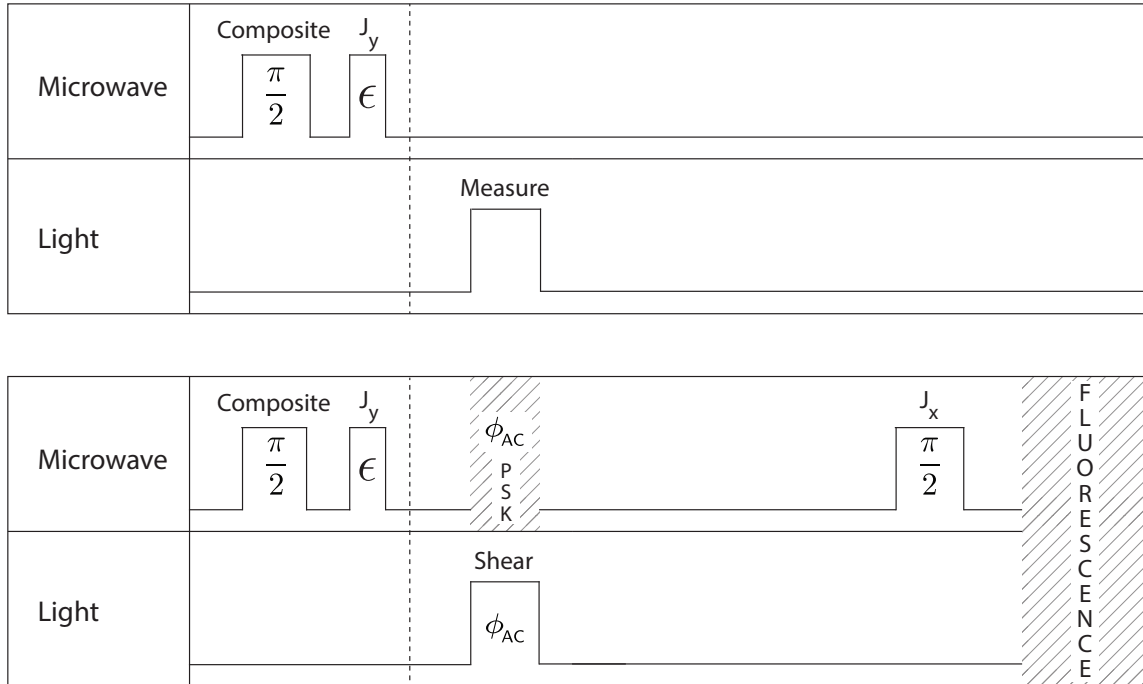


Figure 6.2: Experimental pulse sequences. The sequences are split into two parts with dashed lines; to the left are the state preparations, to the right are the magnification protocols and measurements. The axis of rotation is indicated above each microwave pulse. The pulse areas for light are given in terms of the mean ac-Stark phase shifts induced on the atomic states. **Top:** Preparation of CSSs at  $\langle J_z \rangle = \pm 200$  followed by a measurement of  $J_z$  with the cavity. **Bottom:** Preparation of the same CSSs followed by the basic magnification protocol and fluorescence imaging. The induced ac-Stark phase shift  $\phi_{AC}$  due to the shearing pulse is compensated for by shifting the phase of the microwave oscillator (shaded region with PSK label). The time axes are not to scale.

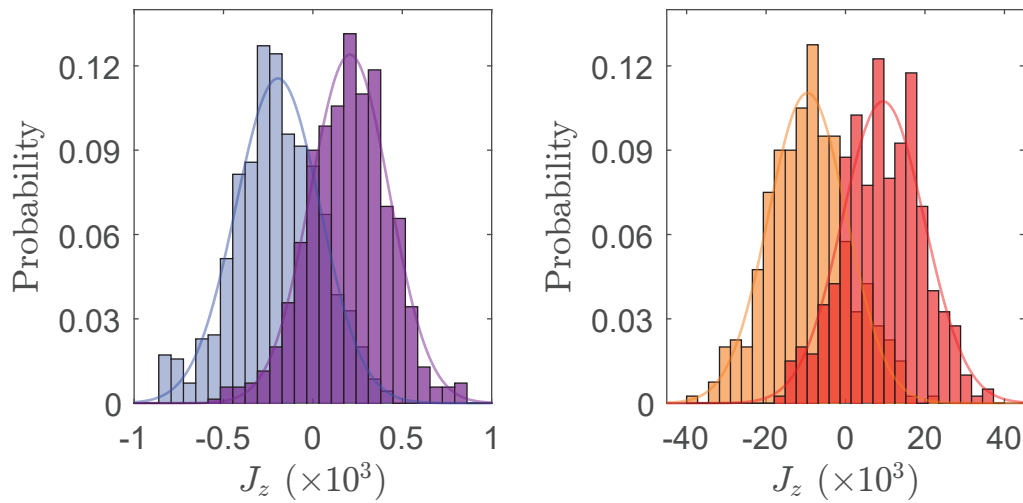


Figure 6.3: Sample distributions (400 samples each) comparing the cavity-based measurements (left) of  $J_z$  with fluorescence imaging-based measurements (right) after a magnification of  $M = 45$ . The two distributions in each plot correspond to different initial states with  $\langle J_z \rangle = \pm 200$  prepared using  $2 \times 10^5$  atoms. Each histogram contains 400 measurements. The fits are Gaussian and have a width agreeing well with the expected (magnified) coherent state noise.

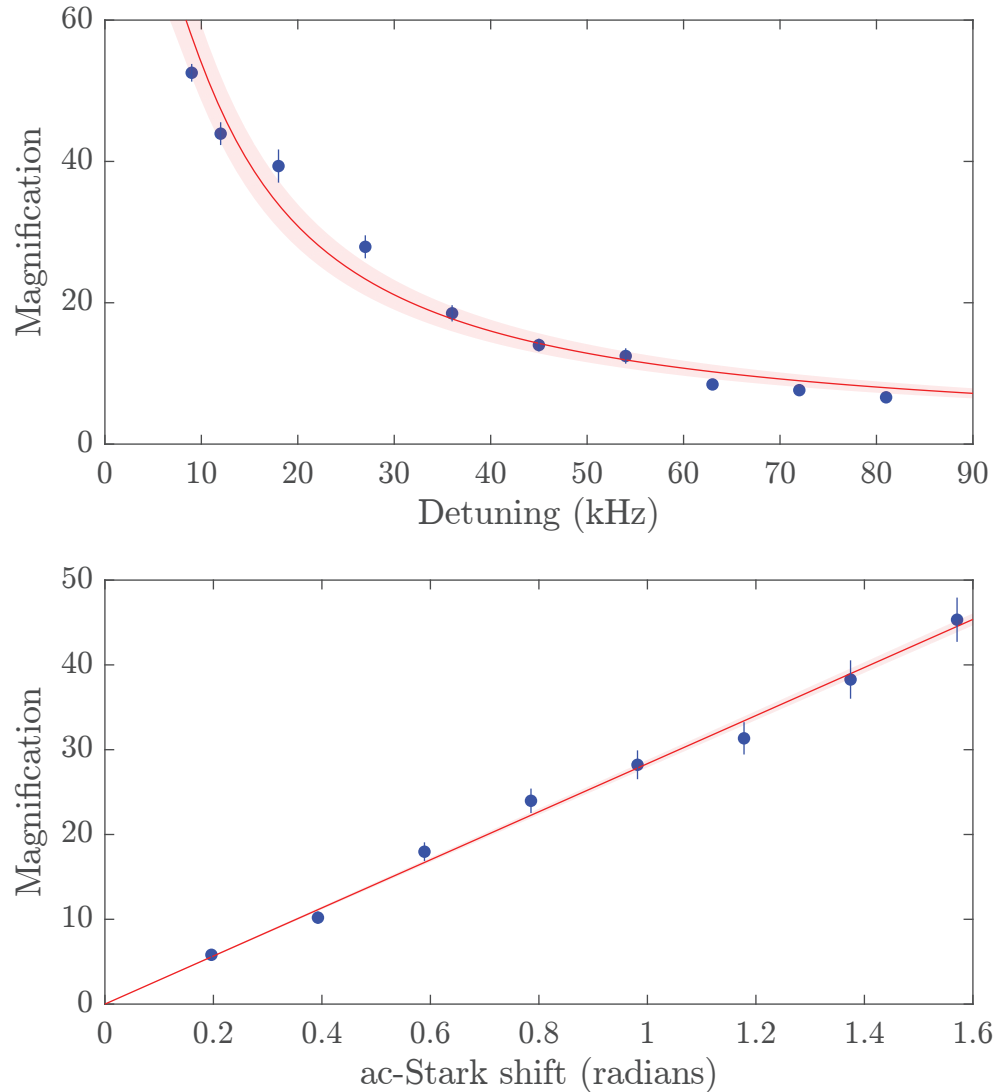


Figure 6.4: Upper: Magnification as a function of the ac-Stark shift incurred by the magnifying pulse with the cavity-light detuning fixed at  $\delta_0 = 36$  kHz. The linear fit agrees with the expected theoretical coefficient to within 10%. Lower: Magnification as a function of the detuning with ac-Stark shift fixed at  $\phi_{AC} = 0.6$  rad. The fit is of Lorentzian form and the coefficients agree with the theoretical expectation to within 10%. The error bars and shaded regions denote the 68% statistical confidence interval for data and fits.

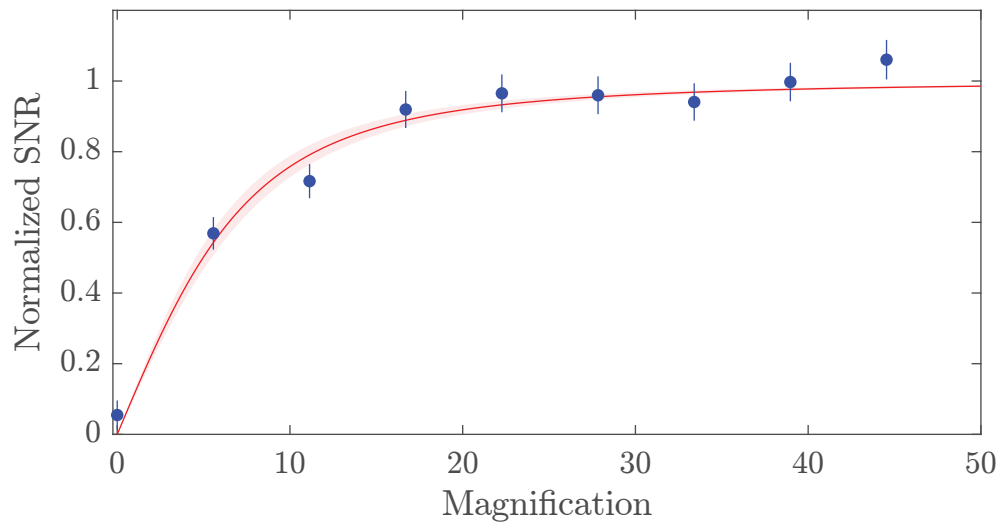


Figure 6.5: SNR associated with the two distributions as a function of the magnification parameter, normalized to that obtained by the cavity measurements (normalized SNR). Magnification is varied by changing  $\phi_{AC}$ . The solid line is a fit of the form  $M/(\alpha^2 + M^2)^{1/2}$ ; the fit parameter  $a$  contains information primarily about fluorescence detection noise. The error bars and shaded regions denote the 68% statistical confidence interval for data and fits.

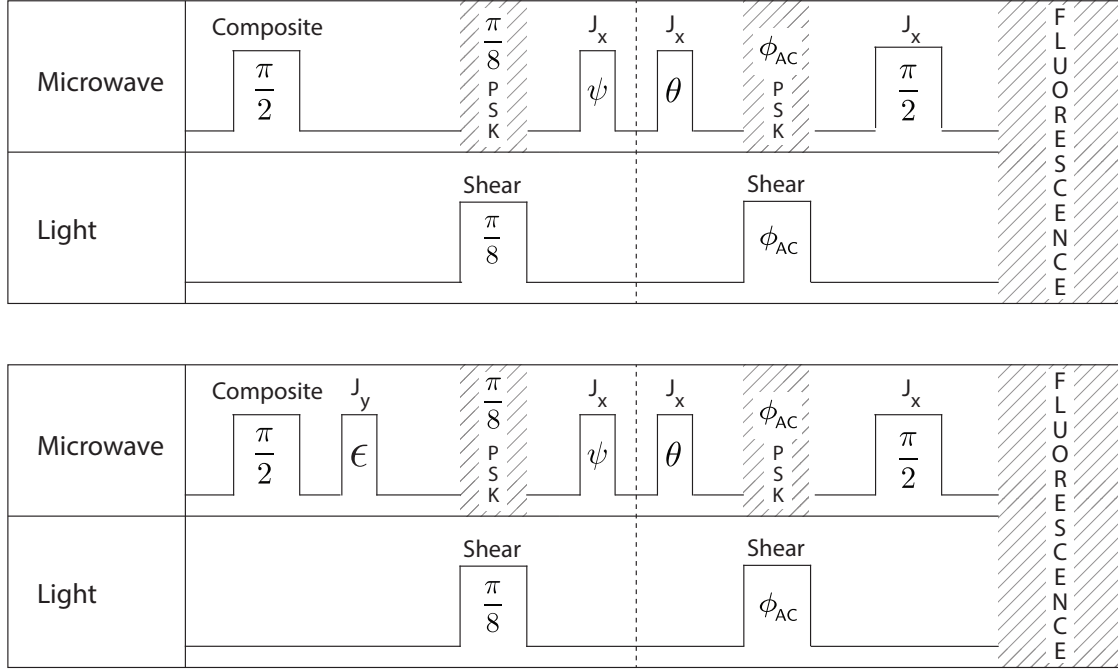


Figure 6.6: **Top:** Preparation of squeezed states with  $\langle J_z \rangle = \langle J_y \rangle = 0$  followed by the noise re-focusing magnification protocol and fluorescence imaging. **Bottom:** Preparation of squeezed states with  $\langle J_z \rangle = \pm 200$  followed by the noise re-focusing magnification protocol and fluorescence imaging. The time axis is not to scale.

### 6.3 Noise re-focusing scheme

As shown in § 2.3.6, the basic magnification scheme outlined in the previous chapter suffers from a fatal flaw - magnification of squeezed states using this method requires prohibitively large magnification values. The primary physical reason for this is that the magnifying pulse increases the antisqueezing in  $J_y$ . At large magnification values, the shearing pulse starts to decohere the state, following the dependence on  $\phi_{AC}$  shown in Figure 4.11. The use of large magnification is therefore not compatible with a desire for metrological enhancement. We developed a new scheme where the initial state is rotated by an angle  $\theta$  around the  $J_x$ -axis prior to magnification. The theoretical basis of this method is also shown in § 2.3.6, but the basic idea is that the rotation allows the magnifying shearing pulse to reduce the amount of antisqueezing instead of

increasing it.

To demonstrate this method, we start with states 8 dB squeezed in  $J_z$  and 32 dB antisqueezed in  $J_y$ . We then apply a small a small microwave rotation  $\theta$  about the  $J_x$  axis, and investigate the noise measured at the end of the magnification protocol (Figure 6.7). As expected, we observe a different optimal magnification value for each  $\theta$ . The shown family of model curves (using Equation 2.85) is a fit to the entire data set with only two free parameters, and the small deviations from these curves are attributable to slow drifts in the initial squeezing level ( $\approx 1$  dB). For the specific example of  $\theta = 29$  mrad (Figure 6.8, we explicitly show that the optimal magnification  $M \approx 30$  replicates the SNR of the initially prepared states. Had we not used noise refocusing, the required magnification would have been  $M_{0.05} = 320$  (for an infidelity  $\epsilon = 0.05$ ), which would have started wrapping the states around the Bloch sphere and caused significant decoherence. Throughout all state preparation and magnification, the coherence of the states measured by Ramsey fringe contrasts remains above 96%. The small reduction arises from residual atom-cavity coupling inhomogeneities.

The quantum phase magnification described in this chapter can be viewed as a noiseless phase-sensitive amplifier, thus bypassing the requirement that a phase-insensitive amplifier must add at least a half-quantum of zero-point fluctuations to the output [141]. In the context of many-body spin 1/2 systems, this limit is equivalent to stating that any phase-insensitive amplifier cannot amplify states that exhibit noise below coherent state noise in any quadrature. In the case of the quantum phase magnifier, the phase-sensitivity of amplification enters in the final step of magnification, where the  $J_y$  difference is rotated into a  $J_z$  difference with a  $\pi/2$ -pulse.

### 6.3.1 Noise-refocusing measurement-squeezed states

The method shown in this chapter can be applied to squeezed states generated by measurement as well. Starting with  $5 \times 10^5$  atoms prepared at  $\langle J_z \rangle = 0$ , we observed 11.4(5) dB of squeezing by magnifying conditionally squeezed states with the noise re-focusing scheme. As shown in Figure 6.9, a measurement was first performed using the cavity probe (labeled as  $M1$ ). The state was then rotated by 7.5 mrad around

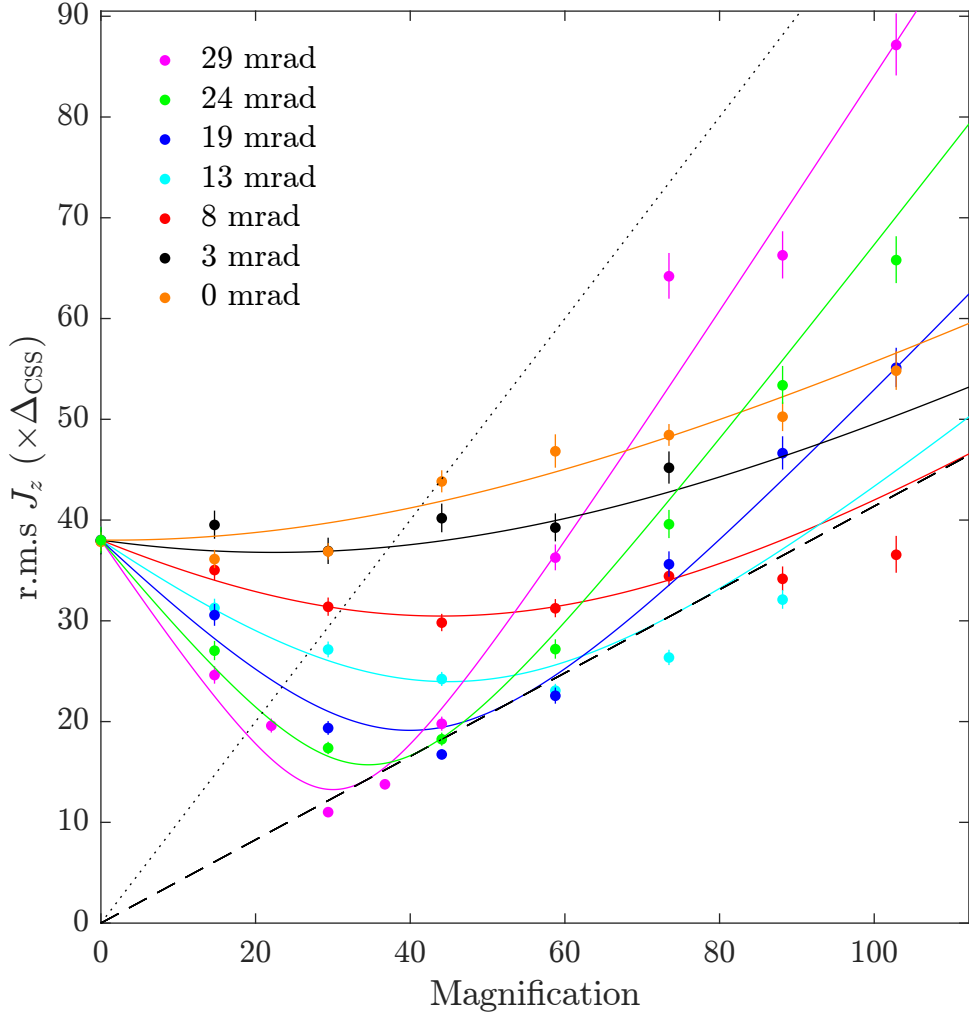


Figure 6.7: Postmagnification  $J_z$  noise in units of CSS noise as a function of magnification for different amounts of prior rotation  $\theta$  about the  $J_x$ -axis. Solid lines are a global fit to the entire data set with two free parameters:  $d\theta/dt$  (the rate of change in  $\theta$  with microwave pulse time) and the  $J_z$  noise of the initial squeezed states. Obtained values are within 15% of the calculated values. The dashed line shows  $M \times (J_z$  noise contribution from the initial squeezed states); the dotted line shows  $M \times (\text{CSS noise})$ . Error bars denote the 68% statistical confidence interval.

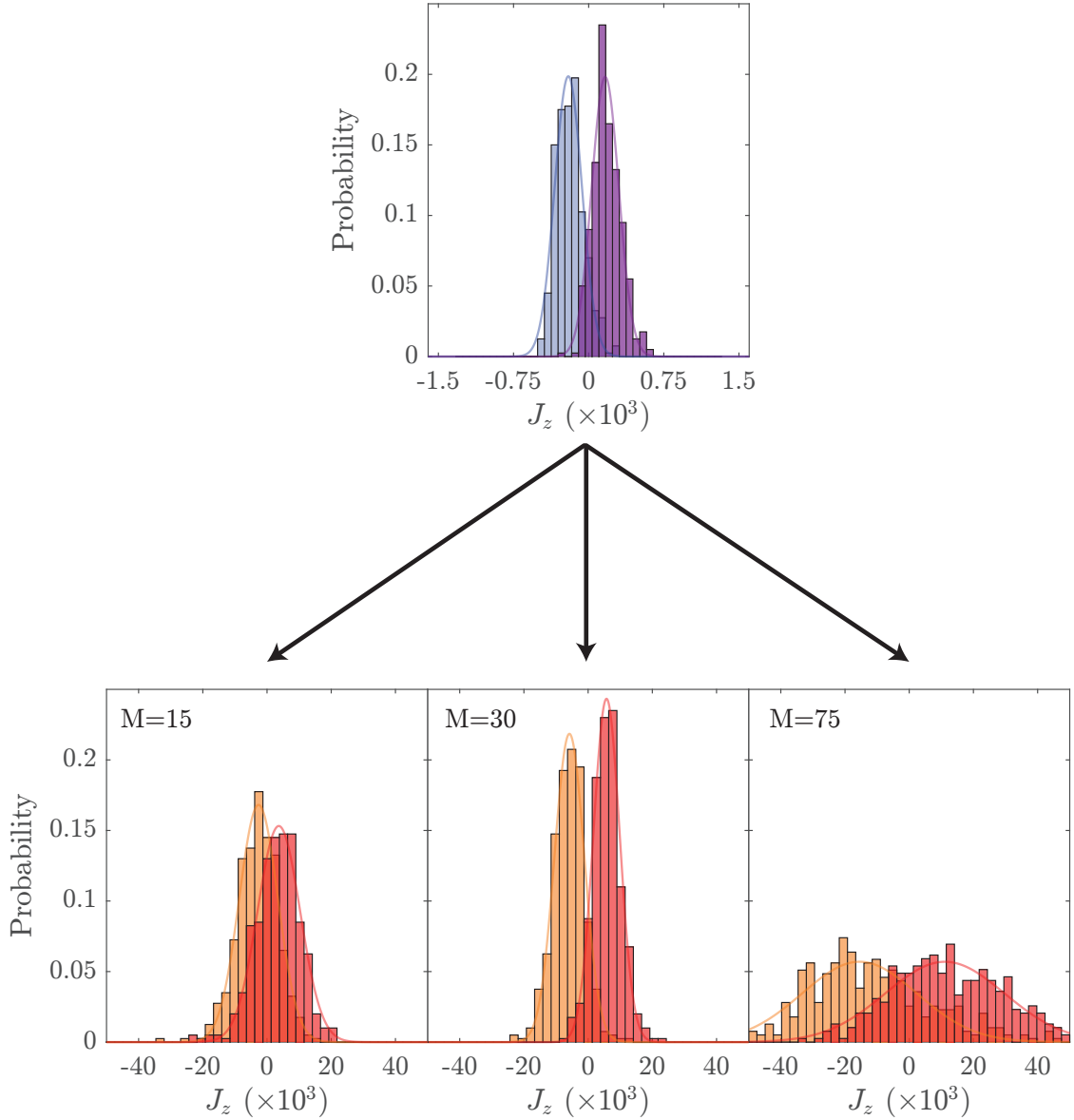


Figure 6.8: The top histogram shows the distribution of two separated 8-dB squeezed initial states ( $5 \times 10^5$  atoms) as identified by cavity measurements (to be compared with the  $M = 30$  distribution below). The three histograms below show the distributions after the magnification protocol at the indicated  $M$  values for  $\theta = 29$  mrad. The normalized SNR becomes  $0.96 \pm 0.06$  at  $M \approx 1/|\theta|$  (middle histogram). For  $M$  values to either side of  $1/|\theta|$ , the two distributions blur into each other (left and right histograms).

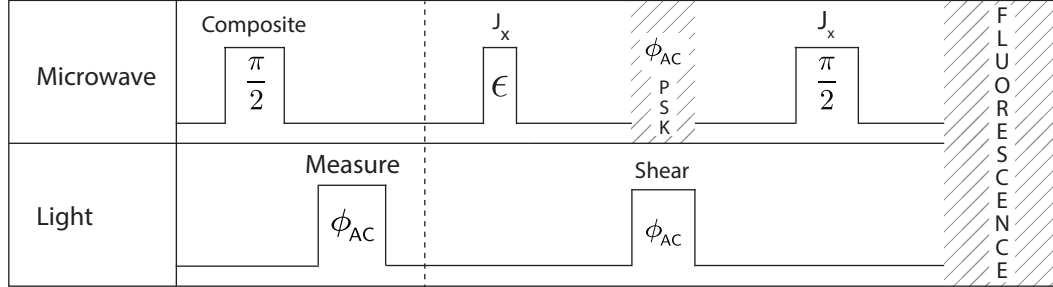


Figure 6.9: The figure shows the sequence used to magnify measurement-squeezed states. The  $\epsilon$  microwave rotation about the  $J_x$ -axis is used to tilt the state prior to magnification such as to use the noise re-focusing scheme. The PSK is used to compensate for the shearing-induced ac-Stark shift such that the final rotation will be around the  $J_x$ -axis. The time axis is not to scale. The time axis is not to scale.

the  $J_x$ -axis before an ac-Stark shift of  $\pi/2$  was applied by the interaction light tuned at  $\delta_0 = 36$  kHz amounting to a magnification of  $M = 118$ . Following a  $\pi/2$ -pulse around the  $J_x$  axis the atoms were imaged with fluorescence imaging (labeled as M2). By subtracting  $M \times M1$  from  $M2$ , the magnified noise of the squeezed state can be obtained. In Figure 6.10 we can here directly observe the amount of magnification the state undergoes. The cavity data was postselected for being within  $\sim \kappa/4$  of resonance such that the variance in the ac-Stark shift caused by the probe would not be too large.

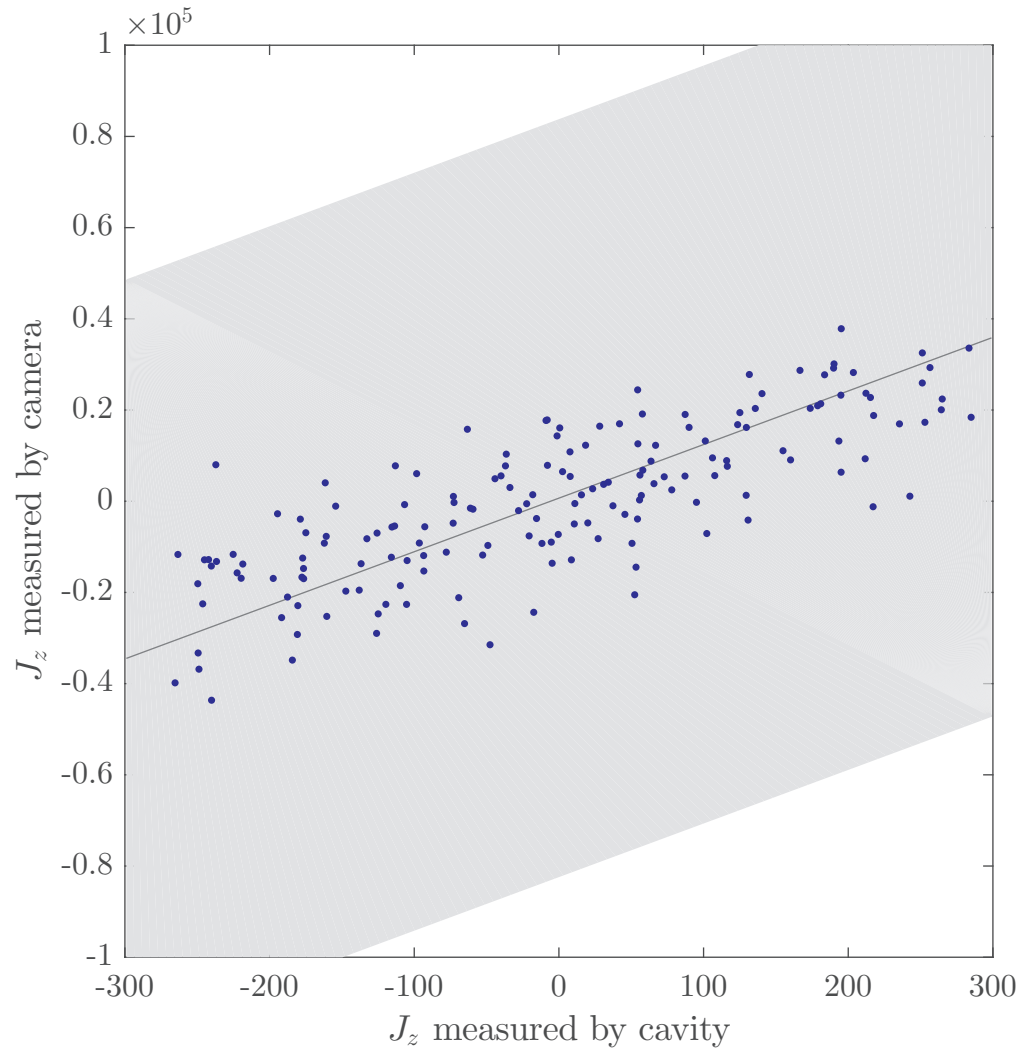


Figure 6.10: The plot shows measurement outcomes from 167 runs. The line is calculated by multiplying  $M_1$  with the expected magnification of  $M = 118$ . The grey shaded area shows  $M \times (M_1 \pm 2\Delta_{\text{CSS}})$ . Here, the measured amount of squeezing is  $11.4(5)$  dB.

# Chapter 7

## Conclusions and further work

The results described in Chapter 4 surpassed all prior records of entanglement-enhanced measurements. Additionally, the squeezed states are the first to be generated in a uniformly coupled cavity and therefore show squeezing in the symmetric  $J_z$  observable. This property allows for the demonstration of free space readout of squeezed states and potentially a squeezed atom interferometer. The vacuum chamber is designed to allow the construction of an atom interferometer with up to 100 ms drop times. The main obstacle here is a technical one, where the collection efficiency of the fluorescence imaging system must be improved. An intermediate step towards this goal would be to release the atoms from the lattice and then retrap the atoms in the cavity for the final readout. If squeezing can still be demonstrated in this case, this would show that the coupling is sufficiently uniform to perform readout in free space. In the long term, the goal is to integrate squeezed states into the 10m Atom Interferometer in the Kasevich lab to do entanglement-enhanced tests of the equivalence principle.

While the work described here focused on using squeezed states to do quantum metrology, a system that enables high precision QND measurements allows for the exploration of other interesting physics such as generation of Schrödinger cat states [142]. The experiment has a single-photon counter that could enable the generation of exotic entangled states of large ensembles of atoms.

In Chapter 5, nonlocal correlations were demonstrated in an ensemble of thermal atoms to a high level of statistical significance. Bell correlations in many-body systems

have potential applications in quantum information science. The states were also shown to contain clusters of 1590(130) entangled atoms.

The method shown in Chapter 6 enables the use of squeezed states in systems without good detection noise. Here we demonstrated 8 dB squeezed state metrology using a detection system with noise 10 dB above the quantum projection noise limit. The hope is that by significantly reducing implementation complexity, this method would allow the use of entanglement-enhanced metrology in a wide range of systems.

# Appendix A

## The dispersive signal

In this appendix I will derive cavity lineshapes starting from the reflectivity and transmission of the cavity mirrors. In particular, I will find the imaginary and real parts of the cavity transmission and reflection coefficients, which are relevant for homodyne detection of the cavity resonance. I will also include the effects of loss, which will generalize to both loss due to absorption in the mirrors and loss due to scattering of atoms coupled to the cavity. While I here consider a generic single-wavelength cavity, the derived equations hold at both wavelengths of our dual-wavelength cavity.

We start with a cavity of identical mirrors with reflectivity  $r$  and transmission  $t$  such that for an incident electric field on one of the mirrors, the transmitted field  $E_t$  and the reflected field  $E_r$  are given by

$$E_t = t E_i \quad (\text{A.1})$$

$$E_r = r E_i \quad (\text{A.2})$$

We shall assume the lossless case where  $r^2 + t^2 = 1$ , and instead put the losses in as a factor  $e^{-\alpha}$  per mirror bounce. This includes the loss due to any medium placed in the cavity - we will later include both loss in the mirror and scattering due to atoms in the factor  $\alpha$ . The cavity has an optical path length  $L$ . Any refractive index due to the medium will be included in this optical path length. When the cavity is excited with

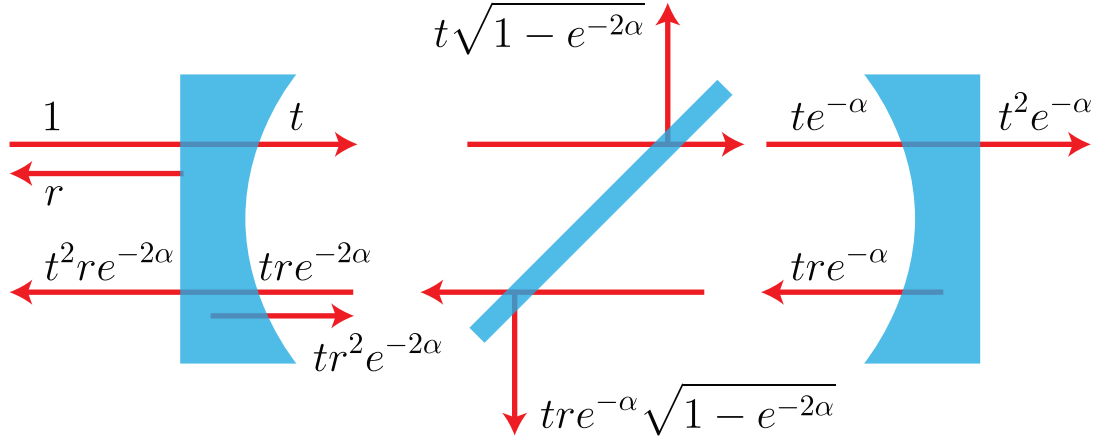


Figure A.1: The diagram shows the coefficients of the electric field over a full round trip through the cavity. We assume the mirrors are perfect and model losses in the cavity mirrors or medium with a partially reflective surface in the center of the cavity. The losses are shown as going vertically out of the cavity. Note that any full round trip in the cavity reduces the field by  $r^2 e^{-2\alpha}$ . Phase factors not included.

light with wavevector  $k$  it can be found (see Figure A.1) that the field transmission coefficient for a cavity is given by

$$\begin{aligned} t_{\text{cav}} &= t^2 e^{ikL} e^{-\alpha} (1 + r^2 e^{2ikL} e^{-2\alpha} + r^4 e^{4ikL} e^{-4\alpha} + \dots) \\ &= \frac{t^2 e^{ikL} e^{-\alpha}}{1 - r^2 e^{2ikL} e^{-2\alpha}} \end{aligned} \quad (\text{A.3})$$

where the second equality comes from summing the infinite geometric series. The light acquires a phase shift of  $e^{ikL}$  per propagation through the length of the cavity. Similarly for the reflected field we have

$$\begin{aligned} r_{\text{cav}} &= r - t^2 r e^{2ikL} e^{-2\alpha} (1 + r^2 e^{2ikL} e^{-2\alpha} + r^4 e^{4ikL} e^{-4\alpha} + \dots) \\ &= r \frac{1 - e^{2ikL} e^{-2\alpha}}{1 - r^2 e^{2ikL} e^{-2\alpha}} \end{aligned} \quad (\text{A.4})$$

We can now calculate the transmitted power to be

$$T = t_{\text{cav}} t_{\text{cav}}^* = \frac{(1 - r^2)^2 e^{-2\alpha}}{1 - 2r^2 e^{-2\alpha} \cos 2kL + r^4 e^{-4\alpha}} \quad (\text{A.5})$$

and similarly the reflected power

$$R = r_{\text{cav}} r_{\text{cav}}^* = r^2 \frac{1 - 2e^{-2\alpha} \cos 2kL + e^{-4\alpha}}{1 - 2r^2 e^{-2\alpha} \cos 2kL + r^4 e^{-4\alpha}}. \quad (\text{A.6})$$

It can readily be seen that  $R + T = 1$  if  $\alpha = 0$ , which would be the case for a lossless cavity. To verify consistency when there is loss, we use the fact that the losses per pass through the cavity is  $\sqrt{1 - e^{-2\alpha}}$  by energy conservation, as one pass through the lossy material attenuates the field by  $e^{-\alpha}$ . While in general, this lossy material can cause some phase shift on the light, we can absorb that into the phase factor  $kL$  to simplify the algebra. We can also see from these equations that the transmitted power is maximized when  $2kL = 2n\pi$ , which is the resonance condition of the cavity. The phase shift from the lossy material will therefore amount to a shift in resonance frequency. To establish consistency including losses, we can then sum up the ‘losses going right’ (labeled 1) and the ‘losses going left’ (labeled 2) to be

$$\begin{aligned} l_1 &= \frac{E_{l1}}{E_i} = t\sqrt{1 - e^{-2\alpha}} (1 + r^2 e^{2ikL} e^{-2\alpha} + r^4 e^{4ikL} e^{-4\alpha} + \dots) \\ &= \frac{t\sqrt{1 - e^{-2\alpha}}}{1 - r^2 e^{2ikL} e^{-2\alpha}} \end{aligned} \quad (\text{A.7})$$

$$\begin{aligned} l_2 &= \frac{E_{l2}}{E_i} = t r e^{-\alpha} \sqrt{1 - e^{-2\alpha}} (1 + r^2 e^{2ikL} e^{-2\alpha} + r^4 e^{4ikL} e^{-4\alpha} + \dots) \\ &= \frac{t r e^{-\alpha} \sqrt{1 - e^{-2\alpha}}}{1 - r^2 e^{2ikL} e^{-2\alpha}} \end{aligned} \quad (\text{A.8})$$

Using these loss coefficients to find  $\mathcal{L}_1 = l_1 l_1^*$  and  $\mathcal{L}_2 = l_2 l_2^*$  it can be shown that  $R + T + \mathcal{L}_1 + \mathcal{L}_2 = 1$  as expected. We now expand  $2kL$  as  $2kL = 2n\pi + 2L\delta/c = 2n\pi + \delta/\nu_{\text{FSR}}$  where  $\delta = \omega - \omega_0$  is the detuning of the light from the cavity resonance and  $\nu_{\text{FSR}}$  is the free spectral range. We can see that the free spectral range is in fact the

spacing between resonances, since the transmission and reflection coefficients repeat every time  $\delta/(2\pi) = \nu_{\text{FSR}}$  as expected. Now, since we want to find the lineshapes of the cavity, we assume that  $\delta/\nu_{\text{FSR}} \ll 1$  and obtain

$$T = \frac{(1 - r^2)^2 e^{-2\alpha}}{(1 - r^2 e^{-2\alpha})^2 + r^2 e^{-2\alpha} \left(\frac{\delta}{\nu_{\text{FSR}}}\right)^2} \quad (\text{A.9})$$

and

$$R = r^2 \frac{(1 - e^{-2\alpha})^2 + e^{-2\alpha} \left(\frac{\delta}{\nu_{\text{FSR}}}\right)^2}{(1 - r^2 e^{-2\alpha})^2 + r^2 e^{-2\alpha} \left(\frac{\delta}{\nu_{\text{FSR}}}\right)^2} \quad (\text{A.10})$$

In one round trip the power is reduced by  $r^4 e^{-4\alpha}$ —the square of the field decay. Each round trip takes  $\delta t = 2L/c$ . We can therefore find the lifetime of a photon by summing the series

$$\begin{aligned} \tau &= \frac{2L}{c} (1 + r^4 e^{-4\alpha} + r^8 e^{-8\alpha} + \dots) \\ &= \frac{2L/c}{1 - r^4 e^{-4\alpha}} \end{aligned} \quad (\text{A.11})$$

We can now define the rate of power loss from the cavity,  $\kappa = 1/\tau$ , such that  $P \propto e^{-\kappa t}$  and find

$$\kappa = (1 - r^4 e^{-4\alpha}) \nu_{\text{FSR}} \quad (\text{A.12})$$

Additionally, as the field decays half as fast ( $P \propto e^{-(\kappa/2)t}$ ), we can similarly find that the rate of field decay is  $\kappa/2 = (1 - r^2 e^{-2\alpha}) \nu_{\text{FSR}}$ . We can now use this to find an equation for the finesse. The finesse is related to the number of round trips a photon makes in the cavity on average, given by  $\mathcal{F}/\pi$ , and we can thus find that  $\mathcal{F}$  is given by

$$\mathcal{F} = \frac{\omega_{\text{FSR}}}{\kappa} = \frac{\pi}{1 - r^2 e^{-2\alpha}} \quad (\text{A.13})$$

from the previous equations for  $\kappa$  in terms of  $\nu_{\text{FSR}}$ . The above holds for low loss and

high reflectivity.

I will now divide through by  $(1 - r^2 e^{-2\alpha})^2$  in Equation A.9. We then identify  $(1 - r^2)^2 / (1 - r^2 e^{-2\alpha})^2$  as  $(\kappa_0/\kappa)^2$  where  $\kappa_0$  is the cavity linewidth without loss, then assume that  $r$  is close to 1 and the losses are small such that  $e^{-2\alpha}$  is close to 1, to obtain

$$T = \left( \frac{\kappa_M}{\kappa} \right)^2 \frac{1}{1 + \left( \frac{\delta}{\kappa/2} \right)^2}. \quad (\text{A.14})$$

Similarly for Equation A.10 we obtain

$$R = \frac{\left( \frac{\kappa_L}{\kappa} \right)^2 + \left( \frac{\delta}{\kappa/2} \right)^2}{1 + \left( \frac{\delta}{\kappa/2} \right)^2} \quad (\text{A.15})$$

where  $(\kappa_L/\kappa)^2 = (1 - e^{-2\alpha})^2 / (1 - r^2 e^{-2\alpha})^2$  and  $\kappa_L$  is the rate of loss from the cavity mode. We can also use  $r_{\text{cav}}$  and  $t_{\text{cav}}$  to find the phase shift on the reflected and transmitted light, as the phase shift will be given by

$$\tan \phi_r = \frac{\Im[r_{\text{cav}}]}{\Re[r_{\text{cav}}]} = \frac{-(1 - r^2) e^{-2\alpha} \sin 2kL}{1 - (1 + r^2) e^{-2\alpha} \cos 2kL + r^2 e^{-4\alpha}} \quad (\text{A.16})$$

$$\tan \phi_t = \frac{\Im[t_{\text{cav}}]}{\Re[t_{\text{cav}}]} = \frac{(1 + r^2 e^{-2\alpha}) \sin kL}{(1 - r^2 e^{-2\alpha}) \cos kL} \quad (\text{A.17})$$

We can again substitute for  $kL$  and insert linewidths for reflection coefficients as done previously, then neglect terms of order  $[\delta/(\kappa/2)]^2$  to obtain

$$\tan \phi_r = \frac{\kappa_M}{\kappa_L} \frac{\delta}{\kappa/2} \quad (\text{A.18})$$

$$\tan \phi_t = \frac{\delta}{\kappa/2} \quad (\text{A.19})$$

as approximations for the phase of the reflected and transmitted light. Taking the

same approximations as for the reflection and transmission coefficients, we can obtain the real and imaginary parts of the reflection coefficients as

$$\Re[r_{\text{cav}}] = \frac{\kappa_{\mathcal{L}}}{\kappa} \frac{1}{1 + \left(\frac{\delta}{\kappa/2}\right)^2} \quad (\text{A.20})$$

$$\Im[r_{\text{cav}}] = -\frac{\kappa_0}{\kappa} \frac{\frac{\delta}{\kappa/2}}{1 + \left(\frac{\delta}{\kappa/2}\right)^2}. \quad (\text{A.21})$$

For the transmission coefficients, we obtain

$$\Re[t_{\text{cav}}] = \frac{\kappa_0}{\kappa} \frac{1}{1 + \left(\frac{\delta}{\kappa/2}\right)^2} \quad (\text{A.22})$$

$$\Im[t_{\text{cav}}] = \frac{\kappa_0}{\kappa} \frac{\frac{\delta}{\kappa/2}}{1 + \left(\frac{\delta}{\kappa/2}\right)^2} \quad (\text{A.23})$$

as displayed in the main text.

# Bibliography

- [1] W. T. Kelvin and P. G. Tait. *Elements of Natural Philosophy*. Cambridge: The University Press, 1879.
- [2] W. F. Snyder. Lord Kelvin on Atoms as Fundamental Natural Standards (for Base Units). *IEEE Transactions on Instrumentation and Measurement*, 22(1):99–99, 1973. DOI: [10.1109/TIM.1973.4314109](https://doi.org/10.1109/TIM.1973.4314109).
- [3] I. I. Rabi, S. Millman, P. Kusch, and J. R. Zacharias. The Molecular Beam Resonance Method for Measuring Nuclear Magnetic Moments. The Magnetic Moments of  ${}^3\text{Li}^6$ ,  ${}^3\text{Li}^7$  and  ${}^9\text{F}^{19}$ . *Physical Review*, 55(6):526–535, 1939. DOI: [10.1103/PhysRev.55.526](https://doi.org/10.1103/PhysRev.55.526).
- [4] N. F. Ramsey. A Molecular Beam Resonance Method with Separated Oscillating Fields. *Physical Review*, 78(6):695–699, 1950. DOI: [10.1103/PhysRev.78.695](https://doi.org/10.1103/PhysRev.78.695).
- [5] H. Lyons. The Atomic Clock, An Atomic Standard of Frequency and Time. *N.B.S. Tech. News Bull.* 33(17), 1949.
- [6] B. J. Bloom, T. L. Nicholson, J. R. Williams, S. L. Campbell, M. Bishof, X. Zhang, W. Zhang, S. L. Bromley, and J. Ye. An Optical Lattice Clock with Accuracy and Stability at the  $\hat{\$10^{-18}}$  Level. *Nature*, 506(7486):71–75, 2014. DOI: [10.1038/nature12941](https://doi.org/10.1038/nature12941).
- [7] J. Ye, H. J. Kimble, and H. Katori. Quantum State Engineering and Precision Metrology Using State-Insensitive Light Traps. *Science*, 320(5884):1734–1738, 2008. DOI: [10.1126/science.1148259](https://doi.org/10.1126/science.1148259).

- [8] D. Sheng, S. Li, N. Dural, and M. V. Romalis. Subfemtotesla Scalar Atomic Magnetometry Using Multipass Cells. *Physical Review Letters*, 110(16):160802, 2013. DOI: [10.1103/PhysRevLett.110.160802](https://doi.org/10.1103/PhysRevLett.110.160802).
- [9] S. J. Smullin, I. M. Savukov, G. Vasilakis, R. K. Ghosh, and M. V. Romalis. Low-Noise High-Density Alkali-Metal Scalar Magnetometer. *Physical Review A*, 80(3):033420, 2009. DOI: [10.1103/PhysRevA.80.033420](https://doi.org/10.1103/PhysRevA.80.033420).
- [10] M. J. Snadden, J. M. McGuirk, P. Bouyer, K. G. Haritos, and M. A. Kasevich. Measurement of the Earth's Gravity Gradient with an Atom Interferometer-Based Gravity Gradiometer. *Physical Review Letters*, 81(5):971–974, 1998. DOI: [10.1103/PhysRevLett.81.971](https://doi.org/10.1103/PhysRevLett.81.971).
- [11] J. M. McGuirk, G. T. Foster, J. B. Fixler, M. J. Snadden, and M. A. Kasevich. Sensitive Absolute-Gravity Gradiometry Using Atom Interferometry. *Physical Review A*, 65(3):033608, 2002. DOI: [10.1103/PhysRevA.65.033608](https://doi.org/10.1103/PhysRevA.65.033608).
- [12] R. Geiger, V. Ménoret, G. Stern, N. Zahzam, P. Cheinet, B. Battelier, A. Villing, F. Moron, M. Lours, Y. Bidel, A. Bresson, A. Landragin, and P. Bouyer. Detecting Inertial Effects with Airborne Matter-Wave Interferometry. *Nature Communications*, 2:474, 2011. DOI: [10.1038/ncomms1479](https://doi.org/10.1038/ncomms1479).
- [13] N. Gaaloul, H. Ahlers, T. A. Schulze, Y. Singh, S. T. Seidel, W. Herr, W. Ertmer, and E. Rasel. Quantum Tests of the Equivalence Principle with Atom Interferometry. *Acta Astronautica*, 67:1059–1062, 9–10 2010. DOI: [10.1016/j.actaastro.2010.06.043](https://doi.org/10.1016/j.actaastro.2010.06.043).
- [14] M. Kitagawa and M. Ueda. Squeezed Spin States. *Physical Review A*, 47(6):5138–5143, 1993. DOI: [10.1103/PhysRevA.47.5138](https://doi.org/10.1103/PhysRevA.47.5138).
- [15] V. Giovannetti, S. Lloyd, and L. Maccone. Quantum-Enhanced Measurements: Beating the Standard Quantum Limit. *Science*, 306:1330–1336, 2004. DOI: [10.1126/science.1104149](https://doi.org/10.1126/science.1104149).
- [16] D. J. Wineland, J. J. Bollinger, W. M. Itano, F. L. Moore, and D. J. Heinzen. Spin Squeezing and Reduced Quantum Noise in Spectroscopy. *Physical Review A*, 46(11):R6797–R6800, 1992. DOI: [10.1103/PhysRevA.46.R6797](https://doi.org/10.1103/PhysRevA.46.R6797).

- [17] D. J. Wineland, J. J. Bollinger, W. M. Itano, and D. J. Heinzen. Squeezed Atomic States and Projection Noise in Spectroscopy. *Phys. Rev. A*, 50:67–88, 1994. DOI: [10.1103/PhysRevA.50.67](https://doi.org/10.1103/PhysRevA.50.67).
- [18] T. L. S. Collaboration. A Gravitational Wave Observatory Operating beyond the Quantum Shot-Noise Limit. *Nature Physics*, 7(12):962–965, 2011. DOI: [10.1038/nphys2083](https://doi.org/10.1038/nphys2083).
- [19] T. Eberle, S. Steinlechner, J. Bauchrowitz, V. Händchen, H. Vahlbruch, M. Mehmet, H. Müller-Ebhardt, and R. Schnabel. Quantum Enhancement of the Zero-Area Sagnac Interferometer Topology for Gravitational Wave Detection. *Physical Review Letters*, 104(25):251102, 2010. DOI: [10.1103/PhysRevLett.104.251102](https://doi.org/10.1103/PhysRevLett.104.251102).
- [20] M. A. Taylor, J. Janousek, V. Daria, J. Knittel, B. Hage, H.-A. Bachor, and W. P. Bowen. Biological Measurement beyond the Quantum Limit. *Nature Photonics*, 7(3):229–233, 2013. DOI: [10.1038/nphoton.2012.346](https://doi.org/10.1038/nphoton.2012.346).
- [21] H. Vahlbruch, M. Mehmet, K. Danzmann, and R. Schnabel. Detection of 15 dB Squeezed States of Light and Their Application for the Absolute Calibration of Photoelectric Quantum Efficiency. *Physical Review Letters*, 117(11):110801, 2016. DOI: [10.1103/PhysRevLett.117.110801](https://doi.org/10.1103/PhysRevLett.117.110801).
- [22] C. Eichler, Y. Salathe, J. Mlynek, S. Schmidt, and A. Wallraff. Quantum-Limited Amplification and Entanglement in Coupled Nonlinear Resonators. *Phys. Rev. Lett.* 113:110502, 2014. DOI: [10.1103/PhysRevLett.113.110502](https://doi.org/10.1103/PhysRevLett.113.110502).
- [23] J. G. Bohnet, B. C. Sawyer, J. W. Britton, M. L. Wall, A. M. Rey, M. Foss-Feig, and J. J. Bollinger. Quantum Spin Dynamics and Entanglement Generation with Hundreds of Trapped Ions. *Science*, 352(6291):1297–1301, 2016. DOI: [10.1126/science.aad9958](https://doi.org/10.1126/science.aad9958).
- [24] C. A. Sackett, D. Kielpinski, B. E. King, C. Langer, V. Meyer, C. J. Myatt, M. Rowe, Q. A. Turchette, W. M. Itano, D. J. Wineland, and C. Monroe. Experimental Entanglement of Four Particles. *Nature*, 404(6775):256–259, 2000. DOI: [10.1038/35005011](https://doi.org/10.1038/35005011).

- [25] A. Kuzmich, L. Mandel, and N. P. Bigelow. Generation of Spin Squeezing via Continuous Quantum Nondemolition Measurement. *Physical Review Letters*, 85(8):1594–1597, 2000. DOI: [10.1103/PhysRevLett.85.1594](https://doi.org/10.1103/PhysRevLett.85.1594).
- [26] A. S. Sørensen and K. Mølmer. Entangling Atoms in Bad Cavities. *Physical Review A*, 66(2):022314, 2002. DOI: [10.1103/PhysRevA.66.022314](https://doi.org/10.1103/PhysRevA.66.022314).
- [27] C. Orzel, A. K. Tuchman, M. L. Fenselau, M. Yasuda, and M. A. Kasevich. Squeezed States in a Bose-Einstein Condensate. *Science*, 291(5512):2386–2389, 2001. DOI: [10.1126/science.1058149](https://doi.org/10.1126/science.1058149).
- [28] J. Estève, C. Gross, A. Weller, S. Giovanazzi, and M. K. Oberthaler. Squeezing and Entanglement in a Bose-Einstein Condensate. *Nature*, 455(7217):1216–1219, 2008. DOI: [10.1038/nature07332](https://doi.org/10.1038/nature07332).
- [29] P. Böhi, M. F. Riedel, J. Hoffrogge, J. Reichel, T. W. Hänsch, and P. Treutlein. Coherent Manipulation of Bose-Einstein Condensates with State-Dependent Microwave Potentials on an Atom Chip. *Nature Physics*, 5(8):592–597, 2009. DOI: [10.1038/nphys1329](https://doi.org/10.1038/nphys1329).
- [30] C. Gross, T. Zibold, E. Nicklas, J. Estève, and M. K. Oberthaler. Non-linear Atom Interferometer Surpasses Classical Precision Limit. *Nature*, 464(7292):1165–1169, 2010. DOI: [10.1038/nature08919](https://doi.org/10.1038/nature08919).
- [31] M. F. Riedel, P. Böhi, Y. Li, T. W. Hänsch, A. Sinatra, and P. Treutlein. Atom-Chip-Based Generation of Entanglement for Quantum Metrology. *Nature*, 464(7292):1170–1173, 2010. DOI: [10.1038/nature08988](https://doi.org/10.1038/nature08988).
- [32] C. D. Hamley, C. S. Gerving, T. M. Hoang, E. M. Bookjans, and M. S. Chapman. Spin-Nematic Squeezed Vacuum in a Quantum Gas. *Nature Physics*, 8(4):305–308, 2012. DOI: [10.1038/NPHYS2245](https://doi.org/10.1038/NPHYS2245).
- [33] C. F. Ockeloen, R. Schmied, M. F. Riedel, and P. Treutlein. Quantum Metrology with a Scanning Probe Atom Interferometer. *Physical Review Letters*, 111(14):143001, 2013. DOI: [10.1103/PhysRevLett.111.143001](https://doi.org/10.1103/PhysRevLett.111.143001).

- [34] W. Muessel, H. Strobel, D. Linnemann, D. B. Hume, and M. K. Oberthaler. Scalable Spin Squeezing for Quantum-Enhanced Magnetometry with Bose-Einstein Condensates. *Phys. Rev. Lett.* 113:103004, 2014. DOI: 10.1103/PhysRevLett.113.103004.
- [35] R. Schmied, J.-D. Bancal, B. Allard, M. Fadel, V. Scarani, P. Treutlein, and N. Sangouard. Bell Correlations in a Bose-Einstein Condensate. *Science*, 352(6284):441–444, 2016. DOI: 10.1126/science.aad8665.
- [36] J. Hald, J. L. Sørensen, C. Schori, and E. S. Polzik. Spin Squeezed Atoms: A Macroscopic Entangled Ensemble Created by Light. *Physical Review Letters*, 83(7):1319–1322, 1999. DOI: 10.1103/PhysRevLett.83.1319.
- [37] J. Appel, P. J. Windpassinger, D. Oblak, U. B. Hoff, N. Kjaergaard, and E. S. Polzik. Mesoscopic Atomic Entanglement for Precision Measurements beyond the Standard Quantum Limit. *Proceedings of the National Academy of Sciences of the United States of America*, 106(27):10960–10965, 2009. DOI: 10.1073/pnas.0901550106.
- [38] T. Takano, M. Fuyama, R. Namiki, and Y. Takahashi. Spin Squeezing of a Cold Atomic Ensemble with the Nuclear Spin of One-Half. *Physical Review Letters*, 102(3):033601, 2009. DOI: 10.1103/PhysRevLett.102.033601.
- [39] R. J. Sewell, M. Koschorreck, M. Napolitano, B. Dubost, N. Behbood, and M. W. Mitchell. Magnetic Sensitivity Beyond the Projection Noise Limit by Spin Squeezing. *Physical Review Letters*, 109(25):253605, 2012. DOI: 10.1103/PhysRevLett.109.253605.
- [40] Z. Chen, J. G. Bohnet, S. R. Sankar, J. Dai, and J. K. Thompson. Conditional Spin Squeezing of a Large Ensemble via the Vacuum Rabi Splitting. *Physical Review Letters*, 106(13):133601, 2011. DOI: 10.1103/PhysRevLett.106.133601.
- [41] M. H. Schleier-Smith, I. D. Leroux, and V. Vuletić. States of an Ensemble of Two-Level Atoms with Reduced Quantum Uncertainty. *Physical Review Letters*, 104(7):073604, 2010. DOI: 10.1103/PhysRevLett.104.073604.

- [42] J. G. Bohnet, K. C. Cox, M. A. Norcia, J. M. Weiner, Z. Chen, and J. K. Thompson. Reduced Spin Measurement Back-Action for a Phase Sensitivity Ten Times beyond the Standard Quantum Limit. *Nature Photonics*, 8(9):731–736, 2014. DOI: [10.1038/NPHOTON.2014.151](https://doi.org/10.1038/NPHOTON.2014.151).
- [43] K. C. Cox, G. P. Greve, J. M. Weiner, and J. K. Thompson. Deterministic Squeezed States with Collective Measurements and Feedback. *Physical Review Letters*, 116(9):093602, 2016. DOI: [10.1103/PhysRevLett.116.093602](https://doi.org/10.1103/PhysRevLett.116.093602).
- [44] O. Hosten, N. J. Engelsen, R. Krishnakumar, and M. A. Kasevich. Measurement Noise 100 Times Lower than the Quantum-Projection Limit Using Entangled Atoms. *Nature*, 529(7587):505–508, 2016.
- [45] I. D. Leroux, M. H. Schleier-Smith, and V. Vuletić. Orientation-Dependent Entanglement Lifetime in a Squeezed Atomic Clock. *Physical Review Letters*, 104(25):250801, 2010. DOI: [10.1103/PhysRevLett.104.250801](https://doi.org/10.1103/PhysRevLett.104.250801).
- [46] O. Hosten, R. Krishnakumar, N. J. Engelsen, and M. A. Kasevich. Quantum Phase Magnification. *Science*, 352(6293):1552–1555, 2016. DOI: [10.1126/science.aaf3397](https://doi.org/10.1126/science.aaf3397).
- [47] A. E. B. Nielsen and K. Mølmer. Atomic Spin Squeezing in an Optical Cavity. *Physical Review A*, 77(6):063811, 2008. DOI: [10.1103/PhysRevA.77.063811](https://doi.org/10.1103/PhysRevA.77.063811).
- [48] Z. Chen, J. G. Bohnet, J. M. Weiner, K. C. Cox, and J. K. Thompson. Cavity-Aided Nondemolition Measurements for Atom Counting and Spin Squeezing. *Phys. Rev. A*, 89:043837, 2014. DOI: [10.1103/PhysRevA.89.043837](https://doi.org/10.1103/PhysRevA.89.043837).
- [49] M. O. Scully and M. S. Zubairy. *Quantum Optics*. Cambridge University Press, 1997. 662 pp.
- [50] D. Walls and G. J. Milburn, eds. *Quantum Optics*. Berlin, Heidelberg: Springer Berlin Heidelberg, 2008.
- [51] A. K. Tuchman, R. Long, G. Vrijen, J. Boudet, J. Lee, and M. A. Kasevich. Normal-Mode Splitting with Large Collective Cooperativity. *Physical Review A*, 74(5):053821, 2006. DOI: [10.1103/PhysRevA.74.053821](https://doi.org/10.1103/PhysRevA.74.053821).

- [52] A. Kuzmich, N. P. Bigelow, and L. Mandel. Atomic Quantum Non-Demolition Measurements and Squeezing. *Europhysics Letters (EPL)*, 42(5):481–486, 1998. DOI: [10.1209/epl/i1998-00277-9](https://doi.org/10.1209/epl/i1998-00277-9).
- [53] G. F. N. Vrijen. Collective Quantum Behavior of Atomic Ensembles in High-Finesse Optical Cavities. Stanford University, 2011.
- [54] M. H. Schleier-Smith. Cavity-Enabled Spin Squeezing for a Quantum-Enhanced Atomic Clock. Thesis. Massachusetts Institute of Technology, 2011.
- [55] H. Tanji-Suzuki, I. D. Leroux, M. H. Schleier-Smith, M. Cetina, A. T. Grier, J. Simon, and V. Vuletić. Interaction between Atomic Ensembles and Optical Resonators: Classical Description. *Adv. At. Mol. Opt. Phys.*, 60(201), 2011.
- [56] J. Zhang, K. Peng, and S. L. Braunstein. Backaction-Induced Spin-Squeezed States in a Detuned Quantum-Nondemolition Measurement. *Physical Review A*, 68(3):035802, 2003. DOI: [10.1103/PhysRevA.68.035802](https://doi.org/10.1103/PhysRevA.68.035802).
- [57] I. Bouchoule and K. Mølmer. Preparation of Spin-Squeezed Atomic States by Optical-Phase-Shift Measurement. *Physical Review A*, 66(4):043811, 2002. DOI: [10.1103/PhysRevA.66.043811](https://doi.org/10.1103/PhysRevA.66.043811).
- [58] M. Takeuchi, S. Ichihara, T. Takano, M. Kumakura, T. Yabuzaki, and Y. Takahashi. Spin Squeezing via One-Axis Twisting with Coherent Light. *Physical Review Letters*, 94(2):023003, 2005. DOI: [10.1103/PhysRevLett.94.023003](https://doi.org/10.1103/PhysRevLett.94.023003).
- [59] K. Hammerer, K. Mølmer, E. S. Polzik, and J. I. Cirac. Light-Matter Quantum Interface. *Physical Review A*, 70(4):044304, 2004. DOI: [10.1103/PhysRevA.70.044304](https://doi.org/10.1103/PhysRevA.70.044304).
- [60] H. M. Wiseman and G. J. Milburn. All-Optical versus Electro-Optical Quantum-Limited Feedback. *Physical Review A*, 49(5):4110–4125, 1994. DOI: [10.1103/PhysRevA.49.4110](https://doi.org/10.1103/PhysRevA.49.4110).
- [61] M. H. Schleier-Smith, I. D. Leroux, and V. Vuletić. Squeezing the Collective Spin of a Dilute Atomic Ensemble by Cavity Feedback. *Physical Review A*, 81(2):021804, 2010. DOI: [10.1103/PhysRevA.81.021804](https://doi.org/10.1103/PhysRevA.81.021804).

- [62] K. Pawłowski, J. Estève, J. Reichel, and A. Sinatra. Limits of Atomic Entanglement by Cavity Feedback: From Weak to Strong Coupling. *EPL (Europhysics Letters)*, 113(3):34005, 2016. DOI: [10.1209/0295-5075/113/34005](https://doi.org/10.1209/0295-5075/113/34005).
- [63] E. Davis, G. Bentsen, and M. Schleier-Smith. Approaching the Heisenberg Limit without Single-Particle Detection. *Physical Review Letters*, 116(5):053601, 2016. DOI: [10.1103/PhysRevLett.116.053601](https://doi.org/10.1103/PhysRevLett.116.053601).
- [64] B. Lücke, J. Peise, G. Vitagliano, J. Arlt, L. Santos, G. Tóth, and C. Klempt. Detecting Multiparticle Entanglement of Dicke States. *Physical Review Letters*, 112(15):155304, 2014. DOI: [10.1103/PhysRevLett.112.155304](https://doi.org/10.1103/PhysRevLett.112.155304).
- [65] A. S. Sørensen and K. Mølmer. Entanglement and Extreme Spin Squeezing. *Phys. Rev. Lett.* 86:4431–4434, 2001. DOI: [10.1103/PhysRevLett.86.4431](https://doi.org/10.1103/PhysRevLett.86.4431).
- [66] L. Dellantonio, S. Das, J. Appel, and A. S. Sørensen. Multi-Partite Entanglement Detection with Non Symmetric Probing, 2016. arXiv: [1609.08516](https://arxiv.org/abs/1609.08516) [cond-mat, physics:quant-ph].
- [67] L. Dellantonio. Entanglement Criteria for Spin Squeezing. University of Copenhagen, 2015.
- [68] G. Vitagliano, I. Apellaniz, M. Kleinmann, B. Lücke, C. Klempt, and G. Toth. Entanglement and Extreme Spin Squeezing of Unpolarized States, 2016. arXiv: [1605.07202](https://arxiv.org/abs/1605.07202) [quant-ph].
- [69] J. Lee. Collective Atom-Cavity Interactions in a High-Finesse Dual-Wavelength Cavity. Stanford University, 2011.
- [70] J. Lee, G. Vrijen, I. Teper, O. Hosten, and M. A. Kasevich. Many-Atom-Cavity QED System with Homogeneous Atom-Cavity Coupling. *Optics Letters*, 39(13):4005–4008, 2014. DOI: [10.1364/OL.39.004005](https://doi.org/10.1364/OL.39.004005).
- [71] S. Chu, L. Hollberg, J. E. Bjorkholm, A. Cable, and A. Ashkin. Three-Dimensional Viscous Confinement and Cooling of Atoms by Resonance Radiation Pressure. *Physical Review Letters*, 55(1):48–51, 1985. DOI: [10.1103/PhysRevLett.55.48](https://doi.org/10.1103/PhysRevLett.55.48).

- [72] S. Chu, J. E. Bjorkholm, A. Ashkin, and A. Cable. Experimental Observation of Optically Trapped Atoms. *Physical Review Letters*, 57(3):314–317, 1986. DOI: [10.1103/PhysRevLett.57.314](https://doi.org/10.1103/PhysRevLett.57.314).
- [73] J. Dalibard and C. Cohen-Tannoudji. Dressed-Atom Approach to Atomic Motion in Laser Light: The Dipole Force Revisited. *Journal of the Optical Society of America B*, 2(11):1707, 1985. DOI: [10.1364/JOSAB.2.001707](https://doi.org/10.1364/JOSAB.2.001707).
- [74] E. L. Raab, M. Prentiss, A. Cable, S. Chu, and D. E. Pritchard. Trapping of Neutral Sodium Atoms with Radiation Pressure. *Physical Review Letters*, 59(23):2631–2634, 1987. DOI: [10.1103/PhysRevLett.59.2631](https://doi.org/10.1103/PhysRevLett.59.2631).
- [75] J. Dalibard and C. Cohen-Tannoudji. Laser Cooling below the Doppler Limit by Polarization Gradients: Simple Theoretical Models. *Journal of the Optical Society of America B*, 6(11):2023, 1989. DOI: [10.1364/JOSAB.6.002023](https://doi.org/10.1364/JOSAB.6.002023).
- [76] A. L. Migdall, J. V. Prodan, W. D. Phillips, T. H. Bergeman, and H. J. Metcalf. First Observation of Magnetically Trapped Neutral Atoms. *Physical Review Letters*, 54(24):2596–2599, 1985. DOI: [10.1103/PhysRevLett.54.2596](https://doi.org/10.1103/PhysRevLett.54.2596).
- [77] P. D. Lett, R. N. Watts, C. I. Westbrook, W. D. Phillips, P. L. Gould, and H. J. Metcalf. Observation of Atoms Laser Cooled below the Doppler Limit. *Physical Review Letters*, 61(2):169–172, 1988. DOI: [10.1103/PhysRevLett.61.169](https://doi.org/10.1103/PhysRevLett.61.169).
- [78] A. Aspect, E. Arimondo, R. Kaiser, N. Vansteenkiste, and C. Cohen-Tannoudji. Laser Cooling below the One-Photon Recoil Energy by Velocity-Selective Coherent Population Trapping. *Physical Review Letters*, 61(7):826–829, 1988. DOI: [10.1103/PhysRevLett.61.826](https://doi.org/10.1103/PhysRevLett.61.826).
- [79] M. H. Anderson, J. R. Ensher, M. R. Matthews, C. E. Wieman, and E. A. Cornell. Observation of Bose-Einstein Condensation in a Dilute Atomic Vapor. *Science*, 269(5221):198–201, 1995. DOI: [10.1126/science.269.5221.198](https://doi.org/10.1126/science.269.5221.198).
- [80] K. B. Davis, M.-O. Mewes, M. R. Andrews, N. J. van Druten, D. S. Durfee, D. M. Kurn, and W. Ketterle. Bose-Einstein Condensation in a Gas of Sodium Atoms. *Physical Review Letters*, 75(22):3969–3973, 1995. DOI: [10.1103/PhysRevLett.75.3969](https://doi.org/10.1103/PhysRevLett.75.3969).

- [81] M. A. Kasevich and S. Chu. Atomic Interferometry Using Stimulated Raman Transitions. *Physical Review Letters*, 67(2):181–184, 1991. doi: 10.1103/PhysRevLett.67.181.
- [82] T. L. Gustavson, P. Bouyer, and M. A. Kasevich. Precision Rotation Measurements with an Atom Interferometer Gyroscope. *Physical Review Letters*, 78(11):2046–2049, 1997. doi: 10.1103/PhysRevLett.78.2046.
- [83] T. L. Gustavson, A. Landragin, and M. A. Kasevich. Rotation Sensing with a Dual Atom-Interferometer Sagnac Gyroscope. *Classical and Quantum Gravity*, 17(12):2385, 2000. doi: 10.1088/0264-9381/17/12/311.
- [84] D. S. Durfee, Y. K. Shaham, and M. A. Kasevich. Long-Term Stability of an Area-Reversible Atom-Interferometer Sagnac Gyroscope. *Physical Review Letters*, 97(24):240801, 2006. doi: 10.1103/PhysRevLett.97.240801.
- [85] G. Rosi, F. Sorrentino, L. Cacciapuoti, M. Prevedelli, and G. M. Tino. Precision Measurement of the Newtonian Gravitational Constant Using Cold Atoms. *Nature*, 510(7506):518–521, 2014. doi: 10.1038/nature13433.
- [86] H. Mabuchi and A. C. Doherty. Cavity Quantum Electrodynamics: Coherence in Context. *Science*, 298(5597):1372–1377, 2002. doi: 10.1126/science.1078446.
- [87] C. Monroe. Quantum Information Processing with Atoms and Photons. *Nature*, 416(6877):238–246, 2002. doi: 10.1038/416238a.
- [88] M. Saffman, T. G. Walker, and K. Mølmer. Quantum Information with Rydberg Atoms. *Reviews of Modern Physics*, 82(3):2313–2363, 2010. doi: 10.1103/RevModPhys.82.2313.
- [89] Z. Hadzibabic, P. Krüger, M. Cheneau, B. Battelier, and J. Dalibard. Berezinskii–Kosterlitz–Thouless Crossover in a Trapped Atomic Gas. *Nature*, 441(7097):1118–1121, 2006. doi: 10.1038/nature04851.
- [90] I. Bloch, J. Dalibard, and W. Zwerger. Many-Body Physics with Ultracold Gases. *Reviews of Modern Physics*, 80(3):885–964, JUL-SEP 2008. doi: 10.1103/RevModPhys.80.885.

- [91] D. Schlippert, J. Hartwig, H. Albers, L. L. Richardson, C. Schubert, A. Roura, W. P. Schleich, W. Ertmer, and E. M. Rasel. Quantum Test of the Universality of Free Fall. *Physical Review Letters*, 112(20):203002, 2014. DOI: [10.1103/PhysRevLett.112.203002](https://doi.org/10.1103/PhysRevLett.112.203002).
- [92] N. Navon, A. L. Gaunt, R. P. Smith, and Z. Hadzibabic. Critical Dynamics of Spontaneous Symmetry Breaking in a Homogeneous Bose Gas. *Science*, 347(6218):167–170, 2015. DOI: [10.1126/science.1258676](https://doi.org/10.1126/science.1258676).
- [93] C. J. Foot. *Atomic Physics*. Oxford University Press, 2005. 354 pp.
- [94] H. J. Metcalf and P. van der Straten. *Laser Cooling and Trapping*. Springer Science & Business Media, 2012. 329 pp.
- [95] C. J. Pethick and H. Smith. *Bose-Einstein Condensation in Dilute Gases*. publisherNameCambridge University Press, 2008.
- [96] C. Cohen-Tannoudji and D. Guéry-Odelin. *Advances in Atomic Physics: An Overview*. World Scientific, 2011.
- [97] C. S. Adams and E. Riis. Laser Cooling and Trapping of Neutral Atoms. *Progress in Quantum Electronics*, 21(1):1–79, 1997. DOI: [10.1016/S0079-6727\(96\)00006-7](https://doi.org/10.1016/S0079-6727(96)00006-7).
- [98] M. Geissbuehler and T. Lasser. How to Display Data by Color Schemes Compatible with Red-Green Color Perception Deficiencies. *Optics Express*, 21(8):9862, 2013. DOI: [10.1364/OE.21.009862](https://doi.org/10.1364/OE.21.009862).
- [99] G. Vrijen, O. Hosten, J. Lee, S. Bernon, and M. A. Kasevich. Raman Lasing with a Cold Atom Gain Medium in a High-Finesse Optical Cavity. *Physical Review Letters*, 107(6):063904, 2011. DOI: [10.1103/PhysRevLett.107.063904](https://doi.org/10.1103/PhysRevLett.107.063904).
- [100] E. D. Black. An Introduction to Pound-Drever-Hall Laser Frequency Stabilization. *American Journal of Physics*, 69(1):79–87, 2001. DOI: [10.1119/1.1286663](https://doi.org/10.1119/1.1286663).
- [101] R. W. P. Drever, J. L. Hall, F. V. Kowalski, J. Hough, G. M. Ford, A. J. Munley, and H. Ward. Laser Phase and Frequency Stabilization Using an Optical Resonator. *Applied Physics B*, 31(2):97–105, 1983. DOI: [10.1007/BF00702605](https://doi.org/10.1007/BF00702605).

- [102] R. W. Fox, C. W. Oates, and L. W. Hollberg. Stabilizing Diode Lasers to High-Finesse Cavities. In: *Experimental Methods in the Physical Sciences*. Ed. by R. D. v. Z. Looney and J. Patrick. Vol. 40. Cavity-Enhanced Spectroscopies. Academic Press, 2003, 1–46.
- [103] R. Grimm, M. Weidmüller, and Y. B. Ovchinnikov. Optical Dipole Traps for Neutral Atoms. In: *Advances In Atomic, Molecular, and Optical Physics*. Ed. by B. B. Walther and Herbert. Vol. 42. Academic Press, 2000, 95–170.
- [104] M. S. Safronova, B. Arora, and C. W. Clark. Frequency-Dependent Polarizabilities of Alkali-Metal Atoms from Ultraviolet through Infrared Spectral Regions. *Physical Review A*, 73(2):022505, 2006. DOI: [10.1103/PhysRevA.73.022505](https://doi.org/10.1103/PhysRevA.73.022505).
- [105] J. P. Brantut, J. F. Clément, M. R. de Saint Vincent, G. Varoquaux, R. A. Nyman, A. Aspect, T. Bourdel, and P. Bouyer. Light-Shift Tomography in an Optical-Dipole Trap for Neutral Atoms. *Physical Review A*, 78(3):031401, 2008. DOI: [10.1103/PhysRevA.78.031401](https://doi.org/10.1103/PhysRevA.78.031401).
- [106] B. Arora, M. S. Safronova, and C. W. Clark. Magic wavelengths for the  $np$ - $ns$  transitions in alkali-metal atoms. *Physical Review A*, 76(5):052509, 2007. DOI: [10.1103/PhysRevA.76.052509](https://doi.org/10.1103/PhysRevA.76.052509).
- [107] M. S. Safronova and U. I. Safronova. Critically evaluated theoretical energies, lifetimes, hyperfine constants, and multipole polarizabilities in  $^{87}\text{Rb}$ . *Physical Review A*, 83(5):052508, 2011. DOI: [10.1103/PhysRevA.83.052508](https://doi.org/10.1103/PhysRevA.83.052508).
- [108] L. Pezzè, A. Smerzi, M. K. Oberthaler, R. Schmied, and P. Treutlein. Non-Classical States of Atomic Ensembles: Fundamentals and Applications in Quantum Metrology, 2016. arXiv: [1609.01609 \[quant-ph\]](https://arxiv.org/abs/1609.01609).
- [109] E. Rocco, R. N. Palmer, T. Valenzuela, V. Boyer, A. Freise, and K. Bongs. Fluorescence Detection at the Atom Shot Noise Limit for Atom Interferometry. *New Journal of Physics*, 16(9):093046, 2014. DOI: [10.1088/1367-2630/16/9/093046](https://doi.org/10.1088/1367-2630/16/9/093046).

- [110] J. Guéna, M. Abgrall, A. Clairon, and S. Bize. Contributing to TAI with a Secondary Representation of the SI Second. *Metrologia*, 51:108–120, 2014. DOI: 10.1088/0026-1394/51/1/108.
- [111] G. W. Biedermann. Zero-Dead-Time Operation of Interleaved Atomic Clocks. *Phys. Rev. Lett.* 111:170802, 2013. DOI: 10.1103/PhysRevLett.111.170802.
- [112] J. Borregaard and A. S. Sørensen. Near-Heisenberg-Limited Atomic Clocks in the Presence of Decoherence. *Phys. Rev. Lett.* 111:090801, 2013. DOI: 10.1103/PhysRevLett.111.090801.
- [113] R. Horodecki, P. Horodecki, M. Horodecki, and K. Horodecki. Quantum Entanglement. *Reviews of Modern Physics*, 81(2):865–942, 2009. DOI: 10.1103/RevModPhys.81.865.
- [114] N. Li and S. Luo. Entanglement Detection via Quantum Fisher Information. *Physical Review A*, 88(1):014301, 2013. DOI: 10.1103/PhysRevA.88.014301.
- [115] C. W. Helstrom. Minimum Mean-Squared Error of Estimates in Quantum Statistics. *Physics Letters A*, 25(2):101–102, 1967. DOI: 10.1016/0375-9601(67)90366-0.
- [116] S. L. Braunstein and C. M. Caves. Statistical Distance and the Geometry of Quantum States. *Physical Review Letters*, 72(22):3439–3443, 1994. DOI: 10.1103/PhysRevLett.72.3439.
- [117] S. B. Papp, K. S. Choi, H. Deng, P. Lougovski, S. J. van Enk, and H. J. Kimble. Characterization of Multipartite Entanglement for One Photon Shared Among Four Optical Modes. *Science*, 324(5928):764–768, 2009. DOI: 10.1126/science.1172260.
- [118] N. Brunner, D. Cavalcanti, S. Pironio, V. Scarani, and S. Wehner. Bell Nonlocality. *Reviews of Modern Physics*, 86(2), 2014. DOI: 10.1103/RevModPhys.86.419.
- [119] J. F. Clauser, M. A. Horne, A. Shimony, and R. A. Holt. Proposed Experiment to Test Local Hidden-Variable Theories. *Physical Review Letters*, 23(15):880–884, 1969. DOI: 10.1103/PhysRevLett.23.880.

- [120] J. Tura, R. Augusiak, A. B. Sainz, T. Vértesi, M. Lewenstein, and A. Acín. Detecting Nonlocality in Many-Body Quantum States. *Science*, 344(6189):1256–1258, 2014. DOI: [10.1126/science.1247715](https://doi.org/10.1126/science.1247715).
- [121] A. K. Ekert. Quantum Cryptography Based on Bell’s Theorem. *Physical Review Letters*, 67(6):661–663, 1991. DOI: [10.1103/PhysRevLett.67.661](https://doi.org/10.1103/PhysRevLett.67.661).
- [122] J. Barrett, L. Hardy, and A. Kent. No Signaling and Quantum Key Distribution. *Physical Review Letters*, 95(1):010503, 2005. DOI: [10.1103/PhysRevLett.95.010503](https://doi.org/10.1103/PhysRevLett.95.010503).
- [123] A. Acín, N. Brunner, N. Gisin, S. Massar, S. Pironio, and V. Scarani. Device-Independent Security of Quantum Cryptography against Collective Attacks. *Physical Review Letters*, 98(23):230501, 2007. DOI: [10.1103/PhysRevLett.98.230501](https://doi.org/10.1103/PhysRevLett.98.230501).
- [124] R. Colbeck and A. Kent. Private Randomness Expansion with Untrusted Devices. *Journal of Physics A: Mathematical and Theoretical*, 44(9):095305, 2011. DOI: [10.1088/1751-8113/44/9/095305](https://doi.org/10.1088/1751-8113/44/9/095305).
- [125] S. Pironio, A. Acín, S. Massar, A. Boyer de la Giroday, D. N. Matsukevich, P. Maunz, S. Olmschenk, D. Hayes, L. Luo, T. A. Manning, and C. Monroe. Random Numbers Certified by Bell’s Theorem. *Nature*, 464(7291):1021–1024, 2010. DOI: [10.1038/nature09008](https://doi.org/10.1038/nature09008).
- [126] T. Kovachy, P. Asenbaum, C. Overstreet, C. A. Donnelly, S. M. Dickerson, A. Sugarbaker, J. M. Hogan, and M. A. Kasevich. Quantum Superposition at the Half-Metre Scale. *Nature*, 528(7583):530–533, 2015. DOI: [10.1038/nature16155](https://doi.org/10.1038/nature16155).
- [127] M. Eibl, S. Gaertner, M. Bourennane, C. Kurtsiefer, M. Żukowski, and H. Weinfurter. Experimental Observation of Four-Photon Entanglement from Parametric down-Conversion. *Physical Review Letters*, 90(20):200403, 2003. DOI: [10.1103/PhysRevLett.90.200403](https://doi.org/10.1103/PhysRevLett.90.200403).

- [128] Z. Zhao, T. Yang, Y.-A. Chen, A.-N. Zhang, M. Żukowski, and J. W. Pan. Experimental Violation of Local Realism by Four-Photon Greenberger-Horne-Zeilinger Entanglement. *Physical Review Letters*, 91(18):180401, 2003. DOI: [10.1103/PhysRevLett.91.180401](https://doi.org/10.1103/PhysRevLett.91.180401).
- [129] M. Giustina et al. Significant-Loophole-Free Test of Bell's Theorem with Entangled Photons. *Physical Review Letters*, 115(25):250401, 2015. DOI: [10.1103/PhysRevLett.115.250401](https://doi.org/10.1103/PhysRevLett.115.250401).
- [130] L. K. Shalm et al. Strong Loophole-Free Test of Local Realism\*. *Physical Review Letters*, 115(25):250402, 2015. DOI: [10.1103/PhysRevLett.115.250402](https://doi.org/10.1103/PhysRevLett.115.250402).
- [131] B. P. Lanyon, M. Zwerger, P. Jurcevic, C. Hempel, W. Dür, H. J. Briegel, R. Blatt, and C. F. Roos. Experimental Violation of Multipartite Bell Inequalities with Trapped Ions. *Physical Review Letters*, 112(10):100403, 2014. DOI: [10.1103/PhysRevLett.112.100403](https://doi.org/10.1103/PhysRevLett.112.100403).
- [132] J. Hofmann, M. Krug, N. Ortegel, L. Gérard, M. Weber, W. Rosenfeld, and H. Weinfurter. Heralded Entanglement Between Widely Separated Atoms. *Science*, 337(6090):72–75, 2012. DOI: [10.1126/science.1221856](https://doi.org/10.1126/science.1221856).
- [133] W. Pfaff, T. H. Taminiau, L. Robledo, H. Bernien, M. Markham, D. J. Twitchen, and R. Hanson. Demonstration of Entanglement-by-Measurement of Solid-State Qubits. *Nature Physics*, 9(1):29–33, 2013. DOI: [10.1038/NPHYS2444](https://doi.org/10.1038/NPHYS2444).
- [134] B. Hensen et al. Loophole-Free Bell Inequality Violation Using Electron Spins Separated by 1.3 Kilometres. *Nature*, 526(7575):682–686, 2015. DOI: [10.1038/nature15759](https://doi.org/10.1038/nature15759).
- [135] J. Tura, R. Augusiak, A. B. Sainz, B. Lücke, C. Klempt, M. Lewenstein, and A. Acín. Nonlocality in Many-Body Quantum Systems Detected with Two-Body Correlators. *Annals of Physics*, 362:370–423, 2015. DOI: [10.1016/j.aop.2015.07.021](https://doi.org/10.1016/j.aop.2015.07.021).
- [136] I. D. Leroux, M. H. Schleier-Smith, and V. Vuletić. Implementation of Cavity Squeezing of a Collective Atomic Spin. *Physical Review Letters*, 104(7):073602, 2010. DOI: [10.1103/PhysRevLett.104.073602](https://doi.org/10.1103/PhysRevLett.104.073602).

- [137] H. Zhang, R. McConnell, S. Cuk, Q. Lin, M. H. Schleier-Smith, I. D. Leroux, and V. Vuletić. Collective State Measurement of Mesoscopic Ensembles with Single-Atom Resolution. *Physical Review Letters*, 109(13):133603, 2012. DOI: [10.1103/PhysRevLett.109.133603](https://doi.org/10.1103/PhysRevLett.109.133603).
- [138] B. Lücke, M. Scherer, J. Kruse, L. Pezze, F. Deuretzbacher, P. Hyllus, O. Topic, J. Peise, W. Ertmer, J. Arlt, L. Santos, A. Smerzi, and C. Klempt. Twin Matter Waves for Interferometry Beyond the Classical Limit. *Science*, 334(6057):773–776, 2011. DOI: [10.1126/science.1208798](https://doi.org/10.1126/science.1208798).
- [139] F. Haas, J. Volz, R. Gehr, J. Reichel, and J. Esteve. Entangled States of More Than 40 Atoms in an Optical Fiber Cavity. *Science*, 344(6180):180–183, 2014. DOI: [10.1126/science.1248905](https://doi.org/10.1126/science.1248905).
- [140] R. McConnell, H. Zhang, J. Hu, S. Cuk, and V. Vuletić. Entanglement with Negative Wigner Function of Almost 3,000 Atoms Heralded by One Photon. *Nature*, 519(7544):439, 2015. DOI: [10.1038/nature14293](https://doi.org/10.1038/nature14293).
- [141] C. M. Caves. Quantum Limits on Noise in Linear Amplifiers. *Physical Review D*, 26(8):1817–1839, 1982. DOI: [10.1103/PhysRevD.26.1817](https://doi.org/10.1103/PhysRevD.26.1817).
- [142] R. McConnell, H. Zhang, S. Cuk, J. Hu, M. H. Schleier-Smith, and V. Vuletić. Generating Entangled Spin States for Quantum Metrology by Single-Photon Detection. *Physical Review A*, 88(6):063802, 2013. DOI: [10.1103/PhysRevA.88.063802](https://doi.org/10.1103/PhysRevA.88.063802).